POLITECNICO DI TORINO

Master's Degree in Aerospace Engineering

Academic Year 2025/2026

Graduation Session March/April 2026

Numerical Investigation of the LAPCAT-II Dual-Mode Ramjet Combustor

Supervisors

Prof. Nicole VIOLA

Prof. Christer FUREBY

M. Sc. Alessandro ERCOLE

M. Sc. Rasmus ROBERTSSON

Candidate

Davide Maria TOSIN

Numerical Investigation of the LAPCAT-II Dual-Mode Ramjet Combustor

Davide Maria Tosin

Abstract

The aim of this work is to perform a numerical investigation (CFD) of the dual-mode ramjet combustor tested at the ONERA LAERTE facility within the European LAPCAT-II (Long-Term Advanced Propulsion Concepts and Technologies II) project. LAPCAT-II explored advanced propulsion concepts for reducing the duration of antipodal flights by combining high-speed performance and sustainability. The proposed configuration relies on hydrogen fuel and consists of an Air Turbo Rocket (ATR) for the acceleration phase, followed by a dual-mode ramjet capable of transitioning from ramjet to scramjet operation, enabling cruise conditions up to Mach 8.

The study is based on high-fidelity reactive Large Eddy Simulations (RLES), which resolve the largest turbulent structures while modeling the smaller scales. This approach allows a detailed representation of the unsteady reacting flow, including shock–flame interactions and turbulence–chemistry interactions, which are key features of dual-mode operation.

Compared to previous numerical investigations of this configuration, the present work focuses on improving the physical modeling by including radiative heat transfer through the P1 radiation model. Radiation can significantly affect temperature fields and wall heat fluxes in high-temperature hydrogen combustion, and its inclusion increases the predictive capability of the simulations.

In addition, a one-dimensional conjugate heat transfer boundary condition (1D-CHT BC) is implemented coupled to the radiation model to estimate wall temperatures and heat loads without explicitly resolving the solid domain. Accurate prediction of thermal loads is essential for the design of such propulsion systems, as wall thermal conditions influence material constraints, structural integrity, and may also affect the internal flow field and combustion behavior.

This work therefore provides a more complete numerical characterization of the coupled aerodynamic, combustion, and thermal phenomena governing hydrogen-fueled dual-mode ramjet operations.

ACKNOWLEDGMENTS

To my family, my girlfriend, my friends and anyone who never stops exploring.

I would like to sincerely thank my supervisor Prof. Nicole Viola, thanks to her, I had the possibility to make one of my dreams come true.

I am also grateful to Prof. Christer Fureby, for entrusting me this difficult yet rewarding task and for the insightful and inspiring discussions about high-speed propulsion. Also, I would like to thank NAISS for the computational resources provided, with honor mentions to “Dardel” and “Tetralith” for having withstand my restless job submissions. I want to express my gratitude to Prof. Xue-Song Bai, Phd. Yuchen Zhou and Pierre Vauquelin for entrusting me CCM and for their support. And I would like to express my gratitude to Tommie Nilsson for his very precise observations and competence.

I am also deeply grateful to Rasmus Robertsson and Alessandro Ercole for their valuable feedback, patience, discussions, and for the time we spent together in the best office of the Heat Transfer corridor. Your presence and competence was really inspiring and motivated me through the journey. And I am very grateful for everyone at the Department of Energy Sciences at Lund University for the time we shared, and for the work environment they create day-by-day. I have learned a lot from this unforgettable experience thanks to everyone.

An honor mentions goes to: Margherita for the energy and good environment she creates; Federico for the laugh and time we had together; Ludvig for the philosophical discussion and the ping pong matches; Carl-Otto for his hospitality and good vibes; Reza for the engaging discussions and laugh; Pamela for the Turin-related discussions and for the welcome; Christian for his incredible language-learning speed; Himani and Bjorn for the long and engaging discussions; and also Yuxian, Eduardo, Rasmus P., Haoyang, and everyone else for the time spent together. I really enjoyed Sweden and the atmosphere you created.

At last but not least, I would like to thank my friends, Manuel in particular, my family, in particular my parents Matteo and Rita and my brother Niccolò for supporting me in the journey of life and for their trust in me, and my girlfriend Natia, to make everything brighter and for believing in me.

Table of Contents

List of Figures

List of Tables

Acronyms

CFD	Computational Fluid Dynamics.
LAPCAT-II	Long-Term Advanced Propulsion Concepts And Technologies-II.
ONERA	Office National d'Études et de Recherches Aérospatiales (National Office for Aerospace Studies and Research).
ATR	Air Turbo Rocket.
HRE	Hypersonic Research Engine.
DMRJ	Dual-Mode Ramjet.
NEZ	No Escape Zone.
BVR	Beyond Visual Range.
SSTO	Single Stage To Orbit.
TSTO	Two Stage To Orbit.
NASP	National Aerospace Plane.
TBC	Thermal Barrier Coating.
YSZ	Yttria-Stabilized Zirconia.
SEM	Scanning Electron Microscopy.
TCI	Turbulence-Chemistry Interaction.

LES	Large Eddy Simulations.
JANAF	Joint Army–Navy–Air Force.
RANS	Reynolds Averaged Navier-Stokes.
1D CHT BC	One-Dimensional Conjugate Heat Transfer Boundary Condition.
LES IQ	LES Index of Quality.
BC	Boundary Condition(s).
CCM	Chemistry Coordinate Mapping.
2D	Two Dimensional/Dimension(s).
3D	Three Dimensional/Dimension(s).
HPC	High Performance Computing.
NAISS	The National Academic Infrastructure for Supercomputing in Sweden.
LDKM	Localized Dynamic k-equation Model.
WMLES	Wall-Modeled LES.
OH-PLIF	Hydroxyl (OH) Planar Laser-Induced Fluorescence.
TKI	Takeno Flame Index.

Chapter 1

Introduction

The aim of this work is to conduct a numerical investigation of the dual-mode ramjet combustor tested at ONERA LAERTE facility within the European LAPCAT-II project (Long-term Advanced Propulsion Concepts And Technologies-II). [1] The goal of the project was to further investigate advanced propulsion concepts for reducing the time of antipodal flights, in other words, flights between two diametrically opposite points on the globe.

The "need for speed" is on the rise. Whatever for civilian, dual-use or military applications, as we evolve as a civilization, there is a strong correlation between the speed of the means of transportation and the advancement of a society. [2] Towards the high-end side of this matter lies aerospace engineering: the use of the third dimension unlocked huge opportunities in our society, and during the past years we witnessed a development with unmatched speed about aerospace related technologies. To give a perspective, we went from the Wright brothers' maiden flight on December 17, 1903 to the X-15 Mach 6.7 record breaking flight on October 3, 1967 in slightly less than 64 years.

Fast forward to the present, new and important challenges arise, and the goal of the LAPCAT-II European project, addressed in this work with the MR2 variant, was indeed ambitious: combine high-speed and sustainability envisioning an hydrogen fueled propulsion system made by an Air Turbo Rocket (ATR, a combined-cycle rocket using atmospheric air as oxidizer) for acceleration and then a dual-mode ramjet, meaning a ramjet with capabilities of transition to scramjet (supersonic combustion ramjet), for reaching Mach 8 at cruise.

The level of complexity is remarkable: the fuel could be a topic on its own, not to mention the transition between the types of engine, heat management, etc., but in this work we will "modestly" address the dual-mode ramjet.

Many new terms and concepts have emerged and will be addressed in the upcoming chapters: the background chapters will give the reader a broader perspective and provide familiarity with the topic from a brief history to the low-level description of the mathematical models. Then, we will dig into the experimental and numerical campaign.

Previous studies were carried out for this case, [3, 4, 5] but the aim of this work is to enhance the fidelity of the simulation, including physical effects not always taken into account: radiation modeling and a more detailed thermal boundary condition to better describe the temperature evolution along the walls.

Chapter 2

General Background

> ***"[. . .] There is currently no conclusive evidence that these requirements can be met: nevertheless, the present study starts with the basic assumption that stable supersonic combustion in an engine is possible. "***
>
> ***Richard J. Weber and John S. McKay, Sep. 1958. From [6]***

The epigraph reported is part of the “Combustion system processes and components” chapter from [6], and highlights the complexity of the leading physical phenomena that needs to find common ground to deliver an efficient high-speed propulsion system.

In this chapter, a brief introduction to the high-speed air-breathing propulsion topic will be given, while for a more detailed overview, both historical and technical, some references for an interested reader are reported.[6, 7, 8]

2.1 Why

The “need for speed” is rising, regarding dual-use, civilian and military applications, as economical growth and means of transportation speed are strongly correlated. [2]

In the high-end of the speed-category, lies aerospace engineering, with its remarkable development speed. During history, new frontiers both endo- and eso-atmospherics[1] have been unlocked from the advancements of this field.

The “core” of an aircraft is the engine, essential to provide the necessary thrust to generate lift and overcome drag forces. Chemical-propulsion is widely used in

---

[1] endo-atmospheric means within the measurable atmosphere (altitude of $60 - 100$ [km]), and eso-atmospheric means outside

aerospace, providing the desired thrust by employing combustion processes that essentially need two components: fuel and oxidizer. [9]

Regarding eso-atmospheric flights, the lack of oxidizer present in the atmosphere (oxygen), requires dedicated tanks to carry the oxidizer if a chemical propulsion system is employed. Meanwhile, regarding endo-atmospheric flights, there is the possibility of using atmospheric air that contains oxygen. Engines that “scoops” air to employ combustion are referred as air-breathing[2] engines.

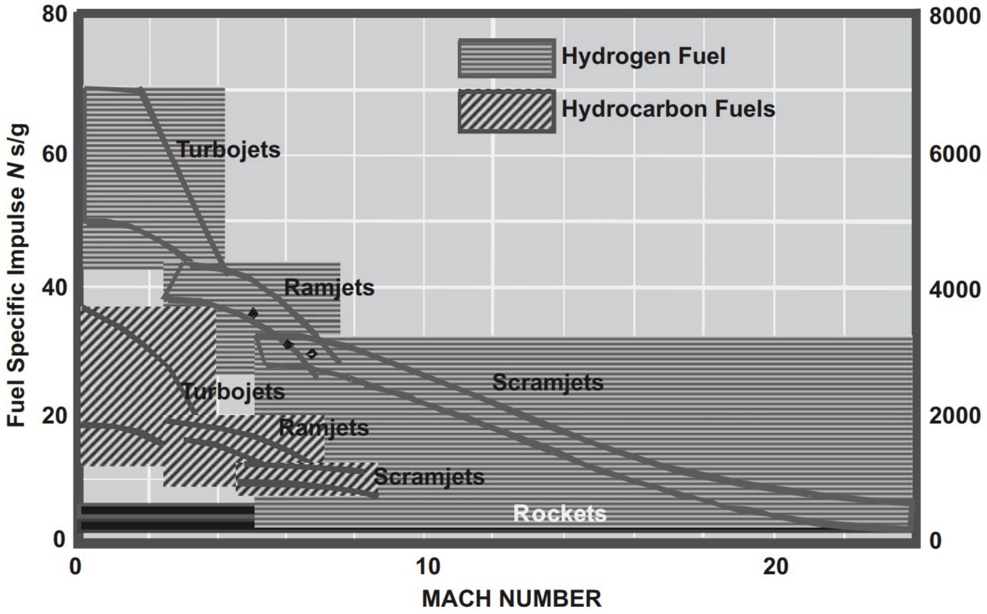

Figure 2.1: Specific impulse plotted against Mach number of hydrogen and hydrocarbon fuels. Reproduced from [8].

The reported plot, shows that the theoretical most efficient way to reach high-speed in endo-atmospheric flights is to use such air-breathing engines.

In principle, a ramjet or a scramjet are much more mechanically simple compared to gas turbines engines, while they share the same underlying working principle, common in air-breathing architectures:

[Take in air] → [Compress it] → [Mix it with fuel and ignite] → [Expands out]

Gas turbines engines do compression and expansion employing compressors and turbines, complex and rotating components that are a topic on its own, while ram- and scramjet are just a duct/tube, with the only common and essential component with gas turbine engines being the combustion chamber, as combustion is needed to increase the gas internal energy prior the thrust-generating expansion.

However, what seems to be gained in mechanical simplicity is compensated by increased challenges. Worth noticing, those engines are not supposed to do a proper take-off starting from “zero velocity” as other engines could do.

---

[2] Sometimes also called “airbreathing” or “air breathing”

In this flow, two main phenomena interacts and contributes:

$$\text{Compressible gas dynamics} \Leftrightarrow \text{Combustion}$$

Combustion and compressibility could be a topic on their own fro their complexities, and more challenges arose due to newly observed phenomena. One example is the HRE (Hypersonic Research Engine) developed in the Unites States that led to the discovery of the so-called "Edney interactions" regarding shock-shock interactions. [10] Other interesting phenomena are observed when shockwaves interacts with combustion, boundary and shear layers all within a duct-shaped engine. [11, 6, 7]

Furthermore, as also showed in Fig. 2.1 , this simplicity becomes crucial after surpassing the speed of sound, where compression is employed by exploiting shock-waves generated from the new compressible phenomena typical of this physic realm (detailed addressed here [12]).

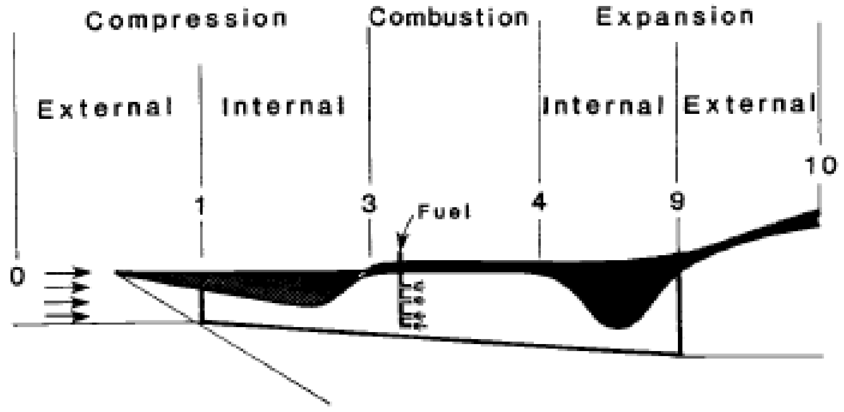

Ramjet

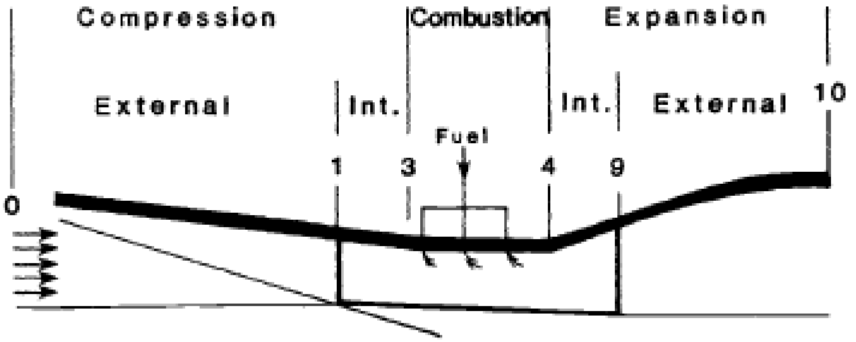

Scramjet

Figure 2.2: Station of ramjet and scramjet engine. Reproduced from [6].

The theoretical core idea of ramjet and scramjet is similar, but the actual implementation is very different. The main difference is the regime of the combustion:

ramjet slows down the high-speed inlet air to subsonic speed, employing combustion in the classical subsonic regime. This has advantages regarding flame stabilization and combustion properties, as the combustion typically used is in subsonic regime, but as the maximum velocity further increases, slow down the supersonic flow to subsonic would mean to have dissociation effects, detrimental for combustion. [6]

Therefore, a scramjet try to inject, mix and ignite the fuel while maintaining the core flow supersonic, avoiding thermodynamics penalties detrimental for the combustor performances. As simple as it may be, the word “supersonic combustion” brings a lot of new challenges. Except the sophisticated interactions mentioned and reported also in [11, 6], the main problem is that supersonic flow through a combustor means that the typical flow-through time is, at most, in the order of some millisecond [ms]. In this time, the fuel needs to be injected, mixed, ignite ans sustain an efficient and fairly stable flame.

The combination of this two engines is the dual-mode ramjet (DMRJ), where a transition between subsonic and supersonic combustion is employed. The case studied here, triggered mode transition by changing inlet conditions.

Through the years, remarkable progresses have been made, and now various air-breathing high-speed engines are emerging or have already emerged.

2.2 Where

In this section, the three main application for the aforementioned high-speed air-breathing propulsion engines are presented.

2.2.1 Civil

Those high-speed engines could unlock the possibility to drastically reduce antipodal flight time around the globe. One remarkable example of this is given by the European STRATOFLY project. [13, 14]

Figure 2.3: STRATOFLY MR3 concept. Reproduced from [13].

In this project, a waverider configuration was studied to achieve hypersonic flight while also employing an hydrogen-fueled propulsion system, where the stored liquid hydrogen (LH_2), also served as the cooling fluid. Detailed features in [13].

It can be observed the striking difference compared to conventional aircraft: the engine (mounted on top, with its intake in dark grey) is merged with the airframe configuration, in order to reduce drag and performance penalties, but has also the necessity to take-off from subsonic speed, operating in a wide window regarding flow regimes.

2.2.2 Military

Another field of application is the military world. Air-breathing missiles have the advantage of not carry oxidizer tanks within the missile structure, constituting a considerable weight-penalty in rocket-powered missiles, even more detrimental if the task to carry out is an interception or any climb phases, for a simple interplay between potential and kinetic energy.

By switching to air-breathing missile engines, range and “no escape zone” (NEZ)[3] are increased.

Figure 2.4: MBDA Meteor air-to-air missile. Reproduced from [15].

A notable example, regarding an air-to-air beyond-visual-range (BVR) missile, is given by the European-developed Meteor missile, from the European consortium MBDA, using a solid-fuel ramjet. [16, 17]

2.2.3 Space

Regarding space, various single-stage-to-orbit (SSTO) and two-stage-to-orbit (TSTO) concepts have been studied. One of the most remarkable effort regarding a SSTO concept was the Rockwell X-30, extensively treated in [6]. Also known as National Aerospace Spaceplane (NASP), had the ambitious goal of employing a multi-stage propulsion system where high-speed air-breathing propulsion was essential prior orbital insertion using a rocket-based propulsion system. Another concept here mentioned is the Sänger II TSTO concept. [19] The goal was to develop a reusable TSTO, with the first stage being an air-breathing stage that “piggybacking” an upper rocket-powered able to deploy the carried payload.

---

[3] A zone where interception is guaranteed from an energy-budget perspective, no matter the target maneuvering abilities

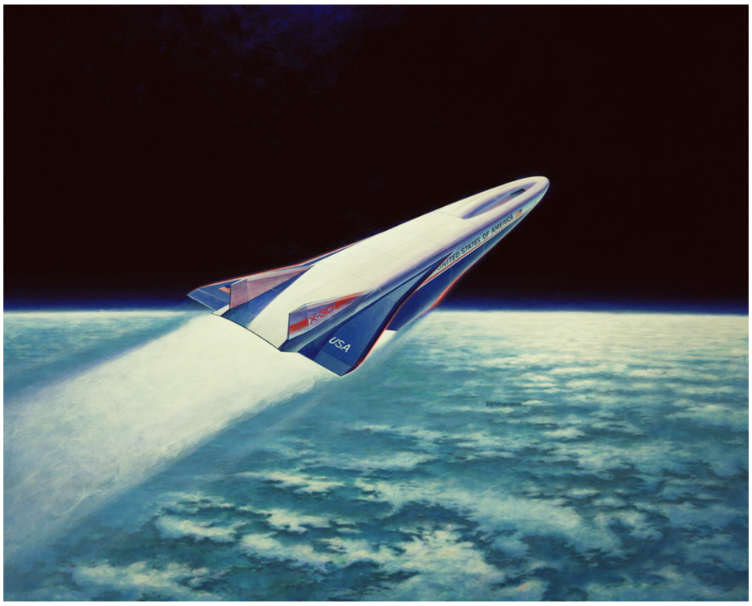

Figure 2.5: Rockwell X-30 (NASP) concept. Reproduced from [18].

Figure 2.6: Sänger II TSTO concept. Reproduced from [18].

Chapter 3

LAPCAT-II Wind Tunnel Experiments

> ***"Was du ererbt von deinen Vätern hast,***
> ***erwirb es, um es zu besitzen."***
>
> *"What you have inherited from your ancestors, you must earn in order to possess it."*
>
> ***J. W. von Goethe,* Faust I, 1828-1829**

Now it is time to unfold the experimental campaign. Since our models have the aim to reproduce reality, it is of the utmost importance to have a look at the "reality" we want to reproduce.

3.1 LAERTE test facility

ONERA-LAERTE test facility, located at Palaiseau (France), was developed during the French PREPHA program [20] with the aim of studying supersonic combustion. A new supersonic combustion chamber has been designed and manufactured for the LAPCAT-II project (European 7^{th} Framework Program). [1]

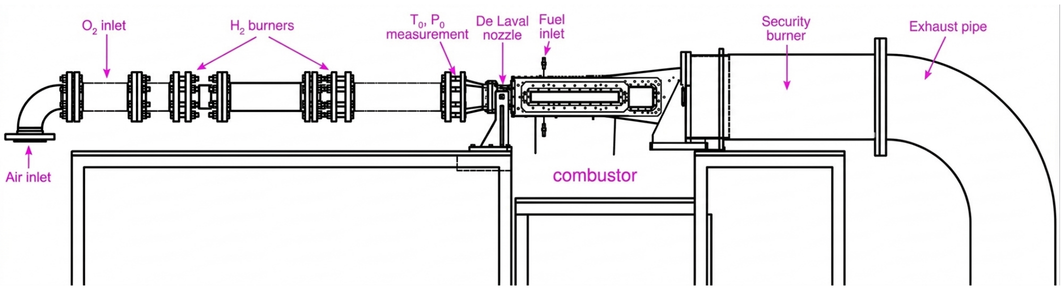

Figure 3.1: LAPCAT-II combustor in ONERA-LAERTE. Redrawn from [21]

The combustor is fed with vitiated hot air provided by a two-stage burner employing H_2 and air combustion and O_2 replenishment to keep the molar fraction at 0.21. Total temperature (T^0) can go up to 1800-1900 [K], total pressure (p^0) 1-1.2 [MPa] and the facility is operated in blow-down mode [1], while the test section works as a heat-sink.

A computer is used to ensure stability and reproducibility of the experiments, and water cooling was not used in this campaign, hence the overall duration of a test was around 1 minute, with a 5-15 [s] time window of useful temperature, depending on test conditions as well. [21]

The total temperature and total pressure are measured in a pipe, with an inner diameter of 105 [mm], 220 [mm] upstream of the Laval nozzle's throat. In particular the pressure measured at the walls is assumed to be the total pressure, while three thermocouples in different radial positions are used to estimate the total temperature which is calculated assuming a parabolic profile. [21]

3.2 Supersonic Combustion Chamber

The chamber is made of a copper alloy and has a constant width of 40 [mm], while axially it is divided into 5 sections.

1. **Section transformation:** to go from a circular section to the rectangular cross section of the chamber. This introduces additional large scale structures that could influence the inlet turbulence and velocity profiles. In a simulation, a careful assessment of that effect should be carried out;

2. **De Laval Nozzle:** a 2D (rectangular cross section) nozzle 64.9 [mm] long with two versions that can ensure a Mach number of 2 or 2.5. In this case the version ensuring Mach 2 was used. It is worth mentioning that the effective Mach number slightly depends on test conditions due to variations in:

   - Air composition;
   - Pressure;
   - Temperature.

   All of them introduced by the burners and the various interactions upstream;

3. **Isolator:** constant cross-area section with a height of 35.4 [mm] and a length of 215 [mm];

4. **Diverging Sections:** made in order to prevent thermal choking (heat release induced critical speed that could cause unstart of the engine). They are three diverging half angles with the following characteristics:

---

[1] A certain amount of high pressure and temperature gas is stored and then released to provide the desired flow conditions. A drawback is that the quantity stored is limited but the flow condition are controllable thanks to the reservoir

   (a) 1 [°] half-angle, 318 [mm] long
   (b) 3 [°] half-angle, 354.5 [mm] long
   (c) 1 [°] half-angle, 305 [mm] long

   The total length of the combustor is 1257.4 [mm].

5. **Exhaust Pipe:** following the outlet of the combustion chamber it is a 400 [mm] diameter pipe with approximately atmospheric pressure. It is worth mentioning that there is also a security burner in it whose effects should be considered.

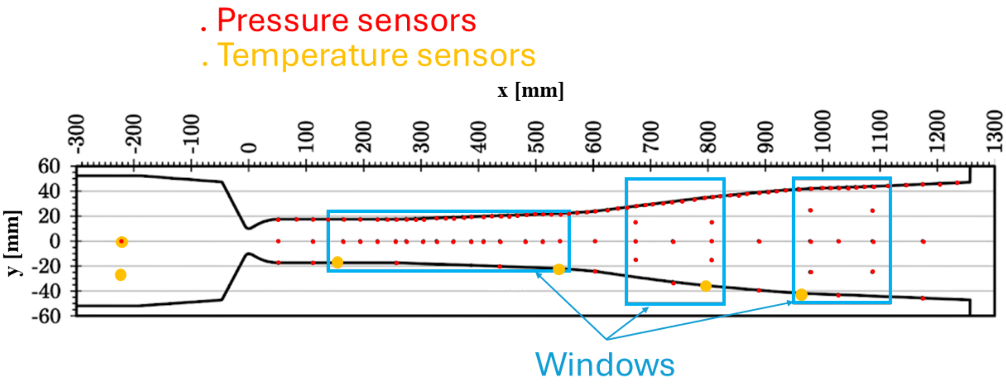

Figure 3.2: LAPCAT-II chamber measurement spots respect the chamber's width symmetry plane. Redrawn from [21]

Measurements include total pressure, total temperature, and static pressure sensors (up to 128 wall pressure transducers scanned at 10 [Hz]) calibrated annually in accordance with ISO 9001 certification located in the spanwise symmetry plane of the rectangular cross-section. [3, 21]

For a total pressure inferior to 90 [kPa] the flow in the combustor is over-expanded, with the transition from supersonic to subsonic within the combustor. The pressure after separation increases until the pressure in the exhaust pipe, and the separation's position is highly influenced by boundary and inlet conditions.

For the static temperature there were 4 thermocouples for measuring the temperature of the lower wall soldered at the inner wall with the TBC deposited afterward. Unluckily, after some runs the TBC had been removed hence measurements are not representative of the temperature over the TBC. [21]

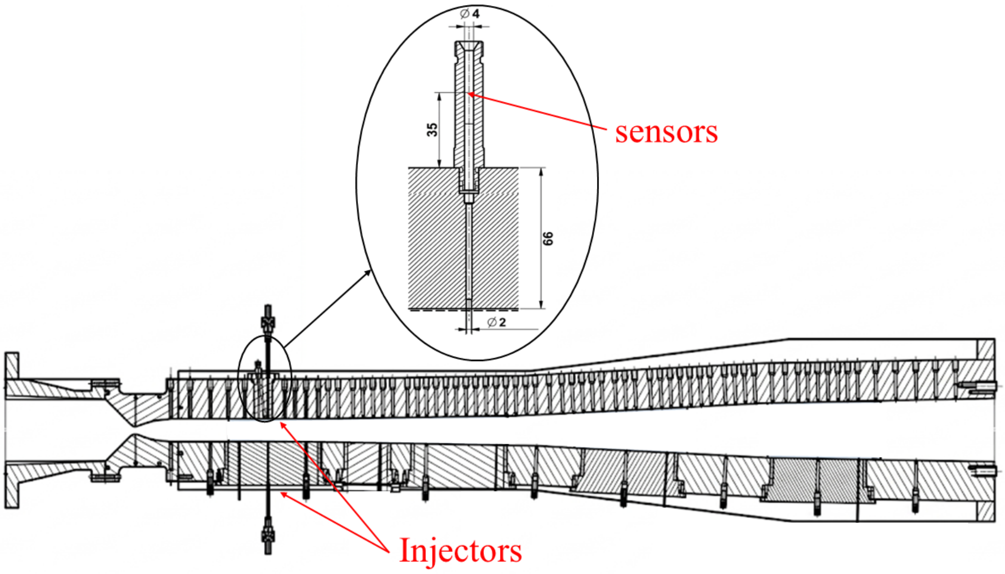

Figure 3.3: ONERA-LAERTE, LAPCAT combustion chamber overview. Redrawn from [21, 22]

The walls are not water-cooled hence, during the run, the wall temperature increases dramatically and continuously during the air heating phase and the experiments; a feature that should be considered in the simulations.

For the internal walls they include a 300 [μm] thermal barrier coating (TBC) of Yttrium Oxyde-stabilized Zirconia (YSZ, also known as Yttria-stabilized Zirconia) deposited after the installation of the measurement sensors. It has an average characteristic roughness size of ~ 65 [μm], resembling sandpaper, measured using scanning electron microscopy (SEM). [21]

Large fused silica windows are also present at different locations allowing both imaging techniques (Schlieren, PLIF, imaging, etc.) and single point measurements (LIF, CARS, etc.).

Injectors are 2 [mm] porthole injectors with pure gaseous hydrogen injected at sonic speed (the possibility of injecting a mixture with hydrocarbons is also reported, not used in this case). Fuel pressure and temperature are measured 104 [mm] upstream of the injection point. [21]

Chapter 4

Numerical Setup

> ***"Who owns the mesh, owns the solution."***
>
> ***Hrvoje Jasak*** [23]

After the experimental setup, it is now time to explore the numerical setup comprised of the models used, the boundary conditions employed, and the mesh: one of the most important parts of the simulation.

4.1 Methods and models

4.1.1 Overview

The solver used, is an in-house developed solver within OpenFOAM 7, an open-source C++ library. [24, 25].

The solver, called *rhoCentralTurbReactingFoam*, is an hybridization of two solvers, including turbulence-combustion interactions (TCI):

- *rhoCentralFoam*: a density-based, transient, shock-capturing solver for high-speed compressible flows, using the Kurganov-Tadmor central scheme [26], solving mass, momentum and energy equations; [27]
- *reactingFoam*: a pressure-based, transient, compressible solver for reacting flows using the PIMPLE algorithm for pressure-velocity coupling, solving species concentrations and energy equations. [28]

The resulting solver is density-based, fully compressible solving mass, momentum, energy and species mass fractions equations; together with thermal [1] and caloric equations-of-state[2]. [3, 29, 30]

Mass, momentum and energy equations are solved numerically using a spatial finite-volume fully explicit method with a high-order monotonicity-preserving

---

[1] $p = \rho R_{mixture} T$, respectively density, mixture-specific gas constant and temperature

[2] $h_s = \int_{T_{ref}}^{T} c_p(T) dT$, for sensible enthalpy h_s, or internal energy u, with c_p function of temperature

reconstruction of convective fluxes (Kurganov-Tadmor central scheme) and central-differencing for diffusive fluxes, [31] combined with a implicit Euler scheme in time, resulting in a second-order algorithm for spatial reconstruction.

Thermal and caloric equations of stare are both using JANAF table for thermodynamical quantities, specific heats and formation enthalpies, under the assumption of thermally perfect gases. For diffusion and heat conduction, viscosity is calculated using Sutherland's law[3], with species thermal conductivity and diffusivity computed from viscosity using constant Prandtl[4] and species-specific Schmidt[5] numbers. [32] Constitutive equations are assumed to be in the linear viscous form, without second-order effect of complete formulation, with Fickian diffusion and Fourier heat conduction. Those equations, under linear assumption, relate mass fluxes to concentration gradients for each species[6], viscous stress to velocity gradients [7] and heat flux to temperature gradients[8], representing the three transport phenomena represented by the equation involved.

For species mass equations, and for the finite-rate chemistry approach adopted, the chemical source terms are calculated using a stiff Rosenbrock solver with an operator-splitting approach [33].

The finite-rate chemistry formulation here used, computes chemical reaction rates using detailed kinetic mechanisms, modeled after Arrhenius equation, accounting for finite speed of chemical reactions, solving species transport equations with source terms derived from reaction kinetics. [34, 35]

Stability is imposed with compact stencils and by enforcing conservation of kinetic energy with a Courant number limitation of 0.5. Due to the explicit nature of the solver, the Courant-Friedrichs-Lewy (CFL) condition is necessary to ensure stability.

$$\mathrm{Co}_{\mathrm{max}} = 0.5 \max \left(\frac{\sum_{\mathrm{faces}}(a_{\mathrm{max}} S_f)}{U} \Delta t \right) < 1 \tag{4.1}$$

Here, Co is Courant number, U is velocity magnitude, Δt is time step, product of a_{max} (maximum signal propagation speed from characteristic lines) and S_f (face surface), for each cell. [36, 37]

The solver was used for the 2D (Sec. 5.1) campaign, where laminar and RANS turbulence model were used combined with laminar and partially stirred reactor (PaSR) model for combustion. For the 3D campaign, the LES model was used combined with the PaSR combustion model.

---

[3]

$$\mu = \mu_{\mathrm{ref}} \left(\frac{T}{T_{\mathrm{ref}}} \right)^{3/2} \frac{T_{\mathrm{ref}} + S}{T + S}$$

Where: μ is viscosity, T temperature, S Sutherland's constant. Subscript values are reference constants

[4] $Pr = \frac{\nu}{\alpha}$, dimensionless ratio of kinematic viscosity ν and thermal diffusivity α, for each species

[5] $Sc = \frac{\nu}{D}$, dimensionless ratio of kinematic viscosity ν and mass transfer coefficient D, for the i-species: $Sc_i = \frac{\nu}{D_i}$

[6] $\mathbf{j}_i \propto \nabla Y_i$, Fickian diffusion

[7] $\tau \propto \nabla u$, Newton's law of viscosity

[8] $\mathbf{q} \propto \nabla T$, Fourier conduction

4.1.2 RANS

The RANS modeling employs the density-weighted averaged Navier-Stokes equations. [38] The chosen turbulence model was $k - \omega$, a two-equation closure model, solving two additional transport equations: one for k, turbulent kinetic energy and one for ω, specific dissipation rate of turbulent kinetic energy. [39] While being sensible to inlet turbulence and boundary condition, it was chosen over the $k - \omega\ SST$ model to avoid further complication deriving from the blending function[9] of the latter. [40] This was done because the chamber studied, as showed in Fig. 3.3, does not rely on any particular feature to stabilize the flame (strut, cavities, etc.). Therefore, boundary layer resolution is of the utmost importance in order to correctly predict flow separation.

4.1.3 LES

The large eddy simulations (LES) model, is a technique that solves the Navier-Stokes equation upon applying a density-weighted, spatial, localized filter. [41] As in this work we are addressing turbulent reacting flows, the equations to be filtered are conservation of mass, momentum, energy and species mass fractions. [34, 30]

$$\begin{cases} \dfrac{\partial \bar{\rho}}{\partial t} + \nabla \cdot (\bar{\rho}\widetilde{\mathbf{v}}) = 0 \\ \dfrac{\partial (\bar{\rho}\widetilde{Y}_i)}{\partial t} + \nabla \cdot (\bar{\rho}\widetilde{\mathbf{v}}\widetilde{Y}_i) = \nabla \cdot (\bar{\mathbf{j}}_i - \mathbf{b}_i) + \bar{\dot{w}}_i \\ \dfrac{\partial (\bar{\rho}\widetilde{\mathbf{v}})}{\partial t} + \nabla \cdot (\bar{\rho}\widetilde{\mathbf{v}} \otimes \widetilde{\mathbf{v}}) = -\nabla \bar{p} + \nabla \cdot (\bar{\mathbf{S}} - \mathbf{B}) \\ \dfrac{\partial (\bar{\rho}\widetilde{E})}{\partial t} + \nabla \cdot (\bar{\rho}\widetilde{\mathbf{v}}\widetilde{E}) = \nabla \cdot \left[-\bar{p}\widetilde{\mathbf{v}} + \bar{\mathbf{S}}\widetilde{\mathbf{v}} + \bar{\mathbf{h}} + \sum_{i=1}^{N} (h_{i,f}^0 \bar{\mathbf{j}}_i) - \mathbf{b}_E \right] + \\ + \sum_{i=1}^{N} (\bar{\dot{w}}_i\ h_{i,f}^0) \end{cases} \tag{4.2}$$

Bold characters represent vectors if lowercase and second-order tensors if uppercase. Regarding the subscript symbols, overlines indicate filtered and tildes density-weighted filtered variables. [34]

The equations are written in the conservative form: the left hand-side presents time variation and convective fluxes of the quantities, while in the right hand-side diffusive and source terms are present.

The first equation represents mass conservation of filtered quantities, with ρ being the density and $\mathbf{v}$ the velocity vector.

The second equation represents species mass fraction conservation, with Y_i being species mass fractions, the species mass fractions vectors (assuming Fickian diffusion) $\mathbf{j}_i \approx D_i \nabla Y_i$[10] (assuming Fickian diffusion), the subgrid species flux vectors $\mathbf{b}_i = \bar{\rho}\left(\widetilde{\mathbf{v}Y_i} - \widetilde{\mathbf{v}}\widetilde{Y}_i\right) \approx -2(\mu_k/Sc_t)\nabla\widetilde{Y}_i$[11] (assuming gradient approximation), and the

---

[9] as the $k - \omega\ SST$ uses a blending function from $k - \omega$ used in the walls to $k - \epsilon$ in the bulk flow

[10] D_i species diffusivities

[11] μ_k subgrid viscosity, Sc_t turbulent Schmidt number

species formation rates $\dot{w}_i = P_{ij}\dot{w}_j$[12]. One equation for each one of the species is needed, but since $\sum_i^N Y_i = 1$ by definition, one species equation is discarded (Y_{N_2} for this case). [34, 35]

The third equation describe momentum conservation, with $\otimes$ representing the "dyadic product" operation of the velocity vectors, generating the second-order velocity tensor. [38, 42] At the right hand-side we have filtered pressure forces, $-\nabla\bar{p}$, and the divergence of the difference between viscous stress tensor $S \approx 2\mu\mathbf{D}_D$[13] and the subgrid stress tensor $\mathbf{B} = \bar{\rho}\widetilde{\mathbf{v}\otimes\mathbf{v}} - \tilde{\mathbf{v}}\otimes\tilde{\mathbf{v}}$, being modeled as $\mathbf{B} \approx -2\mu_k\widetilde{\mathbf{D}_D} + \frac{2}{3}\bar{\rho}k\mathbf{I}$.[14] [34]

The fourth equation represents energy conservation, with E, total sensible energy, derived from the static enthalpy: $E = \sum_{i=1}^N \left(Y_i \int_{T_{ref}}^T c_{p,i}\, dT\right) - \dfrac{p}{\rho} + \dfrac{v^2}{2}$. In the right hand-side, diffusive fluxes are made, starting from left, of filtered pressure work ($-p\mathbf{v}$), viscous work ($\mathbf{Sv}$), heat fluxes calculated with Fourier conduction and radiative heat flux from radiation model and/or boundary condition ($\mathbf{h} \approx k\nabla T + q_{rad}$)[15], enthalpy diffusive fluxes ($\sum_{i=1}^N (h_{i,f}^0 \bar{\mathbf{j}}_i)$), N number of species)[16], and subgrid energy flux vector $\mathbf{b_E} = \bar{\rho}\left(\widetilde{\mathbf{v}E} - \tilde{\mathbf{v}}\widetilde{E}\right) + (\overline{p\mathbf{v}} - \bar{p}\tilde{\mathbf{v}}) - \left(\overline{\mathbf{S}\mathbf{v}} - \bar{\mathbf{S}}\tilde{\mathbf{v}}\right) \approx -2(\mu_k/Pr_t)\nabla\widetilde{E}$[17] (using gradient approximation). [34]

The core part of the LES modeling is providing closure models for μ_k and k. In this work, the localized dynamic k-equation model (LDKM) have been used. This model computes the subgrid viscosity as $\mu_k = c_k\bar{\rho}\Delta\sqrt{k}$, where k (subgrid kinetic energy) is calculated solving the following transport equation:

$$\frac{\partial(\bar{\rho}k)}{\partial t} + \nabla\cdot(\bar{\rho}k\tilde{\mathbf{v}}) = -\mathbf{B} : \widetilde{\mathbf{D}} + \nabla\cdot(\mu_k\nabla k) - \frac{c_\epsilon\bar{\rho}k^{3/2}}{\Delta} \tag{4.3}$$

In this equation, Δ is the filter width equals to the cubic root of each cell volume, while the constants c_ϵ and c_k are calculated dynamically assuming scale similarity. [34, 35]

4.1.4 Combustion model

The laminar combustion model, used in the 2D campaign, to decouple turbulence-chemistry interaction (TCI), while to model those interactions, the partially stirred reactor (PaSR) was used.

In this work, a finite-rate chemistry approach has been adopted. This method directly calculates the filtered reaction rates ($\dot{w}_i$ in Eq. 4.2) from each species. The filtered formation rates, here discussed for the aforementioned LES quantities (a detailed derivation can be found here [35]), can be expressed as:

$$\overline{\dot{w}_i} = M_i\sum_j P_{ij}\overline{\dot{w}_j} = M_i\sum_j P_{ij}\left[\Omega_{f,j}\tilde{k}_{f,j}\prod_{k=1}^{M}(\widetilde{C}_k)^{P_{ij}} - \Omega_{b,j}\tilde{k}_{b,j}\prod_{k=1}^{M}(\widetilde{C}_k)^{P_{ij}}\right] \tag{4.4}$$

---

[12] P_{ij} stoichiometric matrix, $\dot{w}_j$ reaction rates

[13] μ viscosity, $\mathbf{D}_D$ deviatoric part of rate of strain tensor

[14] μ_k subgrid viscosity, k subgrid kinetic energy

[15] k thermal diffusivity

[16] $h_{i,f}^0$ mixture components enthalpy of formation

[17] μ_k subgrid viscosity, Pr_t turbulent Prandtl number

Where M is the number of irreversible reactions, M_i is the molar mass of the i-species, P_{ij} stoichiometric matrix coefficients, $k_{(f,b),j}$ respectively forward and backward reaction rates for the j-reaction, $C_k = \frac{\rho Y_k}{M_k}$ concentration of k-species, and $\Omega_{(f,b),j}$ respectively forward and backward segregation factors, which require closure and carry the filtering and subgrid turbulence effects. [35] The reaction rates are assumed to be in the Arrhenius form: $k_j = A_j T^{b_j} exp(-E_{a,j}/RT)$, where A_j and b_j are constants of the j-reaction, T is the temperature, R is the universal gas constant and $E_{a,j}$ activation energy of the j-reaction.

In the PaSR model, it is assumed that combustion is in small-scale dissipative structures surrounded by lower-reactivity regions. By defining γ^* as the volume fraction of the fine-scale burning structures and assuming $\Omega_{f,j} = \Omega_{b,j} = \gamma^*$, we obtain:

$$\overline{\dot{w}_i} = M_i \gamma^* \sum_j P_{ij} \left[\widetilde{k}_{f,j} \prod_{k=1}^{M} (\widetilde{C}_k)^{P_{ij}} - \widetilde{k}_{b,j} \prod_{k=1}^{M} (\widetilde{C}_k)^{P_{ij}} \right] \tag{4.5}$$

The modeling is now based on the choices for γ^*, which consider the timescales related to mixing and reacting timescales in the form: [34]

$$\gamma^* = \frac{\tau_c}{\tau_c + \tau_m} \tag{4.6}$$

Where τ_c is the chemical time-scale, modeled as $\tau_c \approx \alpha/s_u^2$, with α thermal diffusivity and s_u laminar burning velocity. While, τ_m representing the mixing timescale, is here modeled as: [43]

$$\tau_m \approx l_D/v_k \approx \sqrt{\tau_K \tau_p} \approx \sqrt{\tau_K \tau_\Delta} \tag{4.7}$$

Here, l_D represents the dissipation length scale, t_k Kolmogorov velocity scale. This ratio is calculated as the geometric mean of τ_K, Kolmogorov time scale[18] and the subgrid kinetic energy dissipation timescale, $\tau_p = k/\epsilon$.[19] In particular, τ_p can be written as $\tau_p \approx \tau_\Delta = \Delta/v'$[20], assuming equilibrium between sub-filter range dissipation and transfer across the cut-off from the filtered (resolved) scales. [35]

The PaSR model is extremely important when studying high-speed combustion in this case, as τ_m and τ_c tends to have comparable values due to the extreme speeds in the chamber.

4.1.5 Hydrogen-air combustion chemistry

The fuel to burn in this study is hydrogen, and a reaction mechanism is needed, regardless of the specific model used. The combustion process is modeled using a reaction mechanism called Z22. [3, 44]

The Z22 mechanism has 9 species (H_2, O_2, H_2O, H_2O_2, HO_2, O, H, OH, N_2), and 22 irreversible reactions. [3] This reaction mechanism successfully predicts hydrogen behavior regarding distribution of both fast radicals (O, H, OH,) and

---

[18] Representing the mixing at the smallest possible turbulent scale

[19] ϵ being the dissipation rate of subgrid kinetic energy

[20] Δ filter width (cubic root of cell volume), and u' characteristic subgrid scale velocity fluctuation (of the unresolved eddies)

slow radical (HO_2). Generating regions of rapid ignition (high temperatures chain-branching explosion), slow ignition (thermal explosion at low temperatures) and an intermediate region where ramjet and scramjet combustion chamber usually operates. [3]

4.1.6 Radiation modeling

Alongside the implementation of a new thermal boundary condition (BC), described in Par. 4.2.3.0.4, the aim of this thesis was also implementing a radiation model, and couple it with the new thermal BC. Of the available models, the P1 model was chosen, [45] along gray gas implementation. Even if it tends to overestimate radiative heat fluxes compared to more sophisticated models, it was chosen due to its robustness and cheapness. The diffusion equation to be solved is presented, obtained after an expansion in spherical harmonics and retaining only the first two terms. [35]

$$\nabla \cdot \left(\frac{1}{3a} \nabla G \right) - aG = -4a\sigma T^4 \tag{4.8}$$

About the quantities:

- $G = \int_0^{4\pi} I d\Omega$: incident radiation. Obtained by integrating along the spherical solid angle $I(s, \Omega,)$, the spectral intensity across all wavelengths, with direction s and per unit of solid angle Ω, after expansion and truncation in spherical harmonics;
- a: mean Planck absorption coefficient;
- σ: Stefan-Boltzmann constant;
- T: temperature

The equation describes incident radiation (G) evolution, with the source on the right-hand-side represented by the volumetric radiative emission calculated as $-4a\sigma T^4$, according to Kirchhoff law for a gray medium. Since gaseous hydrogen is the fuel, a simplified version without considering scatter and emission contribution is employed, justified by the absence of soot formation, droplets or condensed species. Due to the high temperature reached in combustion, radiation and the related heat fluxes have usually a suppression effect on combustion due to the temperature relation of the volumetric radiative emission In OpenFOAM, this equation is included using a dictionary, specifying model and related properties.

4.2 Boundary Conditions

4.2.1 Inlet

Various cases with corresponding different operating conditions were investigated. As for the present study, the cases investigated are:

- Non-reacting case, case 0;
- Subsonic reacting case, case 1;
- Shock-induced supersonic combustion case, case 4.

The corresponding inlet conditions are reported in the following table.

Case:	0	1	3a	3b	4	5
Mode	Non-reacting	subsonic	unsteady super-sonic	thermal choking	shock-induced	shock-induced
p^0 $[kPa]$	397.74	397.74	401.55	400.9	410.22	402.55
T^0 $[K]$	1414	1414	1505	1506	1697	1707
$\dot{m}_{air}$ $[\frac{m}{s}]$	0.2931	0.2931	0.2931	0.2931	0.2931	0.2931
$\dot{m}_{H_2}[\frac{m}{s}]$	0	1.53	1.47	1.49	1.4	1.37
ϕ (ER)	0	0.15	0.15	0.15	0.15	0.15
v_{in} $[\frac{kg}{s}]$	686	686	707	708	751	754
T_{in} $[K]$	1199	1199	1276	1277	1439	1448
ρ_{in} $[\frac{kg}{m^3}]$	0.614	0.614	0.583	0.582	0.525	0.515
T_{H_2} $[K]$	294	294	297	299	306	304
ρ_{H_2} $[\frac{kg}{m^3}]$	0.176	0.176	0.173	0.173	0.165	0.163

Table 4.1: Cases inlet conditions [3]

Where p^0 represents total pressure (reservoir), T^0 total temperature (reservoir), $\dot{m}$ mass flow rate for air (subscript air) and hydrogen (subscript H_2), ϕ equivalence ratio (ER)[21], v_{in} inlet velocity (at throat), T_{in} inlet temperature, ρ_{in} inlet density, T_{H_2} hydrogen temperature, ρ_{H_2} hydrogen density.

In general it is difficult to provide accurate values for inlet turbulence quantities. For the RANS $k-\omega$ model, inlet condition for k and ω where estimated assuming an inlet turbulence intensity (I) of 15% using the best-practice formulas provided here. [23]

For the LES, the inlet value for k (subgrid kinetic energy) was kept from the obtained case.

4.2.2 Outlet

For the outlet condition, due to the expected subsonic flow at the outlet patch, a pressure condition was imposed. Due to difficulties in obtaining stable results due to acoustical and thermo-acoustical instabilities regarding a fixed-pressure outlet, a *waveTransmissive* pressure outlet condition was imposed. This condition, avoids wave

---

[21] $\phi = \frac{f}{f_{st}}$Ratio of fuel-to-air ratio f, to its stoichiometric value f_{st}

reflections at the patch, preventing instabilities that could destabilize the domain by virtually extending the outlet. However, if a supersonic flow leaves the domain, this could result in a loss of absolute pressure. This drift effect of the absolute pressure sums up with the loss of waves reflections, resulting in a trade-off between absolute pressure values and stability. The boundary condition needs three parameters to be specified:

- γ: imposed to be 1.3, from measured values, is the specific-heats ratio needed to estimate the waves local Mach number;
- p_∞: the far-field pressure value, assumed to be 101300 [Pa], as in previous studies;
- l_∞: relaxation length, this parameters represents the relation between the far-field pressure and the actual pressure outlet, the virtual outlet patch extension. Increasing values represents weaker far-field pressure effect on the outlet. It was chosen to be 0.1 [m];

4.2.3 Walls

As in previous studies, the side walls of the chamber (where the windows are located, Fig. 3.3) are assumed to have *Slip* boundary conditions, not considering walls effects in turbulence and thermal conditions. This could be a reason introducing more limitations to the model, however previous measurements showed that those effects could be considered second-order effects. [21]

For chemical species and chemical source terms, the walls are assumed to have a non-catalytic behavior, imposing a *zeroGradient* boundary condition for species, therefore resulting in no volumetric heat-release rate ($\dot{Q}$) generated along wall patches.

4.2.3.0.1 RANS Due to a practical trick employed related to the mesh for the 2D case, explained in Subsec. 5.1.1, the advanced thermal boundary condition, aim of the thesis coupled with radiation modeling, were not employed. For temperature, a Dirichlet boundary condition have been employed, imposing a value of 450 [K], while for the walls, a boundary layer refinement was employed to ensure a proper boundary layer resolution suitable for a wall-model chosen to be $nutkWallFunction$ for ν_t[22]. A robust wall model that employs, in combination to $omegaWallFunction$ for ω and $kqRWallFunction$ for k, a switch based on the local y^+ values to ensure proper boundary layer resolution.

4.2.3.0.2 LES

---

[22] $\nu_t = \frac{k}{\omega}$, the ratio between turbulent kinetic energy (k) and its specific dissipation rate (ω), relating turbulence-induced momentum transfers.

4.2.3.0.3 Roughness Due to the measured roughness, deriving from the deposited YSZ thermal barrier coating, reported in Sec. 3.2, the *nutURoughWallFunction* was chosen, a wall model employing roughness, also used in previous studies. [3]

The main parameter described here is K_s, which represents the roughness height of the sand, chosen to be 60 [μm] for case 0 and case 1 (Subsec. 5.2.1 and Subsec. 5.2.2), while it was increased to 150 [μm] in case 4 (Subsec. 5.2.3).

4.2.3.0.4 One-dimensional conjugate heat transfer coupled with radiation modeling The goal of the thesis was to implement a new thermal boundary condition coupled with radiation modeling, compared to the previously used Dirichlet thermal boundary conditions. Various choices are already validated and available within OpenFOAM 7 with various levels of accuracy. Since a supersonic combustion case is already complicated as it is, those models and the respective coupling stress the stability of the calculation to the limit. Therefore, as a first-iteration approach, robustness and cheapness are the preferred requirements in this first attempt to explore the unknowns.

Regarding radiation modeling, as reported in Subsec. 4.1.6, the P1 model was chosen, which required the *MarshakRadiation* wall conditions, with a constant emissivity of the YSZ coating of 0.85. [46, 47] As an inlet condition, an estimation of the incoming incident radiation field G (described in Eq. 4.8) is given by σT_{in}^4, considering upstream effects, while the outlet condition was imposed to be *zeroGradient*.

Regarding the thermal boundary condition, the *externalWallHeatFluxTemperature* boundary condition was implemented. This boundary conditions, employs a one-dimensional conjugate heat-transfer boundary condition (1D CHT BC), also coupled with radiation in this implementation. It has the possibility to carry out a thermal characterization of the walls without the increased cost of resolving the solid boundaries.

The version implemented here uses the ambient temperature (outside of the chamber, T_a) and the corresponding heat transfer coefficient (also external to the chamber, h). Other relevant parameters to be specified are:

- *thicknessLayers*: of the wall layers;
- *kappaLayers*: thermal conductivity coefficient of the corresponding wall layers;
- *qr*: the radiation heat flux calculated from the radiation model, with an available relaxation factor to ensure stability;
- *emissivity*: of the first layer facing the computational domain.

4.3 Mesh

Three meshes were used:

- **Legacy Mesh**
- **2D Mesh**
- **Modified Mesh**

4.3.1 Legacy Mesh

The legacy mesh, obtained from previous studies, was made using the OpenFOAM *SnappyHexMesh* meshing utility. It is a ~ 25.7 million cells mesh, corresponding to the “coarse” case analyzed by previous studies. [3]

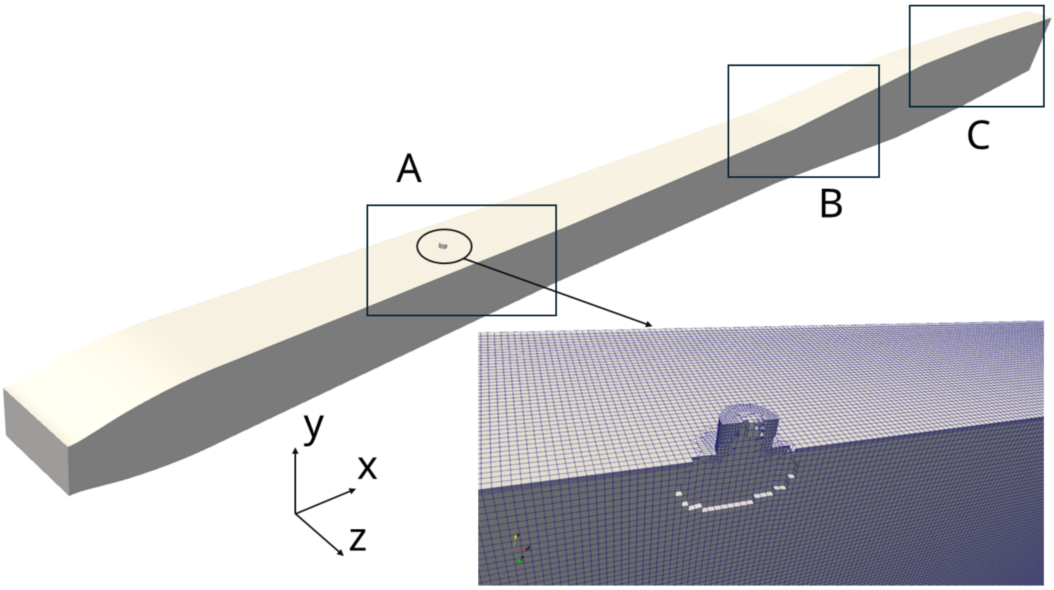

Figure 4.1: Legacy mesh: 3D view

It starts from the throat of the de Laval nozzle and ends with an extended final part sitting towards the exhaust pipe of the experimental setup of Fig. 3.1. Even if not part of the chamber, this region was necessary to obtain a stable solution. However, to contain the cell count, the height is not the same of the exhaust pipe diameter connected to the chamber.

It is worth noticing that in the damp tank there is also a security burner whose upstream back-pressure effects are not taken into account.

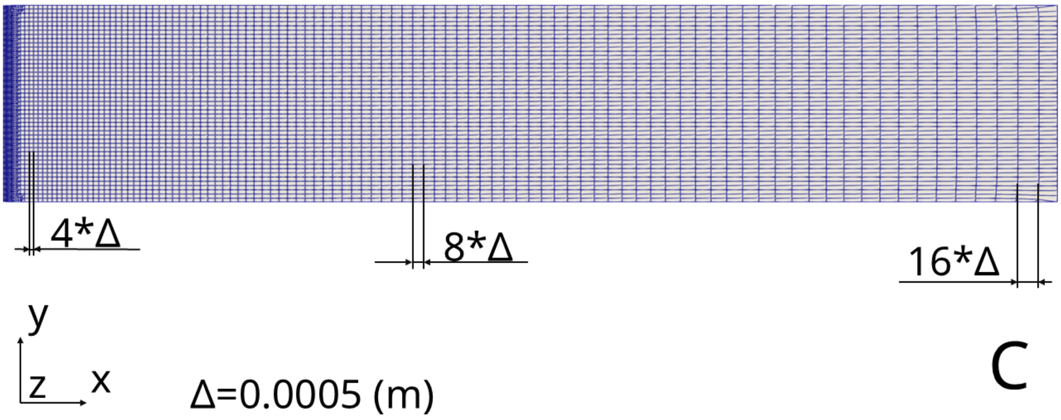

Figure 4.2: Legacy mesh: extended final part

The extended final part also presents a coarsening in the axial direction in order to further develop the flow and damp the strong oscillations particularly strong in the reactive cases. The Index of Quality (Pope's criterion) for this mesh is 87%, meaning that the kinetic energy resolution is suitable for a LES being above 80%. The cells are all hexes with the same size, ensuring an homogeneous behavior of the filtered quantities in the LES simulation.

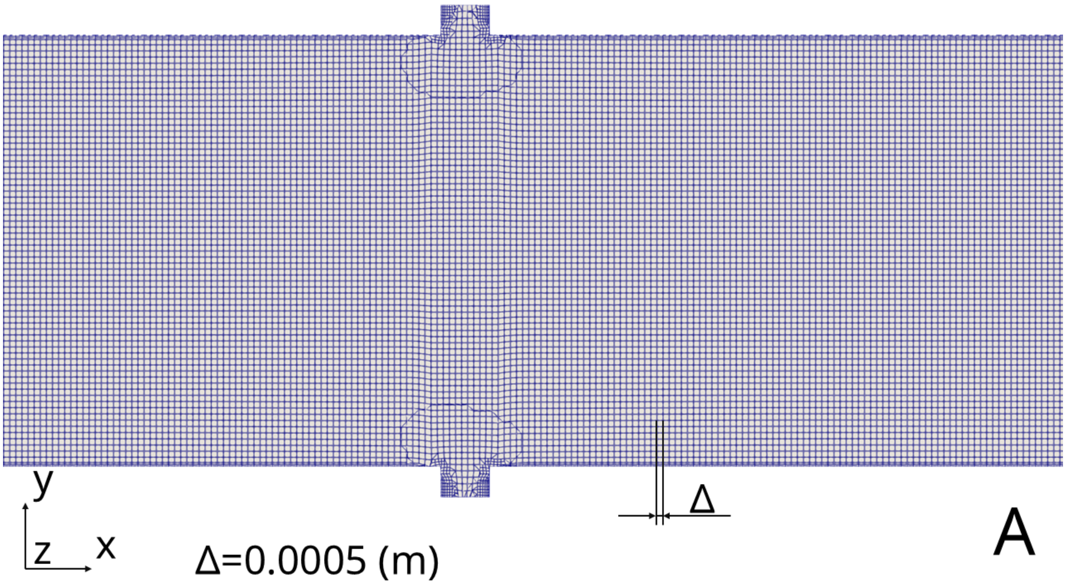

Figure 4.3: Baseline mesh: injectors

The injectors, modeled after the 2 mm porthole injectors used in the experiments, are made from cylinders "stitched" to the main mesh, as also visible from the magnified slice in Fig. 4.3. Boundary layer refinement ensured a cell height of $\Delta/3$ in the first layer along the top and bottom walls and within the injector walls.

The boundary layer of the side walls was not considered, as *Slip* BC are applied.

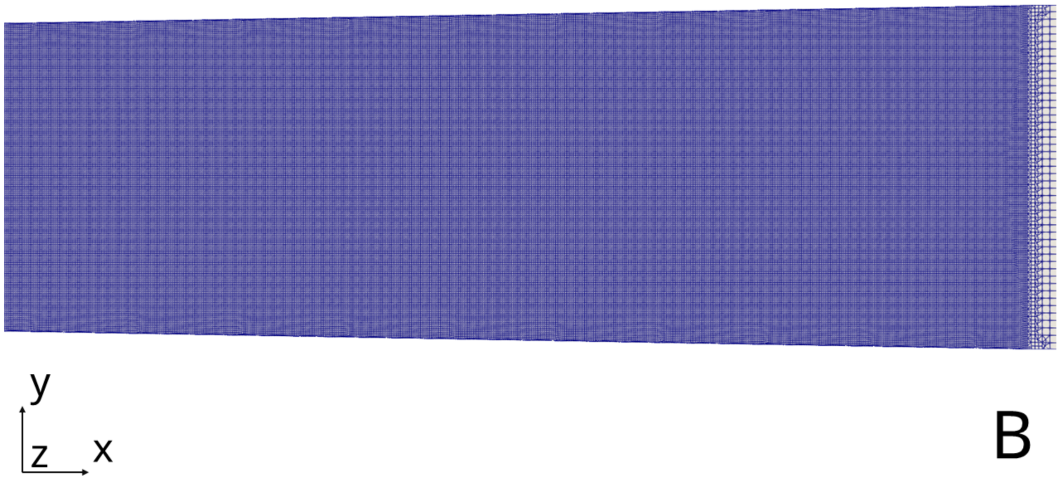

Figure 4.4: Baseline mesh: transition from chamber to exhaust pipe

In this mesh, the characteristic dimension of the hexes, Δ, was constant along the chamber, avoiding changes in the turbulence properties due to the different properties calculated from the subgrid model. This mesh was used to test and compare the parameters of the thermal 1D CHT BC coupled with the radiation model against the prescribed temperature, without introducing biases from a different mesh and refinement regions. This is very important for a LES since the mesh is filtering the equations, and a different resolution, especially near the walls, could change how the heat fluxes are calculated.

4.3.2 2D Mesh

The mesh was generated using *gmsh*. The bright side of generating a mesh in *gmsh* is the excellent quality and robustness of the topology. Since OpenFOAM still needs a 3D mesh even if the calculation is 2D, it was decided to use a thickness equivalent to the real 3D geometry soon to be employed.

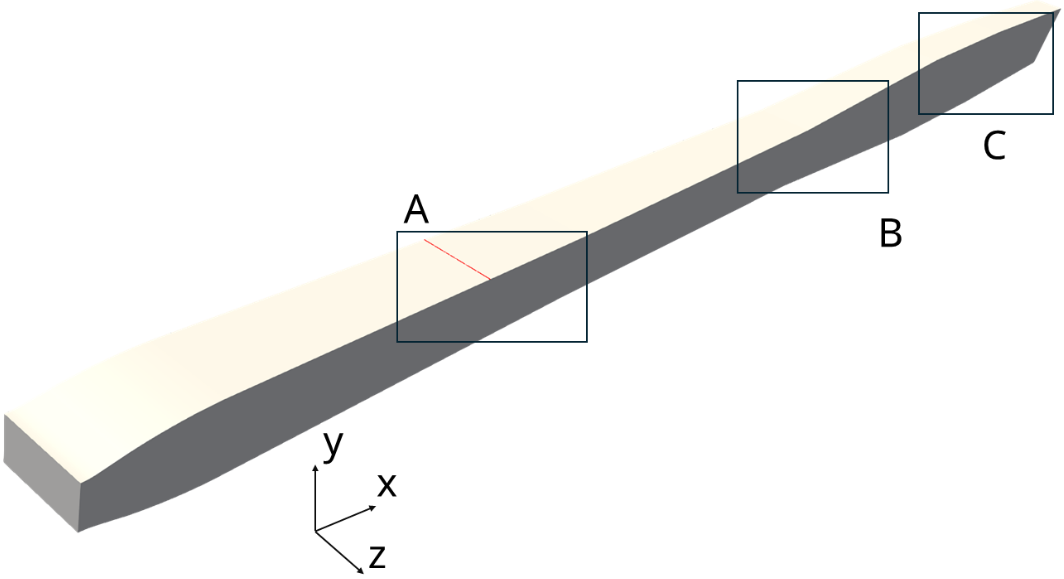

Figure 4.5: 2D mesh: overview

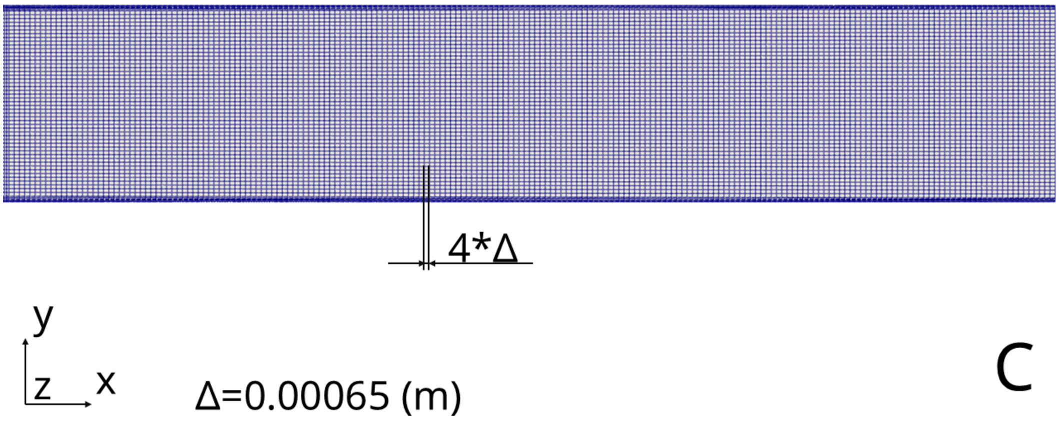

Figure 4.6: 2D mesh: extended final part

The buffer zone to the outlet was kept mainly to avoid the mentioned instabilities. The cells were coarsened axially in the legacy mesh in Fig. 4.2, but further axial coarsening was not reproduced in this mesh. The boundary layer refinement was extended in this region for the reasons explained in Subsec. 5.1.1. Since it is a 2D simulation, to avoid additional complexity, no injectors were realized, meaning that the injectors are just patches within the walls. This means that to accommodate the injectors in the 2D geometry while retaining the correct mass flow rate it was necessary to spread the injector's area in the chamber width assuming a rectangular area. For each injector:

$$\dot{m} = \rho U A = \rho U (b\ H) \quad \rightarrow \quad b = \frac{\dot{m}}{\rho U H}\ [m] \tag{4.9}$$

Were b represents the axial thickness and H the constant width of the rectangular chamber. A further rework was made to adapt the quantities to the available ones: sonic injection ($Ma = 1$), measured mass flow rate ($\dot{m}$), pressure (p) and temperature (T) measured at injection.

$$b = \frac{\dot{m}_{H_2}\sqrt{\dfrac{R}{M_{H_2}}T_{H_2}}}{\sqrt{\gamma}\ p_{H_2}\ Ma\ H} = \frac{\dot{m}_{H_2}\sqrt{\dfrac{R}{M_{H_2}}T_{H_2}}}{\sqrt{\gamma}\ p_{H_2}\ H}\ [m] \tag{4.10}$$

The result is the red line highlighted in Fig. 4.5.

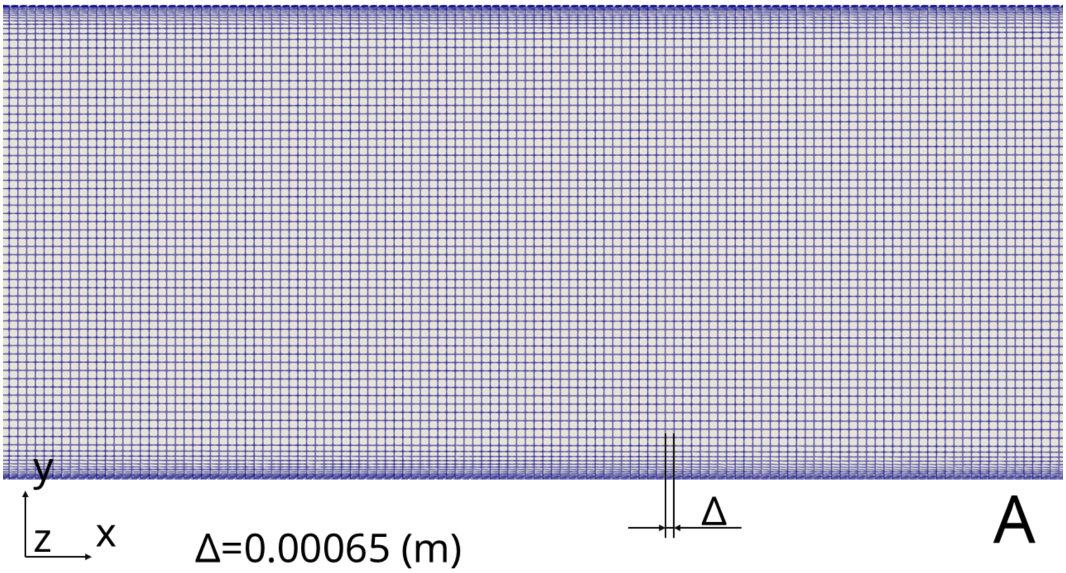

Figure 4.7: 2D mesh: injectors

Therefore, in the isolator, the injectors are not visible in this case. The characteristic cell dimension Δ in this case is a higher compared to the legacy mesh because in the 3D modified mesh there will be refinement regions.

A boundary layer refinement was employed to ensure proper resolution of the boundary layer with a growth rate[23] of 1.1. This is important for the turbulence model used described in Par. 4.2.3.0.1. The core idea of this new mesh was to preserve the orthogonality between the consecutive cell layers to ease the flux calculation. The lower side is that by doing so, the cells aspect ratio between x and y directions is not unitary as the cross-section is diverging going downstream, growing gradually up to 1.7 in the y direction. The mesh obtained is made of ~ 145000 cells, and a first analysis with the OpenFOAM *checkMesh* utility checked the basic requirements. This is a good first step, but only after obtaining the final results will be clear if the mesh is "good".[24].

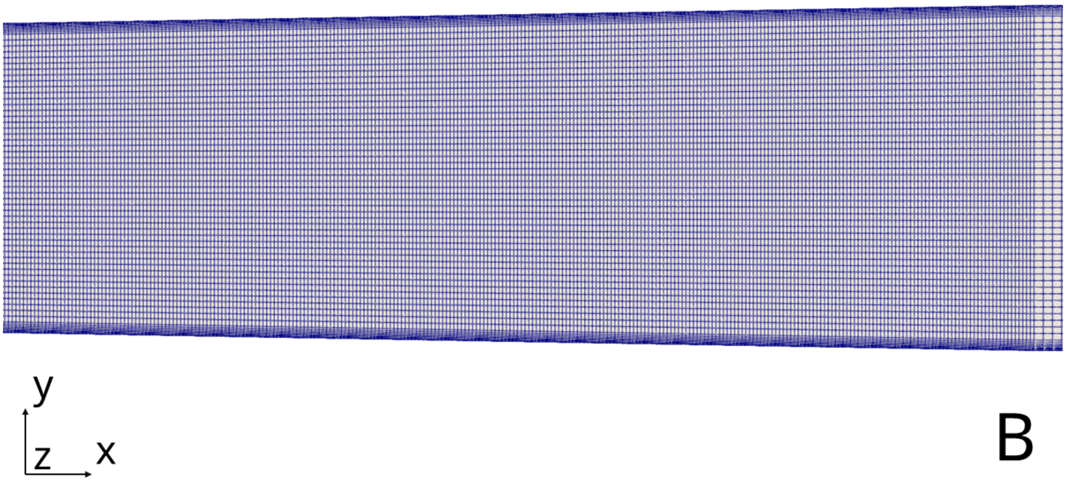

Figure 4.8: 2D mesh: final part and transition

4.3.3 Modified Mesh

The 2D mesh was kept as the "core" for the bulk of the geometry, maintaining the same proportion of the characteristic dimension Δ. Even if the hexes are slightly coarser compared to the legacy mesh, it was decided to do so in order to reduce as much as possible the cell count, always high in a LES simulation, while trying to deliver the highest quality possible.

---

[23] Meaning the ratio between the lower and upper cell layer height

[24] Quoted because there is no common consensus in defining what a good mesh is. After some baseline indications, the metric is highly dependent on experience and wit

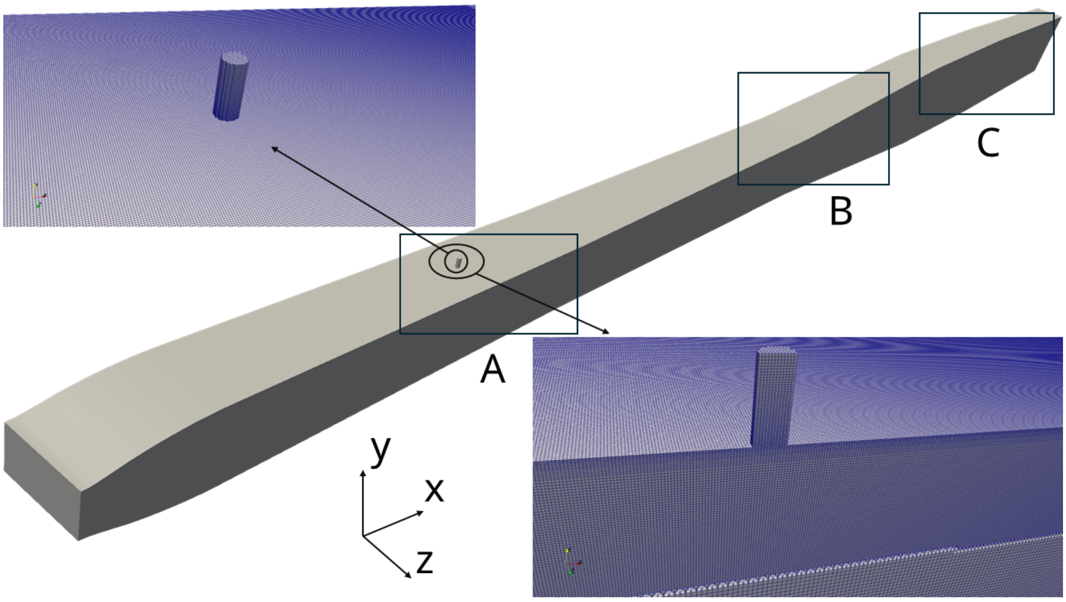

Figure 4.9: Modified mesh: overview

A complete re-design of the injectors was envisioned: try to “stitch” a cylindrical mesh to a hexes-dominant mesh produces transition cells that could be problematic for a LES simulation. This is particularly true in injection and mixing regions, where steeper gradients are expected. High skewness cells were produced in the legacy mesh. For that reason, it was decided to extrude the injectors from the mesh directly using the OpenFOAM utilities for geometry manipulation (*topoSet*, *createPatch*, *extrudeMesh*, etc.).

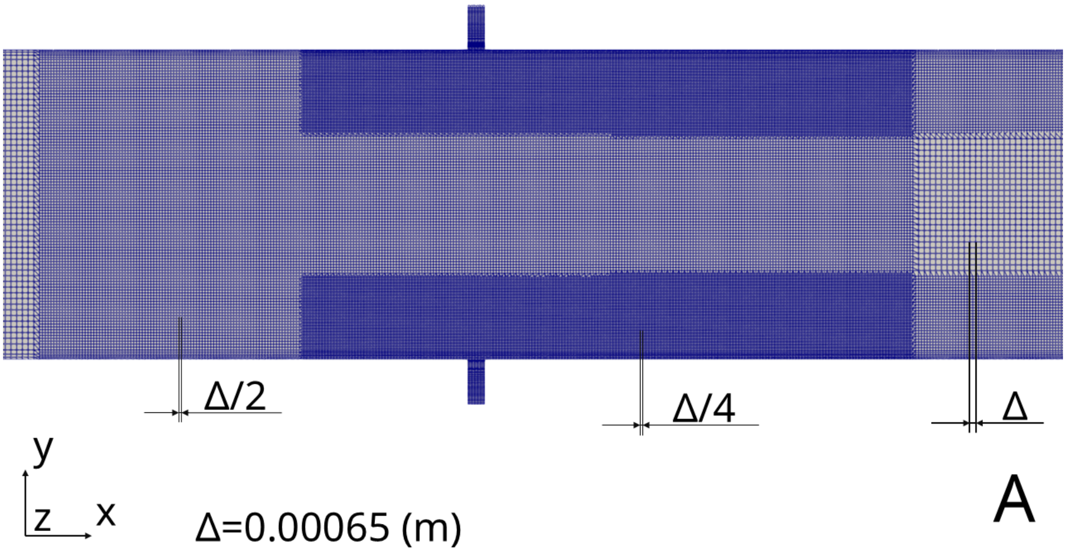

Figure 4.10: Modified mesh: injectors

A drawback is that now the resolution of the circular cross-section is dependent on the cell size of the bulk mesh.

Since much more definition was deemed necessary to magnify the shock train structure and fuel mixing after injection, two refinement regions were employed:

- The first covering all the cross-section to capture correctly the boundary layer growth and spanwise instabilities developing right before the injectors. It is extended after the injectors to also provide better resolution in capturing the barrel shock interactions and reflections;
- The second ones are along the walls, following the expected trajectory and penetration of the fuel plume in order to better capture the structures generating along the plume while interacting with the bulk supersonic flow and other compressible phenomena.

In the overlapping region the injectors are located, now with a resolution of $\Delta/4$ for the extrusion from the main mesh. As in the legacy mesh, there is a boundary layer refinement that ensures a height of the first layer of $\Delta/3$,that got refined in the refinement regions providing $\Delta/6$ along the walls and $\Delta/12$ in the overlapping region. To avoid a sharp transition in the cell size near the injectors exit, the growth ratio of the newly generated mesh was mirrored in the first layers within the injectors, as in Fig. 4.9. Another characteristic is the length of the injectors: they were made longer in order to prevent perturbations interacting with the inlet patches.

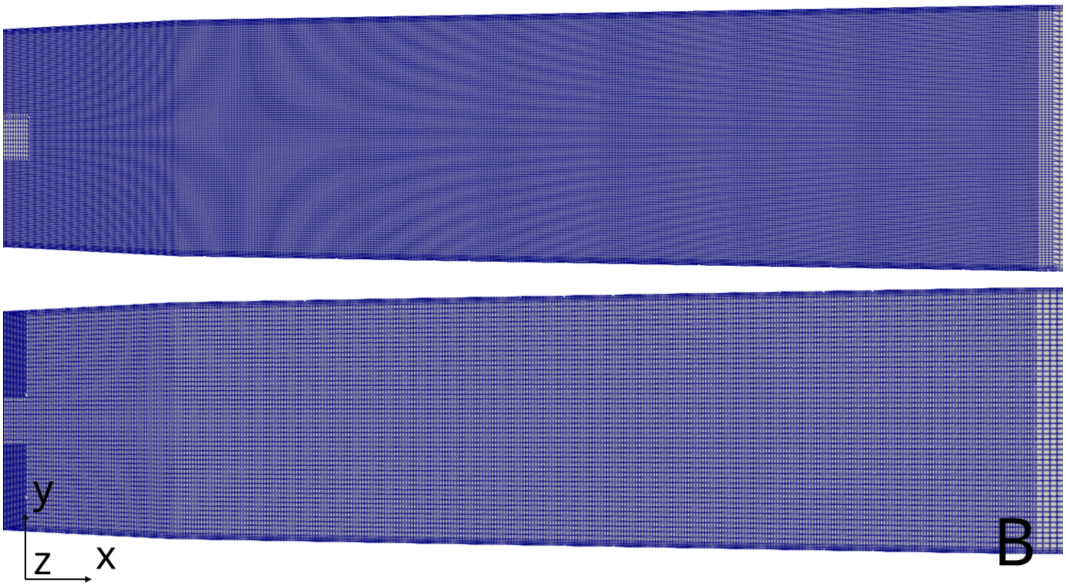

Figure 4.11: Modified mesh: end of the chamber

At first, the refinement along the walls was ending, as showed by the bottom configuration of Fig. 4.11. However, due to some problem with the near-wall resolution in a region where the flame is supposed to be, as in Fig. 5.57, a further refinement was employed to ensure stability with the thermal boundary condition.

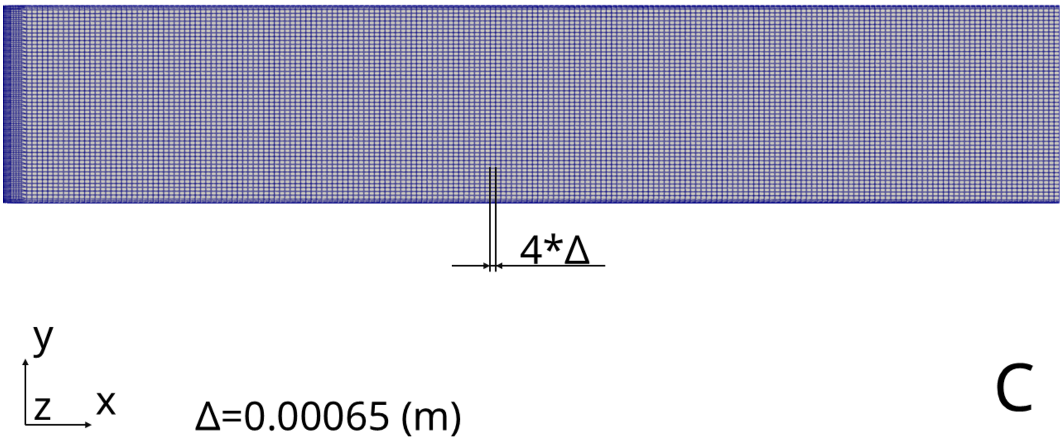

Figure 4.12: Modified mesh: exhaust

It was decided to keep the damping region towards the outlet to prevent instabilities, where combustion induced oscillations become important. The new mesh has a cell count of ~ 45 *mln* cells with a LES IQ of 89%, being a compromise between the coarser and finer mesh of previous studies. [3]

Chapter 5

Numerical Results

> ***"Übung macht den Meister."***
>
> *"Practice makes perfect."*
>
> ***German proverb***

After having defined the numerical setup, it is time to finally discuss the results obtained. Since the cases investigated are respectively case 0, 1 and 4 reported in Tab. 4.1, the chapters will be divided based on that. But, as a first step, it is worth to spend some time talking about the two-dimensional (2D) campaign. Since the 2D case was started from scratch, a brief history of flow development has been reported in App. A, highlighting the flow evolution. This is really important also in standard practice: doing a 3D LES directly and develop the flow from non-reacting to reacting passing through all of the transient phenomena would be prohibitive in terms of both time and resources, at least out of scope of this thesis. In practice, a sequence starting from scratch could be (from the cheapest to the most expensive):

1. 2D RANS: the cheapest and fastest way to develop the flow from scratch, possibly catching the main features before switching to more expensive tools;

2. 3D RANS: starting either from scratch or starting from mapped fields from the 2D case, could be used to more precisely capture the physical behavior since the third dimension does not introduce non-physical effects. Satisfying conclusions could be drawn even for this case [4], especially for testing models, boundary and initial condition values. However, more fundamental and dynamical analysis (investigating ignition delay, frequencies, shedding behaviors, etc.) are difficult to formulate since the turbulent phenomena are heavily modeled through a statistical representation. Another problem is that sometimes the most sophisticated models need constants that are not easily measurable, yet the solution is highly dependent on those values.

While sometimes results are satisfactory, there is a high chance that at some point everything boils down to “constants tweaking” for fit some measured data without addressing the underlying physics;

3. 3D LES:[1] usually exploit fields mapped from the aforementioned RANS to ease the overall cost, which could be as high as someone wants to resolve the smaller turbulent scales, and to make things worse is not even linear. However, it is now possible to capture unsteady phenomena, investigate structures and interactions between turbulence, combustion and compressibility previously modeled. [3, 21, 34] LES on coarser meshes could be employed instead of 3D RANS in order to capture the overall features not captured by RANS models while obtaining fairly quick results. Since the larger scales are directly resolved, the modeling part could be considered less heavy, provided that a good sub-grid model is used;

4. Grid refinement: in the end, especially when doing an LES, but not only, it all boils down in how much your “resolution budget” is, and how many cells are available to capture discontinuities and value changing between each cell. Regardless of the mesh size, there will always be regions where you could, or wish you could, have better resolution. This is especially true with compressible phenomena and combustion. But since an engineer is an “artist in making compromises and providing the maximum output with the minimum input”, choosing where and how to refine requires some wit.

However, as it will follow, in this case a different approach was used: since the fields for one case of the reacting 3D LES was already available, a direct mapping has been employed for the 3D LES. The 3D RANS was not investigated, while the 2D cases where investigated to familiarize with OpenFOAM and visualize the developing of the flow.

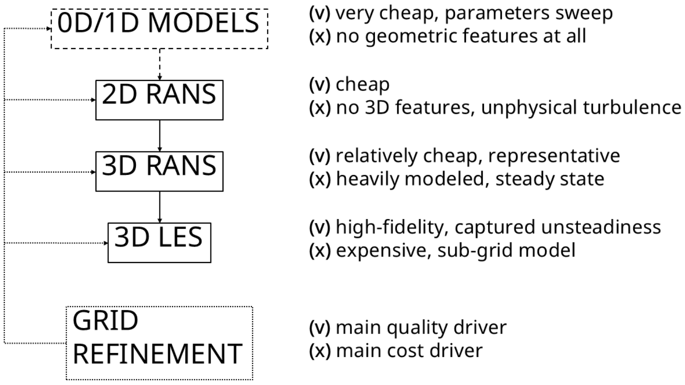

Figure 5.1: Best-practice workflow summary

---

[1] Known as the “silver bullet” between the “authorized personnel”

5.1 Two Dimensional Campaign

Even though from a physical perspective simulating turbulence in a 2D simulation is non physical, due to the non physical behavior of the turbulence structures in absence of vortex stretching. [48] Tests were made in 2D due to the speed of the calculation for familiarizing with OpenFOAM, and to test the resolution of the prototype mesh. Due to the configuration of the chamber, it is important to have an estimation of the position of the separation region. However, to make things worse, even starting from scratch from a 2D case was very difficult. Some modifications have been made to the mesh to develop the flow throughout the entire geometry, which does not correspond to the real geometry, as will be highlighted. As a direct consequence, the parameters for the 1D CHT BC coupled with the radiation modeling were not tested in the 2D case. As for the thermal BC, Dirichlet BC's have been employed prescribing walls temperature at 450 [K], the same used from the obtained case. As for turbulence model, the $k-\omega$ model was chosen. Even if it is sensitive on initial and boundary conditions, it was chosen to avoid further complexity from the blending function of the $k-\omega$ *SST* model near walls, and because the mesh refinement towards the walls provided satisfactory resolution (see Subsec. 4.3.2).

5.1.1 Initial Flow Development

Even setting the base case for the development of the flow was a problem: in the initial configuration, *Slip* BC have been applied to the extended final part (Fig. 4.6). However, by doing so, the pressure waves generated by the inlet conditions do not retain enough intensity to induce the separation when reflected by the outlet, which is also a *waveTransmissive* type to prevent acoustical feedback problems. To solve that issue, the exhaust pipe's top and bottom patches were "plugged" applying wall-type boundary conditions, thus providing an adequate build up and reflection for successive developments. In that way, the artificial “Fanno-like enclosed flow” generates enough instabilities to induce the separation after being reflected at the outlet. The results for the plugged configuration are reported, meanwhile the full evolution showing initial waves traveling back and forth are reported in App. A

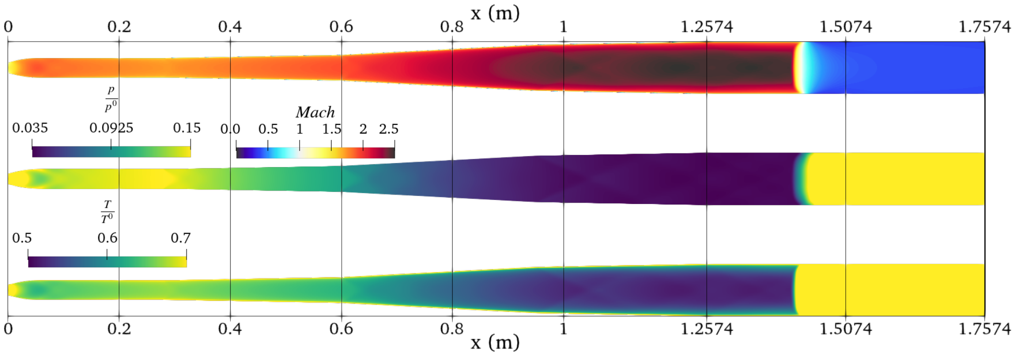

Figure 5.2: 2D RANS, fully supersonic flow, 2D mesh, Mach number and normalized temperature and pressure

It was also possible to have a brief comparison with the reported expansion values of the fully supersonic flow throughout the chamber from previous studies. [21] First, the overall slices are presented showing the evolution in the computational (Fig. 5.2). The values of temperature and pressure are normalized with their respective reservoir values and rescaled to the target range.

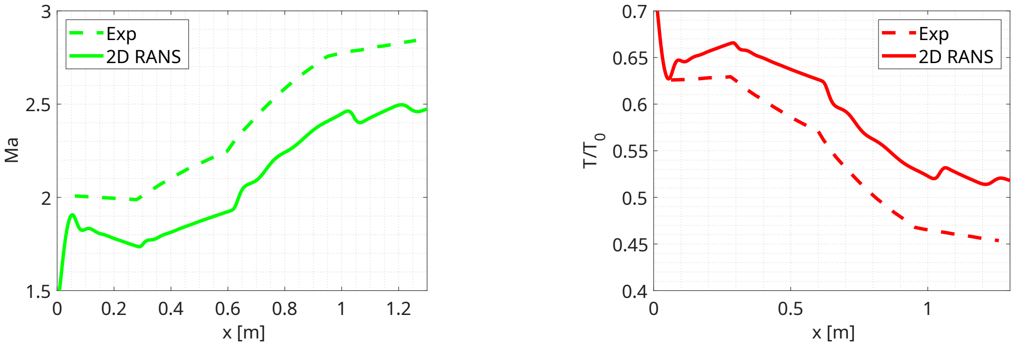

(a) 2D, fully supersonic, Mach **(b)** 2D, fully supersonic, temperature

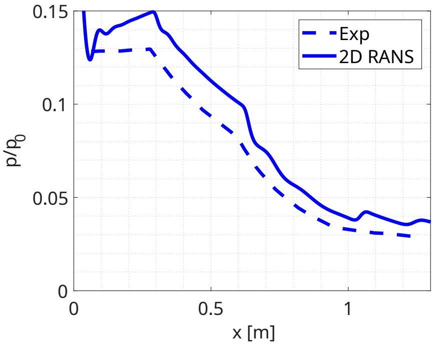

(c) 2D, fully supersonic, pressure

Figure 5.3: 2D RANS, 2D mesh, fully supersonic flow compared with experimental data. [21]

A more quantitative comparison is reported with the plot of those quantities along the mid-line. The general trends are respected, showing decent agreement in the normalized pressure. However, an offset can be observed for the temperature and consequently the Mach number. The main reasons could be:

- Experimental data: there were no further informations on how the data were obtained. Also, it is not clear if the TBC was already removed, thus invalidating the measured temperature, as reported; [21]
- Inlet conditions: there are uncertainty about the inlet conditions due to different component upstream, as shown in Fig. 3.3. Worth mentioning are the two burners to provide vitiated air and the cross-section transition from circular to rectangular;
- Boundary conditions: the wall temperature was prescribed, further cropping the predictive capability and eventual values in the mid-plane influenced are not accounted in this case;

- Numerical models: the case simulated was 2D using a turbulence model, hence predictions are probably not spot on due to the approximations used. Also, the plugged exhaust pipe could cause a new drift from the physical configuration.

5.1.2 Developed Non-Reacting Flow (Case 0)

Try to develop the flow initially was a great challenge: the practical trick of initially plugging the exhaust pipe walls was employed (Subsec. 5.1.1). In that way, it was possible to successfully establish the separated region. Otherwise, no separation was possible to trigger without heavily tweaking the parameters to non-physical values. Nevertheless, after some time, the separated region oscillates back and forth,with the lower-wall separation location stabilized around $x \approx 0.8$ $[m]$. Surprisingly, the flow, as observed in previous works [3], presents a bias towards the upper wall, and probably if let run longer, this bias will be somewhat transmitted to the lower wall and back at the top after a while on repeat, recalling a low-frequency shedding motion.

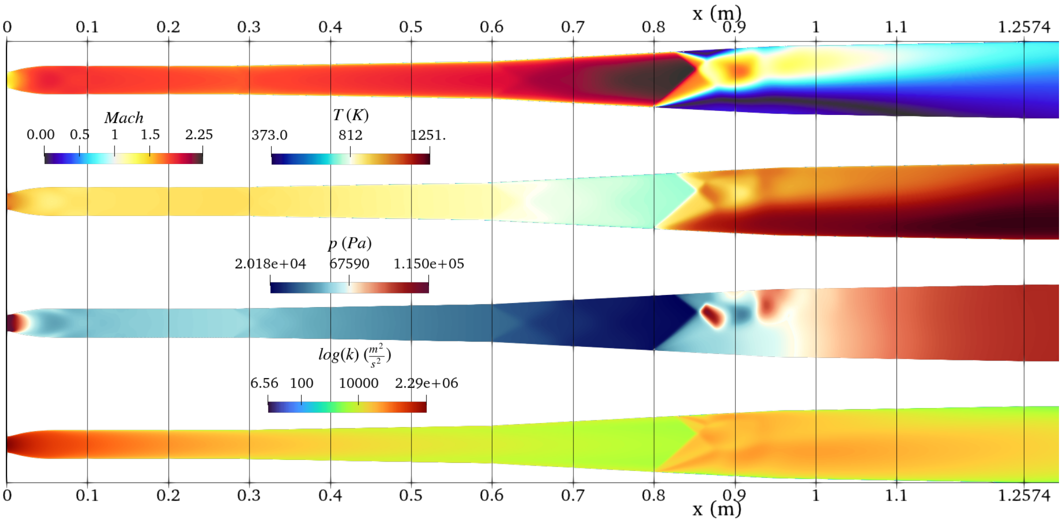

Figure 5.4: Case 0, 2D RANS, 2D mesh, Mach number, temperature, pressure and turbulent kinetic energy k in logarithmic scale

The prediction for this feature is quite remarkable considering the tricks employed, and will be present also in following results. A comparison of the mean measured pressure at the lower wall with experimental results [21, 3] is reported in Fig. 5.5. It is worth to mention that the calculated absolute pressure values were not matching the experimental ones, probably due to modeling approximations, the outlet *waveTransmissive* boundary condition damping acoustical waves, or even uncertainties with the measurements. The offset applied for this case was 5000 [Pa], in order to match the pressure values right after the inlet expansion, before downstream features could further complicate the calculated values. Notably, this offset value is lower compared to the tolerance of ± 10000 $[Pa]$ related to the reservoir conditions. [29] The general trends exhibit a surprisingly good agreement, showing that both the models and the boundary conditions successfully predict the behavior of the flow up until the separation: there a mismatch is observed, hinting that the back-pressure is slightly over-predicted probably due to a combination the initial "plugged" configuration, the *waveTransmissive* outlet condition and the turbulence model or other back-pressure effects not taken into account.

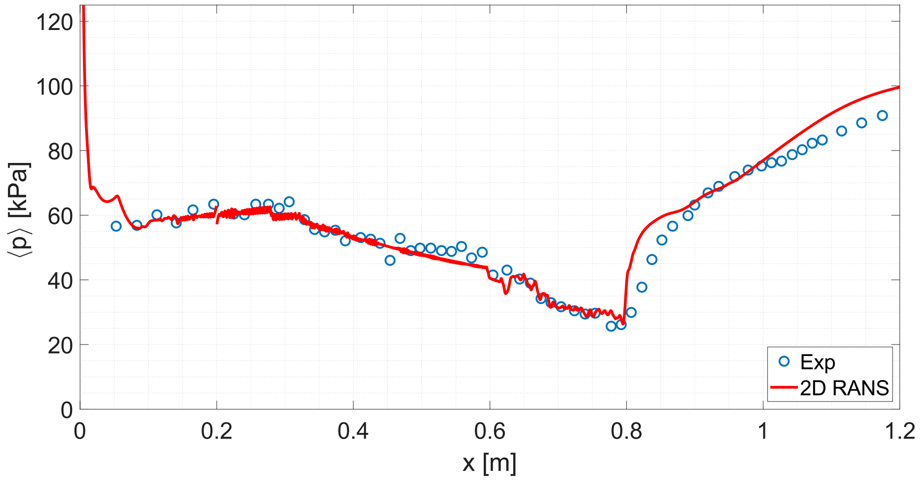

Figure 5.5: Case 0, 2D RANS, 2D mesh, lower-wall mean pressure levels comparison with experimental data. [3]

Pressure oscillations are observed along the wall probably due to large pressure gradients and some compressibility effects from the interaction with the boundary layer leading to discretization-induced fluctuations.

5.1.3 Developed Reacting Flow (Case 1)

From the non reacting case, hydrogen was injected. A history of the flow ignition is reported in App. B, here only the converged results are discussed. The separated subsonic region is now where the combustion occurs, after the plume is convected, mixed and provided the right pressure and temperature values for ignition. This combustion-induced pressure rise then further communicates with the flow upstream through the boundary layer or wherever a subsonic region is present. This exchange of information, at some point, reached a stable condition where the transient is over and all of the upstream and downstream values are matched. The temperature field is very handful in showing the lower temperature fuel that penetrates and got mixed with the bulk flow, and then ignites after the oblique shockwaves.

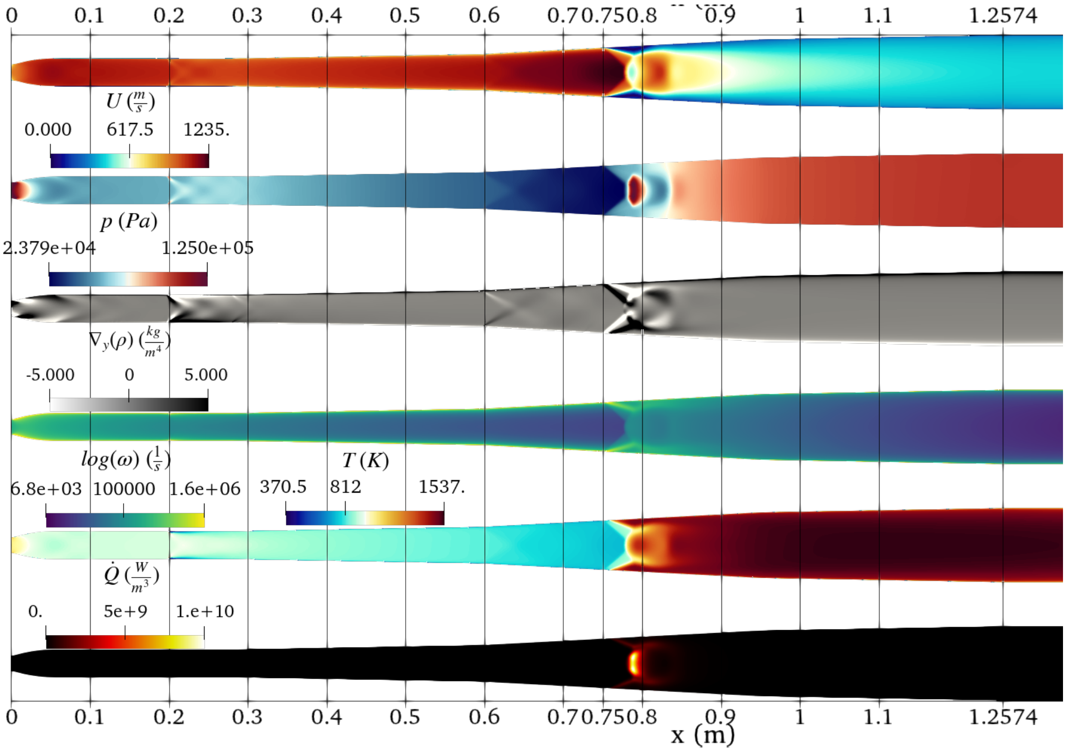

Figure 5.6: Case 1, 2D RANS, 2D mesh, velocity magnitude, pressure, numerical Schlieren, ω (specific dissipation rate of turbulent kinetic energy) in logarithmic scale, temperature and heat-release

The velocity field on top shows the real values, confirming the high speed in the DMRJ chamber and the thin combustion zone in the subsonic region, while the numerical Schlieren gives a better representation of all the compressible structures generated due to ignition, expansion in the chamber and the flame front shaping and being shaped by the oblique shockwaves after separation. The peak heat-release is observed around the axis of symmetry, where the oblique shockwaves, generated from the separation points at the walls, interacts generating a bow shock-like structure. As a final touch, the logarithmic scale of ω (specific rate of dissipation of turbulent kinetic energy), shows that high values are met near walls for the boundary layer, at the inlet due to the strong expansion but also around the flame front, as the combustion increasing viscosity and density, having a “turbulence-killer effect”.

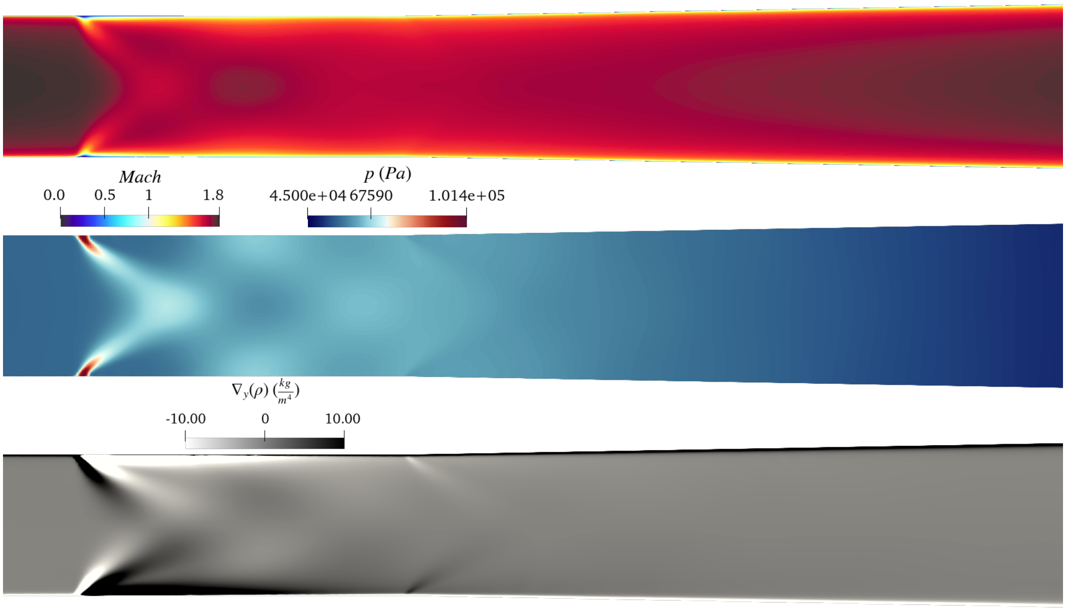

Figure 5.7: Case 1, 2D RANS, 2D mesh, magnification of Mach number, pressure and numerical Schlieren

A magnification of the injectors zone shows that indeed there is a hint of a shock-train, and a barrel shock is formed, but the lack of the third dimension weights a lot, especially when compared with other numerical models as in Fig 5.62. The lack of dimensionality do not reproduce the same separation regions near the injectors, being now more like a "semi-infinite slot" injected in a supersonic flow. The jet penetration appears to be almost zero due the 3D features not represented. Even tweaking the fuel inlet quantities did not produce a different behavior. Thanks to the diffusion and the high level of turbulence, the plume diffuses along the chamber's height and mixes until filling the entire chamber before the separated region, as showed in Fig. B.13.

For the most relevant chemical species in hydrogen combustion, depicted in Fig. they appear to be all stacked up near the combustion zone. It is worth mentioning why each of those species is important. [9]

- OH, H: drives mainly chain-branching reactions, particularly OH guides the heat-release at mid-lower temperatures meanwhile H is responsible for explosive reactions;
- HO_2, H_2O_2: the first very important in low-temperature and auto-ignition chemistry, meanwhile the second is also important as a "radical reservoir": at higher temperature dissociate in 2 OH further contributing in chain-branching reactions;
- O, H_2O: the former very important for chain-propagation reactions, meanwhile the latter is the only product of hydrogen's combustion, since no carbon atoms are present.

However, due to the lack of the third dimension, nothing quantitative could be said about ignition properties, and compare them with what could be inferred from the experiments.

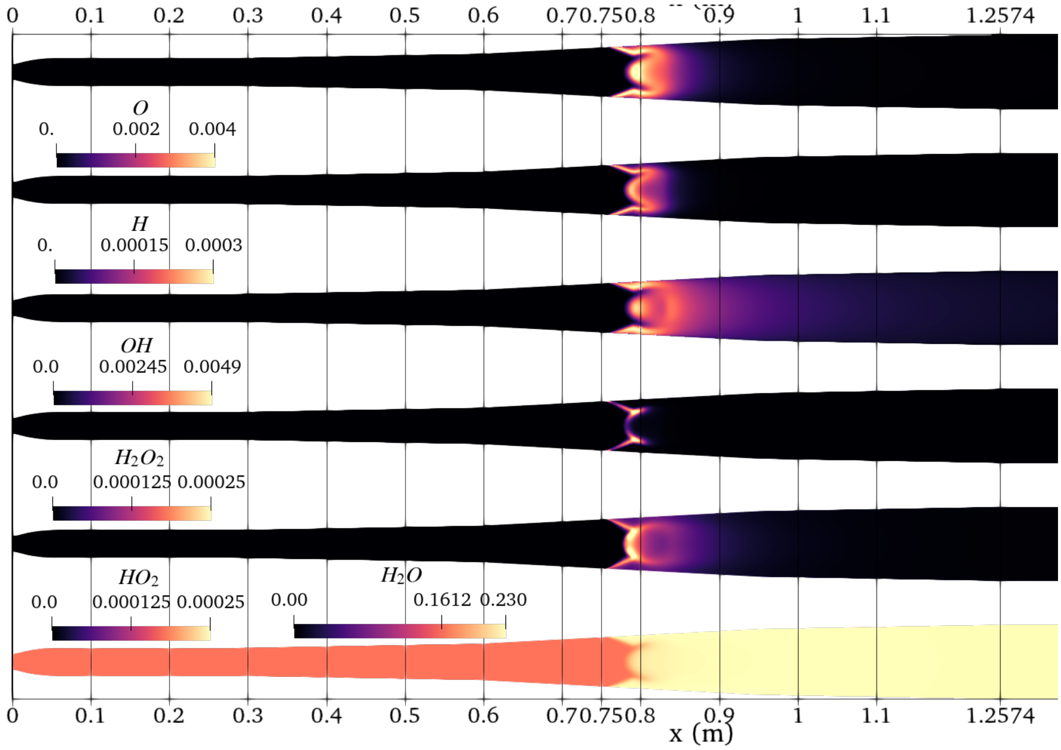

Figure 5.8: Case 1, 2D RANS, 2D mesh, atomix oxygen O, atomic hydrogen H, hydroxyl OH, peroxide H_2O_2, hydroperoxyl HO_2, water vapor H_2O

Regarding the combustion model, it appears that the PaSR (Partially Stirred Reactor) coefficient is 1 everywhere. From Eq. 4.6, could be inferred that it is like assuming very fast mixing, as the chemical time scale, τ_c, is much larger than the mixing time scale τ_m.

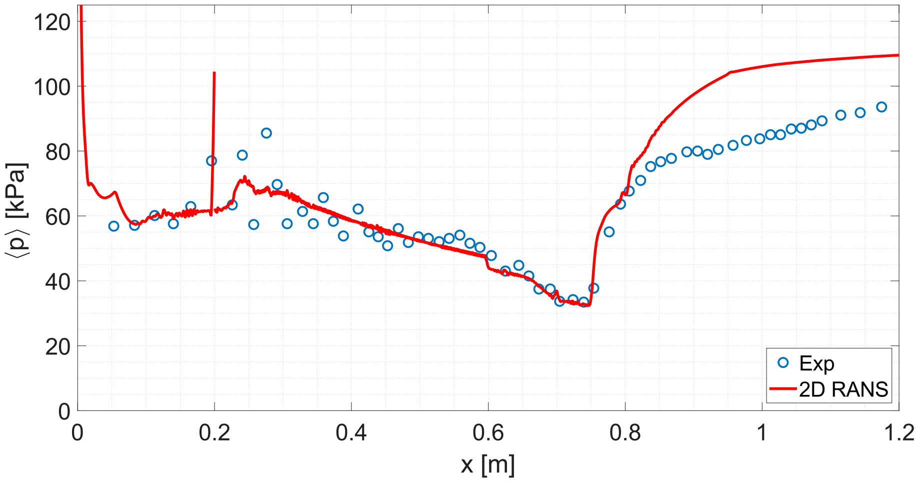

Figure 5.9: Case 1, 2D RANS, 2D mesh, lower-wall mean pressure comparison with experimental data. [3]

Also for this case, as for the non-reacting case in Fig. 5.5, the absolute pressure was not matched. To compare the relative trends with the experimental results was necessary to apply an offset of 6000 [Pa], different compared to the 5000 [Pa] of the non-reacting case, probably due to the downstream combustion modifying the thermodynamic quantities. The offset is within the tolerance for the reservoir pressure of ±10000 $[Pa]$ [29], and the aim was to match the pressure level of the expanded supersonic flow prior injection, avoiding other downstream influences. The calculated mean pressure is plotted against the experimental mean pressure [3], showing that the overall trends are captured, especially in the first part up to the separation point. However, the pressure after the combustion front appears to be over-predicted. This could be, as for the reacting case, for some factors: besides the aforementioned "plugged" configuration and *waveTransmissive* outlet condition for pressure, now the mismatch could be related to over-prediction of the heat-release due to the dimensionality reduction or other modeling approximation, not to mention the hot gases interaction with the plugged exhaust walls, that could play a role in the pressure level towards the outlet. The same jitter could be observed in some regions, probably for some boundary layer-compressibility interactions discussed in Subsec. 5.1.2.

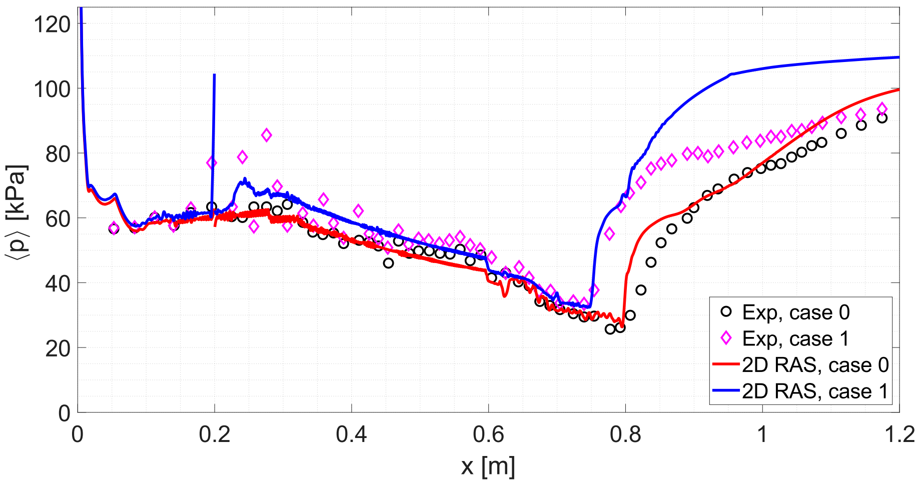

Figure 5.10: 2D RANS, 2D mesh, non-reacting and reacting lower wall mean pressure comparison with experimental data. [3]

As also showed by the comprehensive non-reacting and reacting pressure profiles at the lower wall, the general experimental behaviors [3] are demonstrated. For a quick and relatively cheap comparison, the 2D RANS shows a satisfactory agreement, even though more quantitative and in-depth assertions are not possible to make.

5.1.4 Developed Reacting Flow: Laminar case

An attempt to decouple turbulence and combustion interactions was made by switching both turbulence and combustion models to laminar. The latter is justified by the fact that the PaSR coefficient is 1 everywhere. For the former it could seem a wrong move at first, but since a model that correctly takes into account all the features in turbulent supersonic combustion is still under development [11], it was a move to further explore the "parameters space" looking for new possible insights. As a "final act", the turbulence model was switched to laminar on a soon-to-be reacting case from the time set. Unsurprisingly, everything blew up towards the injectors, but his time with a further development: before crashing, even a normal standing shock was generated just upstream of the injectors, hinting some "unstart-like behavior". To ease the interpretation, the first snapshot will be named t_0 and will be the starting time, meanwhile the following snapshots time will be considered from t_0 and named t'. The fields represented are Mach number, pressure in logarithmic scale, hydrogen mass fraction, heat-release, hydroxyl (OH) mass fraction and temperature. Unsurprisingly, no stable solutions were obtained mainly due to the non-modeled turbulence, non-modeled interaction with the combustion and the non physicality of the 2D burning slot. Everything ended with a spectacular explosion towards the inlet, with a strong standing shock upstream of the injectors.

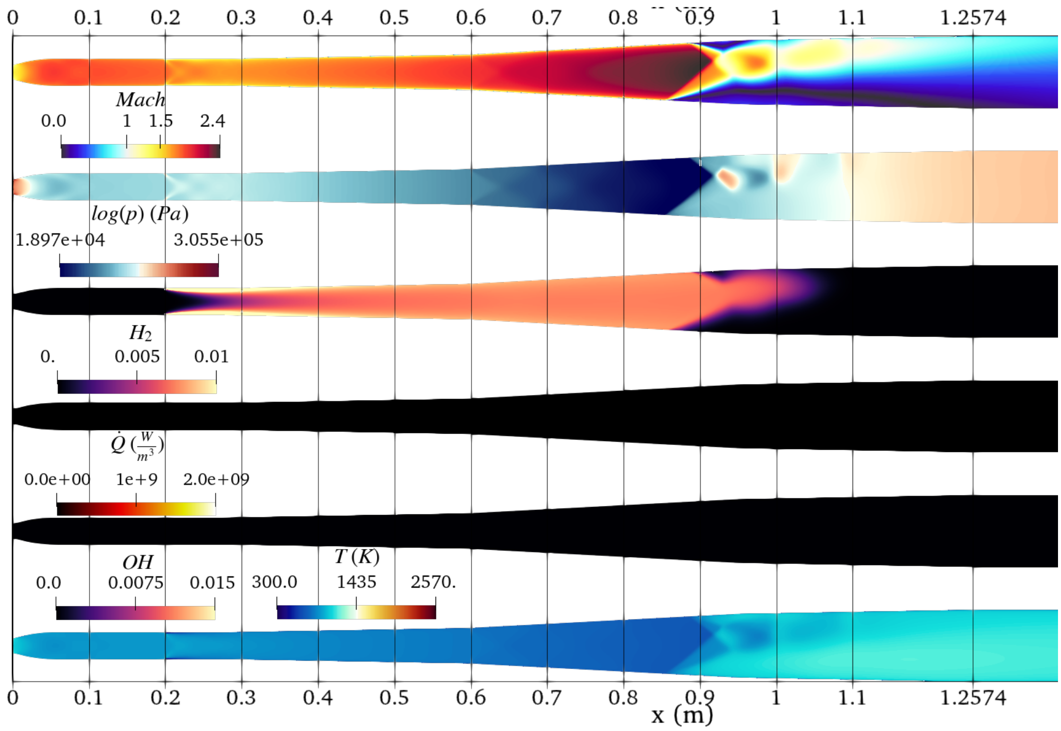

Figure 5.11: 2D, laminar, $t_0 = 0$ [s]

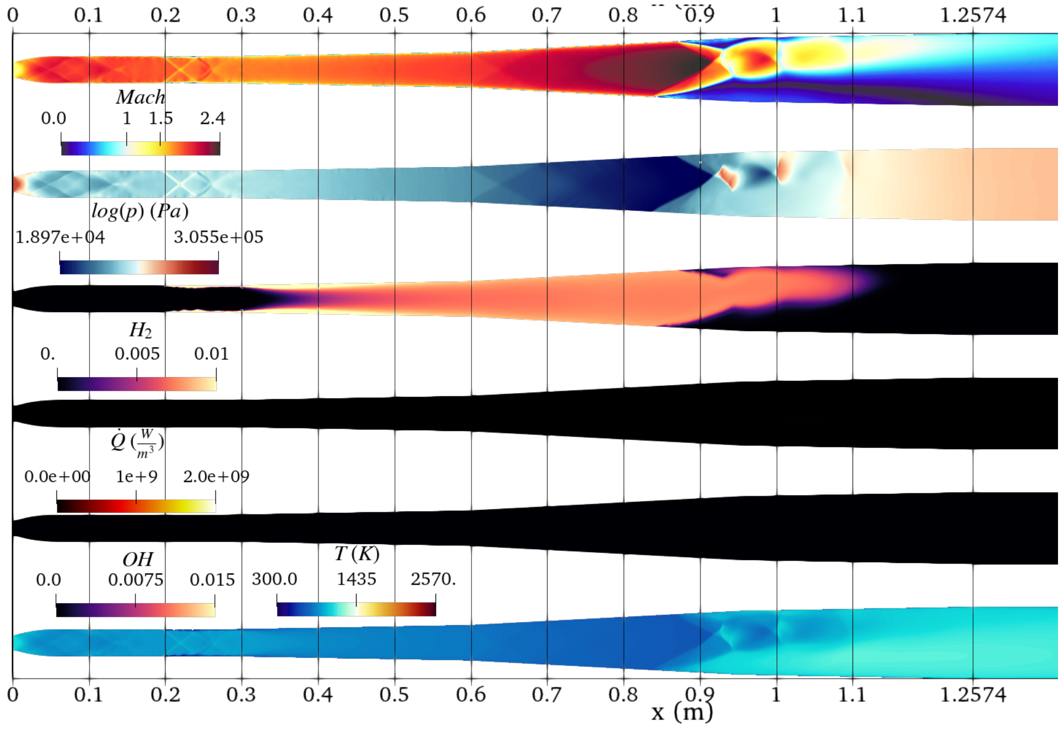

Figure 5.12: 2D, laminar, $t' = 0.0001$ [s]

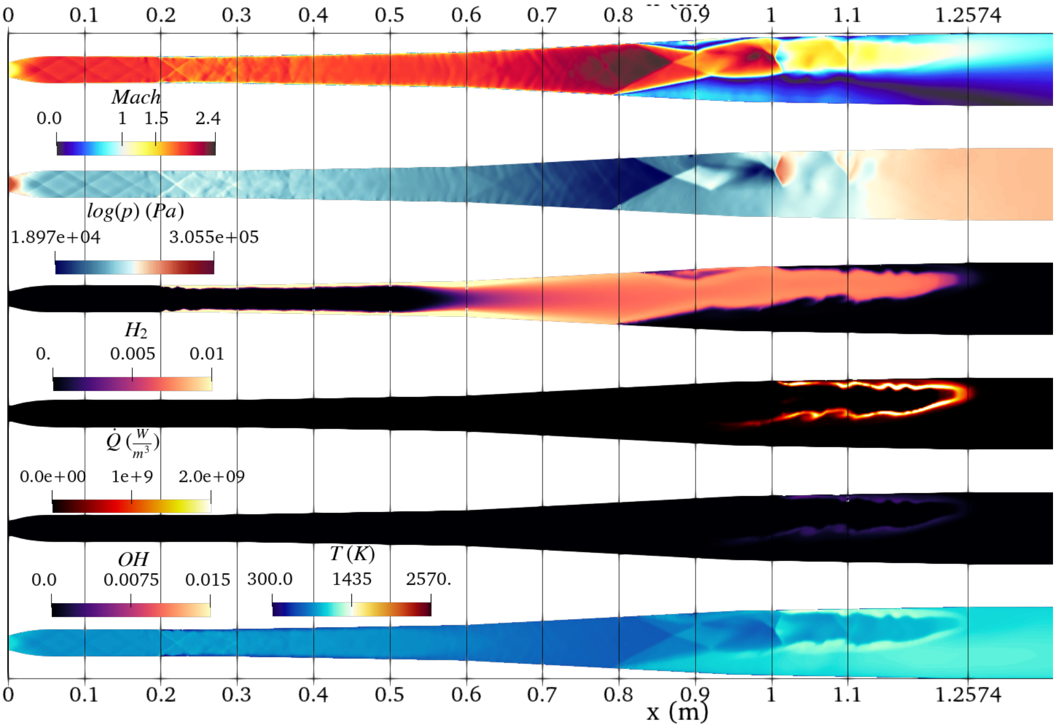

Figure 5.13: 2D, laminar, t'= 0.0003 [s]

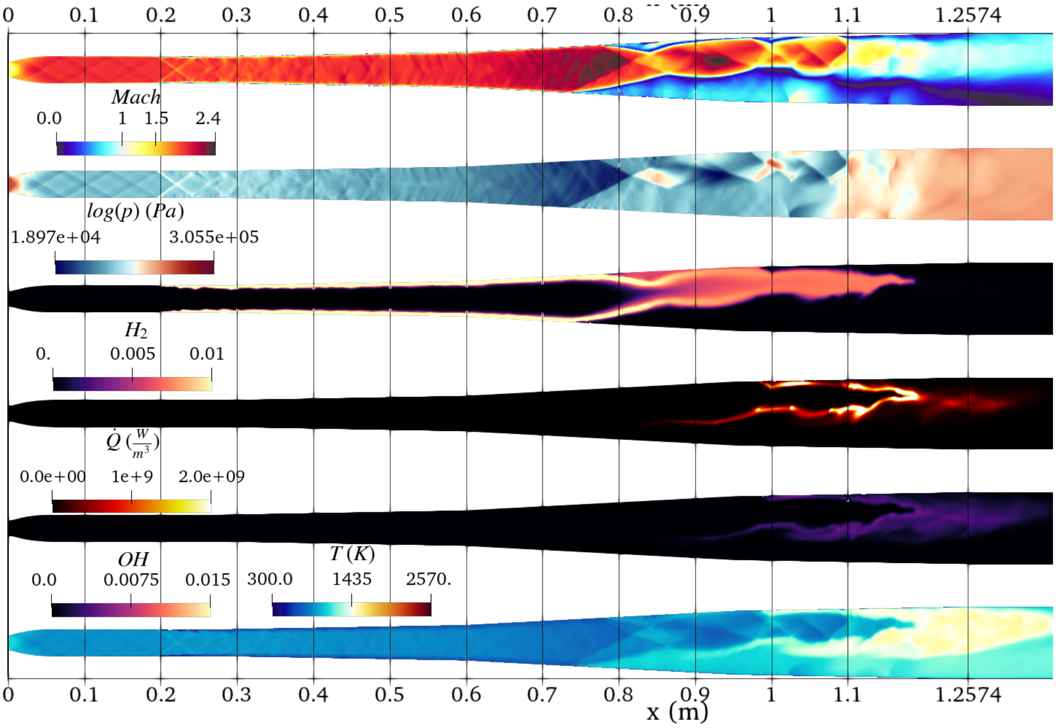

Figure 5.14: 2D, laminar, t'= 0.0005 [s]

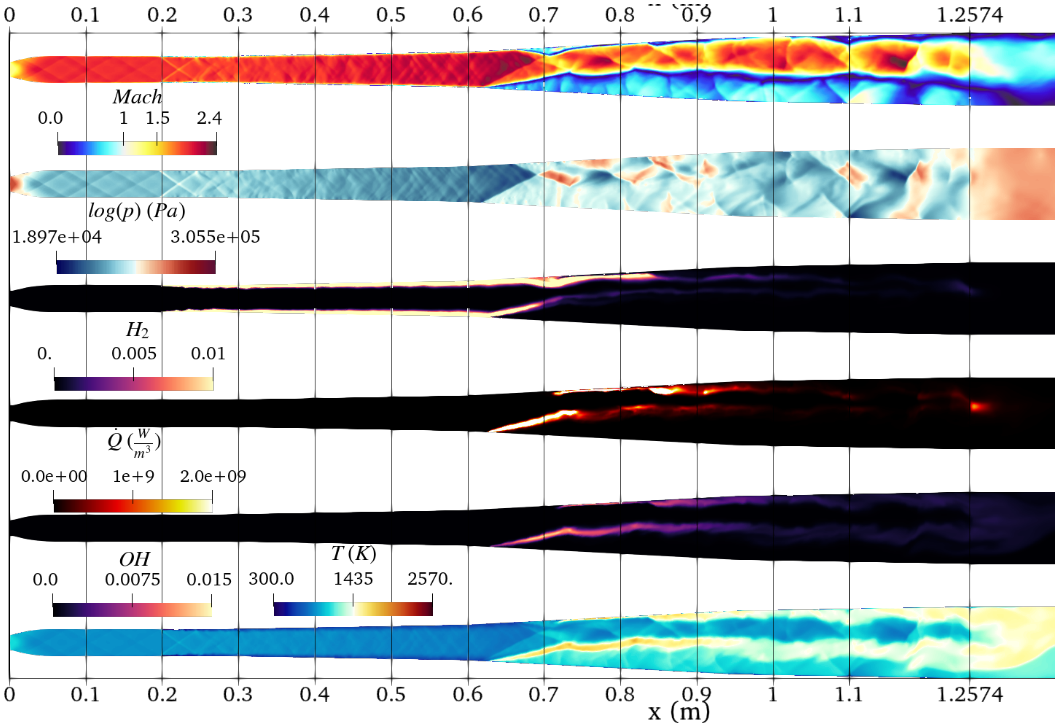

Figure 5.15: 2D, laminar, t'= 0.0009 [s]

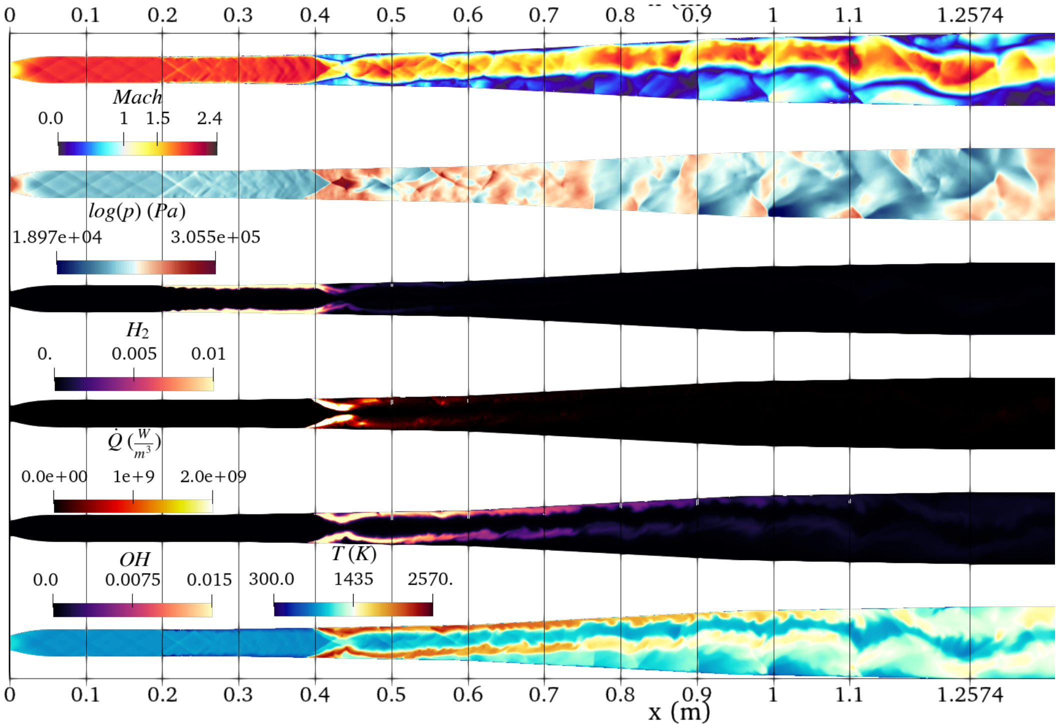

Figure 5.16: 2D, laminar, t'= 0.0014 [s]

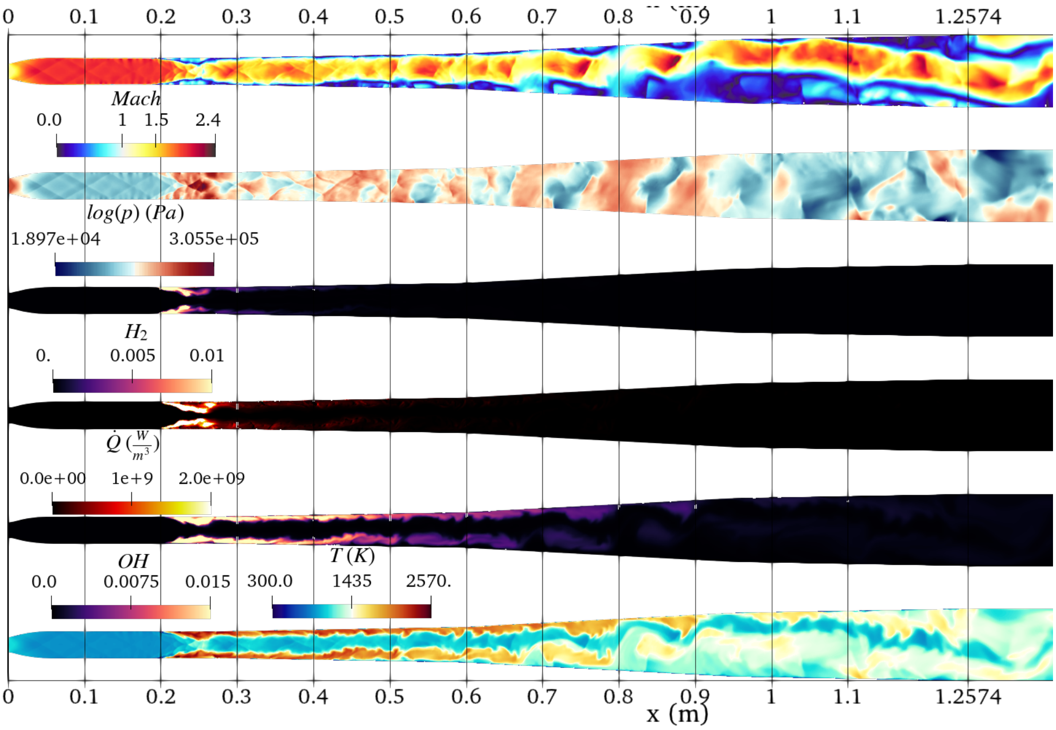

Figure 5.17: 2D, laminar, t'= 0.00173 [s]

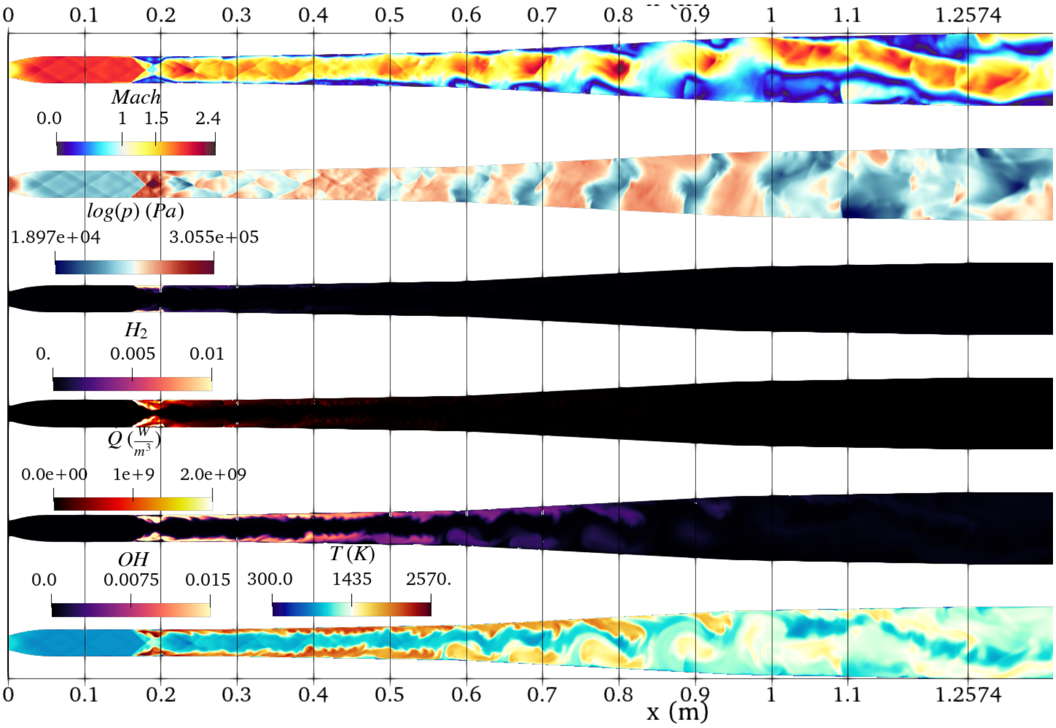

Figure 5.18: 2D, laminar, t'= 0.00183 [s]

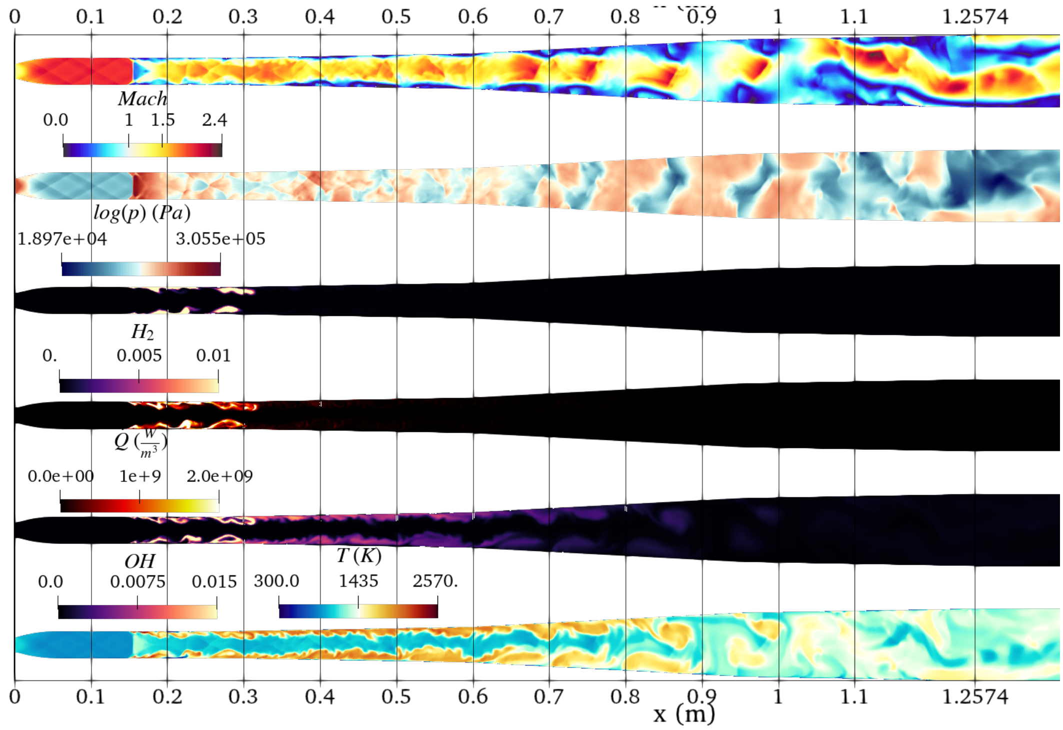

Figure 5.19: 2D, laminar, t'= 0.00194 [s]

5.1.4.0.1 Developed Reacting Flow: CCM While trying to stabilize the laminar cases and speed up even more the calculations, a version of *CCM* [49] (Chemistry Coordinate Mapping) was used. Even if the Z22 mechanism for hydrogen is not “heavy” on the chemistry side, a speed up of 2-3 times per timestep was observed, providing a remarkable improvement even in a density-based solver, provided adequate cell clustering. The logical next step will be a more chemistry-heavy fuel. If the "plug" in the exhaust pipe was removed from the beginning[2], no separation was observed, and even if an attempt of ignition was made, it was not possible to ignite the case. As testified by the fuel mass fraction plotted and the weak chemical and reactive activity.

---

[2] Applying *Slip* conditions to the extended mesh walls after the chamber’s end

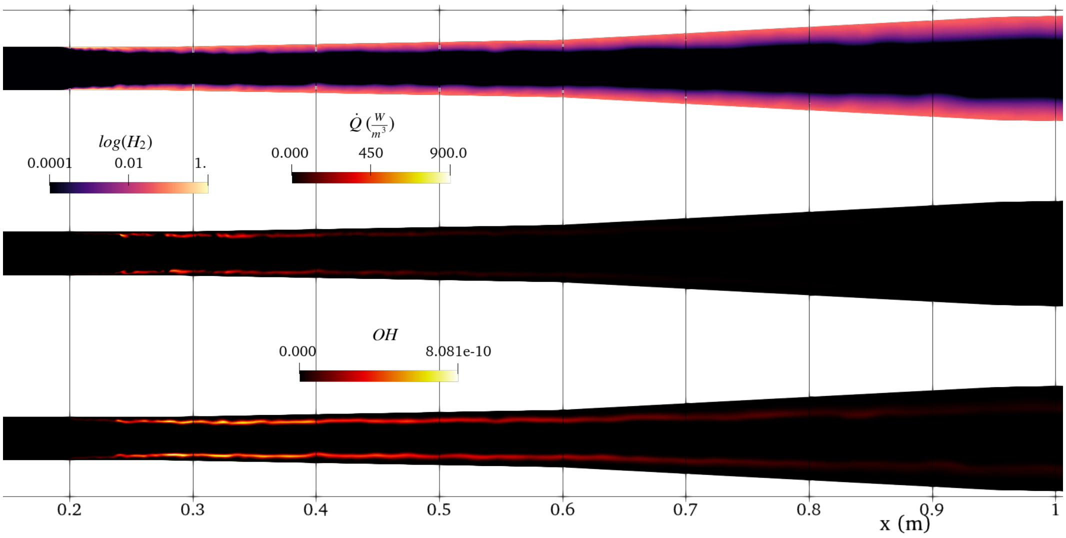

Figure 5.20: 2D laminar, 2D mesh, unplugged exhaust walls, hydrogen mass fraction in logarithmic scale, heat-release, hydroxyl, OH, mass fraction

It was possible to have another comparison with the non-reacting fully supersonic flow done in the mid-line, as done in Subsec. 5.1.1.

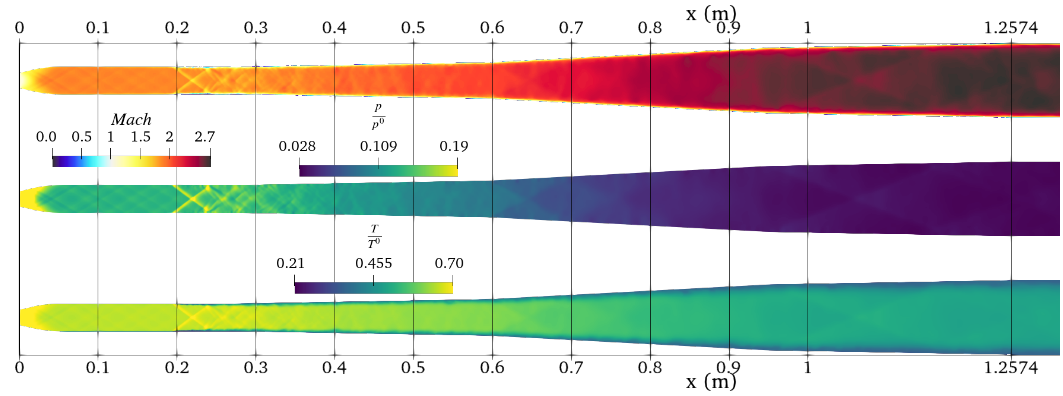

Figure 5.21: 2D laminar, 2D mesh, unplugged exhaust walls, Mach number, normalized temperature and pressure

It appears that now, by changing model, the values are closer to the measured data [21], hinting that also some phenomena are shadowed within the RANS simulations. Some oscillations may be induced by the fuel injected, meanwhile the pressure is in good agreement.

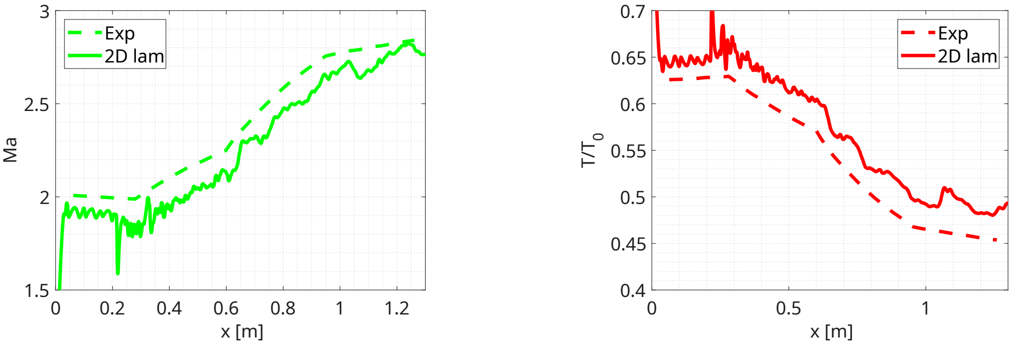

(a) 2D, laminar, Mach **(b)** 2D, laminar, temperature

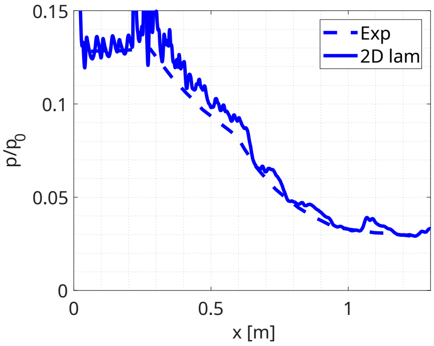

(c) 2D, laminar, pressure

Figure 5.22: 2D laminar, 2D mesh, unplugged exhaust walls, fully supersonic flow comparison

5.1.5 Summary of 2D cases

Except some images and the methodology used, it was not possible to infer more. A full three-dimensional (3D) simulation was deemed necessary for a better description. Furthermore, to have even faster results, a chemistry accelerator, *CCM* (Chemistry Coordinate Mapping), was used, providing an acceleration on the single time step to be up to ~ 3 times, provided an adequate grouping process. To inquire further on the knowledge edges, even switching to a laminar simulation was attempted. It was not possible to obtain a stable solution: other losses in the model capability, and the burning “slot” derived from the dimensionality reduction, were not giving room in the domain for the development of the required structure, and the laminar simulation resulted in being unstable with the flame crawling back to the injectors. On top of that, the conclusions obtained were possible thanks to a practical trick, which does not reflect the experimental configuration, hence a 3D simulation was deemed necessary for a more detailed description.

5.2 Three Dimensional Campaign

After some simulations in the 2D domain, it is finally time to unlock the third dimension. To do that, it was necessary to scale up the computational power and have access to High Performance Computing (HPC). For that matter, I would like to acknowledge once more the resources provided by NAISS (National Academic Infrastructure for Supercomputing in Sweden), otherwise it would have been impossible to carry out this work. An honor mention goes particularly at "Dardel" [3] and "Tetralith" [4]. Without them what follows would not have been possible. The cases studied were the same investigated by previous studies with the conditions reported in Tab. 4.1. Follows a quick summary of the case studied here:

- Case 0: non reacting case;
- Case 1: reacting subsonic combustion mode;
- Case 4: shock-induced combustion mode;

5.2.1 Case 0

The case 0, or non-reacting case, was only made with the new mesh (modified mesh, in Subsec 4.3.3) with mapped initial fields from the provided case 1. It served as a first benchmark to see if the boundary layer features were correctly captured, to see if the parameters for the boundary condition were correct, and to assess the quality of the new mesh. Here, the 1D CHT BC parameters and the coupled radiation model were finally tested. As for the radiation model, the P1 model was selected: even if it tends to over-estimate the radiative heat fluxes, it was chosen for its robustness and for being the cheapest model possible, compared to other models.

The case without hydrogen injection has been studied, and the fields were mapped from a subsonic reacting case, case 1, provided by previous benchmark studies previously done. Not injecting the fuel is accountable for having the possibility of roughly doubling the time step respect the other cases (while keeping the same CFL$\leq$0.25), as the violent expansion from the hydrogen injectors is not present in the most refined zone, compared to case 1, Subsec. 5.2.2 and case 4, Subsec. 5.2.3.

---

[3] Part of PDC, KTH Royal Institute of Technology HPC infrastructure (Stockholm, Sweden)

[4] Part of NSC, Linköping Univerisity HPC infrastructure (Linköping, Sweden)

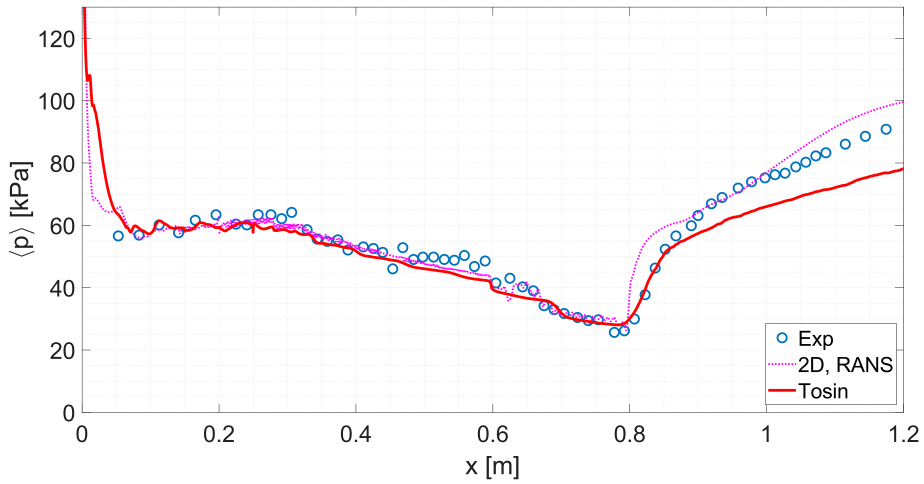

Figure 5.23: Case 0, modified mesh, lower-wall mean pressure along the mid-line compared with experimental data. [3]

The comparison between the measured and the numerical mean pressure at the lower wall along the mid-line is presented, with the 2D case in the background to have a comparison. Due to possibly model approximations, uncertainties of inlet turbulence during the experiments and the extended final part on the mesh, the exact absolute pressure values were not captured, with also the outlet boundary condition *waveTransmissive* not reflecting back acoustical waves worsening the situation. To have a comparison of the relative behavior, an offset of 6500 [Pa] was applied to the numerical results, in order to match the mean pressure values in the first part until the injectors location at 0.2 [m], avoiding further arbitrary choices that could be influenced by other factors not considered. Furthermore, the offset applied is far within the uncertainties reported for the reservoir conditions being ±10000 [Pa] [29]. Following the axial location from the inlet, the trend is well captured within the first half of the combustor, a small underestimation is observed around 0.6 [m], possibly due to a small step present in the chamber not taken into account in the computational model [3]. Nevertheless, the agreement is satisfactory up until the separation point, with also the axial location and the slope being correctly represented. However, from roughly 0.9 [m] to the chamber's end there is a drift on the calculated pressure. Probably, the outlet boundary condition not reflecting acoustical waves and the loss of mesh resolution in the extended final part are contributing to that. The extended mesh exhaust was necessary to obtain stable combustion, but not present in the experimental configuration, as the flow is not expanding as in the exhaust pipe. Another factor could be the fact that the inlet turbulence from upstream features and boundary layer growth are not considered, not to mention that also a security burner is operating downstream, whose effects are unknown. Also, since no combustion is present, Mach values towards the outlet are higher due to the lower temperature in the absence of combustion, and the exhaust final part does not expand the flow as it would be in the experimental configuration.

It has been observed that sometimes a supersonic flow pocket goes through the outlet. This could be contributing in the loss of reflected pressure waves from the outlet, in addition to the *waveTransmissive* outlet condition, as those pockets will be over-specified from a numerical standpoint. Thus, the pressure values reaching the outlet in the supersonic pocket, will not be reflected back since the value will be imposed from the extrapolated values of the internal domain. To verify the reliability of the results, some quantities have been sampled during two milliseconds (roughly two times the chamber residence time) from the data set to have a rough estimation of the lost pressure content and if convergence is affected:

- M_{max} since the turbulence model is represented by the dynamic k-equation, LDKM, a warning threshold was set at 0.9 as triggering “transonic behavior” at the outlet;
- $\frac{A_{r.c.}}{A_{out}}$: to have an idea of the area interested by this overspecification of the pressure, “r.c.” means “Region Considered”;
- $p_{min,\ r.c.}$: minimum pressure of the region considered;
- $\langle p_{r.c.} \rangle$: mean pressure of the region considered by transonic effects. The imposed far-field pressure is 101.3 [kPa], applied uniformly;
- m_{tot}: total mass in the computational domain, to verify if mass conservation is affected;
- $\frac{\phi_i - \phi_o}{\phi_i}$: normalized mass flow rate difference, to further monitor the mass flow mismatch between inlet and outlet patches. Even if instantaneous values are reported, the most important is the average values, as oscillations are expected due to the unsteadiness from the LES.

Time [s]	M_{max}	$\frac{A_{r.c.}}{A_{out}}$ [%]	$p_{min,\ r.c.}$ **[kPa]**	$\langle p_{r.c.} \rangle$ **[kPa]**	m_{tot} [g]	$\frac{\phi_i - \phi_o}{\phi_i}$ [%]
0.01482	0.906	0.13	97.33	97.86	0.8934	-4.52
0.01492	0.846	-	-	-	0.8950	6.48
0.01502	0.868	-	-	-	0.8950	7.03
0.01512	0.885	-	-	-	0.8966	-1.15
0.01522	0.708	-	-	-	0.8959	-3.18
0.01532	0.944	0.92	92.73	93.93	0.8948	-5.26
0.01542	1.161	2.29	95.43	96.83	0.8945	2.27
0.01552	0.798	-	-	-	0.8960	5.36
0.01562	0.769	-	-	-	0.8966	-1.38
0.01572	0.825	-	-	-	0.8964	2.5
0.01582	1.142	2.61	84.18	89.85	0.8970	0.81
0.01592	0.841	-	-	-	0.8972	-1.97
0.01602	0.778	-	-	-	0.8980	1.75
0.01612	0.705	-	-	-	0.8976	4.3
0.01622	0.735	-	-	-	0.8980	1.52
0.01632	0.734	-	-	-	0.8970	-4.99
0.01642	0.932	0.23	90.40	90.79	0.8950	-6.09
0.01652	0.918	0.61	96.51	96.70	0.8948	2.37
0.01662	0.853	-	-	-	0.8957	6.63
0.01666	0.882	-	-	-	0.8965	7.84
0.01676	1.041	0.27	99.66	101.11	0.8988	2.52
0.01686	0.796	-	-	-	0.8987	2.99
0.01696	0.810	-	-	-	0.8989	2.00
Average	0.864	0.31	93.75	95.25	0.8964	1.21

Table 5.1: Case 0, modified mesh, sampled evolution of the outlet patch

In addition, the average values have been calculated. Starting from M_{max}, it appears that it does not manifest very often, hinting at some sort of intermittent behavior probably generated by the structures being convected downstream from the mixed subsonic/supersonic region. A plot of magnitude and components of the pressure gradient (∇p) shows those structures convected. The coarsened exhaust pipe is very important to reduces these very strong variations.

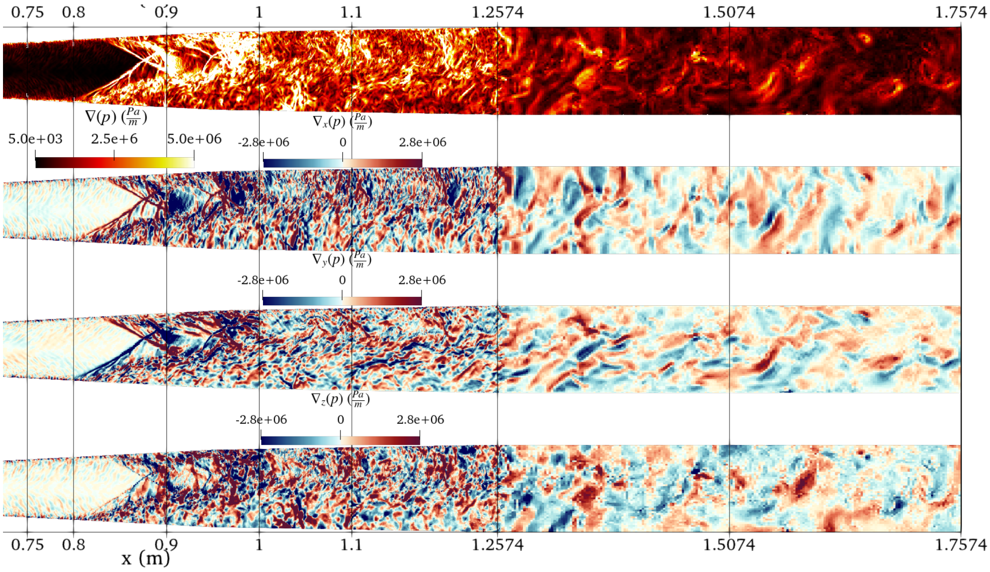

Figure 5.24: Case 0, modified mesh, instantaneous pressure gradient at t=0.01542 [s]

Those are good news for the validity of the results, as also total mass and normalized mass flow difference show acceptable variations. Even if the transonic pockets always display lower pressure compared to the far-field pressure of 101.3 [kPa] from the *waveTransmissive* outlet condition, this is not an issue for the results credibility. Regarding the observed pressure drift, a more in-depth analysis considering other factors should be carried as the transonic area is not high and always present.

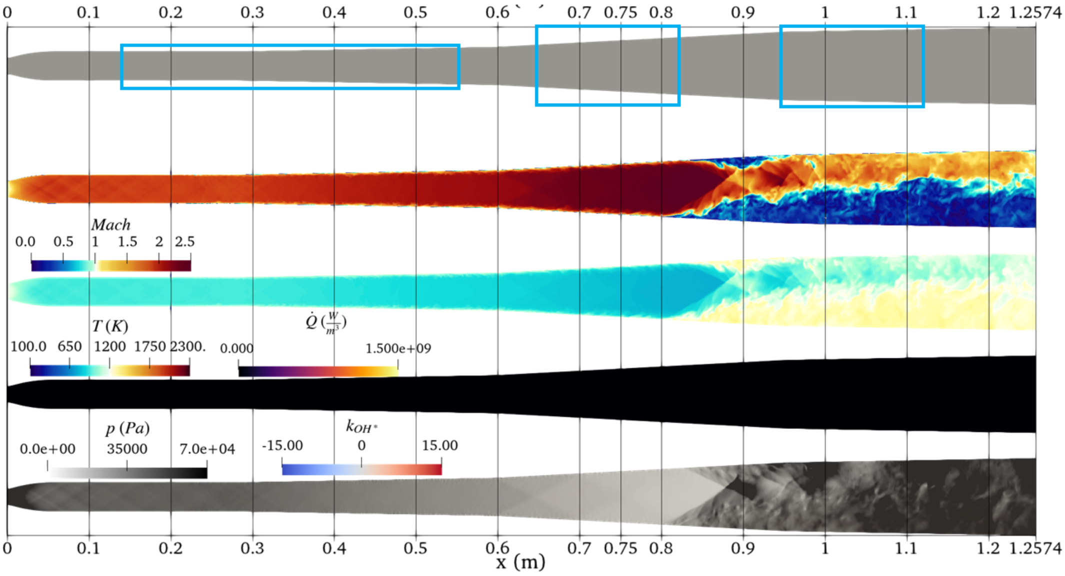

Figure 5.25: Case 0, modified mesh, instantaneous Mach, temperature, heat release, pressure and modified photon emission rate k_{OH} at the symmetry plane

A first set of slices along the symmetry plane were made, inspired from the work on [3]. The top picture shows the chamber prospect with windows placed within the cyan-colored boxes. The instantaneous Mach magnitude, centered around 1, marks the separation within blue subsonic regions, in the boundary layer and in the separation, and the red supersonic region, representing the bulk flow. The separated regions are also responsible for the generation of oblique shockwaves that got reflected and interacts with the transonic shear layer, while the recirculation zone at the lower wall appears to be bigger compared to the one in the upper wall, where the relatively cold supersonic flow, impinges the wall. This upper-wall bias has been observed in the 2D campaign, Subsec. 5.1.2 and in pervious studies.[3] The temperature behavior follows and shows the temperature levels of the separated regions, where the high-speed flow is brought to rest increasing the temperature. As expected, nothing is visible from specific heat-release and modified photon emission rate (k_{OH}), only the overlapped pressure is visible hinting a dynamic-rich behavior captured, starting from the expansion fans from the inlet to the 3D eddies downstream interacting with compressible features. In this work, the so-called modified photon-emission rate, named k_{OH}, is calculated as:

$$k_{OH} = A\frac{\rho Y_{OH}}{M_{OH}} \tag{5.1}$$

Where A represents the spontaneous-emission Einstein coefficient[5], ρ the density, M_{OH} hydroxyl molar mass, and hydroxyl mass fraction (Y_{OH}) used instead of excited species OH^*. Due to that, the modified photon-emission rate still acts as a good indicator for flame brush, but not for the flame front.

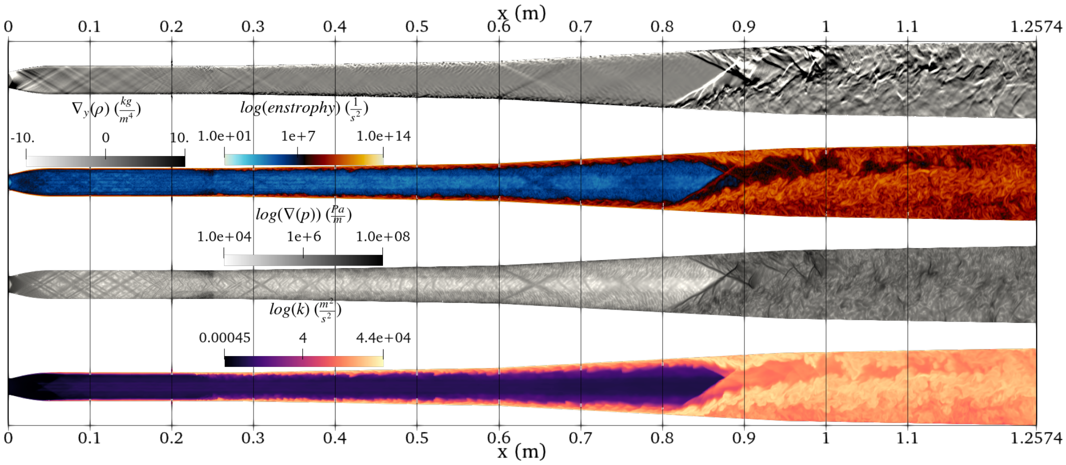

Figure 5.26: Case 0, modified mesh, instantaneous numerical Schlieren,enstrophy in logarithmic scale, pressure gradient in logarithmic scale, k (subgrid kinetic energy) in logarithmic scale at the symmetry plane

Another set of slices was made to further visualize the compressible and turbulent

---

[5] Serving as a proportionality constant from species mass fractions to light intensity

features. Those pictures show the capability of the LES in capturing an intertwinement of complex phenomena. The logarithmic scale of subgrid kinetic energy (k) and enstrophy magnify the boundary layer growth along the walls, and the eddies generated upon and after boundary layer separation. The numerical Schlieren displays a strong turbulent flows after the injectors at 0.2 [m], where jitter near the walls can be observed due to strong spanwise vortical structures growing.

It emerges how the LES capability is highly sensitive with the mesh resolution, particularly evident in the pressure gradient, as the overlapping refinement regions near the injectors is responsible for a consistent growth in the eddies near the walls, following the formation of structures from the throat.

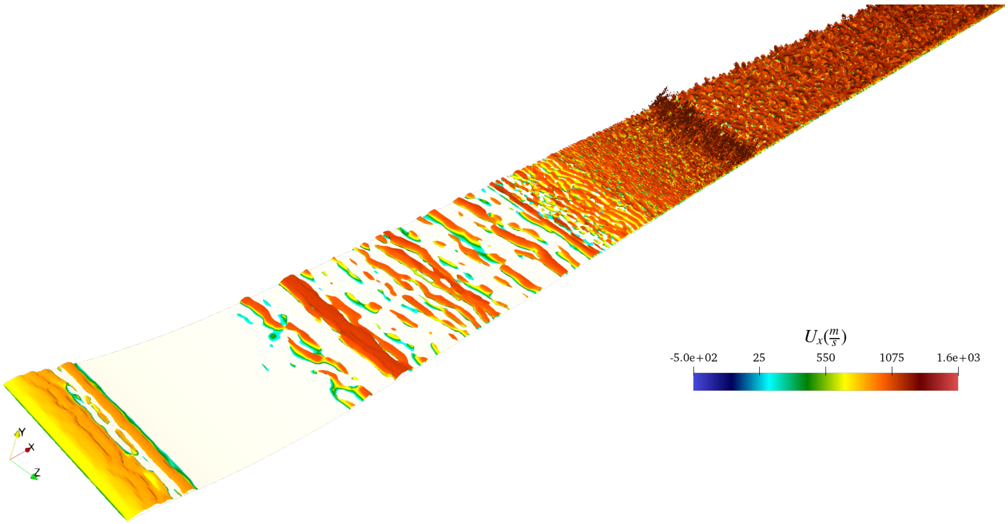

Figure 5.27: Case 0, modified mesh, Q-criterion contour colored with axial velocity, near the inlet

To better visualize the turbulent features, the Q-criterion contour colored by the axial velocity shows the growth and cutoff of the structures starting from the inlet, where the flow seems almost laminar, to the refined region, where strong turbulence is observed, along some “numerical garbage” right before the refined region cutoff related to the values chosen for the contour. This aspects show the strong dependence of the mesh size in capturing the structures, as expected.

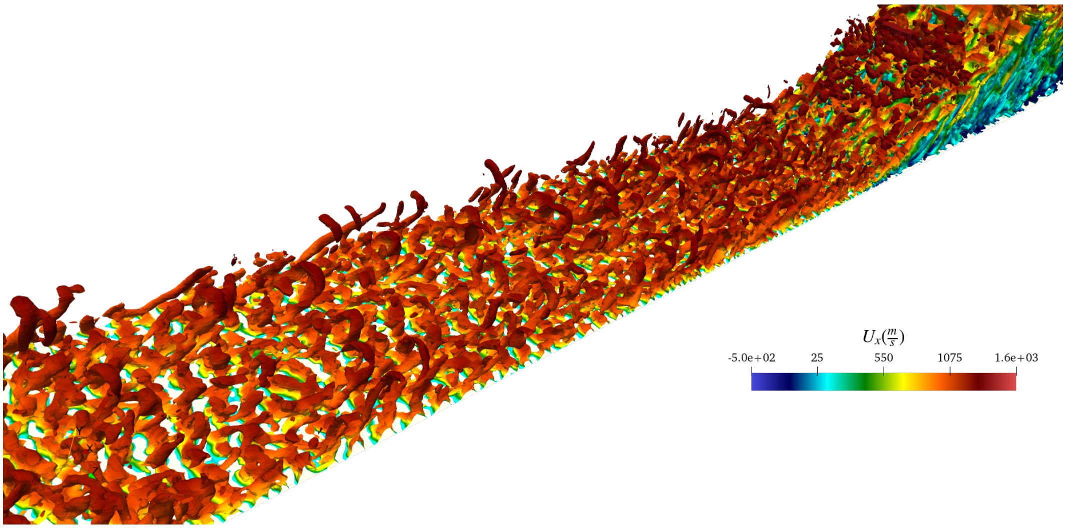

Figure 5.28: Case 0, modified mesh, Q-criterion contours colored with axial velocity. near the separation region

Nevertheless, as the flow develops along the combustor, the eddies further grow in strong correlation with the flow acceleration, until the separation point, with the Q-criterion contour capturing strong hairpin vortices from the boundary layer near the separation region. Those large eddies from the boundary layer, as also captured by Fig. 5.26, are responsible for the oscillation of the combustion front as they go through the front of the oblique shockwaves generated from flow separation. After the separated regions, the oblique shockwaves strongly interact and got distorted by the separated eddies, as showed by the Mach slices in Fig. 5.25. As a final touch, a comprehensive picture of the growth of those eddies is presented.

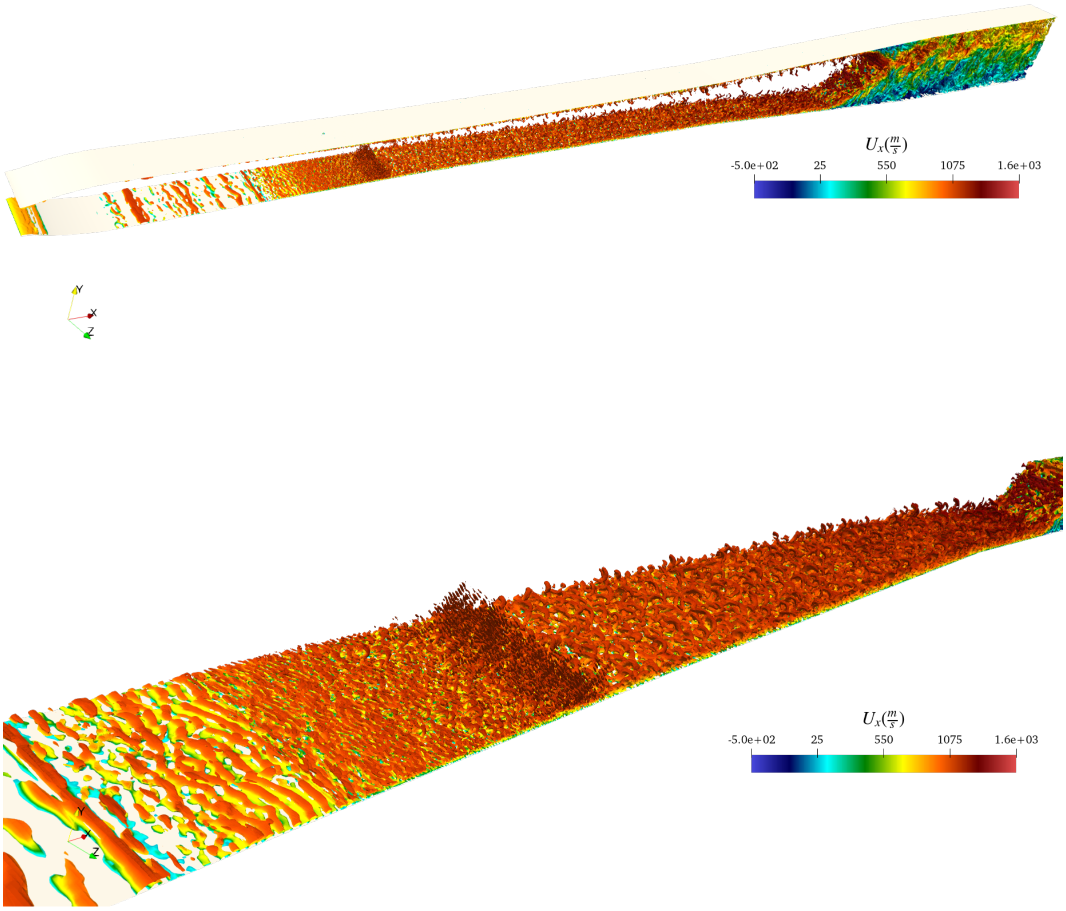

Figure 5.29: Case 0, modified mesh, Q-criterion contour colored with axial velocity

It is also interesting to look at the mean fields. Notably, the bias of the flow towards the upper wall is still observed, as predicted during the 2D campaign. Another important aspect are the normalized deviations (root-mean square) of the mean quantities. They further show the oscillating shockwave front near the separation points, where high values are observed, while maintaining a fairly stable axial location, which is consistent with the experimental data. [21]

The velocity magnitude and Mach number magnitude standard deviations are not normalized due to the zero-velocity line within the shear layer separating the separated subsonic region from the supersonic bulk flow region, with enstrophy and turbulent kinetic in Fig. 5.26 displaying those vortical-rich regions generated from the separation points.

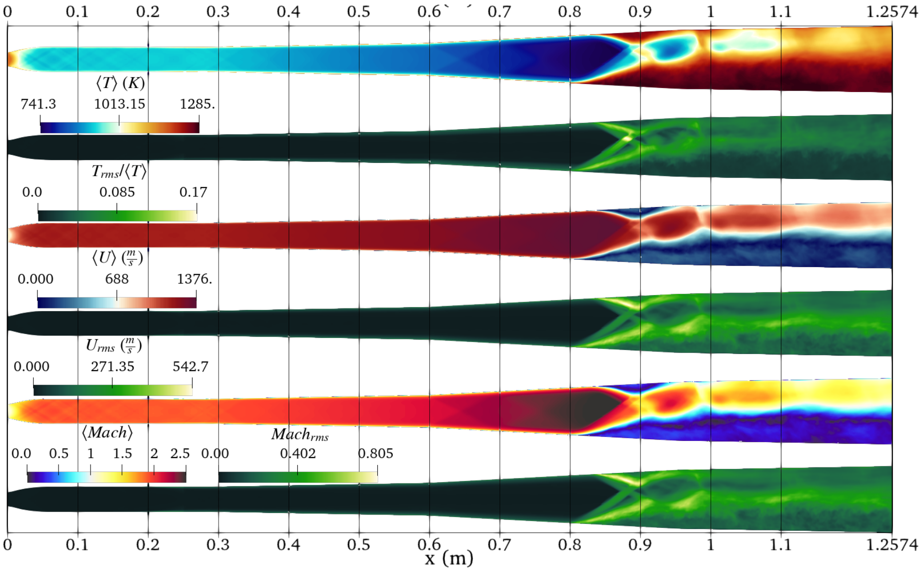

Figure 5.30: Case 0, modified mesh, mean fields of temperature, velocity magnitude and Mach with their standard deviations

The standard deviation of the mean Mach number reaches almost sonic velocities (0.8), meaning that the oscillations of the separation line have a fairly high frequency.

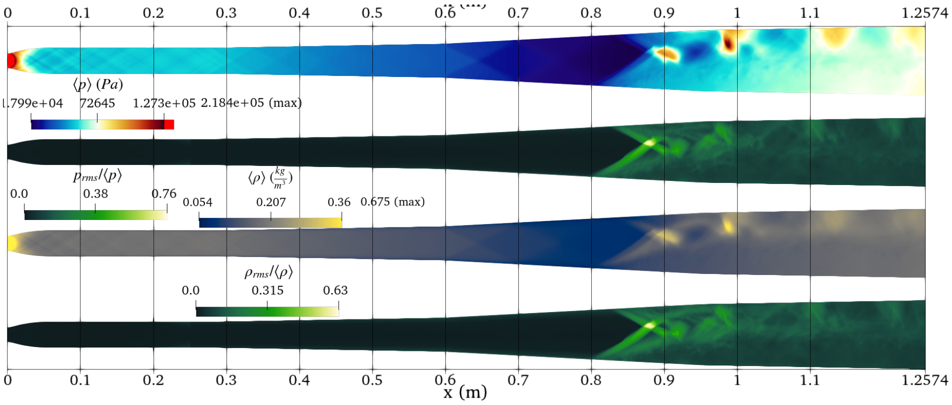

Figure 5.31: Case 0, modified mesh, mean fields of pressure and density with their standard deviations

The pressure and density mean fields further strengthen the observations made for other quantities. As for the root-mean square normalized values they further confirm the shock's front moving accordingly to the large scale turbulent structures impingement, while displaying a stable axial position of the separation points. Finally, y^+ values have been estimated "*a posteriori*" using the built-in function *yPlus* available within the *postProcess* utility in OpenFOAM.

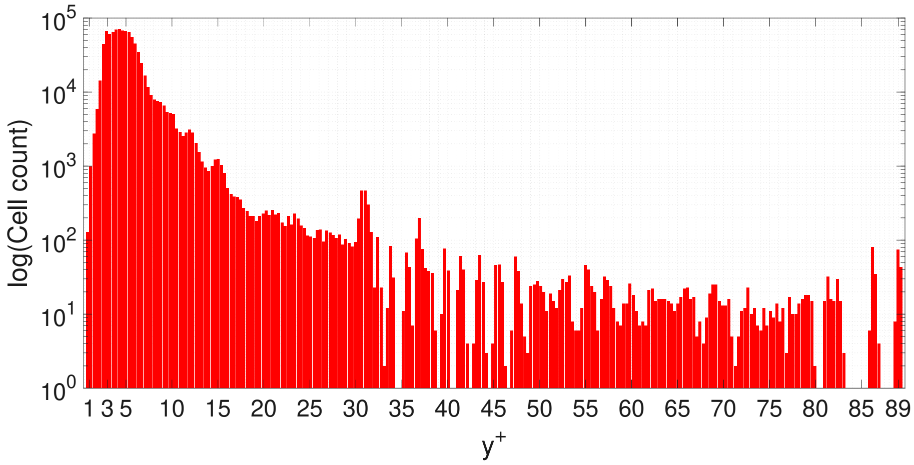

Figure 5.32: Case 0, modified mesh, histogram of instantaneous y^+ values

The histogram is reported, showing that most cells have values of y^+ between 1 and 30. The values for the latest instantaneous snapshot are presented, and are between 0.37 and 89.61 with a mean of 5.74. Lower values are located near the shock impingement at the walls, where the strong gradient stresses the numerical stability to the limit, while higher values are located near the non-refined upstream part of the chamber. The average value is in the suitable range for a "*wall-modeled LES*" (WMLES), with the *nutkRoughWallFunction* employing an automatic switch based on the local y^+ values. However, the roughness and the 1D CHT BC employed could be underestimating those values due to the boosted subgrid kinetic energy (k) and viscosity ν_t.

5.2.1.0.1 Radiation Model and coupling with the 1D conjugate heat transfer boundary condition (1D CHT BC) It is important to talk more about the radiation model and the 1D CHT BC employed. Regarding the radiation model, the P1 model was chosen (more on the boundary condition can be found in Sec. 4.1). Even if it is not the best model, as it tends to overestimate the radiative heat fluxes, it is a good first attempt for its low cost and robustness. This is important especially in complicated cases like the one studied, where even minimal perturbations can result in abrupt changes and/or numerical instabilities, and complex interactions are a serious stability challenge. No comparisons with experimental results are possible for thermal quantities of this case. It is interesting to have a look, for example, at the net radiative energy, here represented in a slice in the symmetry plane.

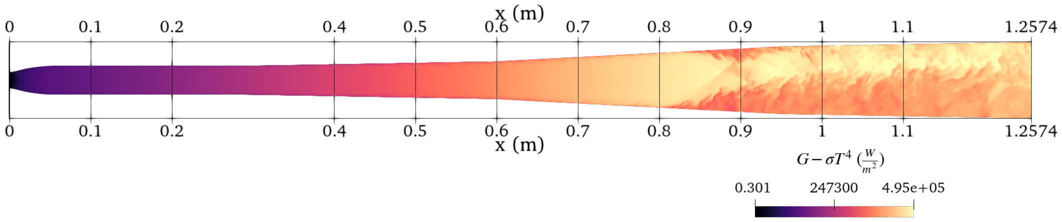

Figure 5.33: Case 0, modified mesh, net radiative energy term in the symmetry plane

The term here named "net radiative energy" or "net radiative term", calculated as $G - \sigma T^4$ (without a factor 4 and absorption in the second term respect Eq. 4.8), corresponds to the difference between incident radiation (G) and (assumed to be) black-body emissive power calculated as (σT^4)[6], which is the maximum radiative energy locally emitted. Even if absolute values are not related to the radiative source term in Eq. 4.8, observation can be made on the relative changes regarding how temperature and incident radiation interacts with the flow features. Reported values increase as the axial location increases. This is consistent with the 1D CHT BC coupled with the radiation, as also the wall is emitting/absorbing radiation.

---

[6] $\sigma = 5.67 \cdot 10^{-8}$ $[\frac{W}{m^2 K^4}]$ is the Stefan Boltzmann constant

Another factor is the temperature drop in the bulk supersonic flow until the separation points due to the ever-expanding geometry of the chamber [7]. It is very difficult to look for the required parameters for the 1D CHT BC, because they are either not reported or not often considered. However, for this experimental facility the most important information for the TBC have been reported [3]. For the thickness of the chamber, it was obtained from the magnification of the injector section in Fig. 3.3. Follows a table with the values for the *externalWallHeatFluxTemperature* boundary condition used:

Patch	h $[\frac{W}{m^2K}]$	T_a [K]	emissivity [-]	YSZ thickness [m]	Cu alloy thickness [m]	k_{YSZ} $[\frac{W}{mK}]$	k_{Cu} $[\frac{W}{mK}]$
Top	15	293.15	0.7	0.00028	0.066	1.3	340
Bottom	10	293.15	0.7	0.00028	0.066	1.3	340

Table 5.2: Case 0, modified mesh, *externalWallHeatFluxTemperature* parameters

About the choices:

- Convective heat transfer coefficient: for h, representing the natural convection, no laboratory features are available. Typical values reported [50], assuming natural convection, are between 2-25 $[\frac{W}{m^2K}]$, with higher limits if the temperature difference between the ambient and the considered surface increases further. The experiment time was short to avoid overheating of the chamber since it was not water-cooled, hence it is difficult to have a fixed h for every condition and it is unknown if there were air recirculation in the laboratory. A value of 10 $[\frac{W}{m^2K}]$ and 15 $[\frac{W}{m^2K}]$ was chosen for bottom and top patches respectively. The difference to take into account the enhanced buoyancy effect due to the favorable up-facing orientation of the top patch;
- T_a: without further data, a value of $20°C$ was chosen;
- Emissivity: of the internal TBC. A value of 0.7, near the upper end to what is available in literature [51] is chosen to consider wall roughness;
- Thickness: the thickness of the TBC was chosen to be 0.28 [mm] respect a reported value of 0.3 [mm] due to degradation and roughness. For the thickness of the chamber, the value of 66 [mm], reported in Fig. 3.3, has been chosen;
- Thermal conductivity: since the chamber was not cooled, it is difficult to estimate a single value for the continuously heating chamber. However, to avoid further complications, for the chamber a *CuCrZr* alloy with a value of 340 $[\frac{W}{mK}]$ has been assumed. [52] For the YSZ a value of 1.3 $[\frac{W}{mK}]$ was assumed, based on the fact that it was deposited and subjected to degradation during the experiments. [46, 47]

---

[7] This is important to prevent thermal choking in combustion cases.

The instantaneous values the top and bottom wall patches related to the 1D CHT BC are reported in Fig. 5.34. The net radiative energy term follows the same axial evolution reported in the symmetry plane slice in 5.33, while the other quantities are instantaneous temperature, *wallHeatFlux*[8], and the radiative heat flux, q_r. Starting from the inlet, the temperature begins to rise axially due to the growing turbulent boundary layer and enhanced wall viscous dissipation that increases the heat fluxes as well, until a sign inversion is observed, mainly driven by the radiative heat flux values. It is worth to notice how the turbulent and compressible features impinging the walls have a strong influence regarding local heat fluxes, and how well they are captured by the LES.

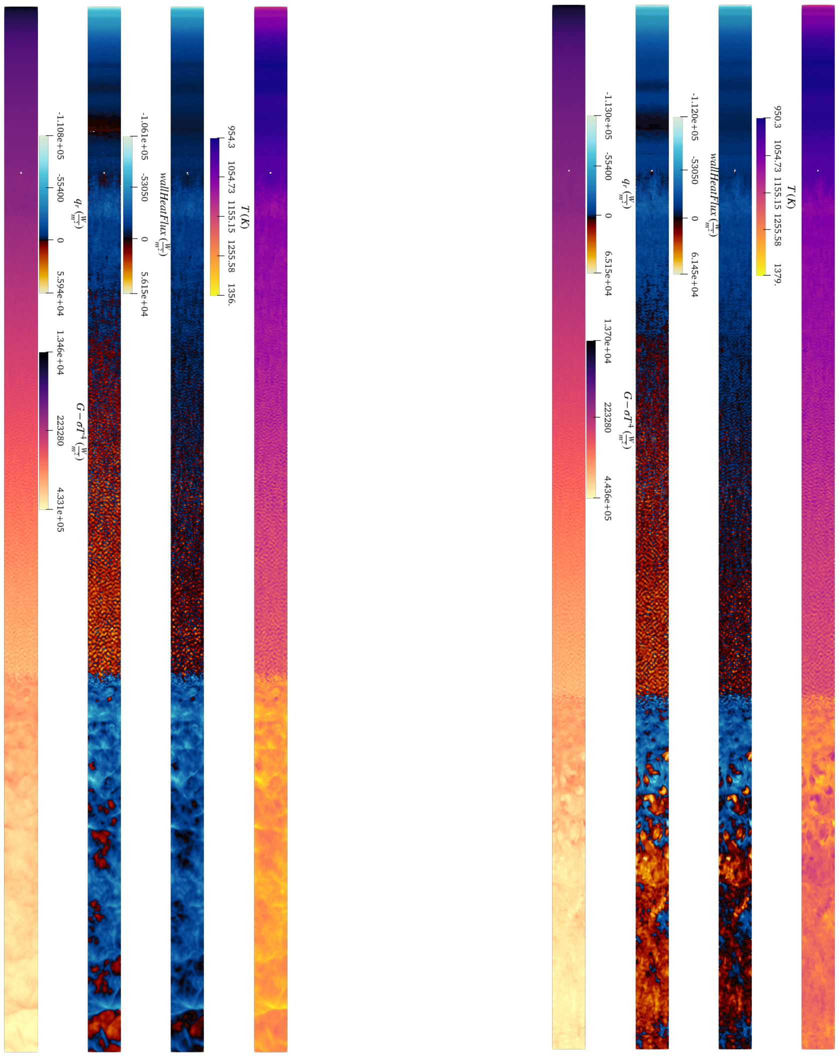

(a) Bottom wall patch

(b) Top wall patch

Figure 5.34: Case 0, modified mesh, instantaneous wall values for temperature, *wallHeatFlux*, radiative heat flux and net radiative term for h of (15,10) $[\frac{W}{m^2K}]$

---

[8] Here only convective heat flux through the wall patches due to a bug of the used OpenFOAM version [53]. It should have been the sum of radiative and convective heat fluxes through the surface calculated using the so-called OpenFOAM built-in function

About the sign convention in OpenFOAM for the heat fluxes:

- **Positive:** heat from the wall to the fluid, the computational domain is being heated up;
- **Negative:** heat from the fluid to the wall, the computational domain is being cooled down.

In the separated regions, the walls reaches its peak temperature values with heat fluxes heating the walls, except the final part of the top patch that corresponds to the relatively cold bulk supersonic flow impingement that also abruptly change wall viscous dissipation causing a pocket of heat fluxes towards the fluid. This heating related to the upper wall bulk flow bias, could contribute to the bulk flow bias patch change reported in [3] after longer simulation times[9], as the heating can induce boundary layer separation triggering bulk flow variations. To have a more quantitative picture, the mean values for temperature and presented fluxes along the mid-line of the patches are presented.

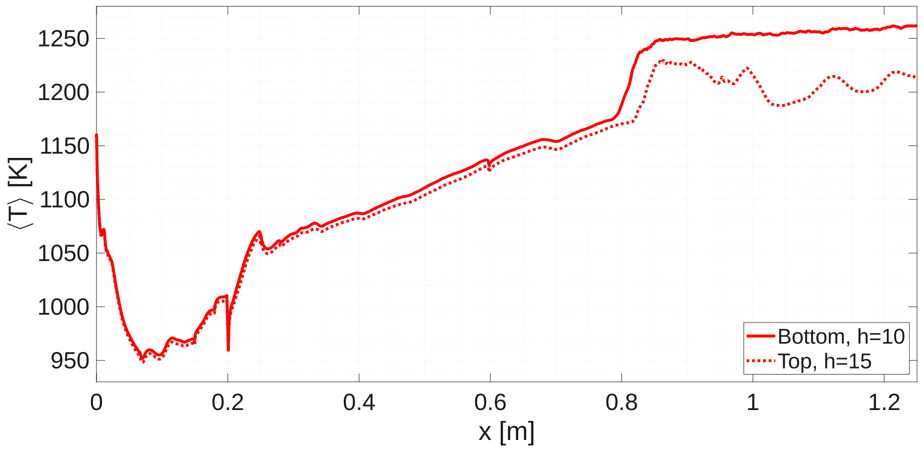

Figure 5.35: Case 0, modified mesh, mean temperature along the mid-line

The evolution follows the analysis for the instantaneous evolution. The temperature rise along the combustor length, a spike around 0.2 [m] correspond to the plugged injectors acting as small cavities, and the separated regions present higher wall temperatures except the top patch due to the supersonic flow impingement. As expected, slightly different convective heat transfer parameters h for the patches produces a slightly different behavior also in the first part of the chamber.

---

[9] Even more surprisingly, with its own shedding frequency

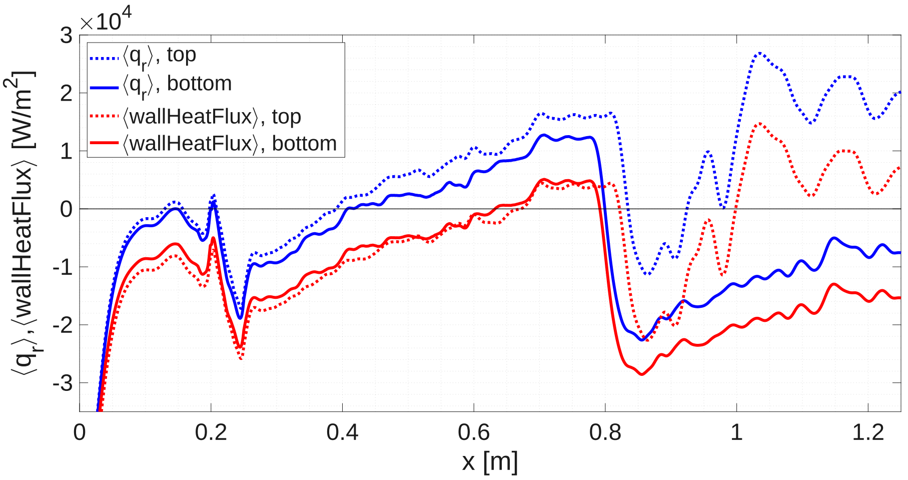

Figure 5.36: Case 0, modified mesh, mean *wallHeatFlux* and radiative heat flux q_r along the mid-line

The mean radiative heat flux (q_r) and *wallHeatFlux* (convective heat-flux, [53]) distribution are presented. Trends closely follows instantaneous and mean temperature features: for both bottom and top patches the walls got heated up until an inversion point happening before in radiative heat fluxes, that appears to have a strong influence. Following flow separation, the sign inversion is observed again due to upper patch impingement by supersonic flow. Notably, they present comparable values, highlighting the importance of radiative heat fluxes in those cases.

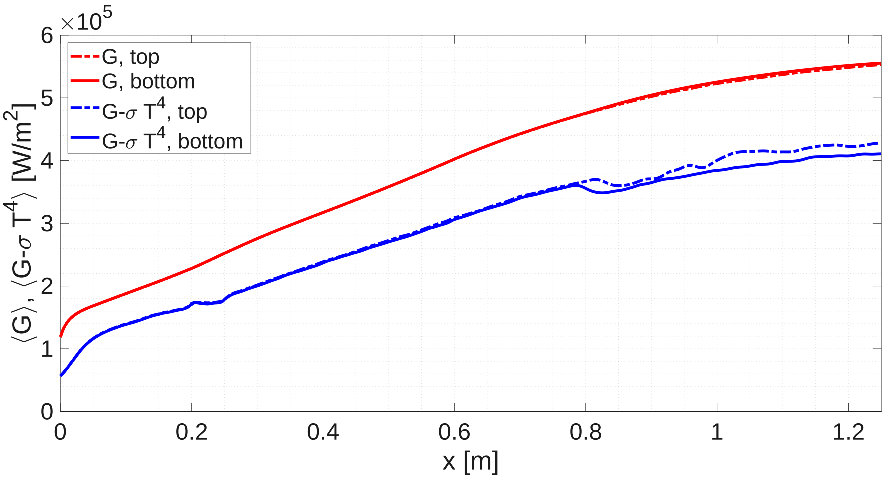

Figure 5.37: Case 0, modified mesh, mean incident radiation G and net radiative energy term $G - \sigma T^4$ along the mid-line

Here, the incident radiation field is represented alongside the net radiative energy, qualitatively related to radiation modeling. It can be observed that temperature causes distortion after flow separation and when the boundary layer is distorted by the injectors.

5.2.2 Case 1

Case 1 is the subsonic combustion mode, as reported in Tab. 4.1, and the provided case, from which all the other results are mapped. Therefore, this subsection will be divided in two paragraphs:

- Legacy Mesh: the case and the mesh initially provided by previous studies;
- Modified Mesh: the case investigated by the author of this thesis.

5.2.2.0.1 Legacy Mesh This mesh and the initial fields were provided by my supervisor from previous studies and, due to time and resource constraints, were used as a baseline for all of the other solutions obtained. More insights on the specific characteristics of this mesh can be found in Sec. 4.3. It is worth mentioning that published numerical results[3], were obtained in a different moment and with a different solver compared to the one used here.This is because the solver and the methodology used in those previous studies are proprietary, hence not usable in this work. This case was obtained with a new solver developed here at Lund University called *rhoCentralTurbReactingFoam*, an hybrid solver between *rhoReactingFoam* and *rhoCentralFoam* (more on Sec. 4.1). The obtained results at Lund University are here reported, using no radiation model and a Dirichlet boundary condition for the temperature, prescribed at 450 [K].

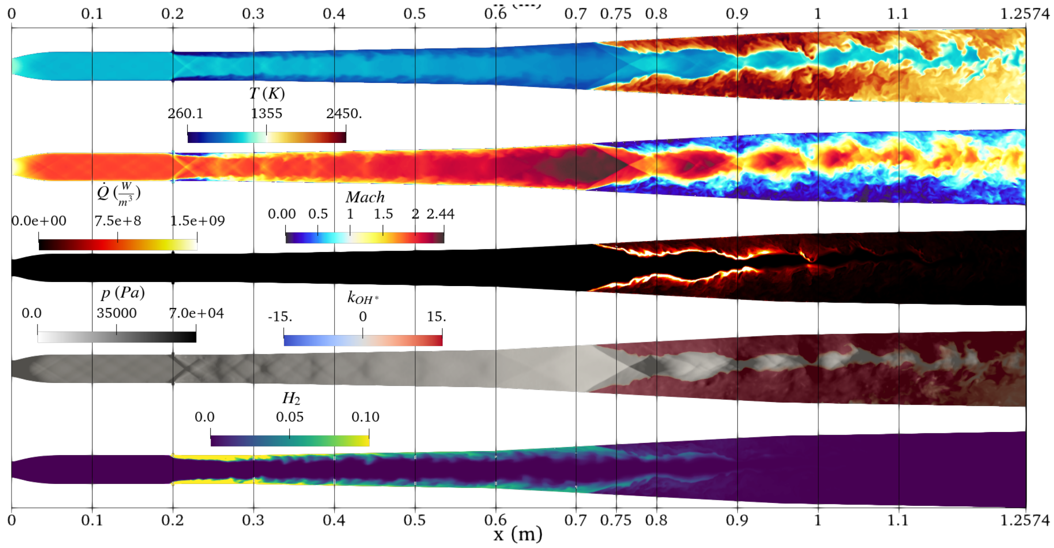

Figure 5.38: Case 1, legacy mesh and results, instantaneous slices in the symmetry plane of temperature, Mach number, heat release, pressure superimposed with modified photon emission rate (k_{OH}, Eq. 5.1), hydrogen mass fraction

The hydrogen is now injected and ignited. A shock train is generated due to the fuel, that got reflected and smeared as the fluid expands, as showed by the pressure slice. The colder fuel depicted in the temperature field is responsible also for boundary layer and flow distortion, as showed by the Mach values near the walls.

Right after flow separation, where proper temperature and pressure levels are met, the vitiated air and hydrogen mixture got ignited and combustion is responsible for a large pressure rise in the subsonic separated regions, while the flame front appears to be between subsonic and supersonic regions. The combustion has the tendency to decrease the bulk flow bias, as also observed in the 2D campaign, in Sec. 5.1.3 and to move the separation location upstream by the combustion-induced thermodynamic variations. This is because due to the subsonic part of the boundary layer, the back-pressure increases information is propagated parabolically upstream distorting the boundary layer, which in turns interacts with the shockwaves that influences the combustion itself, generating a “feedback loop” stabilizing around a location where pressure levels upstream and downstream are matched. This is one the reasons why those cases are difficult to study, where even a small miscalculation or even oscillation can have dramatic consequences. For that matter it is important to have a good model that correctly takes into account the challenging intertwinement between turbulence, combustion and compressible phenomena of this regime. From temperature and hydrogen mass fraction values is also possible to observe how the shear layer and the diffusion of the fuel evolve towards the combustion zone. The photon emission rate, saturated to show the flame location, superimposed on the pressure field, shows that the combustion is occurring in the subsonic region and the reactive region stretches almost to the end of the chamber. Furthermore, the Mach at the end of the chamber further confirms the necessity of prolonging the outlet and evolve the flow until subsonic velocities are reached. In all the fields, it is also possible to notice how the LES is remarkably good at capturing the flame dynamical features.

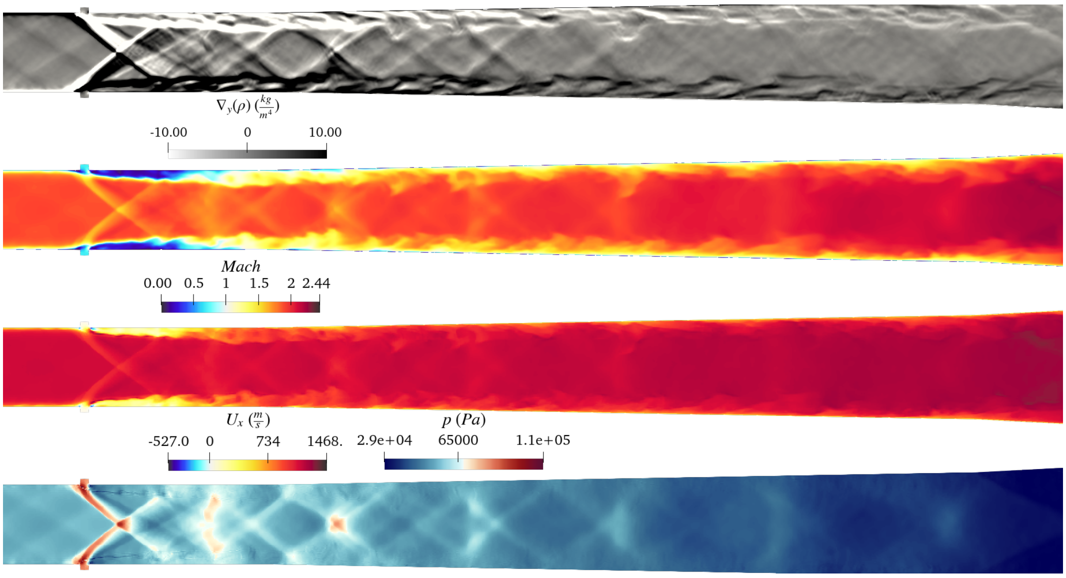

Figure 5.39: Case 1, legacy mesh and results, instantaneous values in the symmetry plane for numerical Schlieren, Mach, axial velocity and pressure

A further look into the injectors region highlights the shock train generated in the isolator and the barrel shocks upon injections, qualitative visible in the numerical Schlieren while the pressure field display the pressure-rise.

The slices also show how the plume is interacting, distorting the shock fronts being reflected at the walls, where also turbulent structures are present. The Mach number highlights the jet development along the walls and its acceleration and diffusion, while the axial velocity shows the strong axial acceleration of the jets, in addition to the small separated recirculation regions with negative axial velocity.

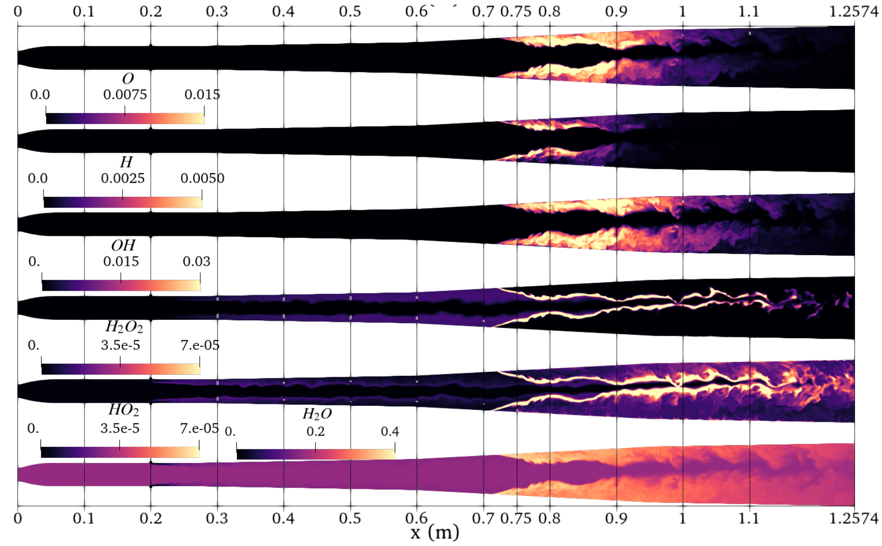

Figure 5.40: Case 1, legacy mesh and results, instantaneous values in the symmetry plane for atomic oxygen O, atomic hydrogen H, hydroxide OH, hydrogen peroxide H_2O_2, hydroperoxyl HO_2 and water vapor H_2O

Regarding combustion, it is important to investigate the formation of the most relevant chemical species. Instantaneous values for mass fraction of O, H and OH show the flame anchoring to the walls and where combustion is occurring. With O and OH representing low-temperature reactions regions and H representing explosive high-temperature regions regarding combustion. [9] Meanwhile H_2O_2 and HO_2, represent ignition and radicals storage, important for chain-branching reactions. Concentration of H_2O_2 increases as the plume proceeds downstream reaching peak values at the flame front and in strong shear and mixing layer regions. HO_2 acts as a radical storing specie, especially high in mixing layers and in combustion regions, with high generation right after injection and at the plume mixing layer, where also large scale structures develop upon mixing with the bulk flow. The combustion product, H_2O, gives a comprehensive view of the aforementioned aspects, with the non-zero inlet values to account for air-vitiation induced by the H_2 burners upstream to heat up the incoming supersonic flow, as in Fig. 3.3. The lowest values correspond to the regions where hydrogen is injected and not yet mixed, showing with the hydrogen mass fraction of Fig 5.38, that the jest are attached to the walls and mixing is achieved shortly after injection.

A provided volumetric rendering, displaying Q-criterion contours colored with temperature and hydrogen mass fraction in green, further shows the plume distorting the boundary layer and the turbulent eddies generated. Iso-surfaces of pressure are also reported in purple, that highlights the shockaves generated along the chamber.

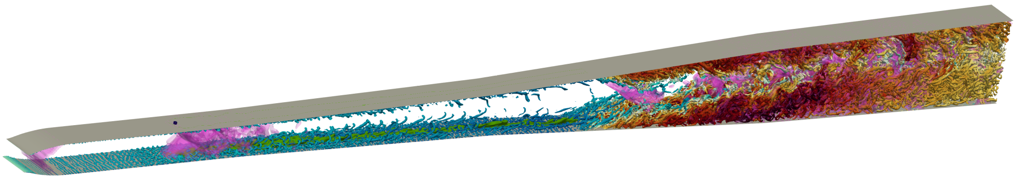

Figure 5.41: Case 1, legacy mesh and results, provided Q-criterion colored with temperature, iso-surfaces of pressure in purple and hydrogen mass fraction in green

5.2.2.0.2 Radiation model and conjugate heat transfer As a first step, the P1 radiation model and the 1D CHT BC have been implemented to validate the parameters chosen for the boundary condition, since a mesh change can have non-trivial effects, difficult to address.

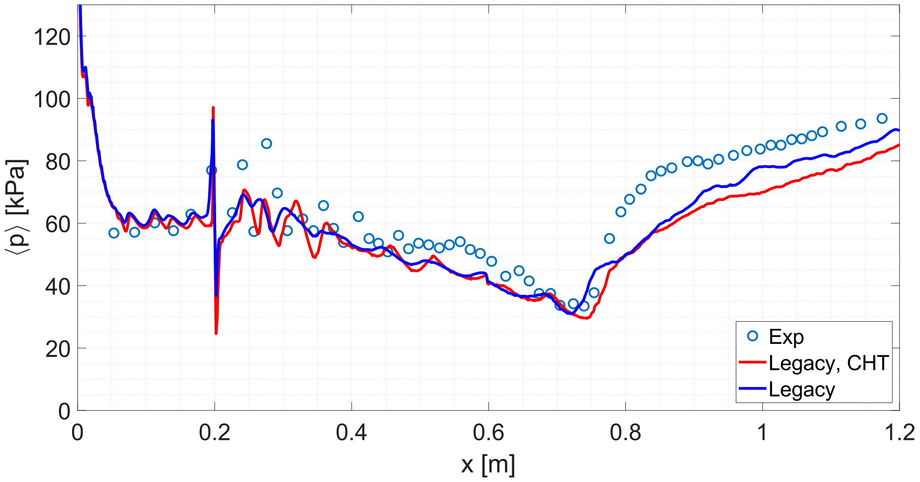

Figure 5.42: Case 1, legacy mesh and CHT results, lower-wall mean pressure along the mid-line between legacy and CHT results compared to experimental data. [3]

The mean pressure on the lower wall of the provided case with prescribed temperature and 1D CHT BC is presented, compared to experimental measurements. [3] It is worth to mention that, as in Fig. 5.23, the absolute mean pressure levels were not matched, so an offset has been applied to match the calculated mean pressure content right after the inlet expansion until 0.2 [m], as it is the only part of the chamber without further effects not accounted that could alter the pressure level. The offset applied for this case was of 9500 [Pa], still within the tolerance provided of ±10000 [Pa] [3] regarding the reservoir conditions. As the offset is different from the non reacting case, possible further complications are introduced by the reactive flow interacting with the *waveTransmissive* outlet condition. Regarding the relative variations, there is good agreement from both the boundary conditions employed, with the pressure recovery in the latter part being a little bit underestimated, possibly due to the outlet pressure condition, the combustion prediction or the insufficient mesh resolution, as the cell count in the coarser case of previous results[3]. Other differences are related to the post-injection region and around 0.6 [m], where a small step not considered in the computational domain is present. Looking at relative differences between the two boundary conditions, it seems that near injectors, the pressure variations along the isolator around 0.25 [m] are better captures with the 1D CHT BC, showing sharper variation. The expansion profiles are similar, but the pocket near the separation point at 0.75 [m] seems to be better captured with the 1D CHT BC, compared to the fixed temperature case where it is more upstream. Compared to the non reacting case of Fig 5.23, combustion move the separation location upstream.

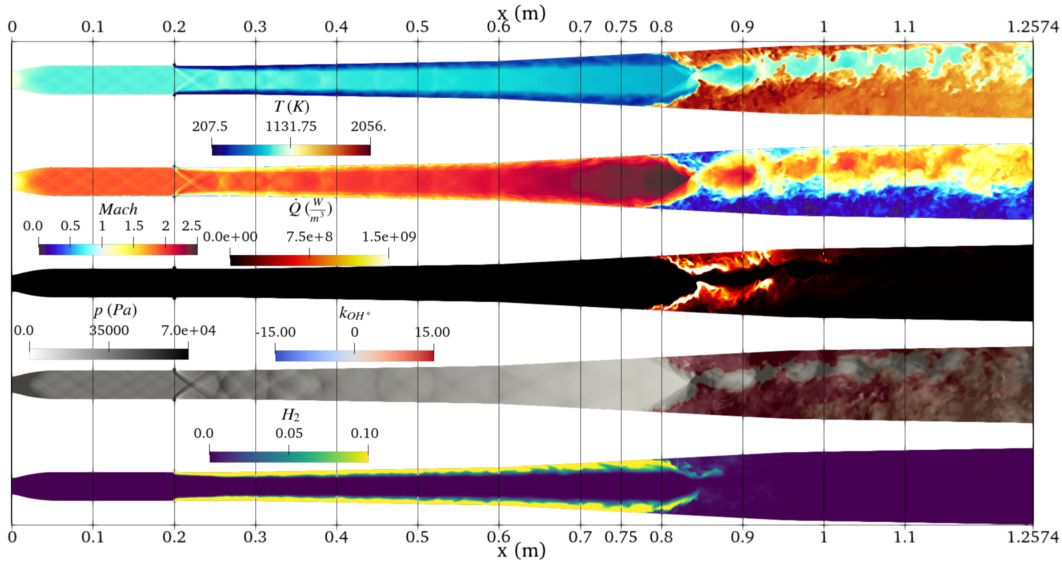

Figure 5.43: Case 1, legacy mesh and CHT results, instantaneous slices at symmetry plane of temperature, Mach number, heat release, pressure superimposed with photon emission rate (k_{OH^*}), hydrogen mass fraction

Due to the radiation model, now the peak temperature is lower and the heat release suggests a flame more compact near the separation region and less extended to the chamber exit, due to the new thermal boundary condition. Other differences can be seen with the temperature and hydrogen mass fraction slices, where the fuel jets appears to be less mixed and diffused as they are convected downstream compared to Fig. 5.38. This could be due to the new boundary condition and radiation model with their heat fluxes modifying thermal and diffusive properties of the colder fuel's plume, impacting on the mixing layer. The pressure and photon emission rate show that the plume and the compressible structures are now different, impacting also the flame region. The Mach slice confirms that the combustion is still subsonic, while the lower recirculation region is still stronger that the upper one, with the same bias of the non-reacting case (see Fig. 5.25).

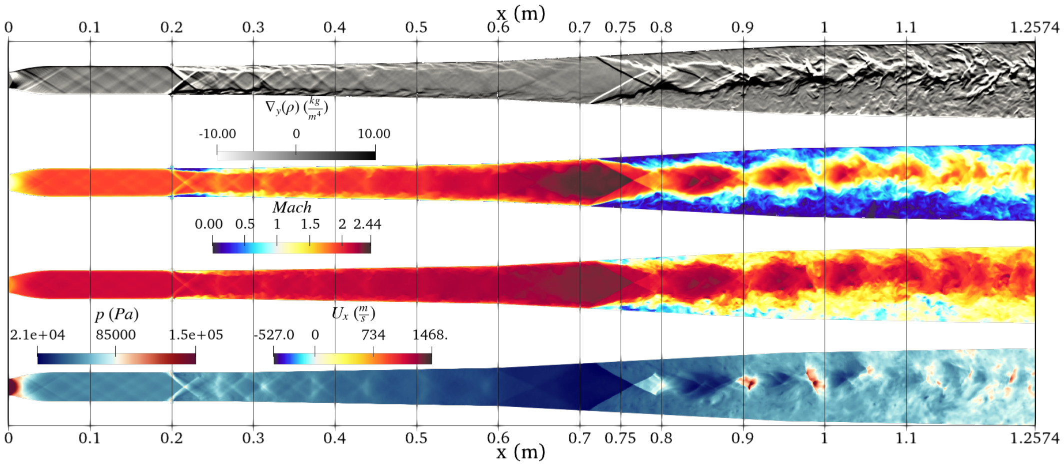

Figure 5.44: Case 1, legacy mesh, instantaneous symmetry plane slices of numerical Schlieren, Mach, axial velocity and pressure of legacy results

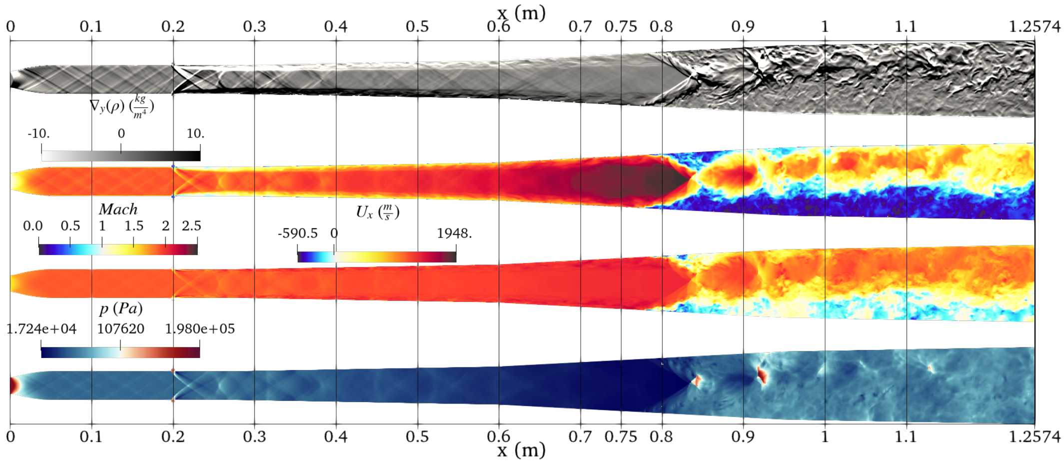

Figure 5.45: Case 1, legacy mesh, instantaneous symmetry plane slices of numerical Schlieren, Mach, axial velocity and pressure of CHT results

A further instantaneous fields set shows the main differences between the different boundary conditions. The numerical Schlieren, captures the different plume behavior affecting the isolator shock train and the aforementioned bulk-flow bias differences. As also visible from the Mach and axial velocity, the combustion for this case seems to be less impacting in modifying the recirculation regions, with an upper wall bias more similar to the non reacting case. Also the separation locations exhibits different features, with the oblique shocks being more distorted by the walls turbulent structures being convected across the shock front. As a consequence, the pressure values are quite different. Regarding the combustion model, it is observed that the PaSR [10] coefficient is almost one after the barrel shocks, showing that the mixing is so intense that the combustion model uses a laminar-leaning flame treatment.

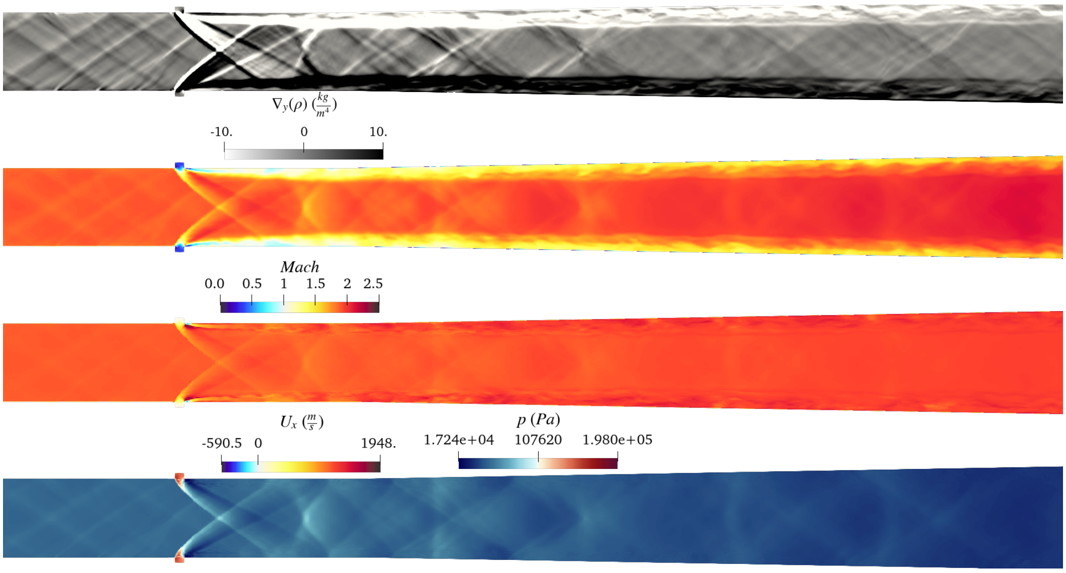

Figure 5.46: Case 1, legacy mesh and CHT results, instantaneous values in the symmetry plane for numerical Schlieren, Mach, axial velocity and pressure

A more detailed look near injection gives a detailed perspective of the mentioned differences. The new 1D CHT BC and radiation model are responsible for the different fuel plume shape and a more intense expansion velocity, as reported with the Mach number and axial velocity. The pressure gives a comprehensive views of the reflected shockwaves along the isolator.

---

[10] Partially stirred reactor

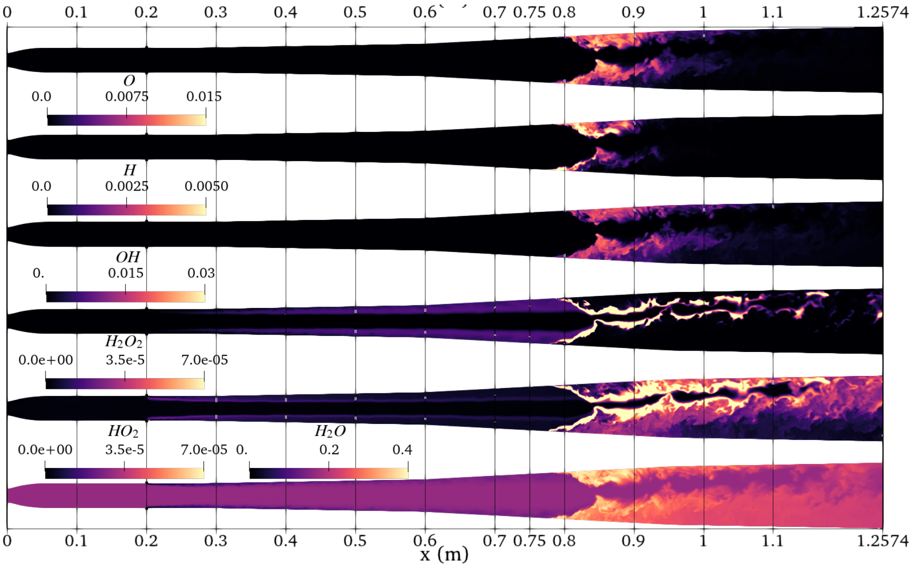

Figure 5.47: Case 1, legacy mesh and CHT results, instantaneous values in the symmetry plane for atomic oxygen O, atomic hydrogen H, hydroxide OH, hydrogen peroxide H_2O_2, hydroperoxyl HO_2 and water vapor H_2O

Also a comparison of the instantaneous chemical species is presented. Notably, O, H and OH present a much more compact axial displacement of the reactive regions, compared to Fig. 5.40. Apart from the different axial displacement mentioned, O, H and OH mass fractions show lower values, indicating a favored lower temperature chemical activity, due to the suppressed production by the radiative heat flux that slows down chain-branching reactions related to H and OH. Meanwhile, the trend along the fuel plume of H_2O_2 and HO_2 is similar, with slightly higher generation along the plume itself. Larger concentrations are observed after separation, further highlighting the shift and enhancement of lower-temperature reactions. Water vapor offers a comprehensive view of the discussed aspects. The non-zero value uniformly present is due to vitiated air from the upstream H_2 burners, as reported in Fig. 3.3, while the near-zero values are relative the fuel plume, attached to the upper and lower wall.

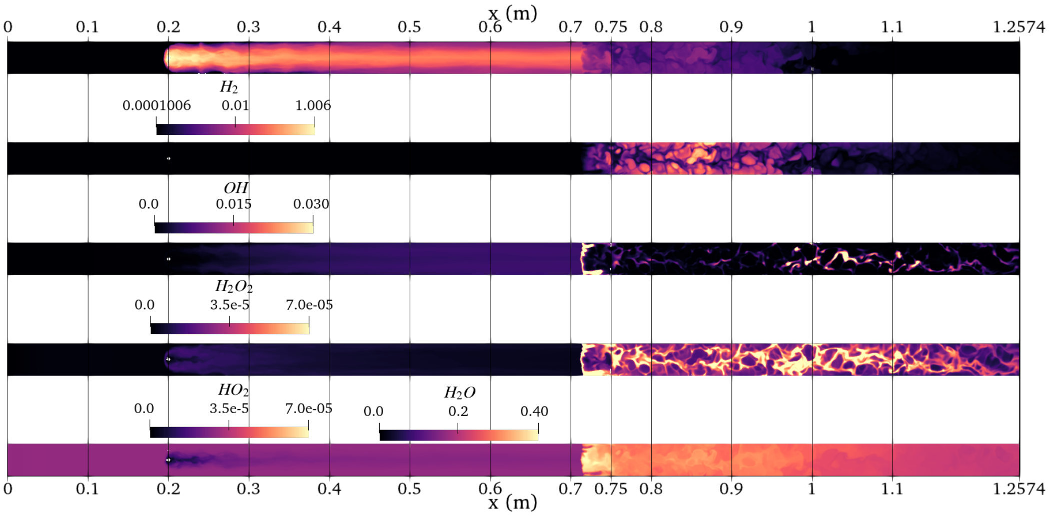

Figure 5.48: Case 1, legacy mesh and legacy results, instantaneous bottom wall fields of hydrogen H_2 (logarithmic scale), hydroxide OH, peroxide H_2O_2 hydroperoxil HO_2 and water vapor H_2O

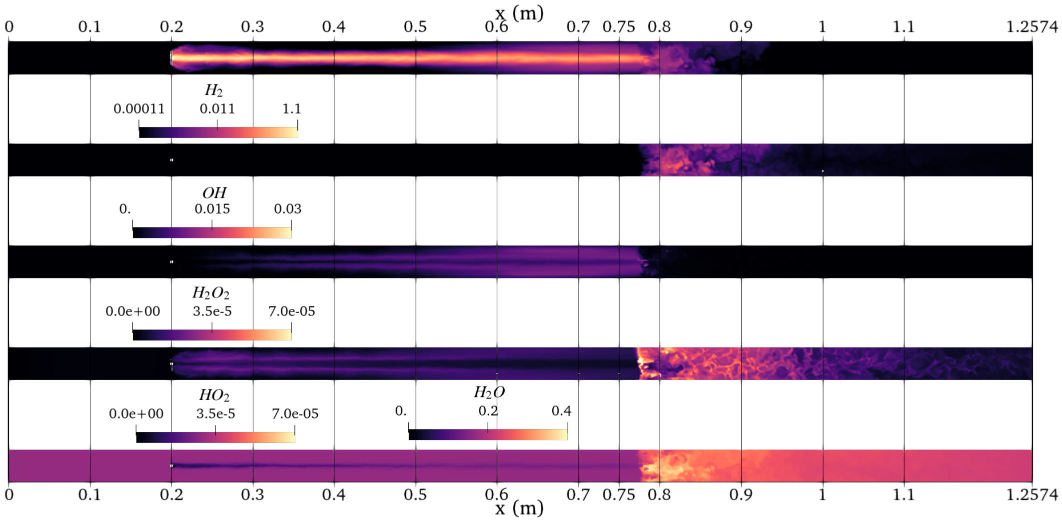

Figure 5.49: Case 1, legacy mesh and CHT results, instantaneous bottom wall fields of hydrogen H_2 (logarithmic scale), hydroxide OH, peroxide H_2O_2 hydroperoxil HO_2 and water vapor H_2O

To dig more into the generation of intermediate species, a comparison of the species generated on the walls is presented between the two cases. The logarithmic scale of H_2 mass fraction shows that different thermal conditions at the walls are responsible for a completely different diffusion of the fuel, especially in the spanwise direction, with more spanwise diffusion with the prescribed temperature case of 450 [K]. In both cases the peak values exceed one, hinting at some numerical instabilities probably related to the low resolution of the mesh near the injectors, justifying the needs for further resolution described in Sec. 4.3. The OH radical, confirms the more compact flame along the axial direction and the lower intensity for the case where the radiation suppression effect is present.

For H_2O_2 and HO_2, important for ignition and low temperature chemistry favoring third-body reactions, they seems to be generated more in the 1D CHT BC, especially along the plume impingement to the wall. Moreover, HO_2 is located near shear layers and regions with high temperature and pressure variations, therefore presenting a first notable generation near the injectors, before being convected and diffused downstream, and then generated again within the separated zone near the flames. The combustion product H_2O offers an overview of the aforementioned aspects, while all of the patches represented hints how flames and turbulent structures are captured in the spanwise direction. Other wall quantities are compared, showing that the new boundary condition favoring the formation of chemical species, is caused by the temperature increasing along the walls, with also the flame impingement being represented.

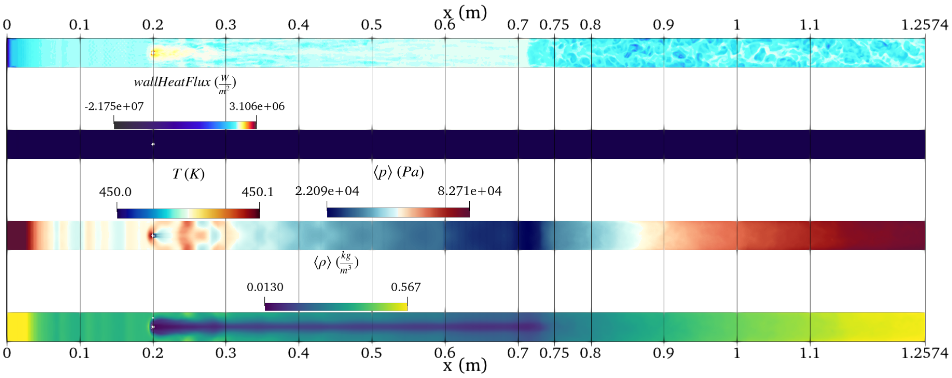

Figure 5.50: Case 1, legacy mesh and legacy results, instantaneous bottom wall fields of *wallHeatFlux* and temperature, mean pressure and density

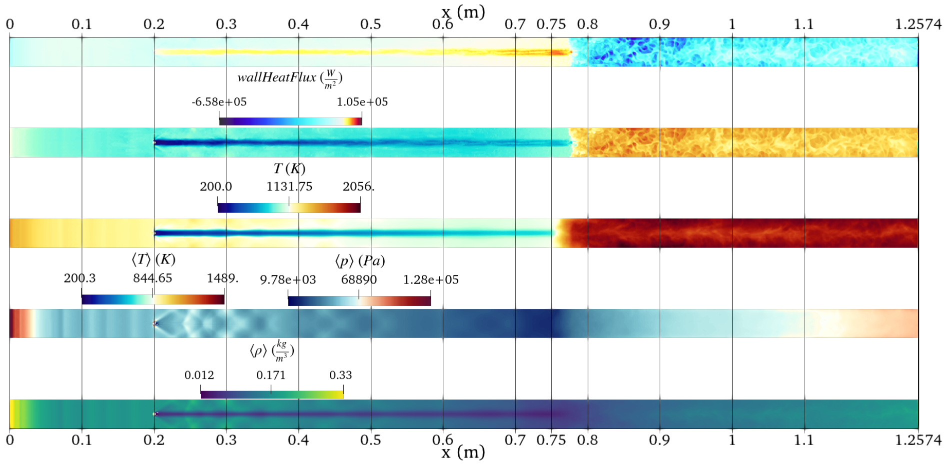

Figure 5.51: Case 1, legacy mesh and CHT results, instantaneous bottom wall fields of *wallHeatFlux* and temperature, mean temperature, pressure and density

A comparison of the mean fields of the main thermodynamic quantities (pressure, density and temperature), between Fig. 5.50 and Fig 5.51 shed light on how the impingement, boundary layer and respective interactions are different within the two cases. This staggering difference, led by the temperature, that also shows the flame impingement at the walls, is more quantifiable by looking at the shear difference of order of magnitudes of the calculated *wallHeatFlux* using the OpenFOAM utility. For the prescribed temperature of 450 [K], except for the recirculation zone where the plume absorbs heat from the wall, a negative heat flux is observed, coherent to the necessity of cool down the fluid domain in order to keep the prescribed temperature constant everywhere. For the 1D CHT BC instead, the plume instead is increasingly heated up as it is convected downstream due to the ever-expanding flow. This increasing supersonic expansion drops the temperature and increases the shear stresses at the walls, therefore more heat is absorbed by the walls heating up the plume.

To have a more quantitative comparison, the plot along the symmetry line of the walls patches is presented, showing the mean temperature evolution along the walls compared to the non-reacting case. Following the axial location, it appears that before the injection the wall temperature is different compared to the cold flow, most probably related to the downstream injection and combustion, that propagates back through the boundary layer disturbances and oscillations that modify the upstream boundary layer in turns.

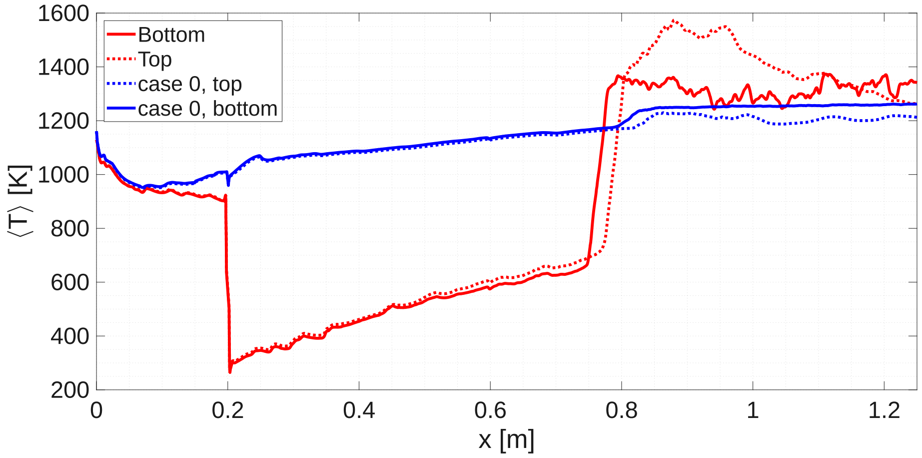

Figure 5.52: Case 1, legacy mesh and CHT results, mean wall temperature along the symmetry line compared to the non-reacting case (case 0)

After the injection point, where the temperature drops for the fuel injected at $\sim 294\ [K]$, the temperature values rise as the fuel is convected downstream due to the heated-up walls for the supersonic flow. After the separation points, a sharp increase due to combustion and separation is observed, increasing the temperature above the non-reacting case. Furthermore, it appears that along the top wall recirculation region, the combustion-induced temperature rise is more compact and followed by a decrease due to the relatively cold supersonic flow impingement, at least colder compared to the reactive region.

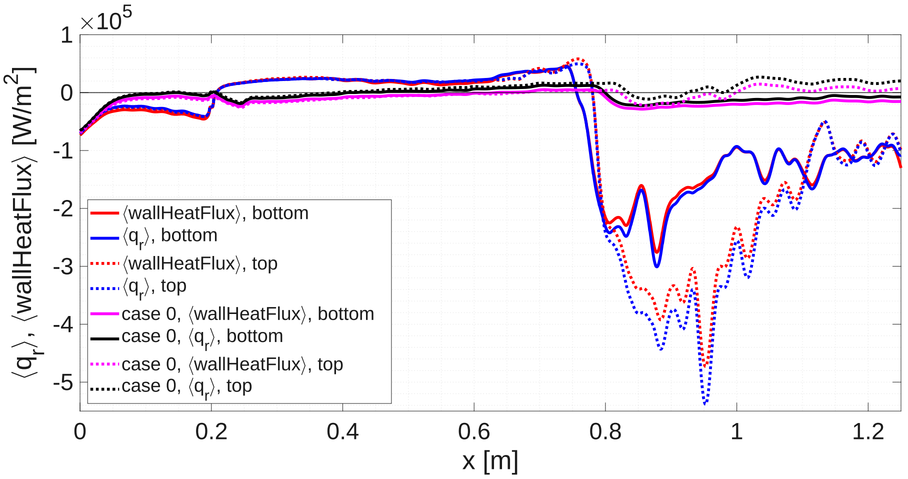

Figure 5.53: Case 1, legacy mesh and CHT results, mean *wallHeatFlux* and radiative heat flux q_r along the symmetry line compared to the non-reacting case (case 0)

Similar considerations are applied to the comparison of the convective heat-flux (*wallHeatFlux*) and radiative heat flux, q_r. The differences between non reacting and reacting case in the near-inlet heat-fluxes, are responsible for the temperature differences observed in Fig. 5.52, indicating a boundary layer influenced by downstream features. The sign change is anticipated due to injection, where the fuel plume is constantly heat up until the recirculation region, while the separated region with combustion is responsible of the high-magnitude negative values. Again, the top wall presents a more strong and compact combustion region before having a "colder" region dominated by the impingement of the supersonic flow.

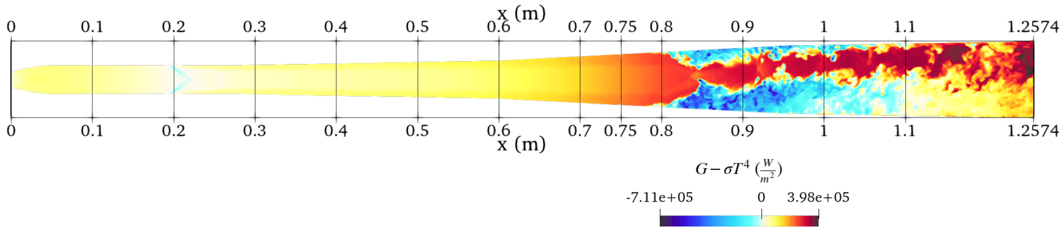

Figure 5.54: Case 1, legacy mesh and CHT results, symmetry plane slice of net radiative term

The so-called "net radiative energy" term is calculated along the mid-plane and here presented, corresponding to the difference of the incident radiation calculated within the G field from the radiation model, and the local (assumed to be) black-body radiative energy emitted of σT^4.[11] The net result represents qualitatively how temperature affects the incident radiation field, since absorption and a factor 4 is not taken into account for the local energy emitted. And further displays how the

---

[11] σ being the Stefan-Boltzmann constant with value of $5.67 \cdot 10^{-8} \quad [\frac{W}{m^2 K^4}]$

high-temperature post-barrel shock and reacting zone are sink terms respect the net radiative term, being optically-thick regions.

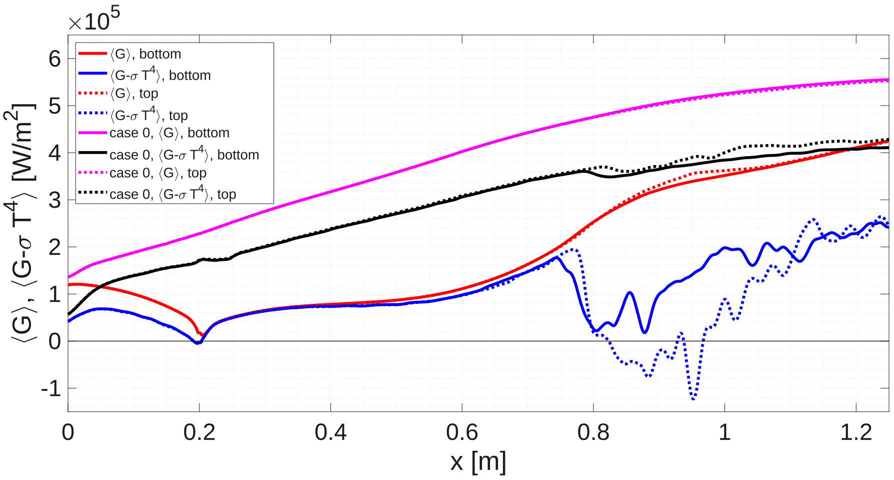

Figure 5.55: Case 1, legacy mesh and CHT results, mean incident radiation G and net radiation term $G - \sigma T^4$ along the symmetry line compared to the non-reacting case (case 0)

The same mid-line comparison is presented for incident radiation G, and net radiative energy values, show the important contribution of the barrel shocks generated in distorting the radiative field by decreasing the values compared to the non-reacting case, since the high temperature region following the shock itself acts as an optically thick medium. As for the new radiative term, the high temperature combustion region in the recirculation region impinging the walls is responsible for the lower values due to high radiative emissions ($\propto T^4$).

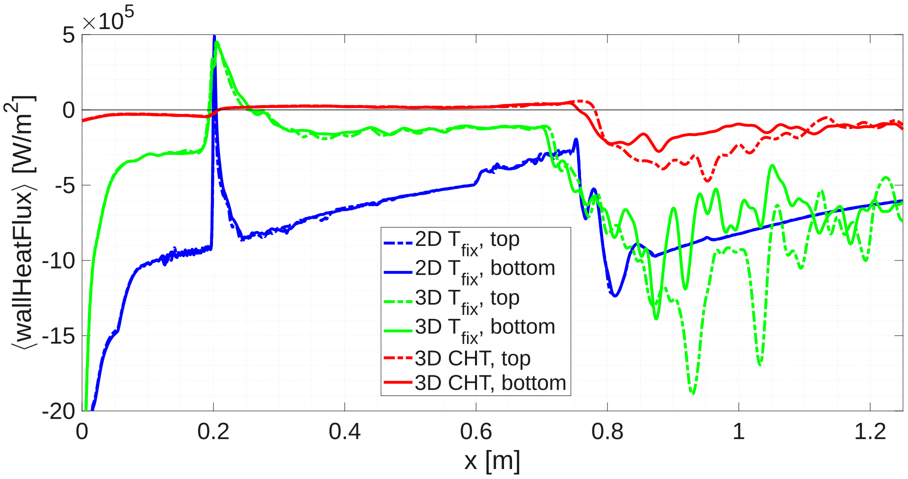

Figure 5.56: Case 1, mean *wallHeatFlux* comparison for legacy mesh with legacy and CHT results against the 2D reacting case

One final comparison regarding the heat fluxes across the walls is done plotting the mean values of *wallHeatFlux* (convective, [53]) obtained with the variations about case 1 done so far, also including the 2D reacting case in Subsec. 5.1.3, where the same prescribed temperature of 450 [K] used in the legacy results was used. For the

Dirichlet boundary condition, as expected, the heat flux is higher.

The comparison of the same fixed temperature of 2D and 3D simulations, further confirms the difference due to dimensionality reduction in the first part of the combustor, with the magnitude of *wallHeatFlux* being roughly doubled. However, the prediction of the separated region are comparable in both cases, except some local peaks due to the highly dynamical structures captured impinging the walls. For the 1D CHT BC, the trend is different and follows the conclusion drawn in the previous analysis, with lower overall magnitude, since the wall temperature is higher.

Finally, also the y^+ was estimated “*a posteriori*” using the OpenFOAM utility, showing that high values are reached in some high skewness cells located near the expansion relative to the injectors. Values are between 0.23 and 1180 with an average of 6.15 and the majority of the cells having a y^+ between 1 and 70.

5.2.2.0.3 Modified Mesh At first, the same parameters used in the non reacting and legacy mesh for the thermal 1D CHT BC were used (Tab.5.2), and the mesh was without the refinement after the one along the walls, as described in Fig. 4.12. However, it was very hard to obtain a stable solution, as the first version of the mesh showed some numerical instabilities related to the 1D CHT BC coupled with the radiation model.

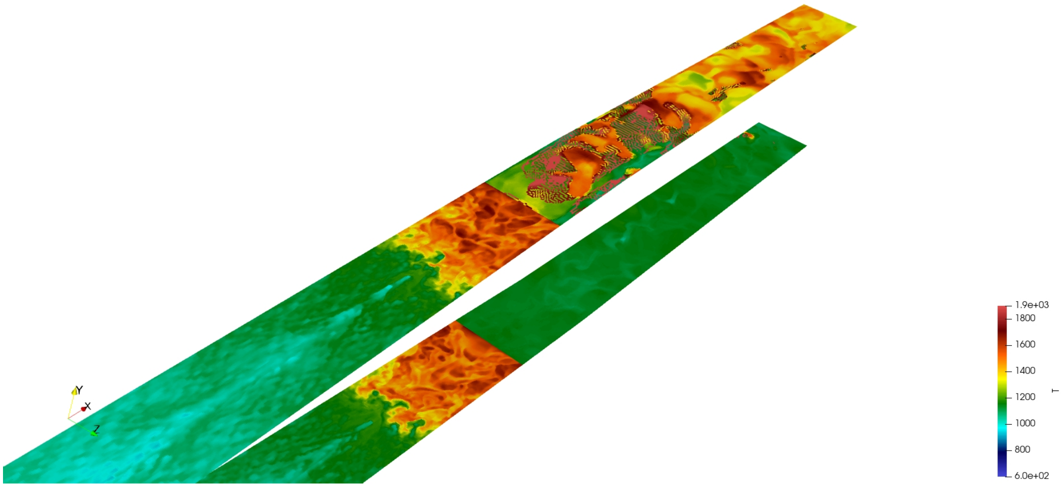

Figure 5.57: Case 1, modified mesh, instantaneous temperature (in [K]) along the wall patches

The mesh size transition poses a serious problem at the boundary layer resolution in the coarsened region, and at first, due to the unresolved part towards the end of the chamber where the combustion was taking place, some cells had their temperature that began oscillating. This zone, would later extend to the inner mesh prior propagating in the boundary layer parabolically both upstream and downstream, causing the simulation to crash. The instantaneous temperature reported along the wall patches in the above picture, Fig. 5.57, depicts how the abrupt transition in resolution also changes how the flame is resolved, by looking at the different values along the walls. To solve that matter, a further mesh refinement was applied downstream, as in Fig. 4.11, and the convective heat transfer coefficients h of the 1D CHT BC were modified from (15,10) $[\frac{W}{m^2K}]$ to (25,20) $[\frac{W}{m^2K}]$ for top and bottom walls respectively. This was done as a safety measure, thinking it could help having lower temperatures. It was possible to have stable results, with the main culprit probably being only the boundary layer resolution near the walls. However, since the starting parameters (15,10) $[\frac{W}{m^2K}]$ were not restored, a direct comparison of the heat fluxes as follows could have been quite misleading. For that matter, also the non-reacting case was simulated again with the same convective heat transfer coefficients of (25, 20) $[\frac{W}{m^2K}]$ for the upper and lower wall patches respectively. Further implications regarding this change for case 0 are discussed in App. C.

Therefore, in this paragraph, all the following quantities computed from the non-reacting case, case 0, are related to the corresponding parameters of the reacting case, case 1.

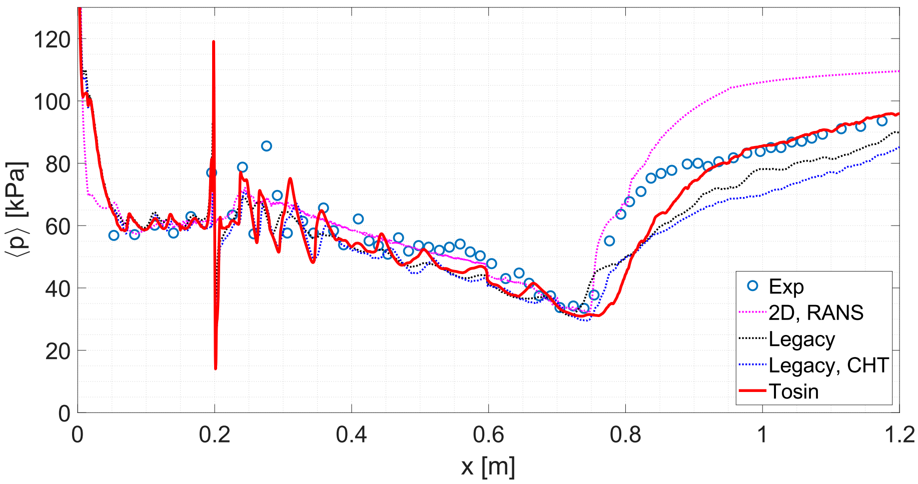

Figure 5.58: Case 1, modified mesh, lower-wall mean pressure values along the mid-line compared with experimental data. [3]

The mean pressure along the mid-line of the bottom patch is plotted against the one obtained experimentally, alongside the 2D case and the results obtained for the legacy mesh using both boundary conditions. As for the other comparisons (Fig. 5.42 and Fig, 5.23), the absolute numerical pressure needed an offset to match the experimental results levels. The offset was given to match the mean pressure in the first part until the injectors location, prior further complications difficult to quantify. The offset applied is of 9500 [Pa], the same in Fig. 5.42, and this is a good news, since the mesh and the parameters of the 1D CHT BC are different. Considering the relative features of the new mean results obtained, they display excellent agreement for most of the locations, expect the exact point of separation that seems to be downstream. A part of lowest-pressure pocket and the slope of the pressure recovery after the separation are well captured to the measurements and the pressure towards the exit chamber is very close to the experimental results, hinting satisfactory description of separation and flame structure, compared to other cases so far. Another difference is the underestimation of pressure around 0.6 [m] as in other cases, probably related to a small step within the chamber not considered in the computational domain that could further modify the boundary layer. This result further highlights the quality of the new solver developed and the predictive capability of the new mesh and thermal boundary conditions, giving satisfactory agreement. The point of separation on the lower wall oscillates between 0.75 [m] and 0.8 [m] as also reported from the experiments and previous studies [3]. As for the position being a little bit downstream, a factor could be the boundary layer prediction: this is of the utmost importance here since no struts or cavities help in stabilizing the flame.

Therefore, major uncertainties in the inlet turbulence, both in the bulk flow[12] and

---

[12] Especially due to the burners upstream to provide vitiated air, as reported in Fig. 3.3

along the walls could be the main culprits for that matter, not to mention the cross-section transition from circular to rectangular in the experimental facility. Another factor is the prediction of the walls roughness: even if measured, degradation after consecutive runs is not taken into account. The underestimated pressure recovery observed in the non reacting case is not a problem here, highlighting the fact that this case is less dependent from the outlet conditions compared to the other one with the pressure recovery depending more on a accurate combustion prediction.

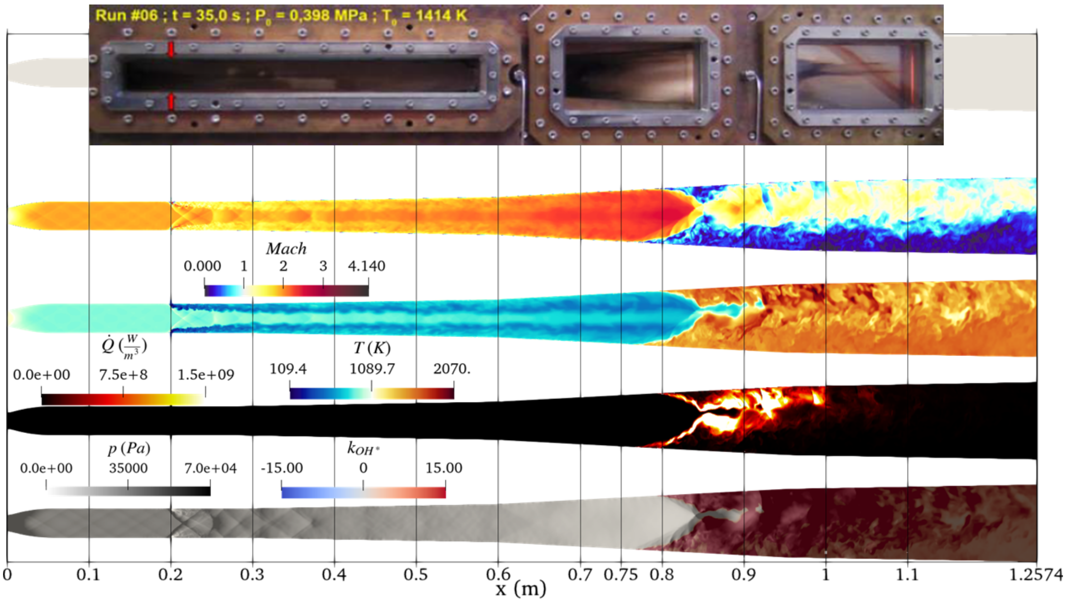

Figure 5.59: Case 1, modified mesh, instantaneous symmetry plane slices of Mach, temperature, heat release, pressure superimposed with the modified photon emission rate (k_{OH}, Eq. 5.1) compared with a photo from the experiments. [3]

A comparison similar previous studies [3] is presented, with the photo from one experimental run with the same inlet conditions on top. Starting from bottom, the modified photon emission rate (Eq. 5.1) superimposed with the instantaneous pressure shows that now the flame is engulfing all the combustor height as in the experiments, while near injectors the shock train has a better resolution, as intended by the refinements. Meanwhile, heat-release and temperature fields have notable differences: as for the former, the flame seems to be more intense near the center of the symmetry line, where the plume, which has now much more penetration in the bulk flow, got ignited after crossing the oblique shocks induced by the flow separation. The separation point is upstream compared to the non-reacting case due to the back-pressure rise induced by combustion, and it appear similar compared to the combustor photo from the experiments. Hydrogen flames are not visible through naked eyes, so the picture represents the heated walls in proximity of the flame. Nevertheless, the simulated high-temperature region, while a little downstream compared to the photo, has the same qualitative features: the third window from the experiments is engulfed completely by the flame and the lower wall flame appears to be more upstream compared to the top wall.

The peak temperature values have the same magnitude of legacy mesh results, as the radiation model is implemented. As for the Mach number on top, it seems that a completely different case compared to the previous ones is depicted. Where the flame is supposed to be, the main features are similar, with the separation bias of the bulk supersonic flow towards the upper wall. However, the most staggering difference is related to the injection zone: the new mesh displays a completely different expansion of the sonic injected fuel, reaching roughly Mach 4 entering the combustion chamber through a strong expansion.

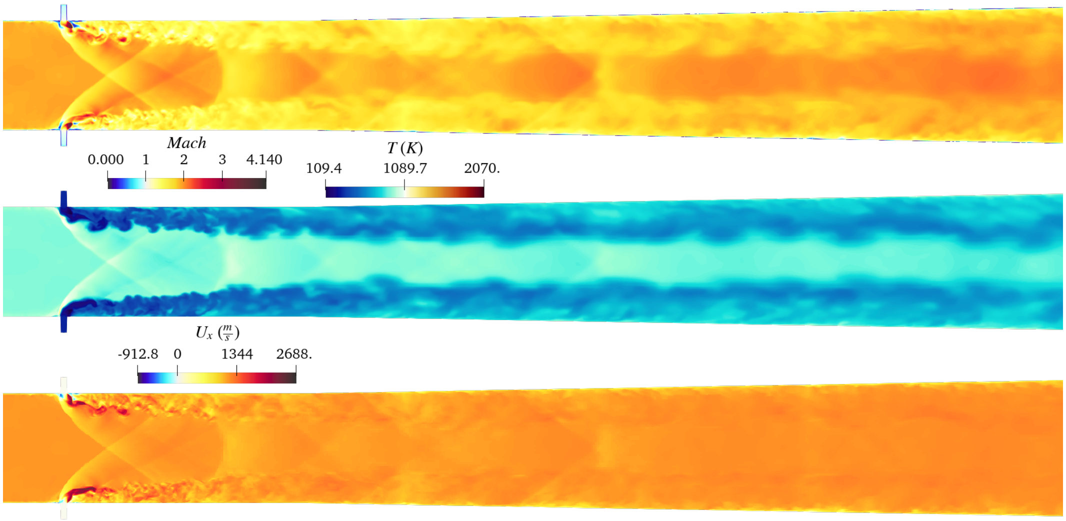

Figure 5.60: Case 1, modified mesh, instantaneous symmetry plane slices of Mach, temperature, and axial velocity

A more detailed look now shows how the injector zone is different: the Mach shows how the recirculation zone near injection are captured, showing that also the boundary layer within the injectors is represented. Furthermore, a violent expansion is captured and the large scale eddies around the plume are successfully reproduced by the overlapping refinement near injection (Fig.4.10), and then develop as the flow is being convected downstream, with a magnitude of axial velocity peaking around 2690 $[\frac{m}{s}]$. This is in turn responsible for the large drop in temperature to $\sim$100 [K] due to the strong expansion thanks to more jet penetration. The temperature field display how the mesh resolution is important: after the end of the refined region, the large scale structure appears to be smeared, while being convected downstream and the plume increases its temperature due to the viscosity at the walls and due to progressive mixing with the bulk supersonic flow.

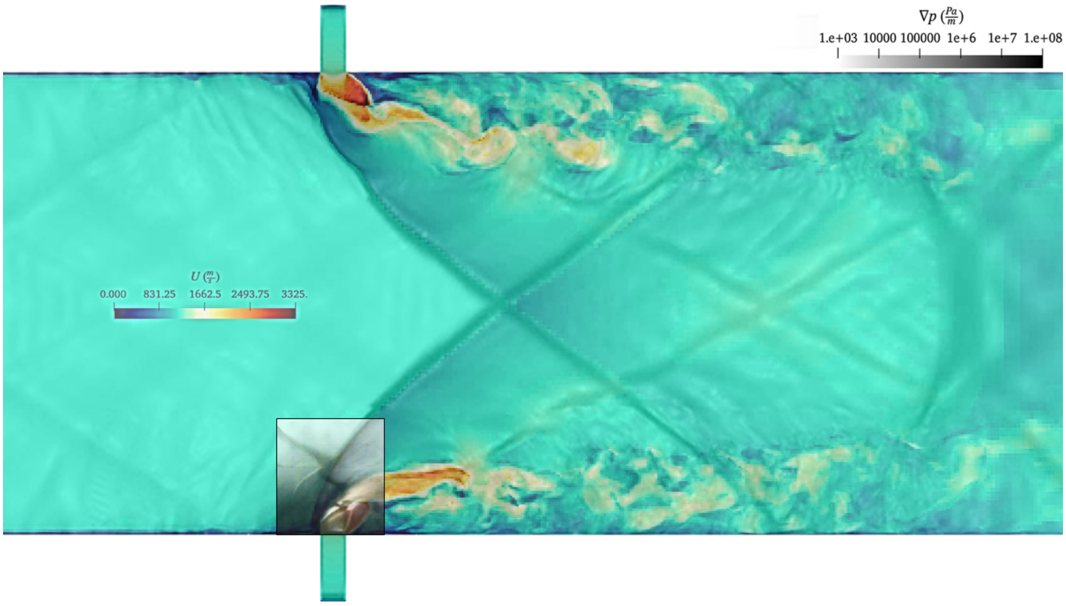

Figure 5.61: Case 1, modified mesh, partially reproduced numerical Schlieren from experiments (black box) [3] and superimposed pressure gradient magnitude on velocity magnitude.

The near injection zone now has a remarkable fidelity, as testified by superimposing a numerical Schlieren of the jet from the experiments to the overlapping velocity magnitude field and pressure gradient magnitude, that enhance the visibility of the compressible structures.

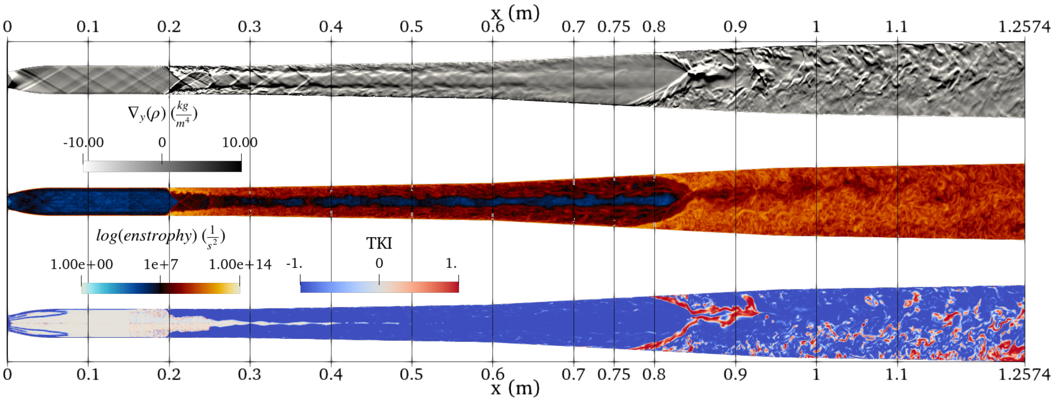

Figure 5.62: Baseline mesh: 3d view

A further set shows how it is important to have a proper resolution in this part of the domain. The numerical Schlieren displays how the barrel shock is reflected and how it interacts with the plume. Now much more penetration within the bulk flow is reached, that also develops Kelvin-Helmhotz instabilities within the shear layers while being convected downstream where they interact with shockwaves and expansion fans. The downstream separated region also capture the plume interacting and distorting the oblique shocks generated from the separated boundary layers.

The logarithmic scale of the enstrophy magnitude better quantify the mixing and the vorticity content generated right after the injectors barrel shocks, confirming that it is of the utmost importance to have a good resolution near the injectors, where the vorticity plays an important role in the fuel mixing right after injection. The separation zone is similar to the one observed in previous cases: the separation points oscillates, with the shock front being distorted by the eddies near the walls and the plume of fuel that crosses the shockwaves upon the separation. After the shockwaves, the plume got ignited after the desired levels of temperature, pressure and premixed-ness are met, as shown by the calculated Takeno Flame Index (TKI)[13]. This parameters, varying from -1 (non-premixed) to 1 (premixed), indicating the premix level of a mixture here calculated as:

$$TKI = \frac{\nabla H_2 \cdot \nabla O_2}{||\nabla H_2||\ ||\nabla O_2||} \tag{5.2}$$

The expected nature of the non premixed flame along the majority of the combustor is met, while near the flame front there is a region where the flame is premixed prior igniting.

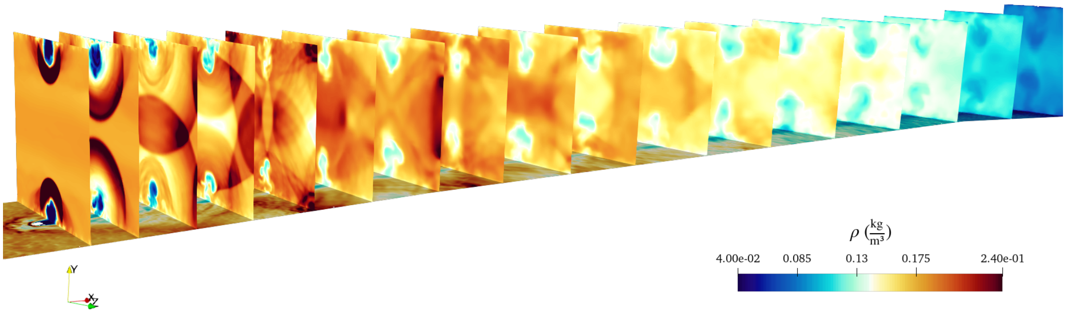

Figure 5.63: Baseline mesh: 3d view

The resolution was adequate enough to offer, through an instantaneous field of the density, a view of the jet penetrating and the various reflections of the barrel shocks along the isolator shock train. Where the half angle begins, the shockwaves start to smear upon interacting with the non directly visible expansion fans, and the density across the cross section drops, while the jet achieve its maximum penetration and mixing with the bulk flow.

---

[13] "TKI" is wrongly reported, but was kept for consistency

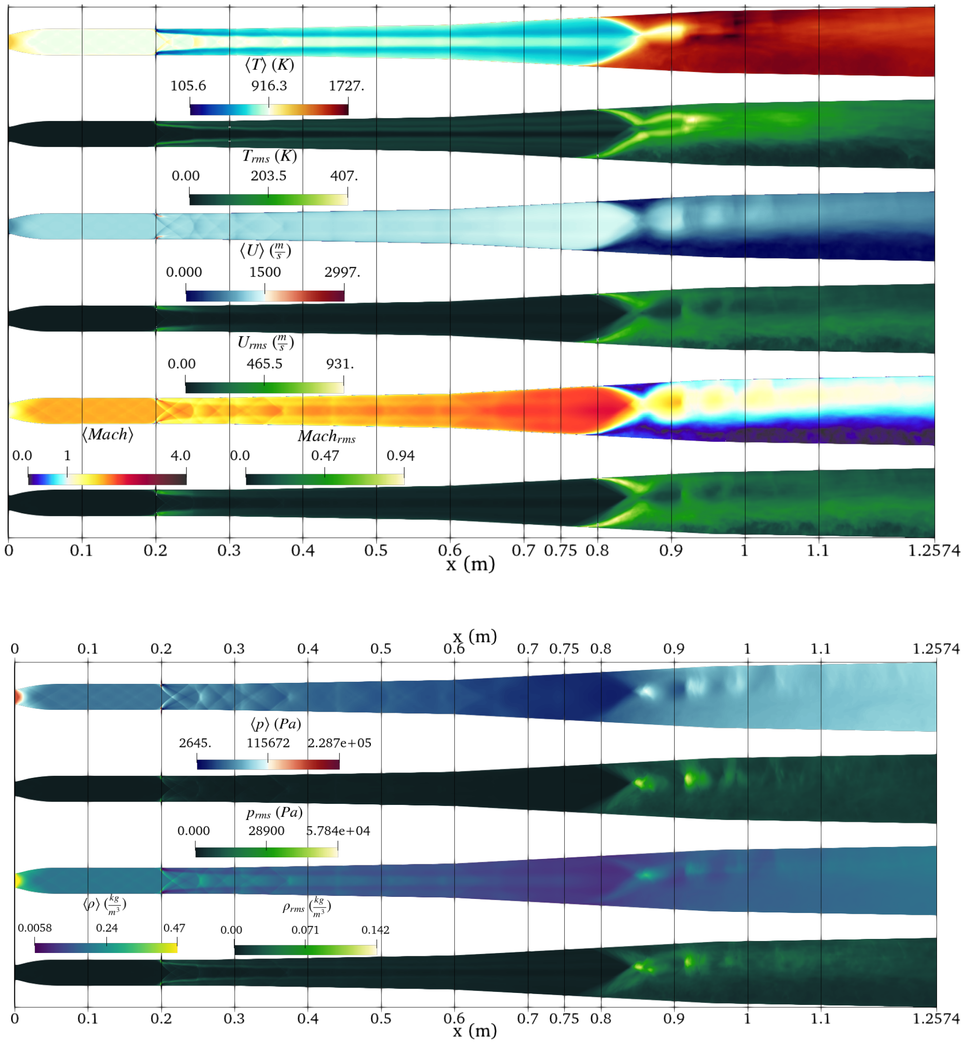

Figure 5.64: Case 1, modified mesh, mean fields and standard deviation along the symmetry plane of Mach, velocity, temperature, pressure and density

The mean fields with their standard deviation (root-mean-square, “rms”) show that the separation points are stable and oscillate between ∼0.77 [m] for the lower wall and ∼0.8 [m] for the upper wall, with the bias observed in previous cases. The oscillations are strong, and are due to the distortion of the shockwave front related to the incoming plume and turbulent structures. Another factor influencing those downstream oscillations is combustion. The mean temperature well-captured the features of the plume and of the combustion, engulfing the entire combustor cross-section. Another area of interest that exhibits remarkable standard deviation is the injection zone.

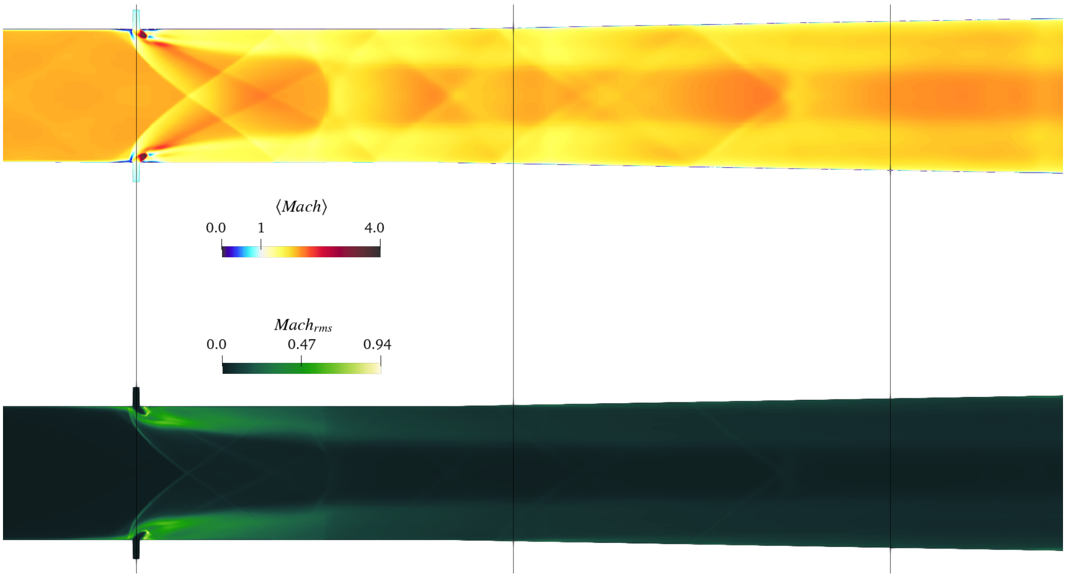

Figure 5.65: Case 1, modified mesh, magnification near injectors of mean Mach number and its standard deviation in the mid-plane

A magnification of the mean Mach and its standard deviation, shows that strong oscillations are present right after the fuel is violently accelerated and slowed down by the normal shock, as reported in the small subsonic pockets. This highly dynamical behavior is because the post-barrel shock zone, as also depicted by enstrophy in Fig. 5.62, presents a strong vortical region, that interacts with the large scale structures from the jets injected, producing spanwise and 3D shedding and oscillations as it is convected downstream.

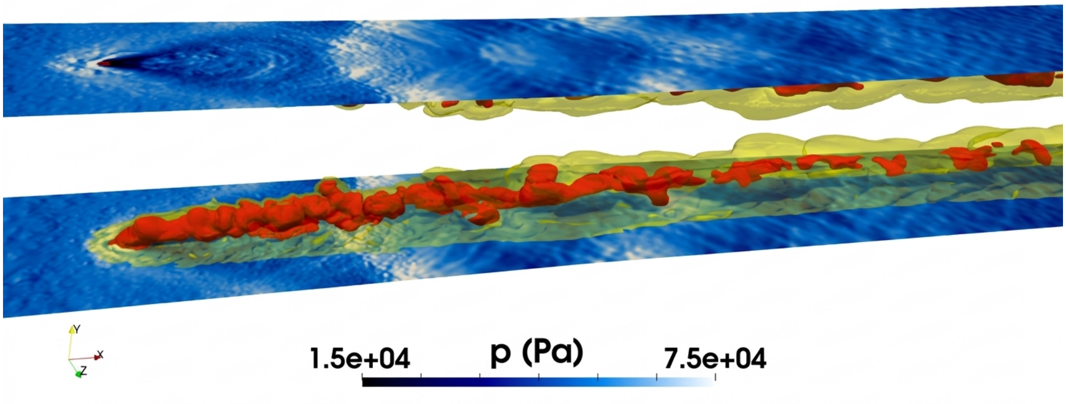

Figure 5.66: Case 1, modified mesh, H_2 mass fraction contours (red 0.01 and yellow 0.001) and instantaneous pressure along the wall patches

To show the highly three-dimensional behavior, two contours of the hydrogen mass fraction (red 0.01 and yellow 0.001) are reported. The walls patches colored by instantaneous pressure show how the shockwaves and the turbulent eddies interact with the rough walls turbulence, depicting a highly turbulent region.

Furthermore, during the simulations, a surface sampling of various consecutive times showed that the two jets interact, introducing an alternate shedding to each other.

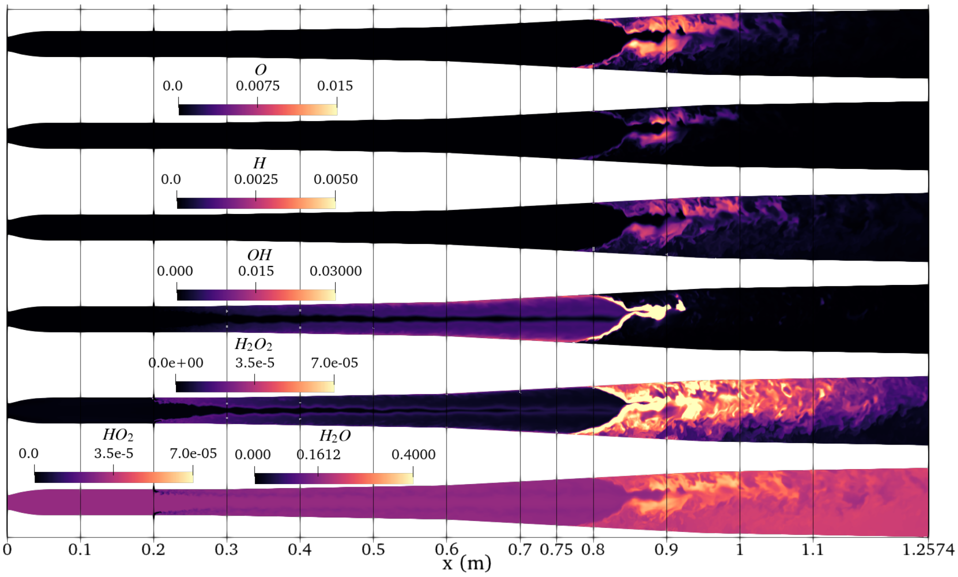

Figure 5.67: Case 1, modified mesh, instantaneous values in the symmetry plane for atomic oxygen O, atomic hydrogen H, hydroxide OH, hydrogen peroxide H_2O_2, hydroperoxyl HO_2 and water vapor H_2O

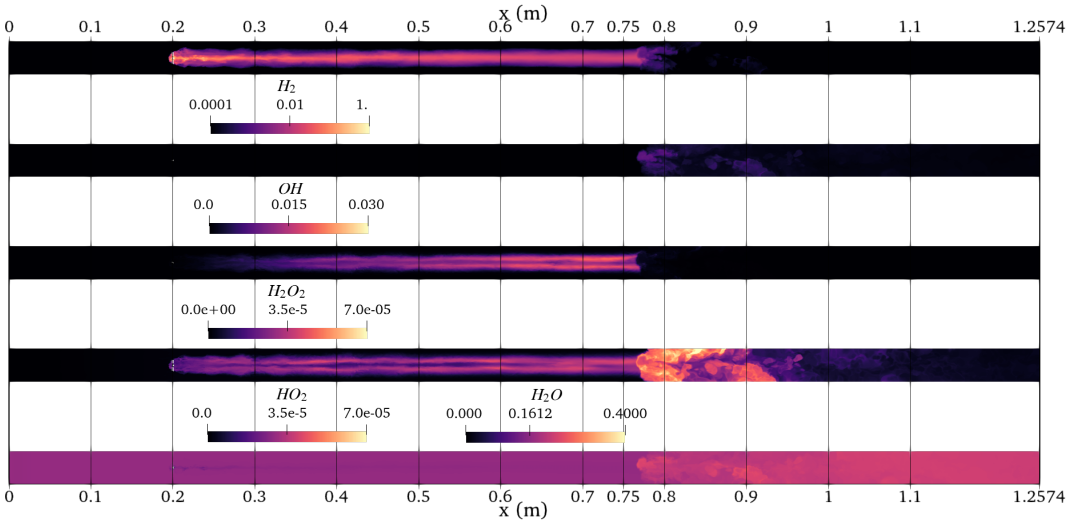

Figure 5.68: Case 1, modified mesh, instantaneous bottom wall patch values for hydrogen H_2 in logarithmic scale, hydroxide OH, hydrogen peroxide H_2O_2, hydroperoxyl HO_2 and water vapor H_2O

An investigation of the mass fractions of the species relevant to hydrogen combustion, shows the different flame behavior. The overall concentration values are consistent with the shift of the chemical activity towards low-temperature chemistry induced by radiation modeling.

Notably, O, H and OH mass fractions, present a more intense generation in the bulk flow, where the bulk supersonic flow shares its shear layer with the separated region, hinting at a stronger combustion region detached from the walls, as also visible from the heat release in Fig. 5.59, consistent with the observed jet penetration. Also the OH concentration along the bottom wall depicts low generation in it, while the fuel, H_2, present a different spanwise diffusion compared to Fig. 5.49, related to the new flow features captured. Meanwhile, H_2O_2 and HO_2 are generated both in the fuel plume and along the walls with more activity compared to previous studies, as expected by the 1D CHT BC employed. In particular, their higher values are located near the flame front, as they are strongly generated before ignition. Water vapor, H_2O, gives a comprehensive view of the aforementioned aspects. Hydrogen, representing near-zero values, is mixed almost completely right after injection, while the background non-zero value is for the air vitiation induced by the upstream hydrogen burner necessary to provide the desired inlet conditions. Higher values identify the combustion zone, being generated mostly within the bulk flow, and following it with its bias towards the upper wall, as also depicted in the experimental photo in Fig. 5.59.

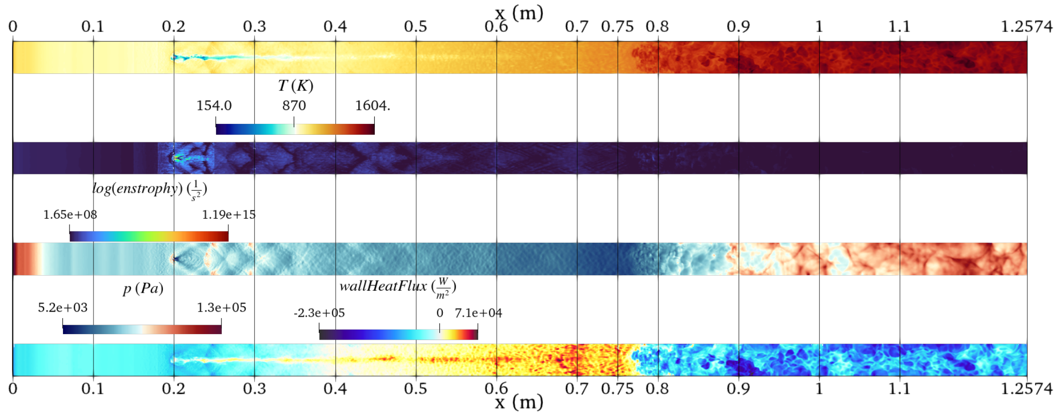

Figure 5.69: Case 1, modified mesh, instantaneous bottom wall patch values for temperature, logarithmic scale of enstrophy, pressure and *wallHeatFlux* (convective heat flux)

For instance, the walls appear to be relatively hotter, since the cold jet injected influences less the wall temperature, and the new mesh probably has a different boundary layer resolution. Once again, with the LES, the temperature field shows the detailed wrinkling of the flame at the wall and how the injected fuel plume is bended and distorted by both turbulent and compressibility effects near injection. The location of those compressible features are captured better in the logarithmic scale of the enstrophy, presenting mesh resolution dependence as seen by the magnitude variation around 0.25 [m].

Nevertheless, this field, alongside the instantaneous pressure, show the highly dynamical structures and spanwise boundary layer distortions at the walls, where also shock reflections are observed. Those structures are highly important in the prediction of heat fluxes at the walls, as showed by the instantaneous *wallHeatFlux*, where peak values and oscillations are strongly correlated to those complex features interacting with each other.

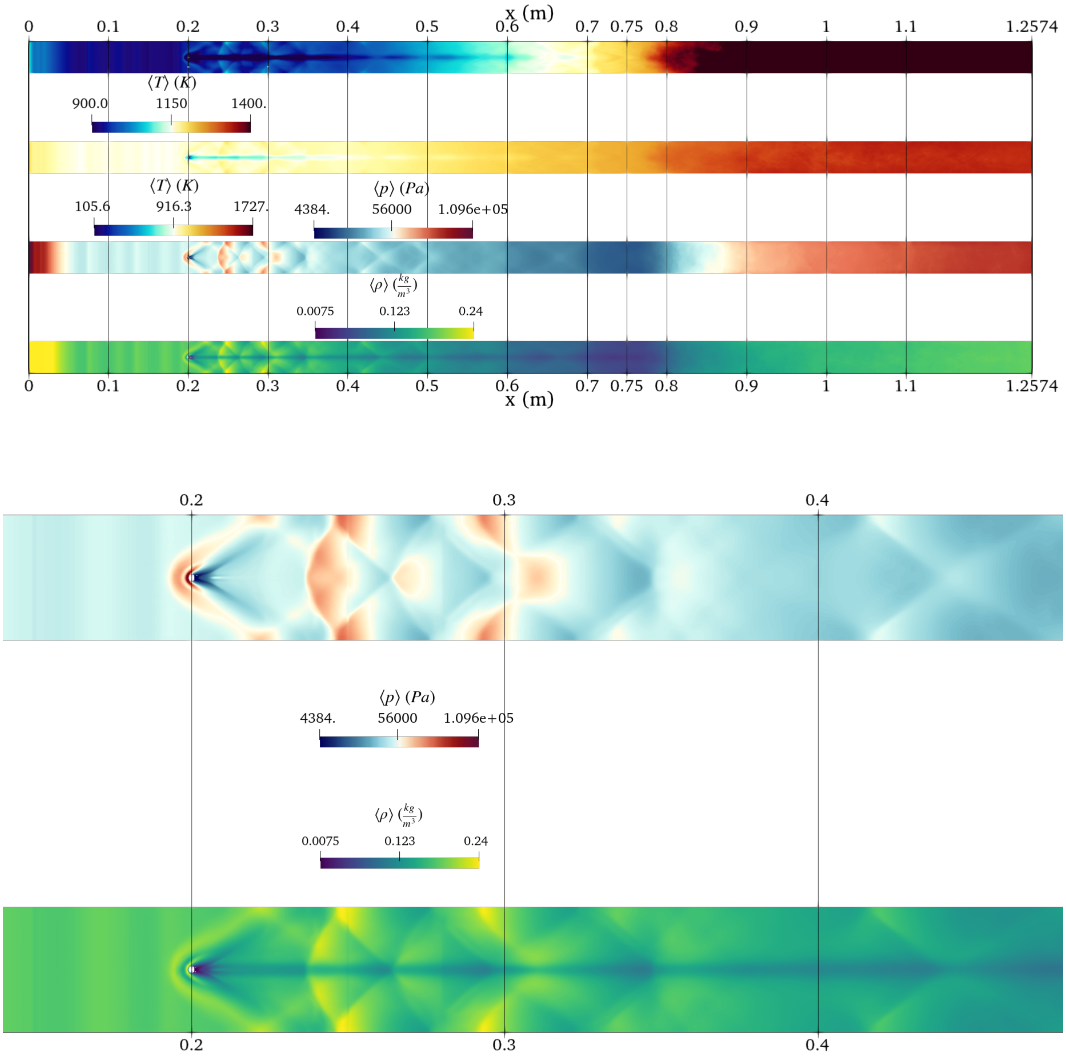

Figure 5.70: Case 1, modified mesh, mean bottom wall patch values for temperature, pressure, density

The mean wall quantities reported, extract from a statistical standpoint the most relevant features. The mean temperature, reported also rescaled respect walls temperature not interested by the combustion zone or the cold hydrogen, shows the evolution provided by the 1D CHT BC. Pressure and density, reported the average wall positions and impingement provided by the shockwaves developed within the shock train. The features are symmetrical on average, while the density also shows the region interested by the jet.

To provide a more quantitative description, the mean temperature values along the mid-line of different cases and meshes are reported.

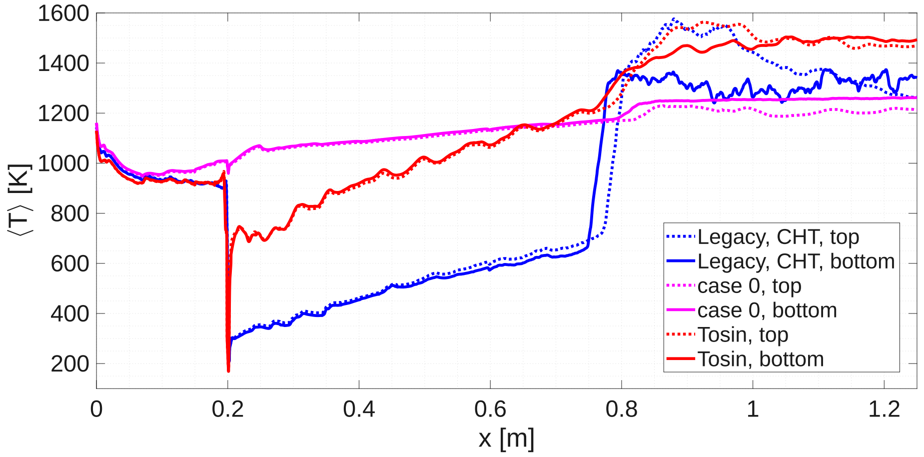

Figure 5.71: Case 1, modified mesh, mean wall temperature along the walls symmetry line

The mean temperature values for the new mesh, is different compared to the non-reacting case as expected, but has similar values before the injectors at 0.2 [m] respect legacy mesh with the same 1D CHT BC. After that, the different impingement of the hydrogen plume is observed, having much higher temperature values before separation, with a similar trend regarding the axial heating. The mean temperature observed between injection and separation, ∼950 [K], is similar to the best-agreement prescribed temperature between experimental data and simulations previously done. [4, 21] After separation, a similar behavior is observed regarding top and bottom patches respect the reacting case previously simulated. The top flame is more compact and decreases a little due to the bulk supersonic flow impinging wall towards the chamber's exit. Meanwhile, the bottom patch reaches higher temperature, probably due to the hotter mixed flow upstream. The weaker temperature rise in the separated region hinting weaker combustion near the walls.

To have a better idea in how the 1D CHT BC behave differently due to the new jet dynamics, also the mean *wallHeatFlux* and radiative heat flux q_r along the mid-line of the wall patches are represented between legacy and new mesh.

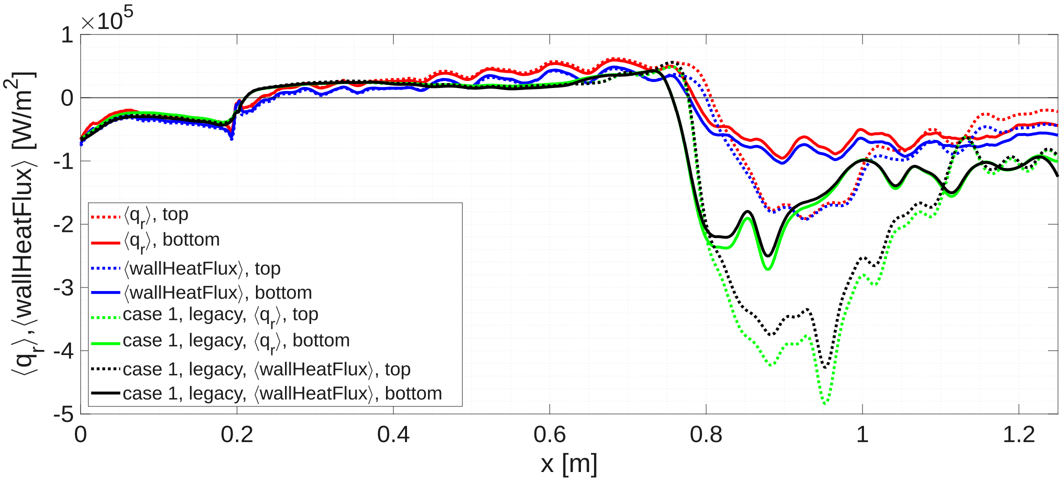

Figure 5.72: Case 1, modified mesh, mean *wallHeatFlux* and radiative heat flux q_r along the walls symmetry line between legacy and modified mesh

Before injection, the profiles are similar despite having used different values for h, but near injection, there are differences related to the new dynamic captured. Following the axial location towards the separation points, the heat fluxes tend to have the same values. After separation, while having the same overall features in top and bottom patches, the order of magnitude is different, further confirming a different flame position respect the walls.

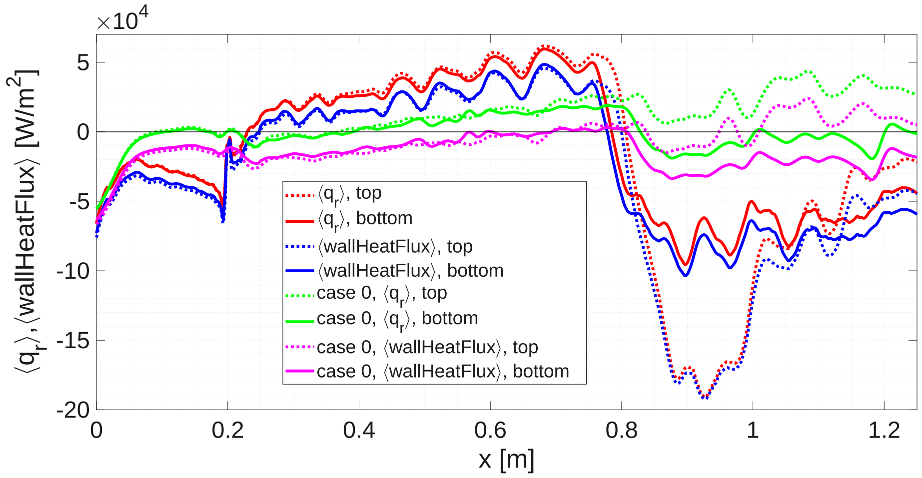

Figure 5.73: Case 1, modified mesh, mean *wallHeatFlux* and radiative heat flux q_r along the walls symmetry line

Follows a comparison with the non-reacting case for both mean radiative heat flux and *wallHeatFlux* (convective). Once again, the thermal layer is affected upstream of the injection, a feature hinting changes and further perturbations in the boundary layer itself. Once again, both convective and radiative have similar values, highlighting the importance of the latter fluxes.

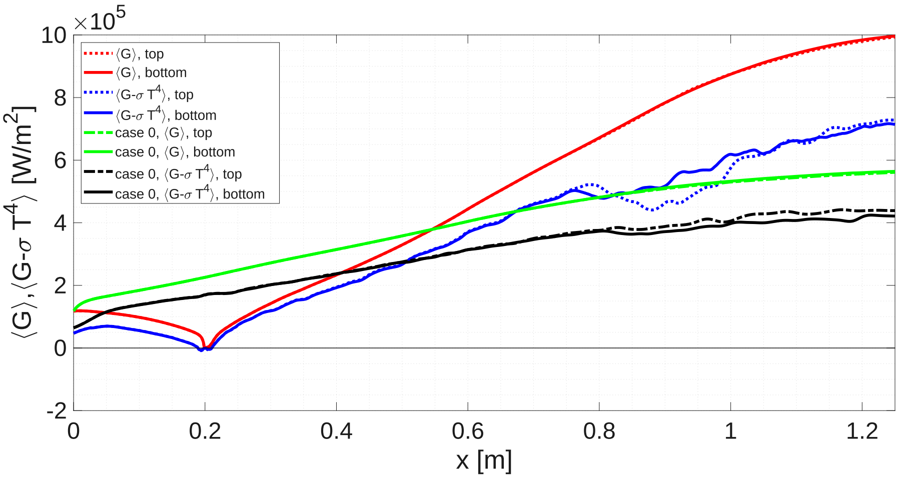

Figure 5.74: Case 1, modified mesh,mean incident radiation G and net radiative term $G - \sigma T^4$ along the walls symmetry line

A final comparison of mean thermal-related quantities along the mid-line displays the difference of both the mean incident radiation field G and the so-named here mean net radiation energy term $G - \sigma T^4$ compared to the non-reacting case. Both the incident radiation and the net radiation term have different features, with the values increasing and surpassing the non-reacting values as the axial location increases. The barrel shocks act as an optically thick medium, suppressing net radiative energy values, while for the combustion zone, the near-wall values are less affected since the combustion zone is more detached.

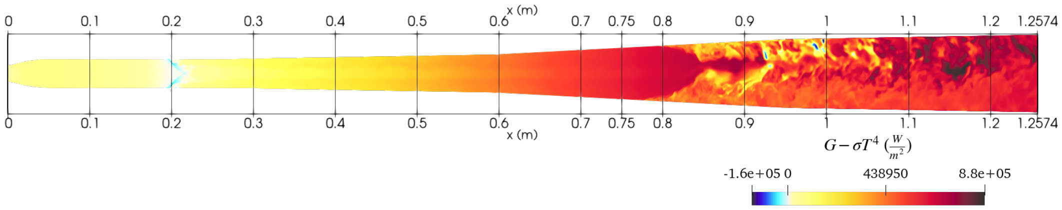

Figure 5.75: Case 1, modified mesh, symmetry plane slice of net radiative term

An instantaneous symmetry plane slice of the net radiative energy shows that while the barrel shocks have the same sink effect of the one displayed in Fig 5.54, the downstream part exhibit a complete different behavior. The culprits could be the jets and the new flame structure, changing the optical thickness of the downstream separated region. Even if the combustion zone act as a local sink term, this temperature increases is not sufficient to drop the net radiative term below zero at the walls for the used formulation, except some small spots located in the inner flow.

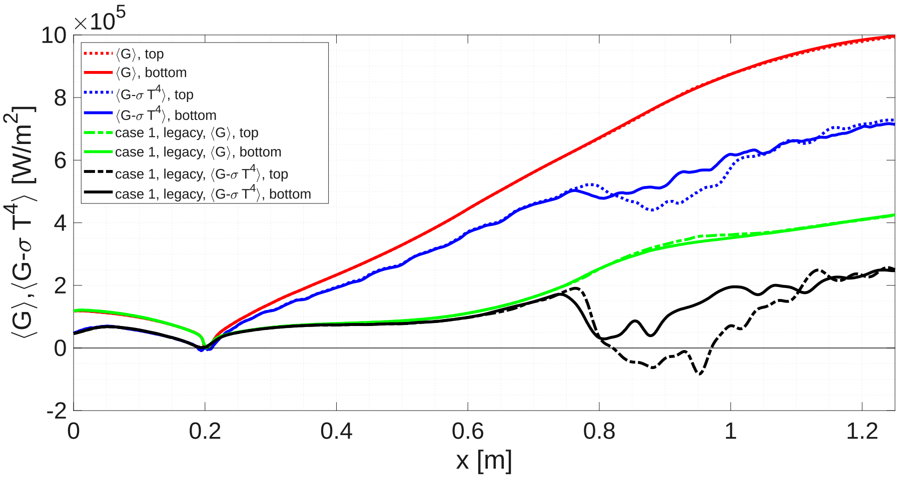

Figure 5.76: Case 1, modified mesh,mean incident rdaition G and net radiative term $G - \sigma T^4$ along the walls symmetry line between legacy and modified mesh

Comparing the quantities with the legacy results, shows that before injection the values are overlapping, but after that, the differences on the optical thickness induced by hydrogen jets and combustion could be the main culprits for the divergence.

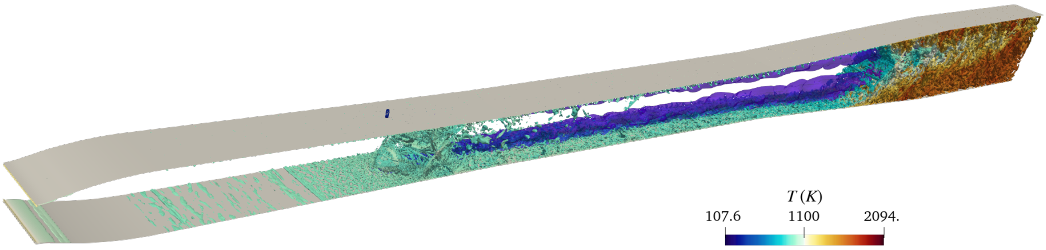

Figure 5.77: Case 1, modified mesh, Q-criterion colored by temperature and a semi-transparent blue-colored hydrogen contour

As a final touch, to show all the mentioned features, the Q-criterion colored by the instantaneous temperature and a semi-transparent blue-colored hydrogen contour is presented. The strong barrel shocks upon injection produce the highly vortical region visible for the contour value chosen, while hairpin vortices interact and got generated until ignition in the separation region, engulfing the totality of the cross-section.

5.2.3 Case 4

The final case presented is a shock-induced supersonic combustion mode, case 4 in Tab. 4.1.

Instead of mapping the results from previous studies, the transition from subsonic to supersonic combustion was triggered by changing the inlet condition to match the experimental ones. Convective heat transfer coefficients, h, for the thermal 1D CHT BC, they were restored to 15 $[\frac{W}{m^2K}]$ and 10 $[\frac{W}{m^2K}]$ for top and bottom walls, because the flame needed to crawl from the separated region to the near-injectors region. Therefore, lower h values were restored, hoping that hotter walls would help to speed up the process by destabilizing the boundary layer. Another modification, with the hope of accelerating the process, was to increase the K_s[14], from the value of 60 $[\mu m]$, similar to measured values [5], to 150 $[\mu m]$. The transition and ignition details are better reported in App. D, here only the final results are discussed.

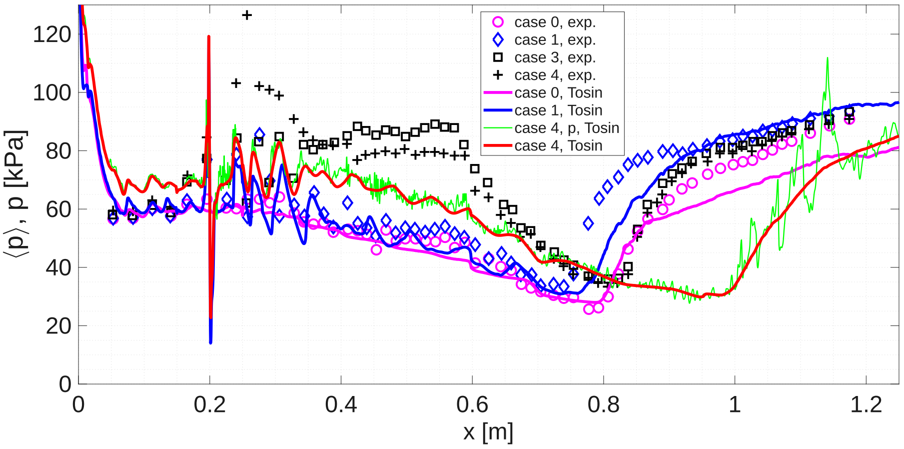

Figure 5.78: Case 4, modified mesh, mean and instantaneous pressure along the bottom wall mid-line compared to experimental data. [3]

A plot along the bottom wall mid-line of the mean pressure is presented, compared with experimental values. As a reference, the other modified mesh cases are reported with the instantaneous pressure of the latest available time step. As in previous cases, the calculated mean pressure absolute values are not matched. Therefore, the subsonic reacting case offset of 9500 [Pa] to match the pressure level upstream of injection was applied. Within the available simulation time, it was not possible to reach the desired configuration (case 4). The wall pressure is overestimated in the first part of the combustor prior injection, and underestimated in the remaining part, with the separation location much more downstream compared to previous cases and experimental data. Even if case 4 was the desired configuration, it seems that the current configuration is a somewhat hybrid version of experimental case 4 (for flame anchoring, as will follow) and case 3.

The isolator pressure levels right after injection are the same of case 3, but the

---

[14] Sand-grain roughness height parameter (more on Sec. 4.1) used in the OpenFOAM *nutkRoughWallFunction*

supersonic-combustion pressure rise is not as high as it should be between 0.4 [m] and 0.6 [m], while a small portion before 0.8 [m] seems to match the experimental results. The case seems to not be converged yet, therefore the instantaneous pressure was reported to look if some differences hinting further developments were present. The behavior seems to match the mean results almost everywhere, but some higher pressure near 0.4 [m] and after separation at 1 [m], hints that probably more simulation time is needed, as also observed in App. D.

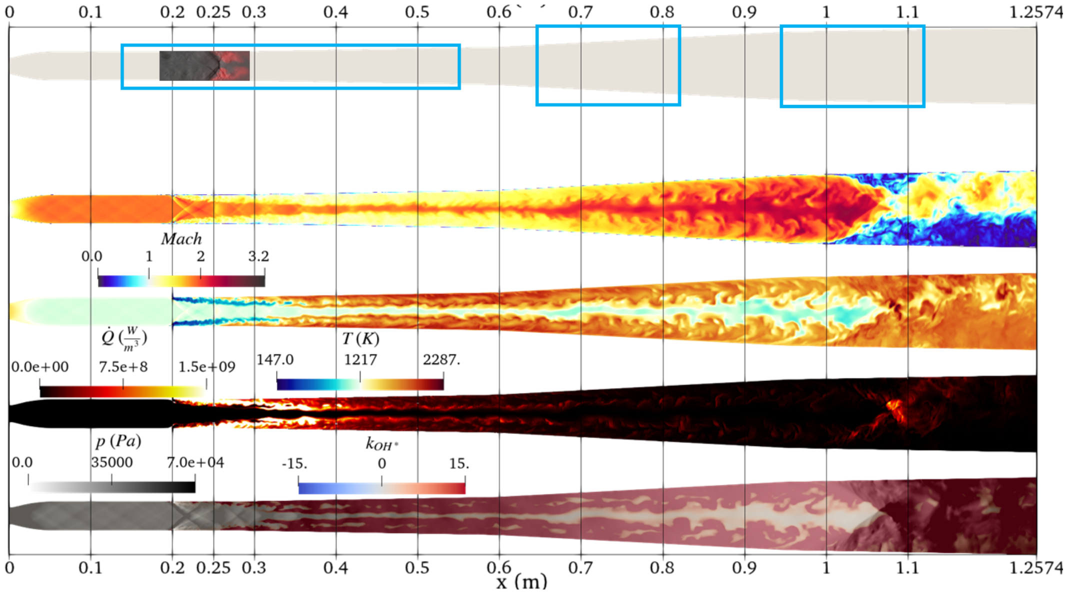

Figure 5.79: case 4, modified mesh, mid-plane instantaneous Mach, temperature, heat release and modified photon emission rate (Eq. 5.1) superimposed with pressure compared to superimposed experimental OH-PLIF and Schlieren. Partially reproduced from [3]

The Mach number have a similar behavior near-injection and in the first part, however, in this new configuration the plume is much thicker as it proceeds downstream because combustion is occurring along it, as it is shown by temperature and heat release. Downstream, the hot plume present strong wrinkled turbulent structures, that impinges a separated region much more downstream compared to the subsonic reacting case (see Fig. 5.59), where weak combustion is present, as depicted in the heat-release. Finally, the modified photon emission rate (Eq. 5.1) superimposed with pressure is reported, highlighting, alongside temperature, a flame anchoring at the walls near the desired location reported from the OH-PLIF [15]. However, the flame surrounding the plume seems to be distributed downstream, missing the strong OH generation after the double lambda shock.

---

[15] OH-PLIF is an experimental visualization technique that visualizes hydroxyl (OH) radical spatial distribution

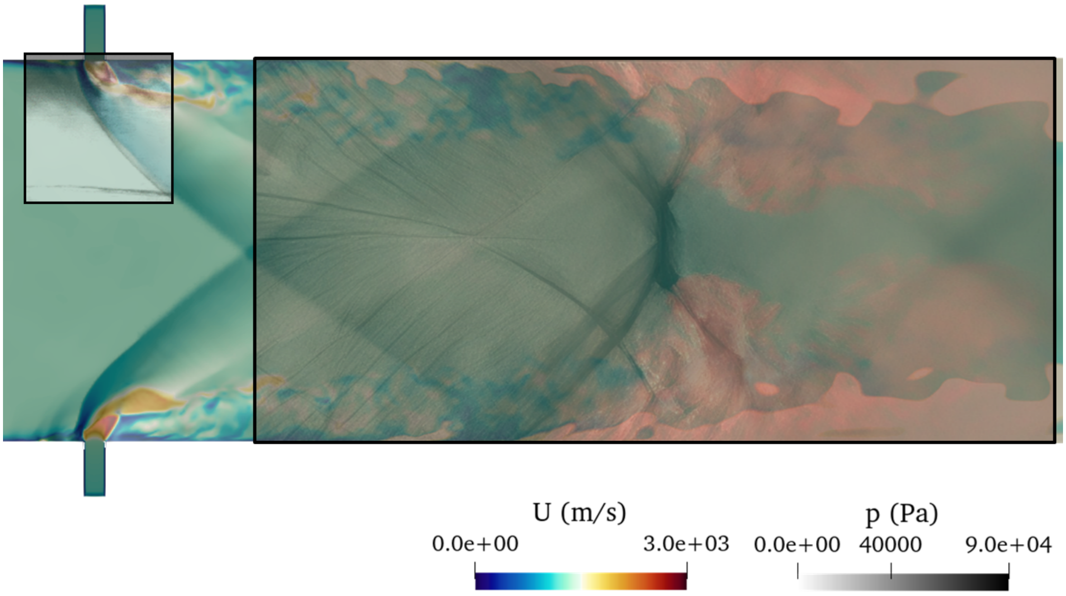

Figure 5.80: Case 4, modified mesh, mid-plane superimposed instantaneous velocity magnitude and pressure compared to experimental OH-PLIF and Schlieren. Partially reproduced from [3, 21]

A detailed look at the injectors, looking at pressure superimposed with the velocity magnitude and H mass fraction[16] in white, visible along the walls, overlapped with experimental OH-PLIF, clearly exhibits much stronger generation after the double lambda shocks distorted by the upstream fuel plume and downstream combustion. Instead, the generation appears to be much more relegated to the walls and then covers all the supersonic plume while being transported downstream, with the flame not yet capable of modifying the shock train structure. A Schlieren at the upper injector is superimposed with the upper injector calculated structures, confirming the high-fidelity of the captured jet and barrel shock formation. A further set near the injectors is presented in Fig. 5.81. The numerical Schlieren, shows that the resolution-cutoff smear the well-captured shockwaves and larger scale eddies along the plume as in other cases, while enstrophy shows the strong mixing occurring. The smeared shockwaves are visible from the pressure field, ideally the resolution near injectors would be extended to the whole mesh. As for the overlapped heat-release, it shows that notable values are observed from the high-pressure zones where the barrel shocks, interacting with the fuel plume, got reflected and then it crosses all of the plume height until after 0.3 [m] the whole cross-section is burning, as seen by the temperature values in Fig. 5.79.

---

[16] Considered a good proxy for the comparison

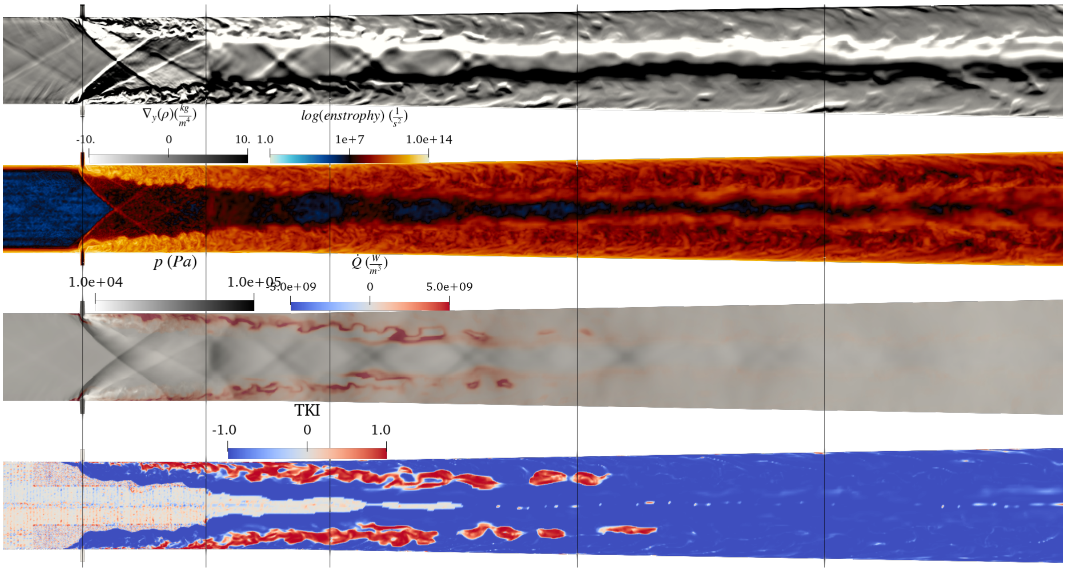

Figure 5.81: Case 4, modified mesh, symmetry plane instantaneous numerical Schlieren, enstrophy in logarithmic scale, superposition of heat-release with pressure and TKI (Takeno Flame Index)

Interesting values are observed with the TKI (Takeno Flame Index, Eq. 5.2). Unitary values, representing full premixed-ness, originates from the subsonic recirculation regions near injectors, and further enhanced generation is observed from the double lambda shock from the barrel shocks impingement near the walls, until covering more area of the supersonic plume while also detaching from the walls. where also combustion occurs.

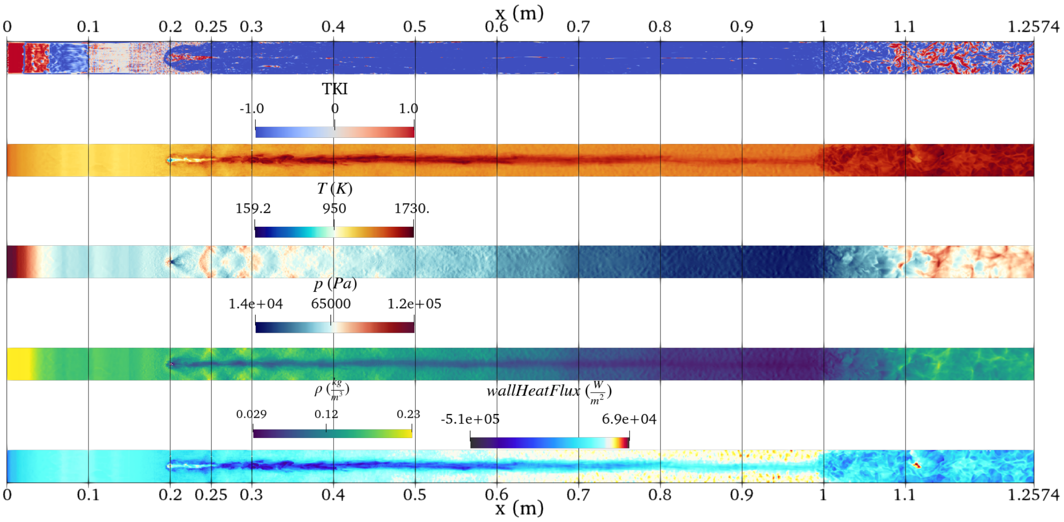

Figure 5.82: Case 4, instantaneous bottom wall patch values fot TKI (Takeno Flame Index), temperature, pressure, density and *wallHeatFlux*

To further inquire about the new Takeno Flame Index values, another set of instantaneous fields at the bottom patch is reported. The Takeno Flame Index values further confirm the previous observation, since premixed-ness is reached all around the injectors.

The temperature shows that the desired anchoring for case 4 around 0.25 [m] is reached, while also temperature rise is observed in the surrounding of the cold plume. After the anchoring location, the flames follow the shedding of the plume while being convected downstream, until the separated region where flames cover all the spanwise wall direction. pressure and density highlight shockwaves impingement in a turbulent-rich region. Finally, also the instantaneous *wallHeatFlux* (convective, [53]) is presented. Coherently with the new combustion occurring along the plume, now the walls have to sustain severe heat loads from the fluid, especially along the hot jet impingement in the shock train. Then, expansion is responsible for an attenuation of the heat flux until the separation region, where temperature rises up again with subsonic combustion covering all the cross-section.

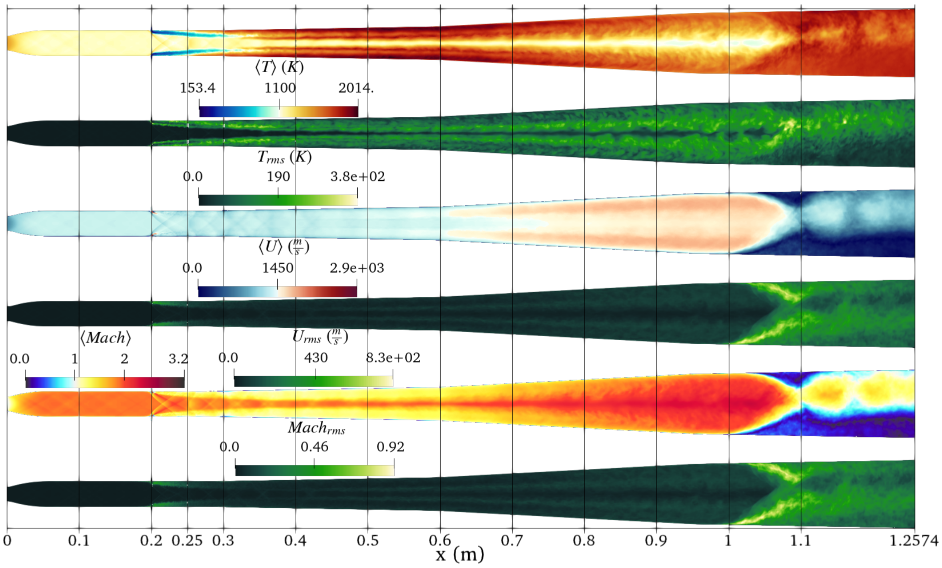

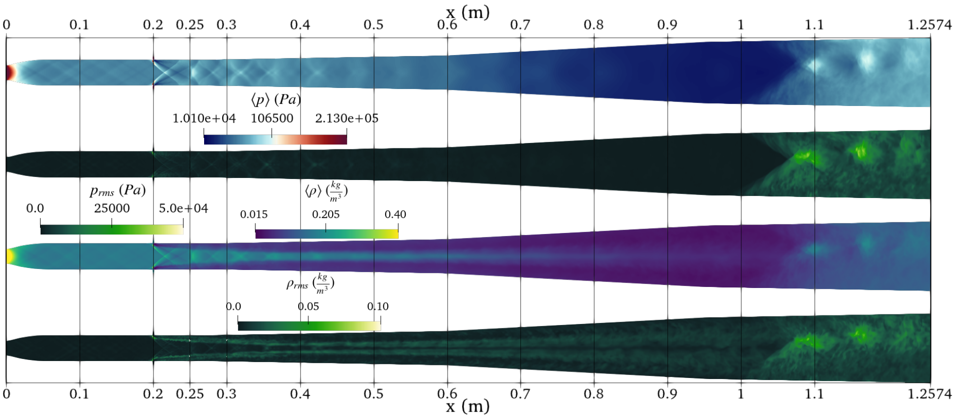

Figure 5.83: Case 4, modified mesh, symmetry plane mean fields of temperature, velocity and Mach magnitude, pressure and density

The mean field calculated with the latest available snapshots are presented. This time, they were calculated within *ParaView*, in order to isolate the latest times from the initial transient. Unluckily this calculation, compared to the the normal *functionObject* in OpenFOAM, introduced some numerical jitter.

Nevertheless, the mean fields are presented, with mean temperature confirming a stable anchoring at the desired case 4 location, and mean velocity showing the more downstream separated region, with its characteristic upper wall bias, preceded by a violent expansion of the burned plume covering almost all of combustor height. The more reactive plume is responsible for more fluctuations in it. Probably due to different temperature values, the peak Mach number reached during expansion upon injection is lower. Strong fluctuations upon the downstream separation points are due to the highly-dynamic plume interacting with the oblique shocks from the separation points. Hopefully, at some point the boundary layers will either separate or crawl upstream and interact with the upstream shock-train to the desired configuration.

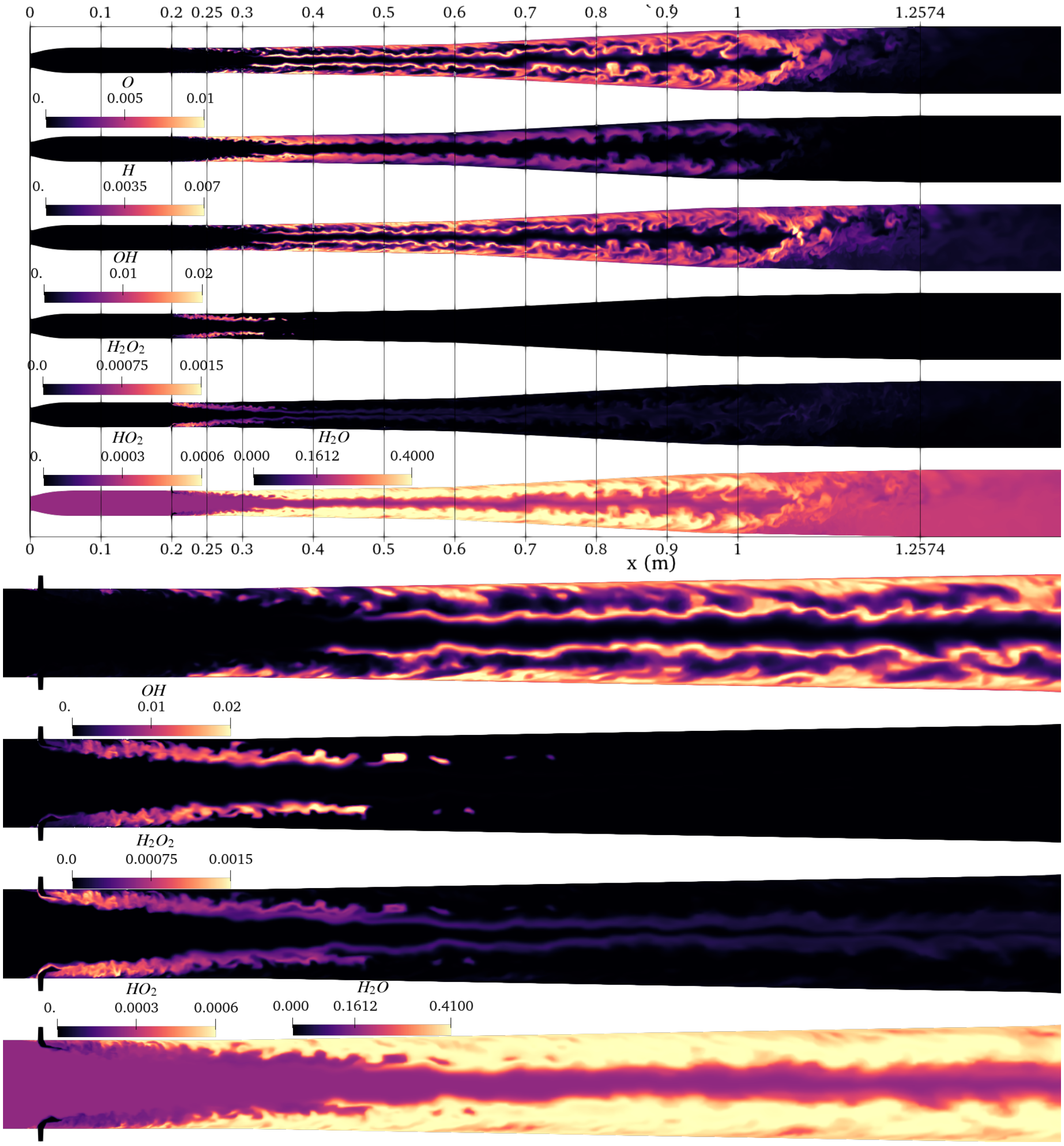

Figure 5.84: Case 4, modified mesh, instantaneous values in the symmetry plane for atomic oxygen O, atomic hydrogen H, hydroxide OH, hydrogen peroxide H_2O_2, hydroperoxyl HO_2 and water vapor H_2O

The instantaneous fields of most relevant chemical species are presented. Starting with O and OH, while showing remarkable concentrations along the supersonic plume, their wall values near 0.25 [m] shows the flame anchoring, while the entire flame seems to stretch downstream before covering all the plume. Furthermore, high H values hint at a violent explosive-like combustion, since high-temperature reactions are triggered. Meanwhile, H_2O_2 and HO_2, present a strong generation right after injection but their concentration drop as the fuel is ignited, as also visible from the magnified near-injectors H_2O, whose concentration values sharply increase in the corresponding regions. The instantaneous picture of the most relevant chemical species is presented. Compared to the subsonic case, almost all of the fields are rescaled. The flame appears to be intense and generating within the supersonic plume, with the most relevant species being generated right after injection. The wall behavior of some of the presented species follows from the above discussion.

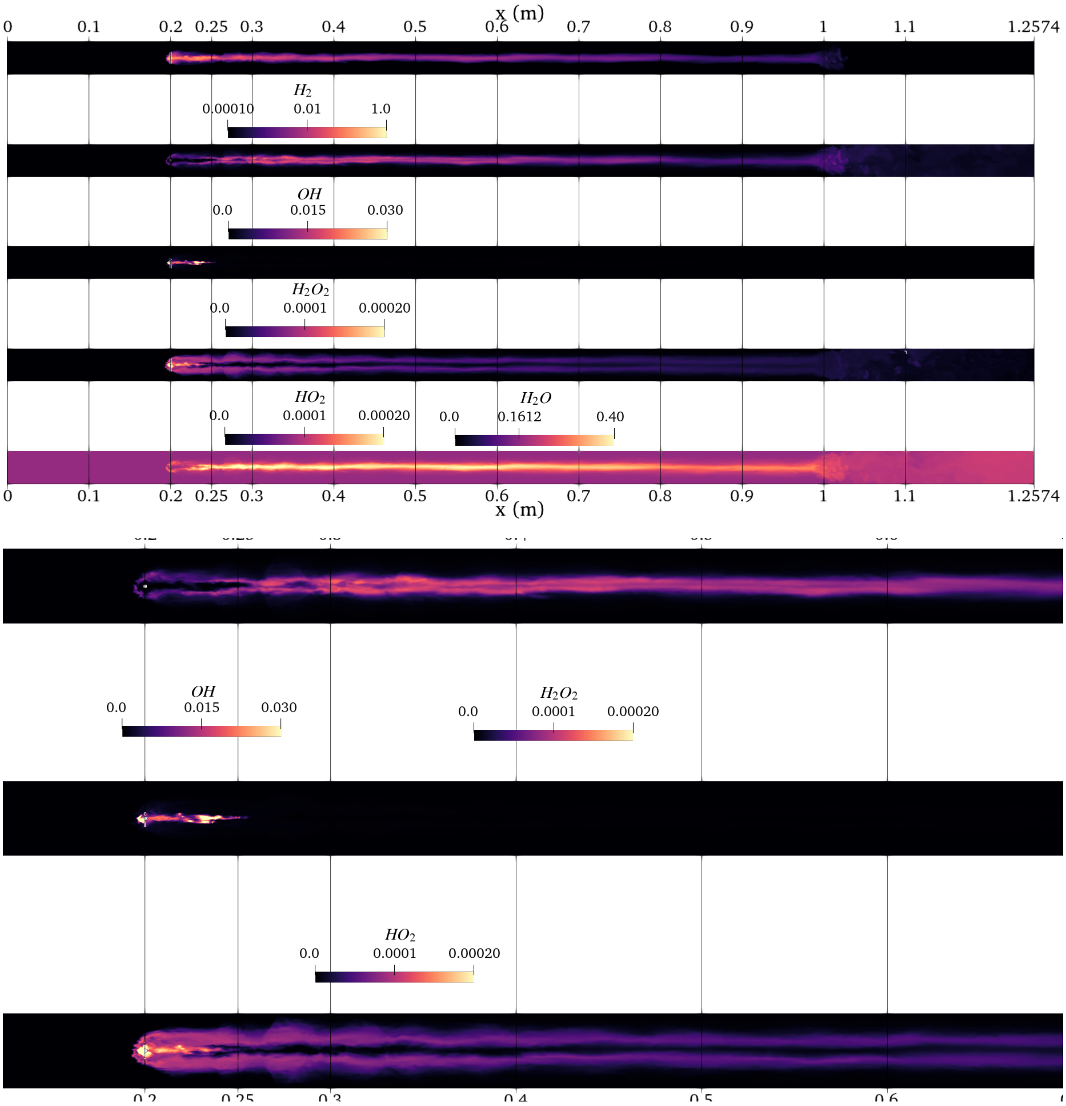

Figure 5.85: Case 4, modified mesh, instantaneous bottom wall values for hydrogen H_2, hydroxide OH, hydrogen peroxide H_2O_2, hydroperoxyl HO_2 and water vapor H_2O

The ignition related species H_2O_2 and HO_2 are magnified alongside OH, showing strong correlation as expected while the overall H_2 distribution display a different wall impingement compared to the subsonic case in Fig. 5.68, because concentration decreases as combustion is occurring. Related to combustion, high water vapor concentration are observed around the injectors. The chemical species H_2O_2 and HO_2 near injection hint at a possible flame diffusion due to high concentrations.

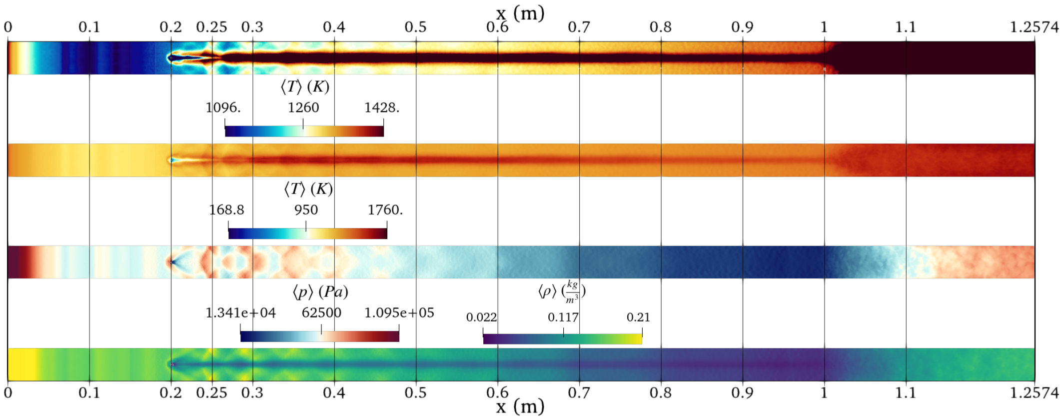

Figure 5.86: Case 4, modified mesh, mean bottom wall values for temperature (rescaled and full-scale), pressure and density

As a final touch for qualitative values along the bottom wall, the mean fields of temperature in two scale, density and pressure are reported. Pressure and density display the same overall features regarding shockwaves impingement and plume interactions showed in Fig. 5.86, but not the one desired for this configuration. The temperature is different due to combustion and different inlet temperature. The mean values further confirm the anchoring of the flame at 0.25 [m].

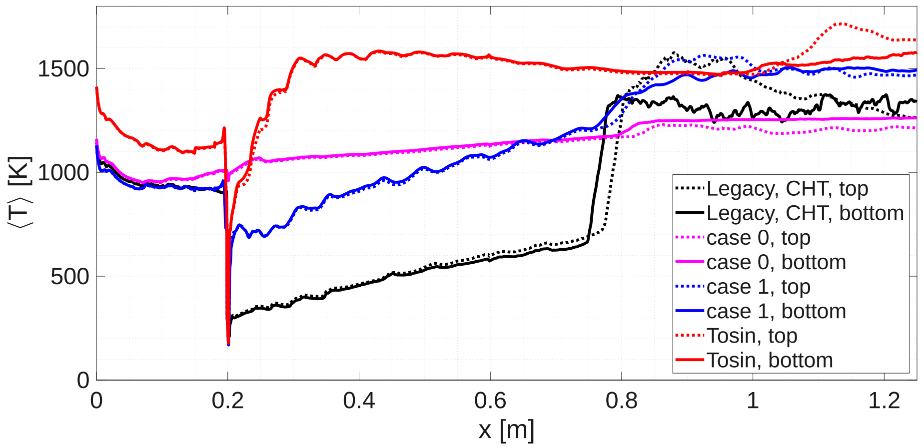

Figure 5.87: Case 4, modified mesh, mean temperature along the walls symmetry line

More quantitatively, mean wall temperature is plotted compared to previous results. Now, the new inlet conditions, and possibly wall roughness, generate higher temperature in the first part, while after injection values drop due to the strong expansion and then increase abruptly for the remaining length due to combustion occurring along the walls. The bottom patch preserves the new temperature reached until the chamber's end, with values closely related to the case 1 with the same mesh. Meanwhile the top patch, presents a compact temperature rise probably due to additional reactions and then decreases at the exit for the bulk supersonic flow impingement.

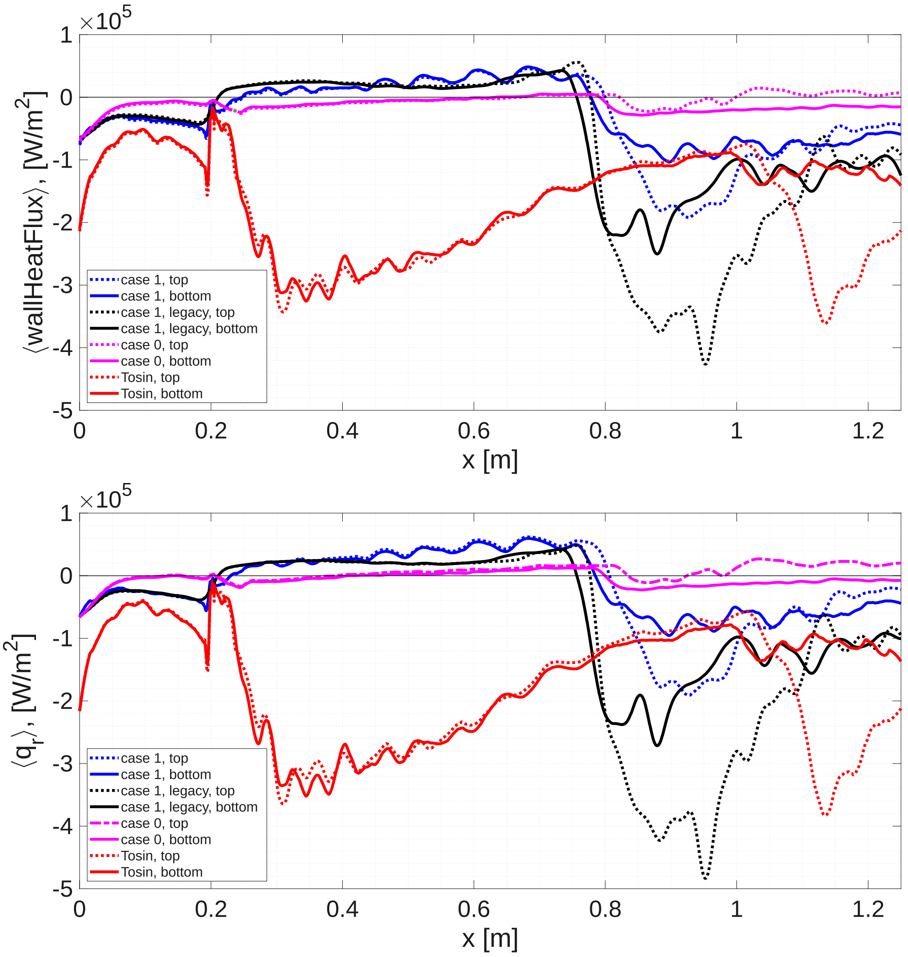

Figure 5.88: Case 4, modified mesh, mean *wallHeatFlux* and radiative heat flux q_r along the walls symmetry line

Both mean values for radiative heat flux q_r and *wallheatflux* (convective, [53]) are presented, closely matching the aforementioned features relating combustion along the walls and displaying similar values, once again highlighting the importance of radiative heat fluxes along the convective ones. Notably, different heat fluxes values upstream of injections are related to new inlet temperature, boundary layer perturbation induced by the upstream features and probably enhanced wall roughness. The negative values following injection are related to heat-release along the plume, while as mentioned, top patch presents a large variation towards the outlet as the bulk supersonic wall impinges the surface. Similar heat fluxes for bottom wall are observed.

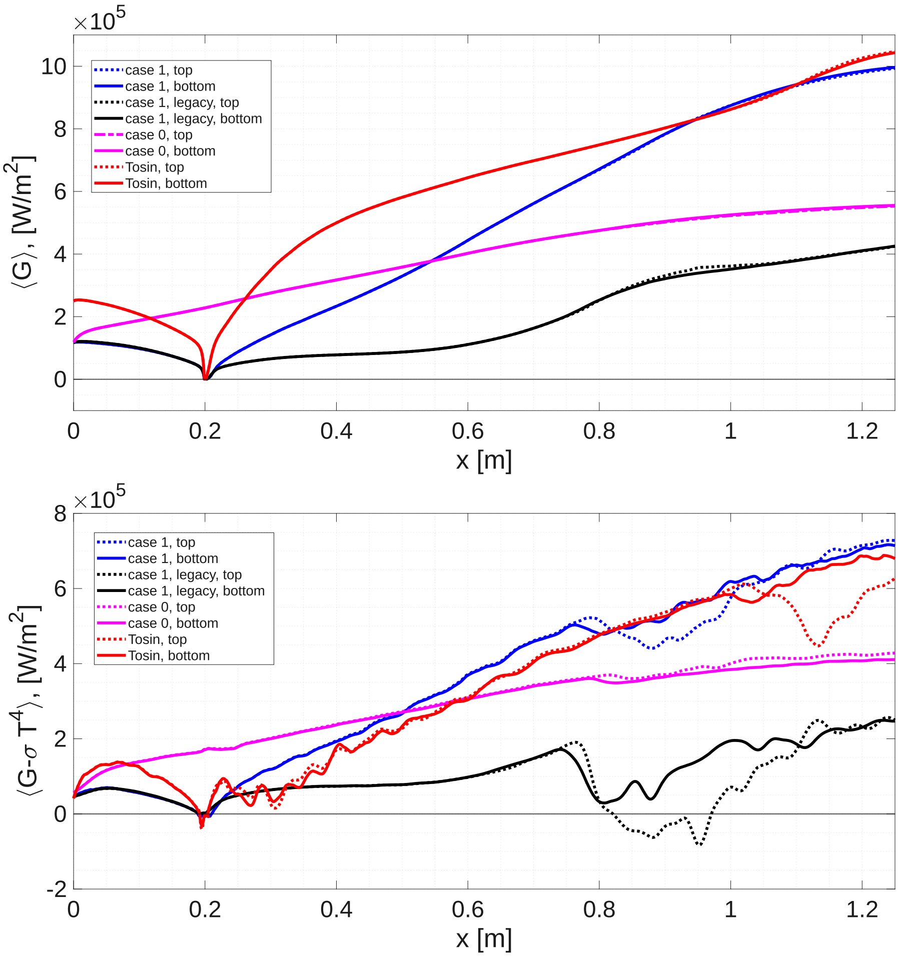

Figure 5.89: Case 4, modified mesh, mean incident radiation G and net radiative energy $G - \sigma T^4$ along the walls symmetry line

Incident radiation follows a similar trend compared to case 1 with the new mesh, with higher values after injectors probably due to supersonic combustion and plume thickening, while before injection differences are related to different inlet temperature values. The net radiative term presents differences before the injectors but after the barrel shocks suppression, closely follows case 1 distribution, except the top wall impingement region from supersonic flow towards the exit.

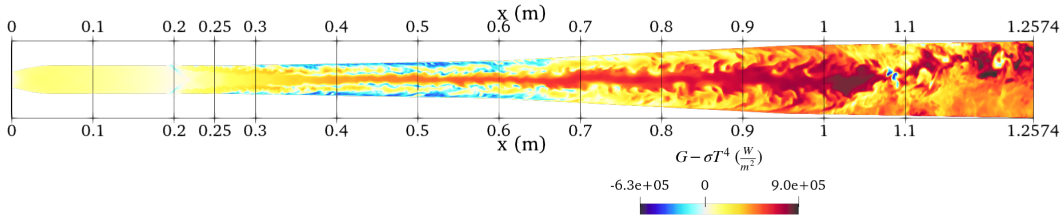

Figure 5.90: Case 4, modified mesh, symmetry plane instantaneous net radiative energy $G - \sigma T^4$

This is an interesting similarities for the net radiative energy along the walls, as the instantaneous symmetry plane values present different features compared to the subsonic reacting case in Fig. 5.75.

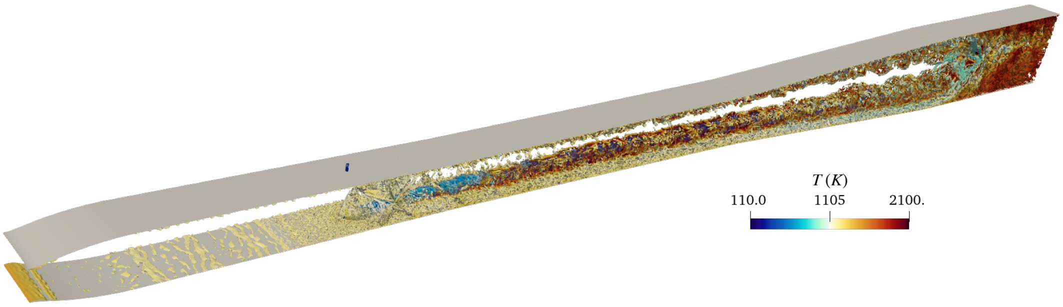

Figure 5.91: Case 1, modified mesh, Q-criterion colored by temperature and semi-transparent blue-colored hydrogen contour

As a final touch, the volumetric rendering of Q-criterion colored by temperature is presented alongside a semi-transparent hydrogen mass fraction contour, highlighting the axial development of supersonic combustion along the jet.

Also a magnification of the lower plume is presented, showing how supersonic combustion interacts with the turbulent eddies generating from the walls. And how combustion, generated at walls, gradually covers all of the plume within the supersonic flow.

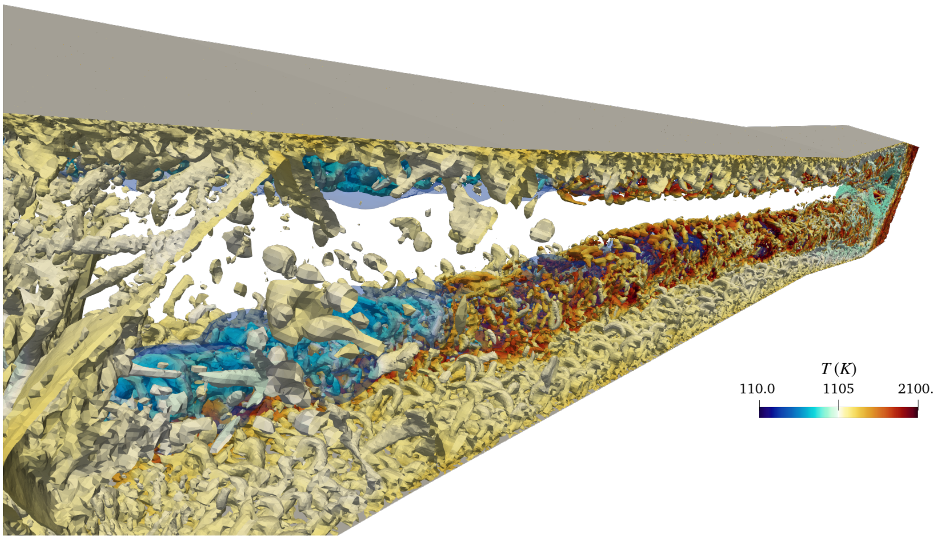

Figure 5.92: Case 4, modified mesh, magnified Q-criterion colored by temperature and semi-transparent blue-colored hydrogen contour

Chapter 6

Conclusion

> ***« Le vent se lève, il faut tenter de vivre. »***
>
> *"The wind is rising; we must try to live."*
>
> ***Paul Valéry,*** **Le Cimetière marin, 1920**

In the present work, a numerical investigation (CFD) of the dual-mode ramjet combustor (DMRJ) tested at ONERA LAERTE, within the LAPCAT-II European project aiming to reduce antipodal flights duration, was carried out.

The hydrogen-fueled DMRJ tested is an engine that transitions from ramjet (subsonic combustion) to scramjet (supersonic combustion) to retains high efficiency in high-speed cruise conditions.

A first part of this work involved a 2D numerical campaign, for both familiarize with OpenFOAM and gain new insights (Sec. 5.1). A chemistry-accelerator (CCM, Par. 5.1.4.0.1) was also tested, providing remarkable improvements with a proper cells clustering, but for a more detailed investigation, a more high-fidelity 3D simulation was deemed necessary.

To do so, non-reactive and reactive LES simulations have been carried out (Sec. 5.2) and compared based on the experimental campaign.

In order to increase the physical fidelity compared to previous studies, a radiation model was implemented (P1, Subsec. 4.1.6) coupled with a one-dimensional conjugate heat transfer boundary condition (1D CHT BC, Par. 4.2.3.0.4), providing a detailed thermal characterization at the walls without explicitly solving the solid domain.

Radiation modeling is important in combustion, as maximum temperature could be very high (> 2000 $[K]$) and induced heat-fluxes could alter the main flow features and properties.

An accurate prediction of wall thermal loads is important for the design of such high-speed engines, where there is a complex intertwinement between structural, aerodynamical and thermal aspects, the latter being the main design-driver.

Both quantitative wall measurements and more qualitative visualizations were compared. For the non-reacting (Subsec. 5.2.1) and subsonic reacting mode (Subsec. 5.2.2), the investigation was a success, providing excellent agreement and proper high-fidelity visualization, especially in predicting the near injection features.

Regarding the supersonic combustion shock-induced mode (Subsec. 5.2.3), the desired configuration was not fully reached in the available simulation time, but provided novel insights about combustion mode transition from subsonic to supersonic (App. D).

For the three cases studied, the modeling employed gave the opportunity to study the interactions of compressible, turbulence and combustion effects, and further highlighted the important influences induced by radiation modeling coupled with a thermal characterizations of the walls.

The high-fidelity thermal characterizations newly proposed, have been compared between the three cases, underlying the importance of radiation modeling and how the wall thermal conditions affect main flow features.

From the validated non-reacting and subsonic combustion mode investigations, further investigations will be carried out to better capture and address the supersonic combustion mode features.

Appendix A

2D, RANS, flow development

In this appendix, the development of the 2D flow is reported.

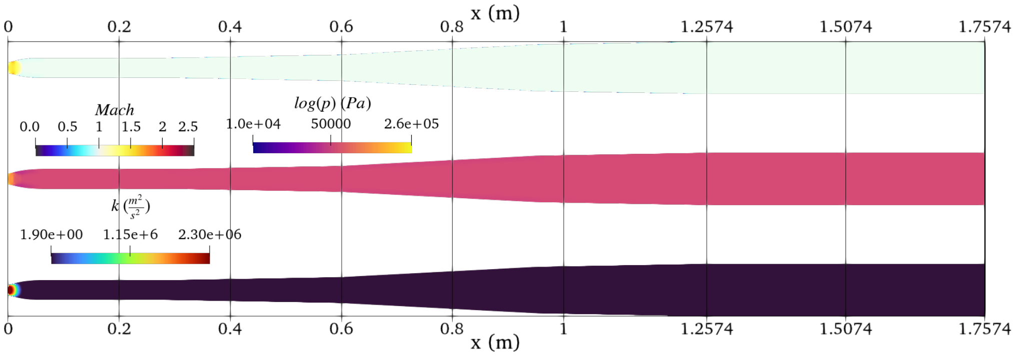

Figure A.1: 2D, flow development, t=0.00001 [s]

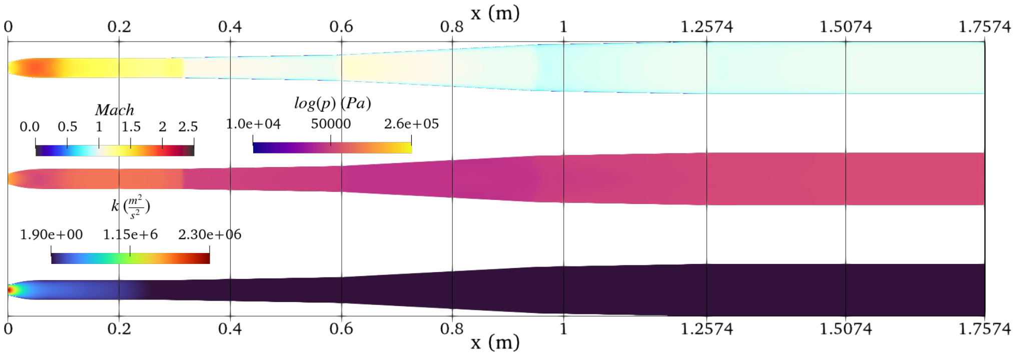

Figure A.2: 2D, flow development, t=0.00021 [s]

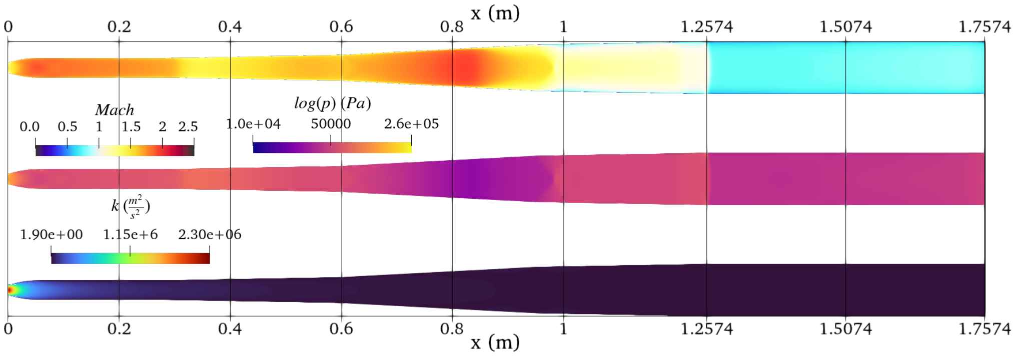

Figure A.3: 2D, flow development, t=0.00087 [s]

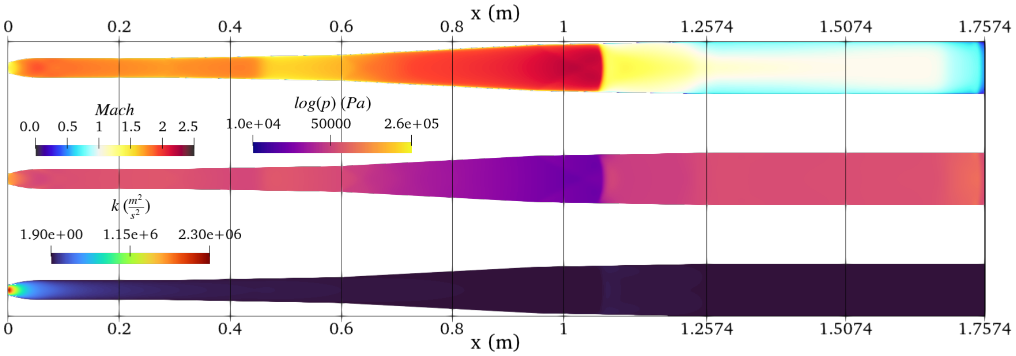

Figure A.4: 2D, flow development, t=0.00126 [s]

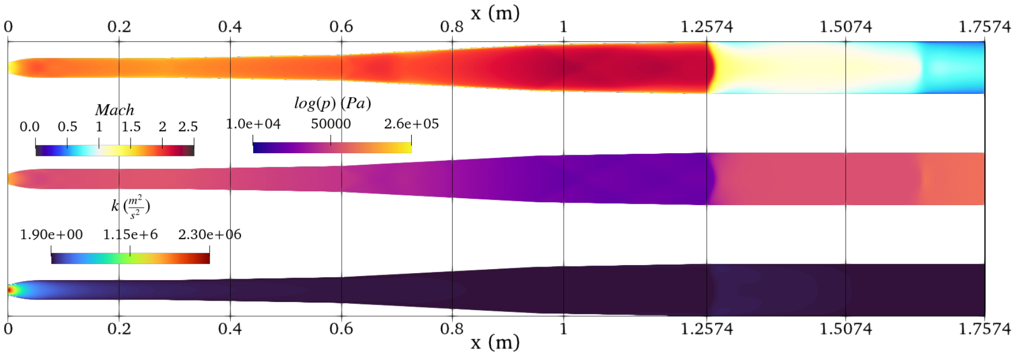

Figure A.5: 2D, flow development, t=0.0018 [s]

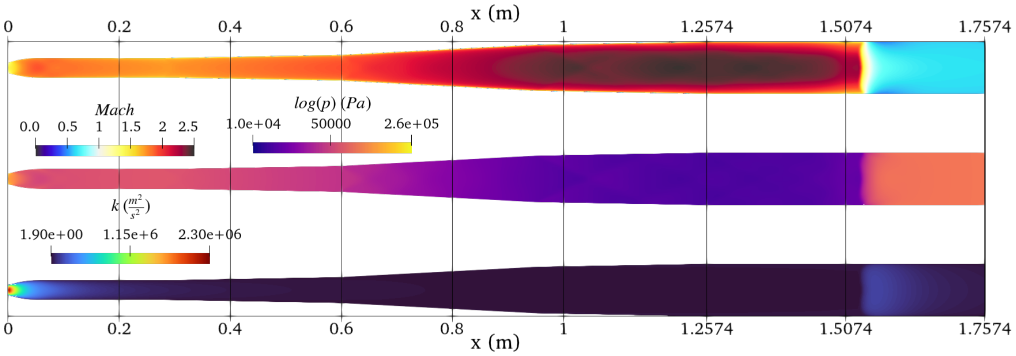

Figure A.6: 2D, flow development, t=0.003 [s]

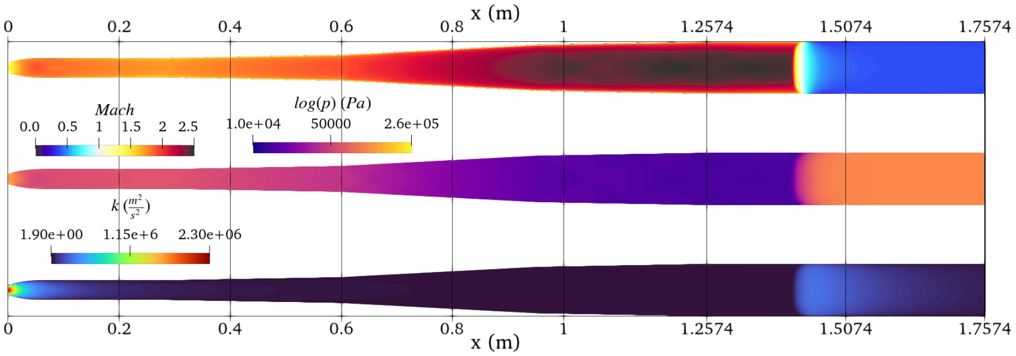

Figure A.7: 2D, flow development, t=0.008 [s]

Appendix B

2D, RANS, case evolution from non reacting to reacting

In this appendix, the evolution from non-reacting to reacting is presented for the 2D RANS simulation in Sec. 5.1. To ease the interpretation, the non reacting case is supposed to be time zero, indicated with t_0, meanwhile t' represents the time right after the new zero time.

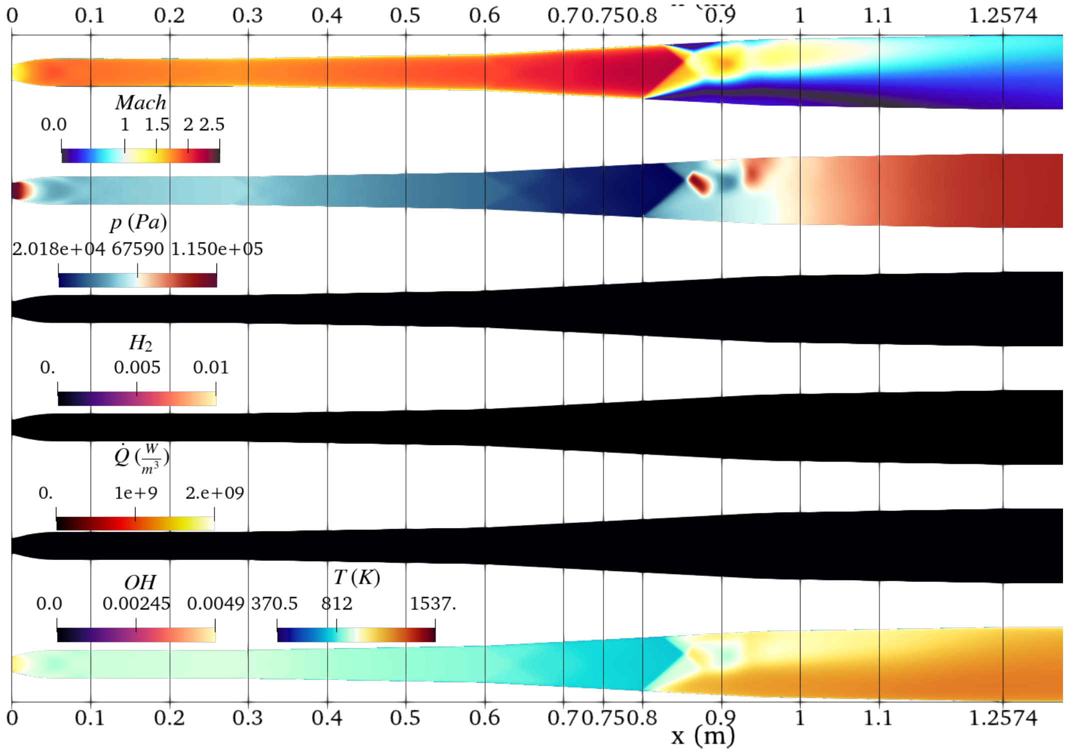

Figure B.1: 2D, RANS evolution, t_0=0 [s]

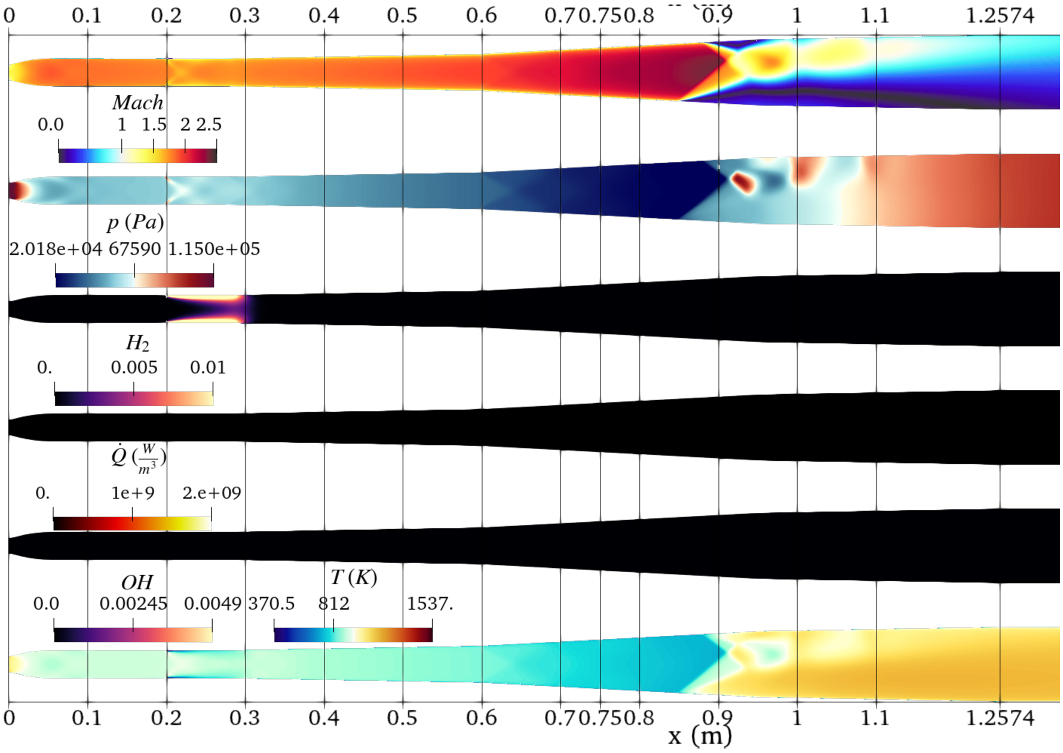

Figure B.2: 2D, RANS evolution, t'=0.0001 [s]

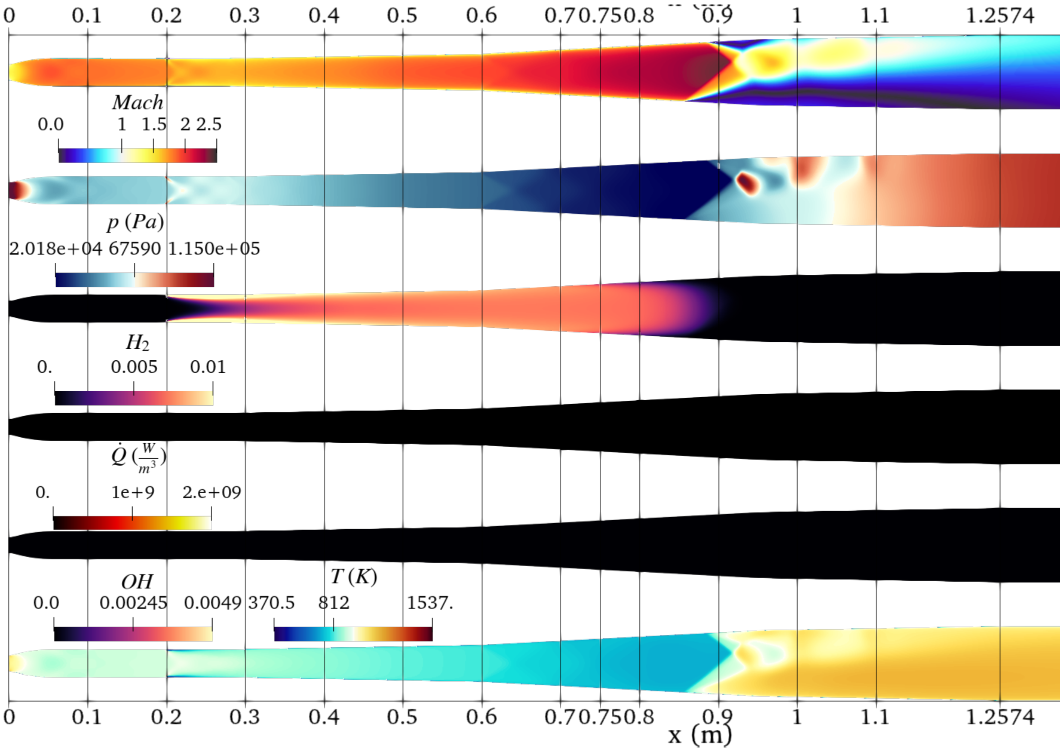

Figure B.3: 2D, RANS evolution, t'=0.0006 [s]

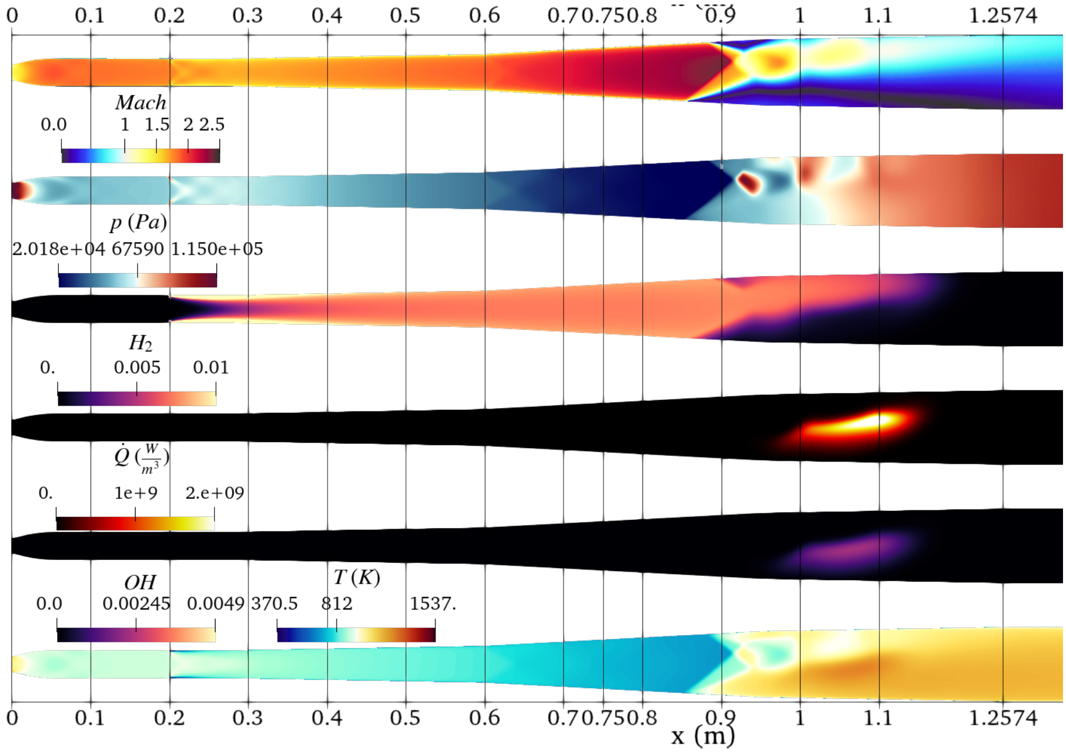

Figure B.4: 2D, RANS evolution, t'=0.001 [s]

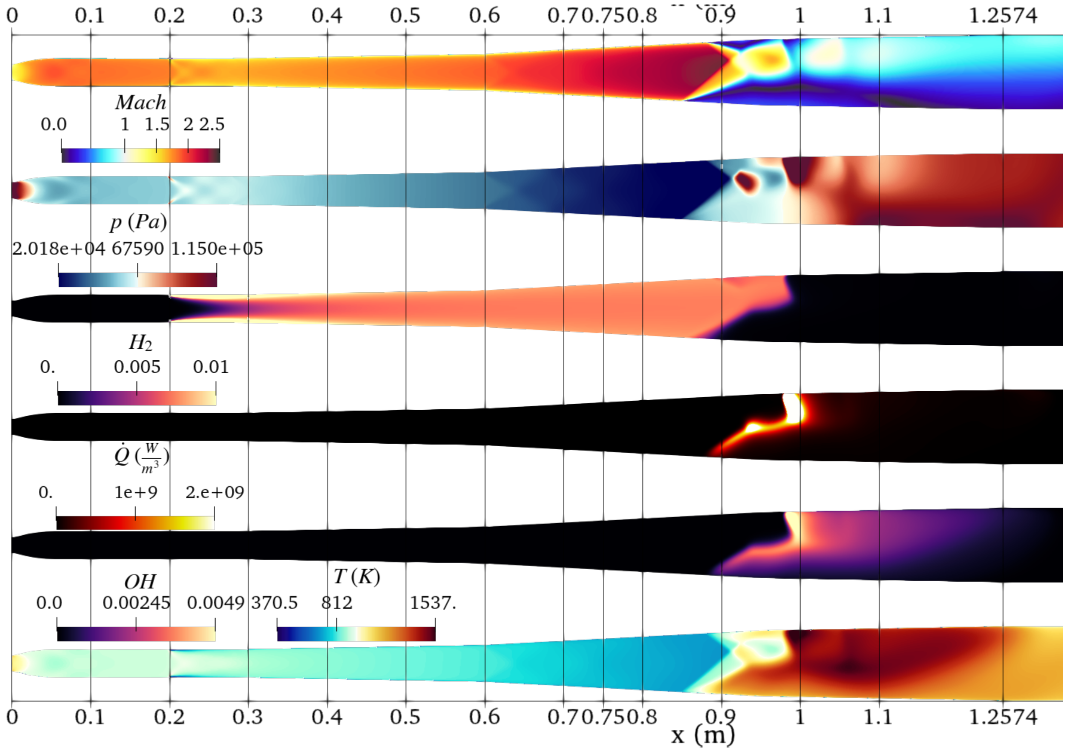

Figure B.5: 2D, RANS evolution, t=0.0012 [s]

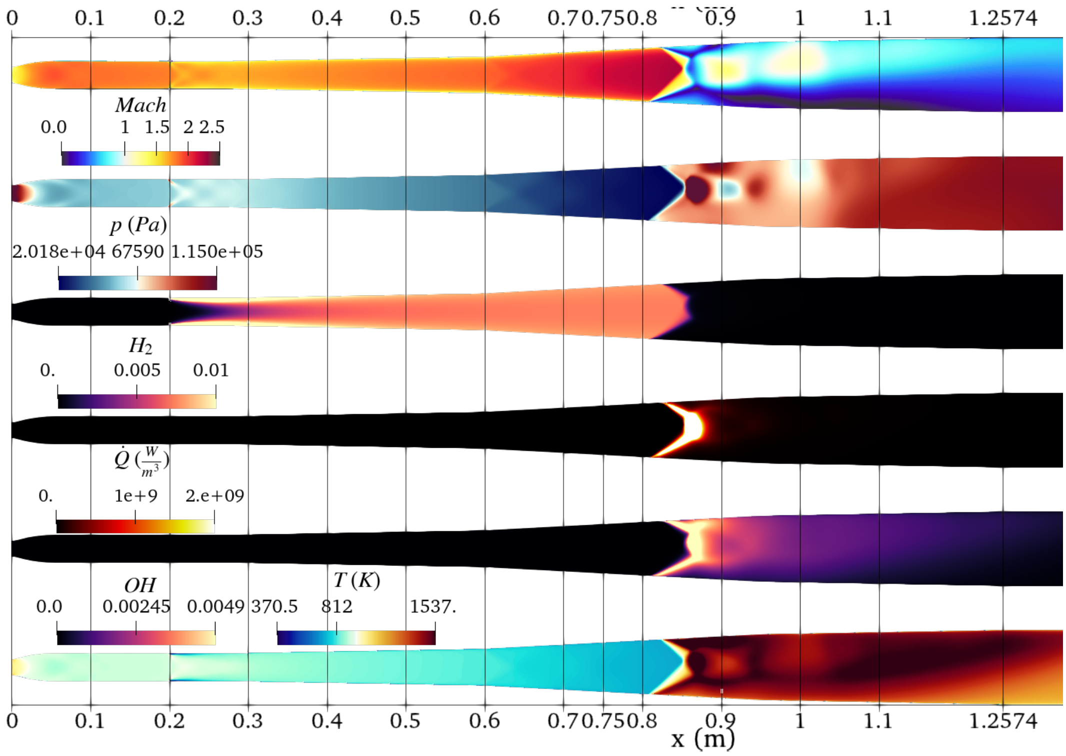

Figure B.6: 2D, RANS evolution, t=0.0015 [s]

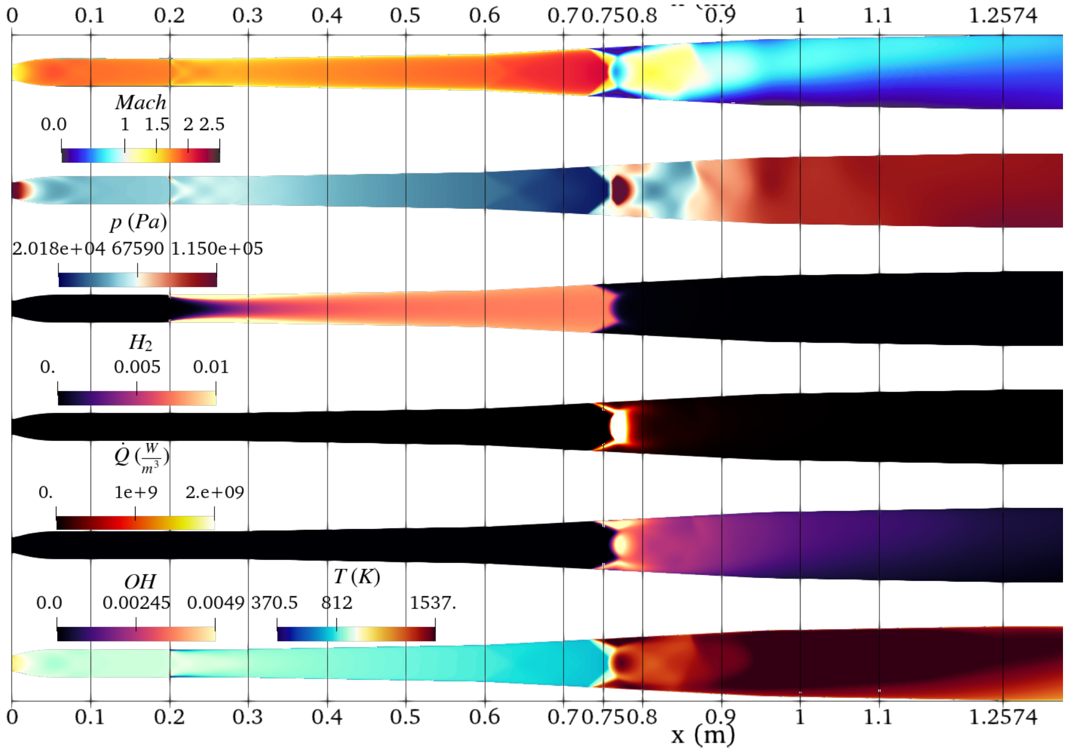

Figure B.7: 2D, RANS evolution, t=0.0019 [s]

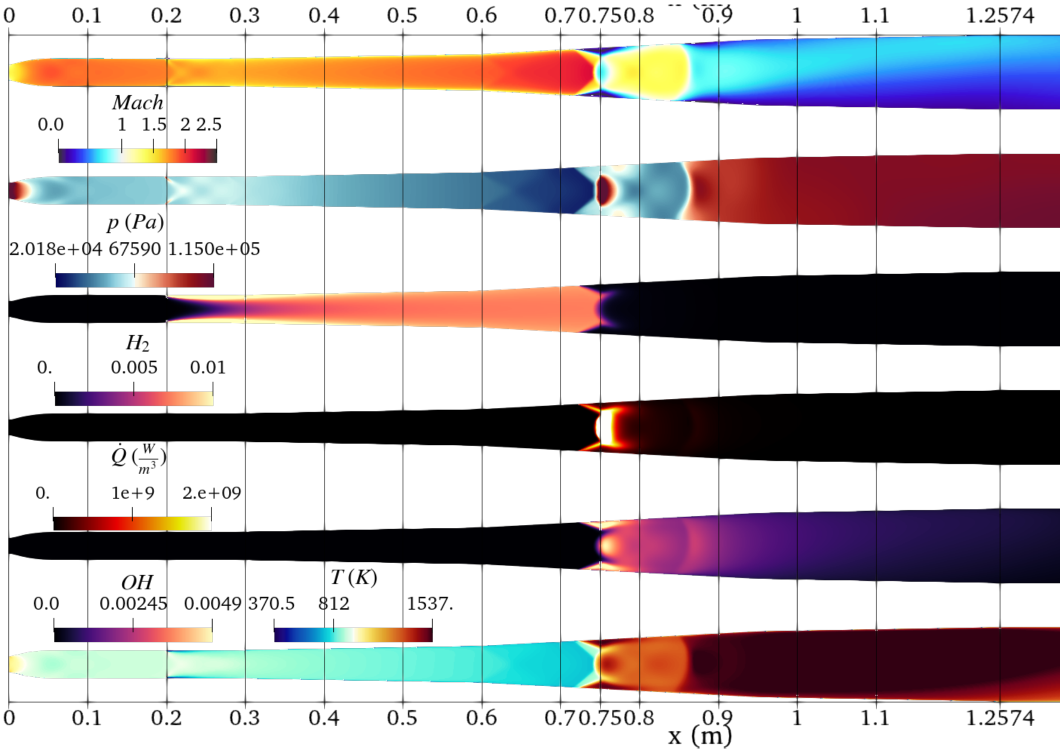

Figure B.8: 2D, RANS evolution, t=0.0022 [s]

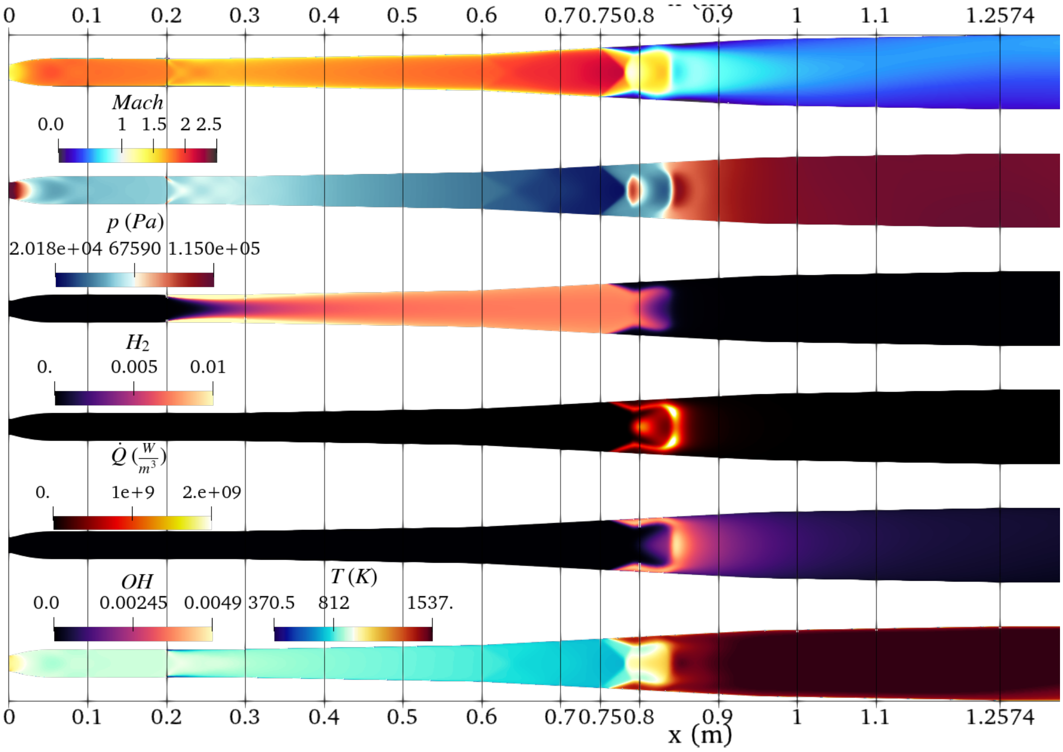

Figure B.9: 2D, RANS evolution, t=0.0027 [s]

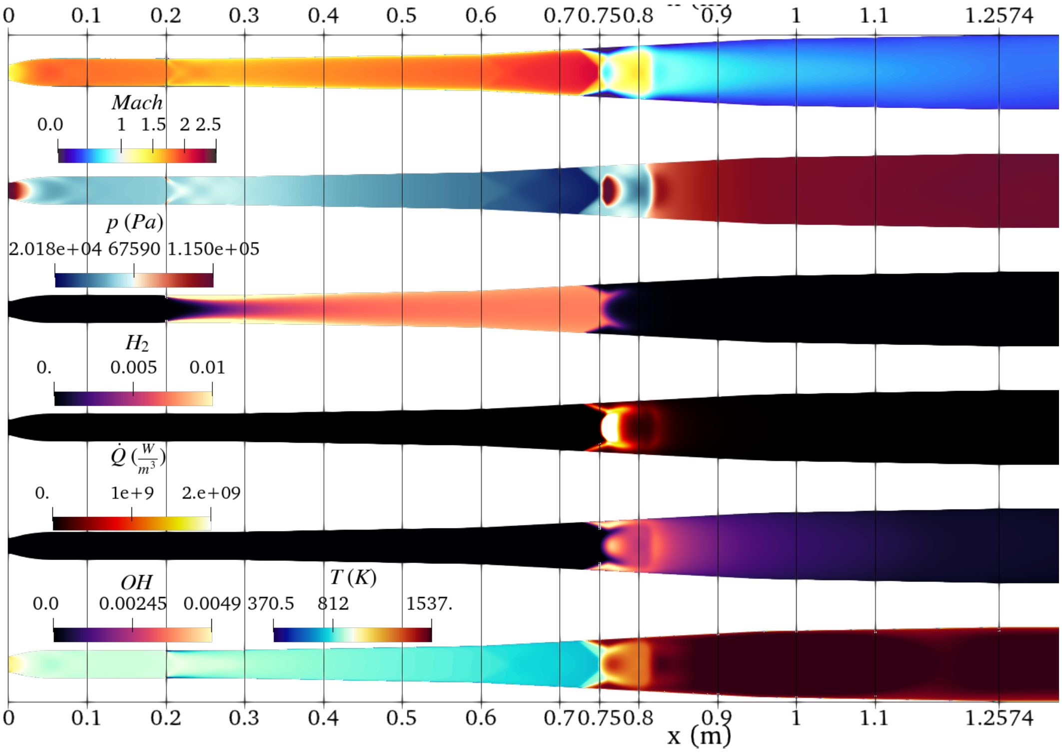

Figure B.10: 2D, RANS evolution, t=0.0036 [s]

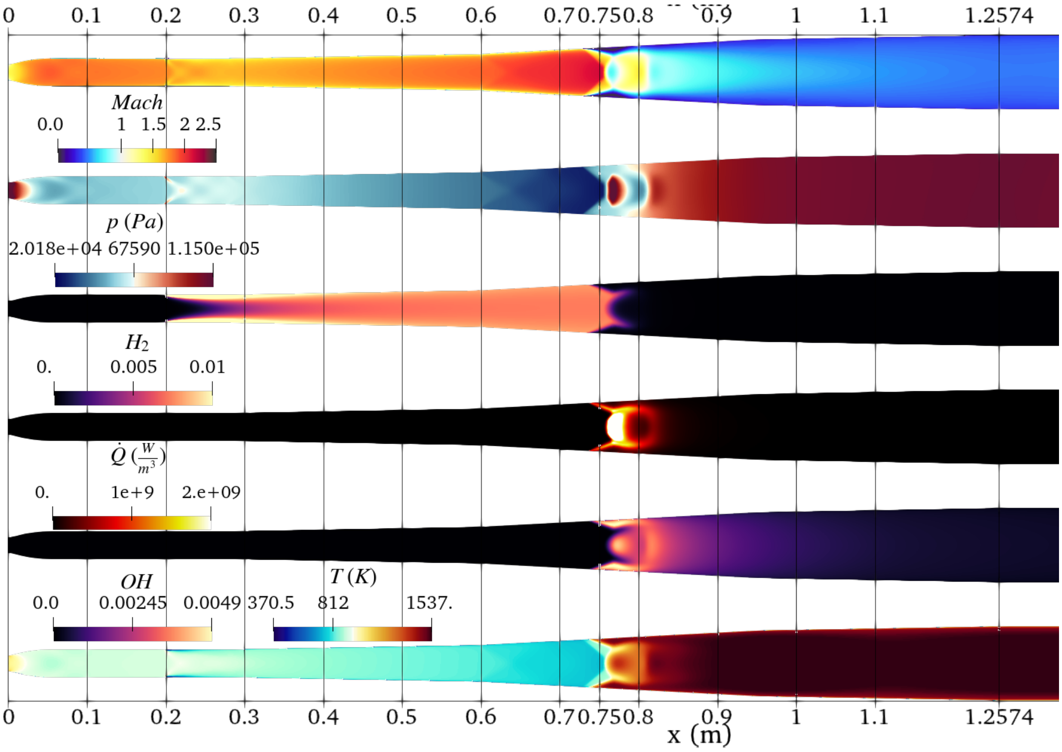

Figure B.11: 2D, RANS evolution, t=0.0046 [s]

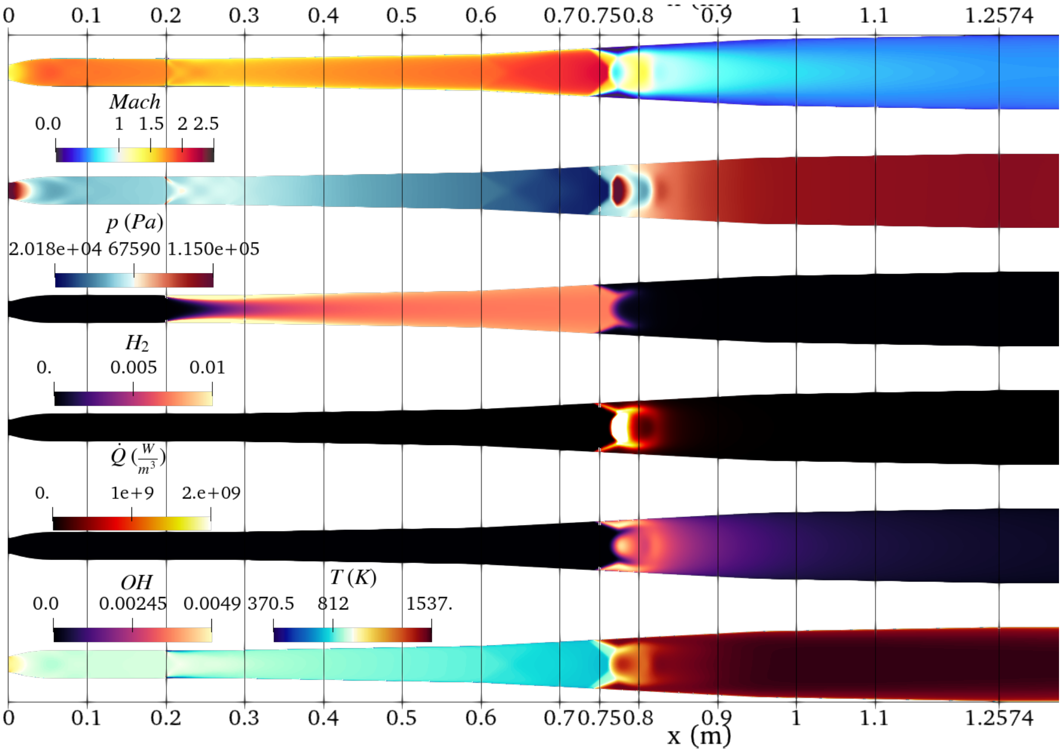

Figure B.12: 2D, RANS evolution, t=0.0066 [s]

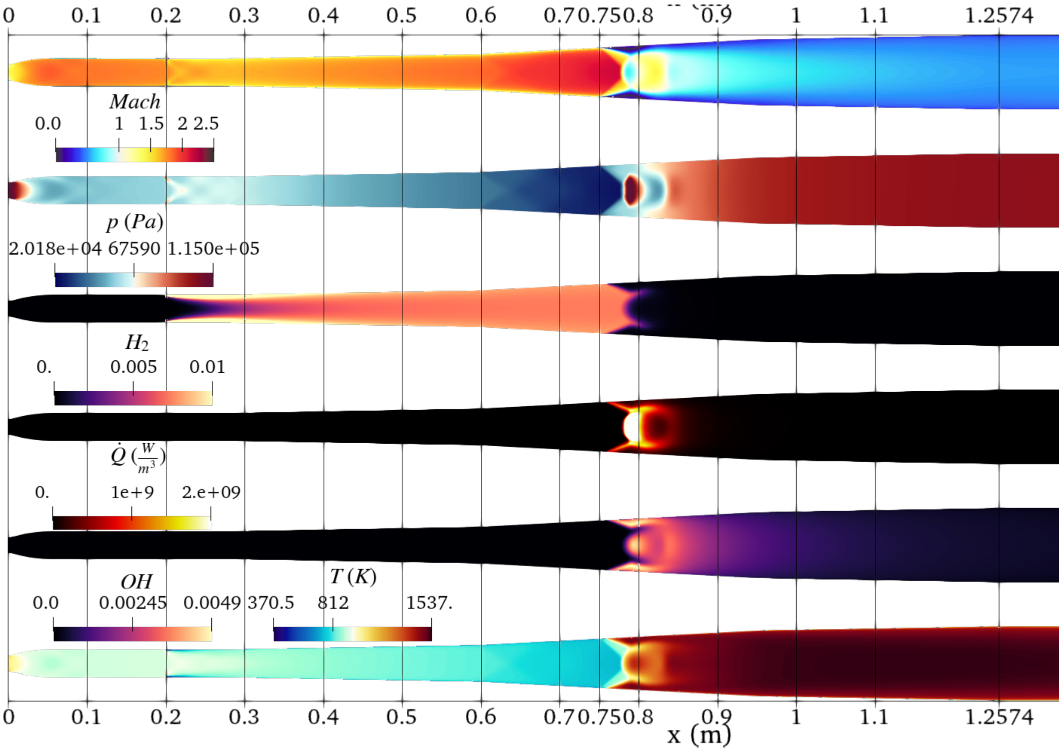

Figure B.13: 2D, RANS evolution, t=0.0072 [s]

This set corresponds to the values of Mach number, pressure, hydrogen mass fraction, heat-release, OH mass fraction and temperature. After fuel injection, the separation zone moves downstream until the fuel's plume reaches it. The system ignited when the plume reaches the temperature and pressure region after the separated zone. By looking at heat-release the flame appears to be generated in the center of the flow and then propagate both upstream and downstream in the subsonic region engulfing the space between the walls, up until the separation points, where further oscillations back and forth of the shock system are observed. There is also an intermediate change of the shape of the flame prior reaching the final configuration. The pressure fields highlight the formation of shockwaves as a result of hydrogen injection.

Unfortunately, drawing quantitative conclusions in ignition is not possible due to the lack of experimental data in that regard and the non-physicality of the 2D case. After a transient, the separation regions seem to be symmetric respect to the upper and lower separation points. Compared to the non-reacting one, the increased back pressure due to heat-release seems to be moving upstream the separated region as also reported in the experiments. [3]

The Mach number shows that by the exit of the real chamber, located at an axial position of 1.2574 [m], the flow is subsonic. The H_2 mass fraction instead shows that, even if the jet penetration is not very high, the high turbulence level diffuses the fuel until the combustor height is filled, while after injection, less than 1 [ms] is needed to reach the reactive region.

Appendix C

3D, modified mesh, comparison of different convective heat transfer coefficient for the non reacting case

In this appendix, a comparison of different convective heat transfer coefficients, h, for the 1D CHT BC of the non reacting case is presented. This is necessary to assess the validity of a statistical comparison regarding the non-reacting case, case 0 (Subsec. 5.2.1), and the subsonic reacting case, case 1 (Subsec. 5.2.2). The latter employed a different choice of parameters in order to remove numerical instabilities in the walls, reported in Fig. 5.57. A table is reported depicting the parameters chosen. An extensive discussion of their choices is reported in Par. 5.2.1.0.1. For the new case, 20 $[\frac{W}{m^2K}]$ and 25$[\frac{W}{m^2K}]$ for bottom and top wall patches are chosen.

Patch	**h** $[\frac{W}{m^2K}]$	T_a [K]	emissivity [-]	YSZ thickness [m]	Cu alloy thickness [m]	k_{YSZ} $[\frac{W}{mK}]$	k_{Cu} $[\frac{W}{mK}]$
Top	15 or 25	293.15	0.7	0.00028	0.066	1.3	340
Bottom	10 or 20	293.15	0.7	0.00028	0.066	1.3	340

Table C.1: Case 0, modified mesh, parameters for *externalWallHeatFluxTemperature*

Going in more depth with the different parameters chosen, it is worth to look at possible differences between the predicted temperature in both bottom and top patch regarding the choices made. Here, the temperatures (instantaneous and mean) from the top and bottom patches are presented. Qualitatively, they seem similar regarding overall trends, except small differences of the axial coordinate of the separation front. Also, the peak and lower values are different.

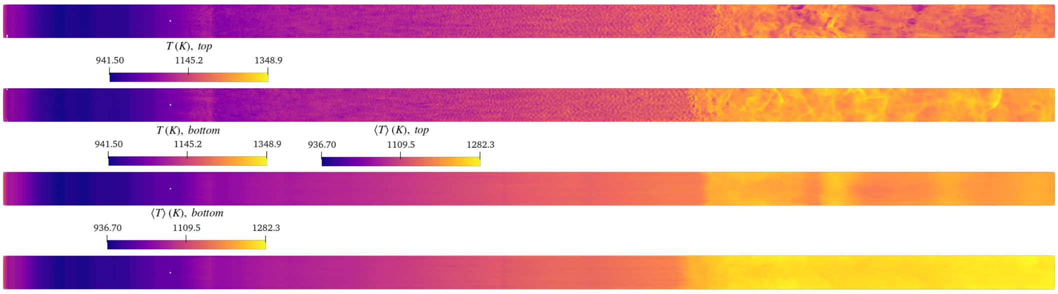

Figure C.1: Case 0, modified mesh, wall temperatures for h of (25,20) $[\frac{W}{m^2K}]$

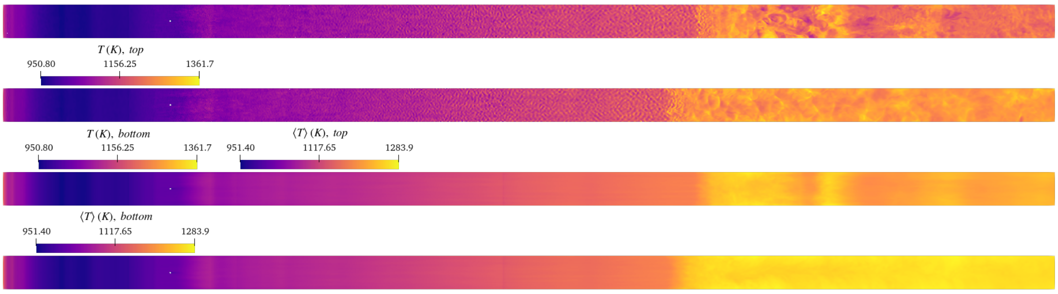

Figure C.2: Case 0, modified mesh, wall temperatures for h of (15,10) $[\frac{W}{m^2K}]$

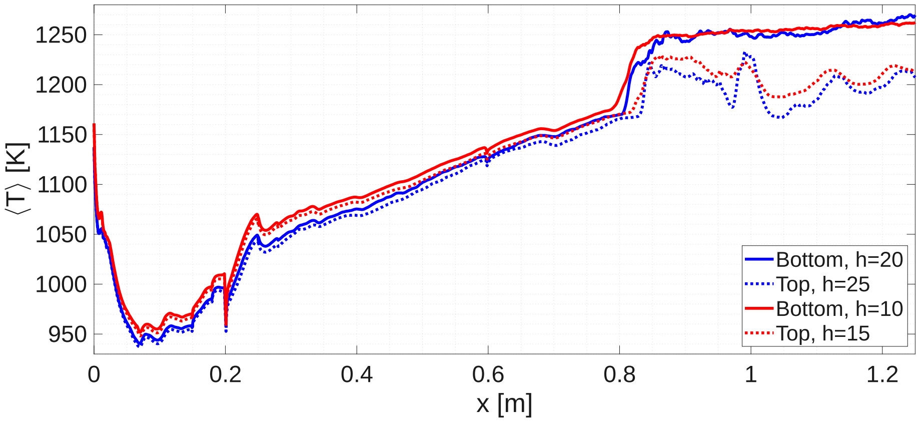

Figure C.3: case 0, modified mesh, mean temperature along the walls mid-line

To have a more quantitative comparison, the distribution of the mean temperature along the mid-line of the wall patches was presented. Looking first within the same pair chosen, it appears that coherently with the parameters picked, the bottom wall is slightly hotter compared to the top wall. After the separation region, oscillations are present due to unsteadiness of the eddies impinging the walls, imposing strong oscillations. In particular the top walls has more strong oscillations due to the bulk supersonic flow impinging the upper wall, that also shift the mean values with its impingement. The down-facing spikes represented at 0.2 [m] are due to the separated flow in the injectors.

As for the different set of parameters, it follows straightforwardly that a lower h means higher temperature values, meanwhile the separation points appears to be approximately in the same position, with the hotter walls with the tendency of anticipating the separation, as predicted by the theory about having a more unstable boundary layer if heated up.

To have a picture on how the complex compressible and turbulent structures influence the heat fluxes, and in turns temperature, a comparison of instantaneous temperature, *wallHeatFlux* [1], radiative heat flux q_r and net radiative term $G - \sigma T^4$ is displayed. The net radiative term is the difference of incident radiation G and local emissivity with the assumption of black body emission σT^4, which is the maximum possible, since local emissivity is assumed unitary.

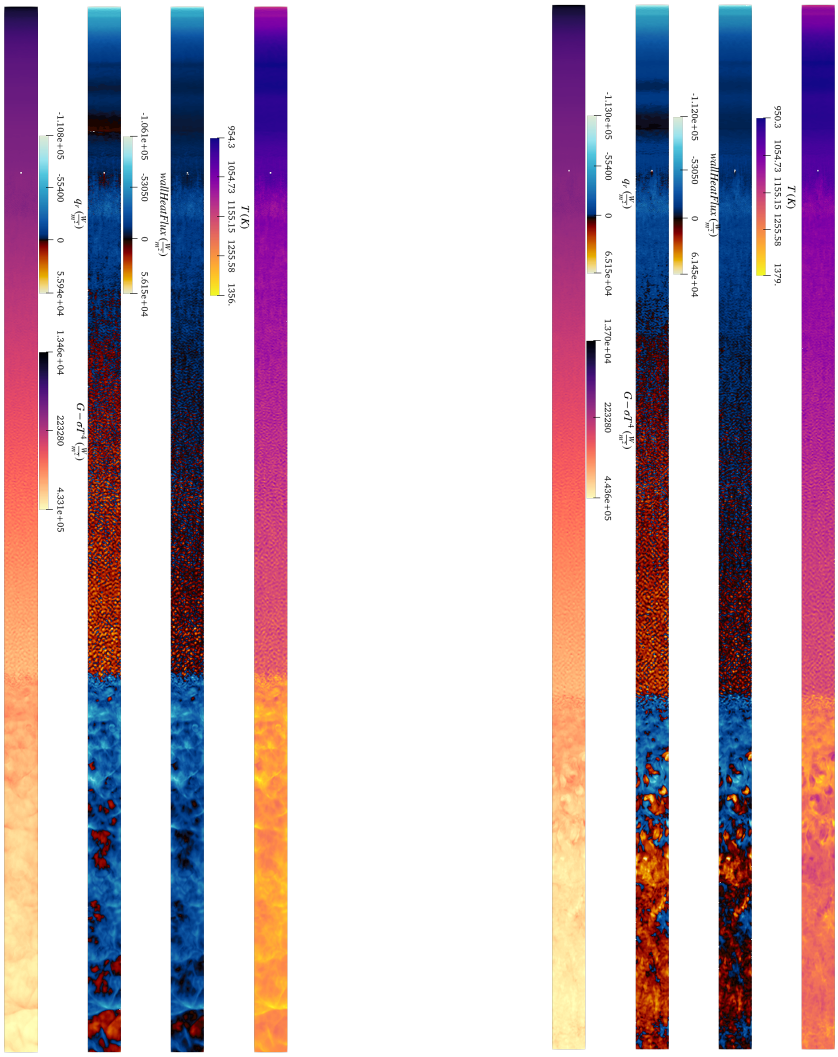

(a) Bottom wall patch **(b)** Top wall patch

Figure C.4: Case 0, modified mesh, instantaneous wall values for temperature, *wallHeatFlux*, radiative heat flux and net radiative term for h of (15,10) $[\frac{W}{m^2K}]$

---

[1] Convective heat flux for a bug [53]. Instead of the sum of convective heat flux and radiative heat flux

About the sign convention of the heat fluxes in OpenFOAM, which is related to the relative orientation of the dot product:

- Positive: heat from the wall to the fluid;
- Negative: heat from the fluid to the wall.

Those patch values, exhibit a strong correlation between turbulent structure and thermal heat fluxes. It is shown how the corrugated values due to highly turbulent flow, produce over and undershooting of heat flux values. In the separated region, the top patch a positive heat flux zone, corresponding to the supersonic wall impingement from the bulk flow bias, as visible in Fig. 5.25.

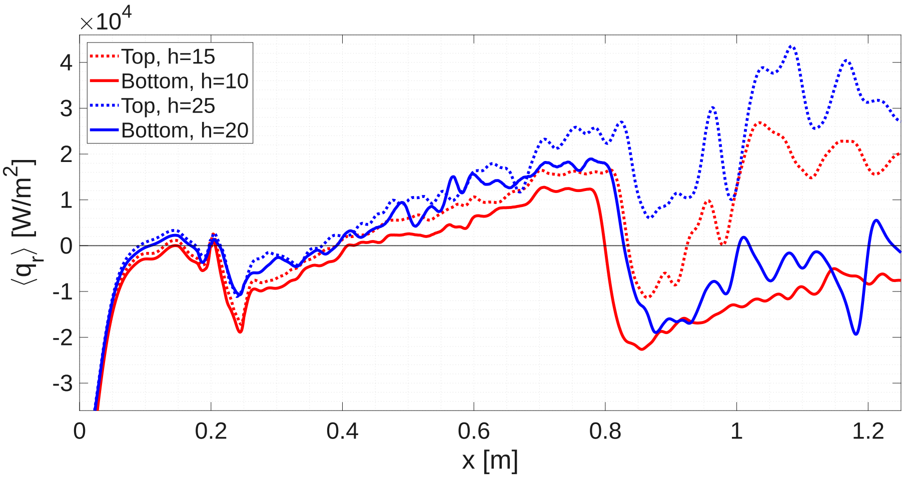

Figure C.5: case 0, modified mesh, mean radiative heat flux q_r along the walls mid-line

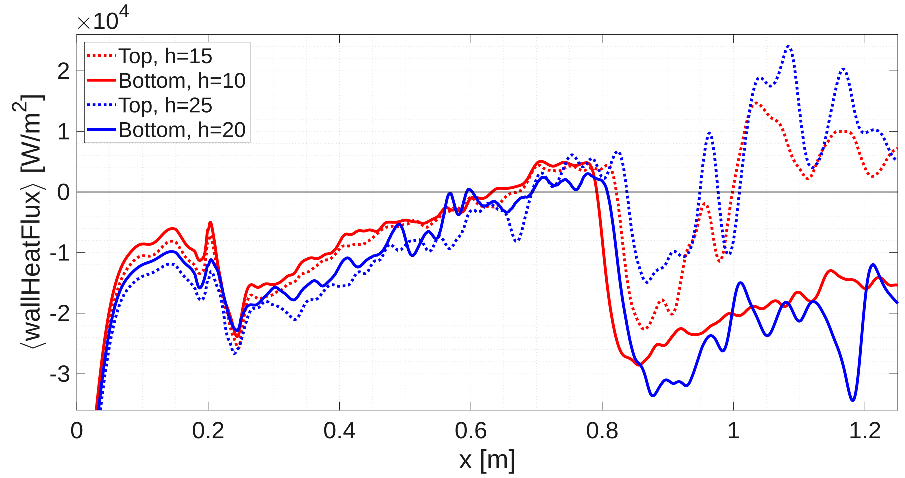

Figure C.6: Case 0, modified mesh, mean *wallHeatFlux* along the walls mid-line

To investigate more quantitatively the differences in the heat fluxes, the mean values for each set of parameters are presented plotted against the mid-line axial coordinate of the chamber. The net radiative term, in Fig. C.5, shows that typically, higher h values means higher radiative fluxes, hinting at hotter walls. In both cases, and between top and bottom wall, they display comparable values in the first part of the combustor. The differences accumulates progressively until separation.

After that, the who different set of h values exhibit comparable fluxes for the bottom patch, while for the top patch higher fluxes are observed for higher h values, while the overall oscillations are induced by the bulk flow wall impingement. As for the mean *wallHeatFlux* (convective), the trends closely follows the radiative heat flux, while also displaying similar values, hinting that its contribution is important in estimating wall thermal loads. Up to the separation regions the behavior is similar: up to ∼0.7[m], the walls are heated by the fluid due to the strong wall shear stress from the hot turbulent flow expansion, with a tendency to a sign inversion for the supersonic expansion of the bulk supersonic flow. After separation, the high-speed flow brought to rest, presents high temperature, and heat is absorbed by the walls. The sole exception is represented by the upper patch: since the separation regions present a bias towards the upper patch, the supersonic flow impinges the wall, being responsible for a large variation towards the chamber exit. For *wallHeatFlux*, this relatively cold and expanded flow, absorbs heat from the walls as prior flow separation.

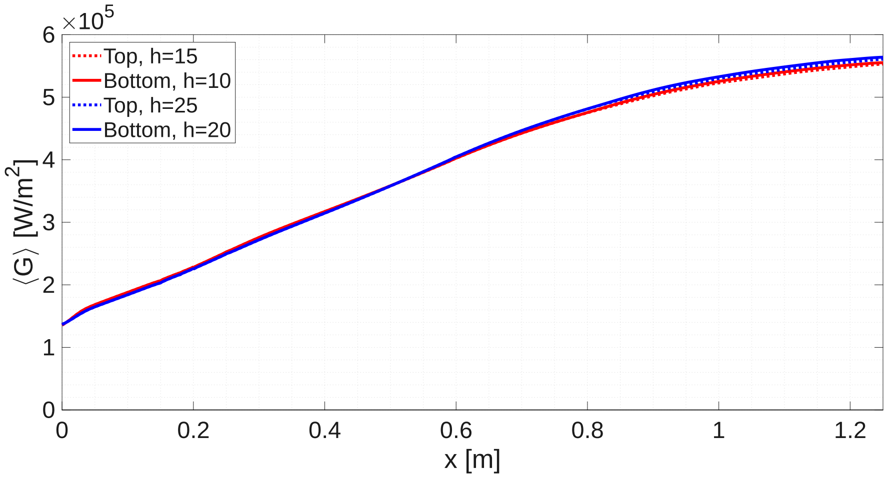

Figure C.7: case 0, modified mesh, mean incident radiation G along the walls mid-line

The incident radiation from the radiation model present almost identical values, showing little dependence from the boundary conditions parameters. Most of the minor changes are related to the separation zones, affected by different temperature and heat fluxes.

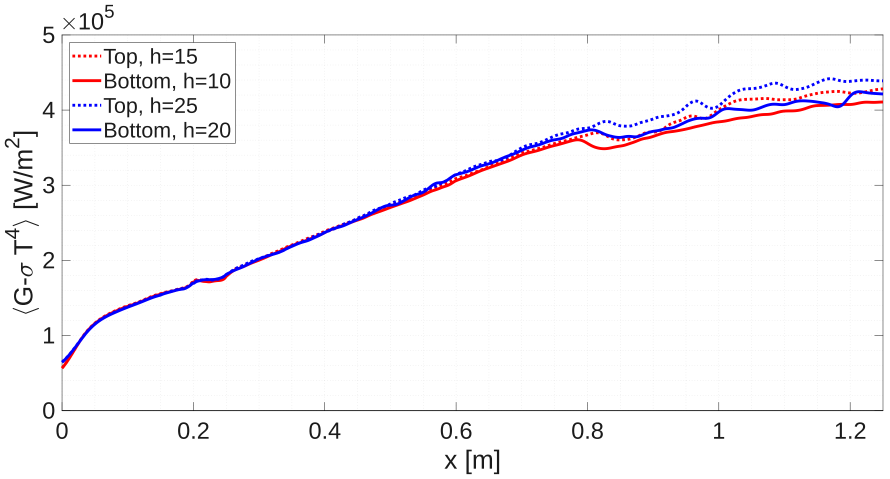

Figure C.8: Case 0, modified mesh, mean net radiative term $G - \sigma T^4$ along the walls mid-line

Finally, the mean net radiative term plot along the wall patches mid-line is presented. Some minor changes are observed in the separated region both position and values, coherently with the aspects discussed above.

It can be concluded that the sensibility on the chosen parameters appears to not be dramatic, based on the monitored mean values, and probably the numerical stability observed in Subsec. 5.2.2 are only due to the low wall resolution. Minor changes are observed near the separation regions, quantified in slopes of the quantities and in the exact position, in accordance with theoretical results. However, the comparison carried out in Subsec. 5.2.2 for case 1, was done with the same set of h values, for consistency and to avoid unexpected variations. Nevertheless, a small assessment of the sensibility of the 1D CHT BC h parameter was carried out.

Appendix D

3D, modified mesh, subsonic to supersonic combustion transition

In this appendix, the evolution of the combustion mode from subsonic (case 1) to supersonic (case 4) is reported. To ease the interpretation, the snapshot of the reacting case, case 1, is supposed to be time zero, indicated with t_0, meanwhile t' represents the time right after the new zero time. A first evolution set is presented, representing slices in the mid-plane of the combustor chamber for instantaneous temperature, heat release, pressure, OH and H_2O mass fractions. The starting point was randomly chosen from the dataset.

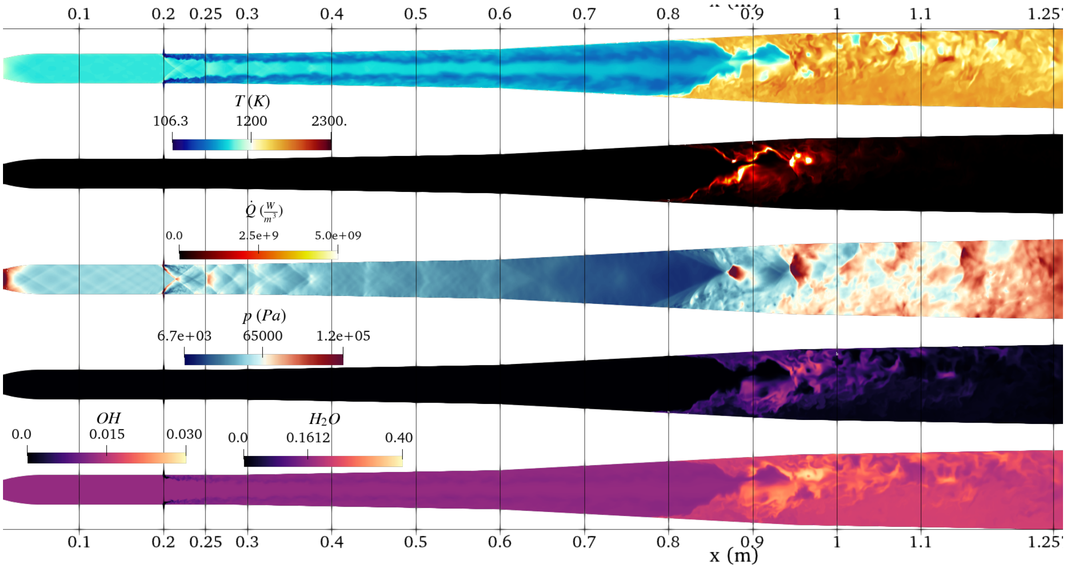

Figure D.1: 3D,subsonic to supersonic combustion mode transition, t_0=0 [s]

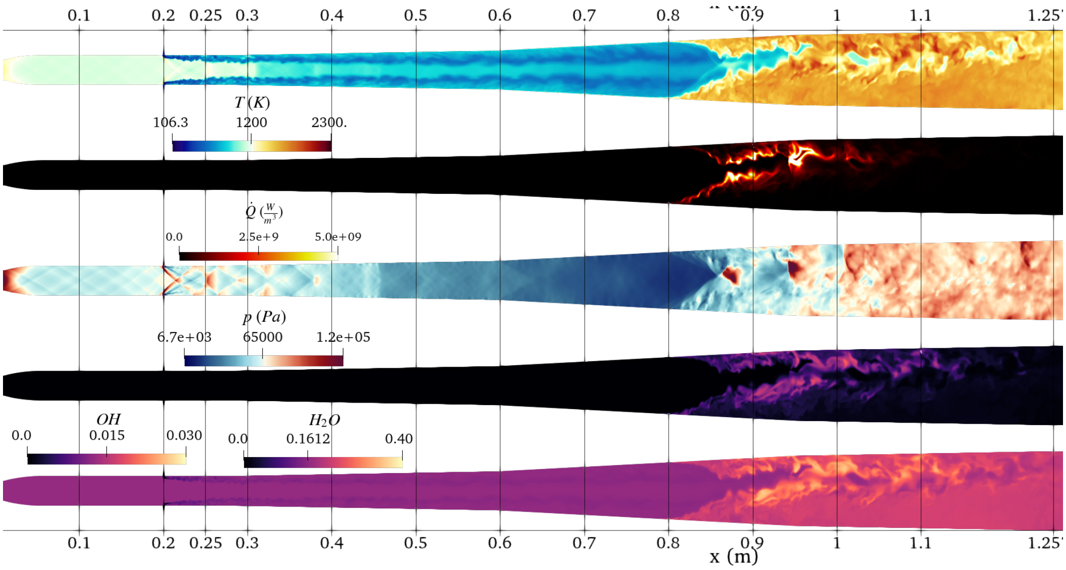

Figure D.2: 3D, combustion mode transition, t'=0.00025 [s]

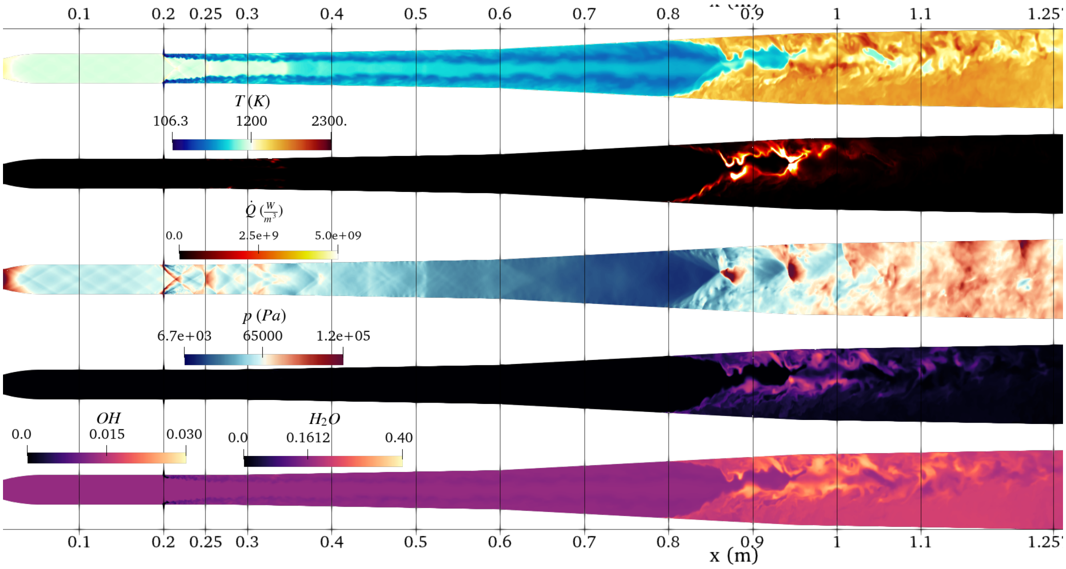

Figure D.3: 3D, combustion mode transition, t'=0.00028 [s]

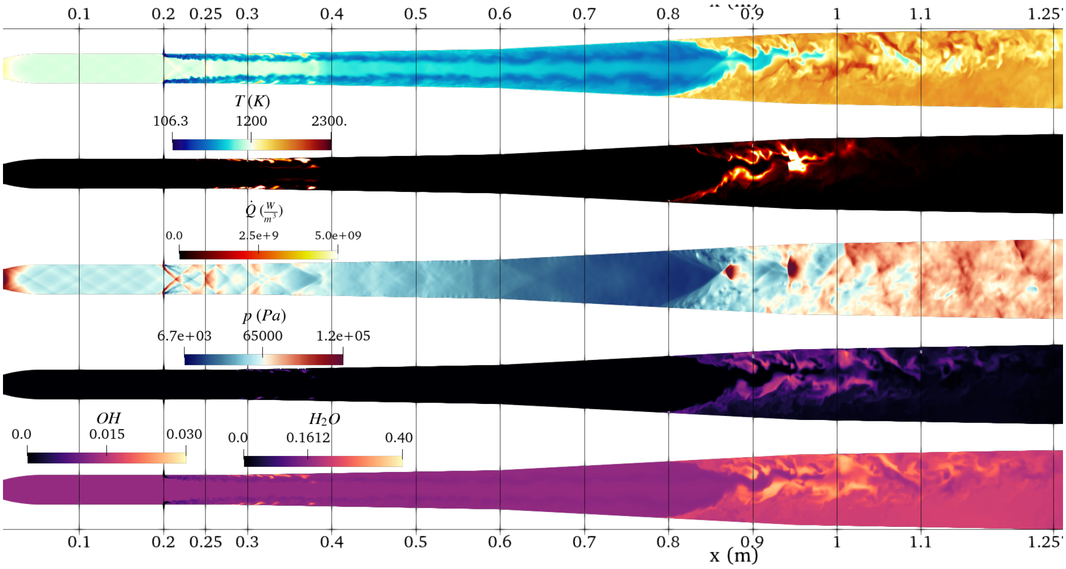

Figure D.4: 3D, combustion mode transition, t'=0.00031 [s]

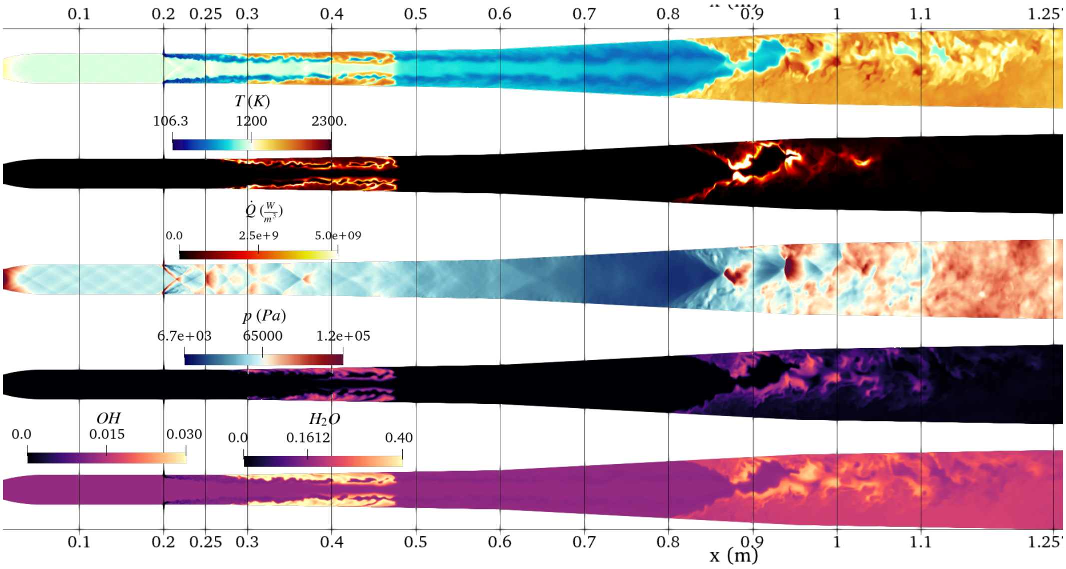

Figure D.5: 3D, combustion mode transition, t'=0.00038 [s]

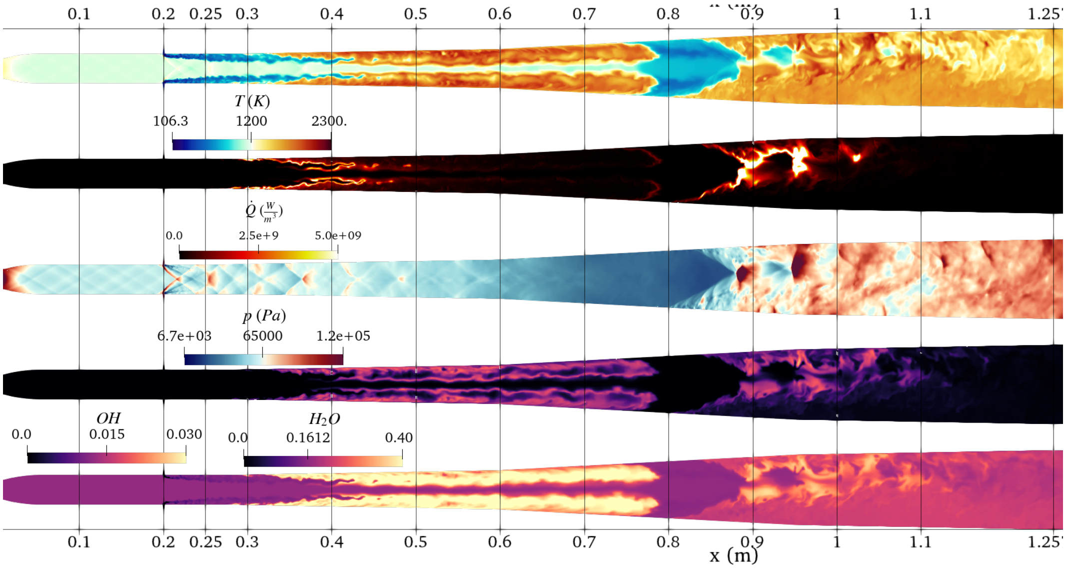

Figure D.6: 3D, combustion mode transition, t'=0.00059 [s]

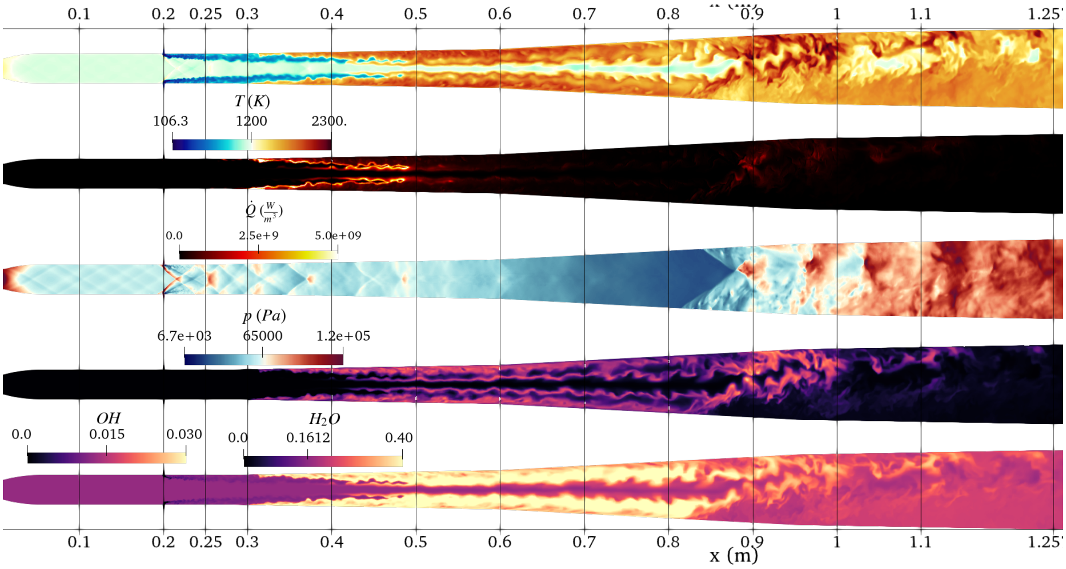

Figure D.7: 3D, combustion mode transition, t'=0.00079 [s]

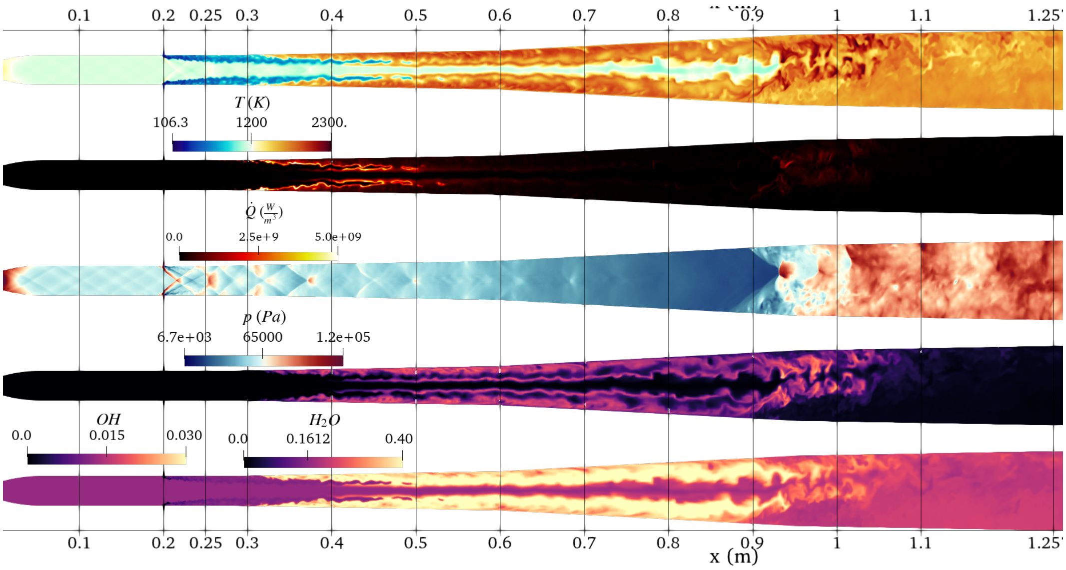

Figure D.8: 3D, combustion mode transition, t'=0.00119 [s]

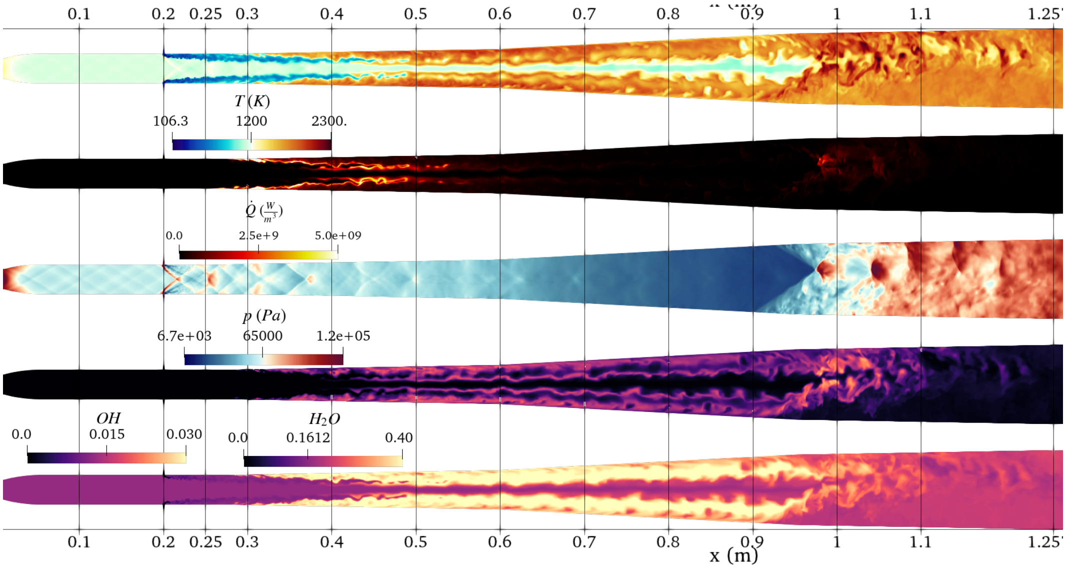

Figure D.9: 3D, combustion mode transition, t'=0.0022 [s]

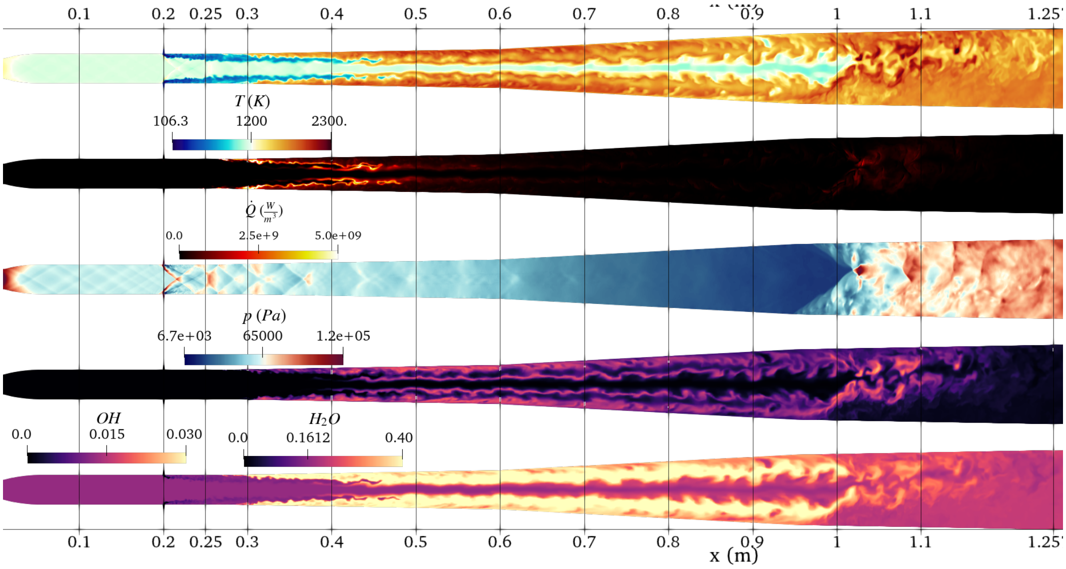

Figure D.10: 3D, combustion mode transition, t'=0.00419[s]

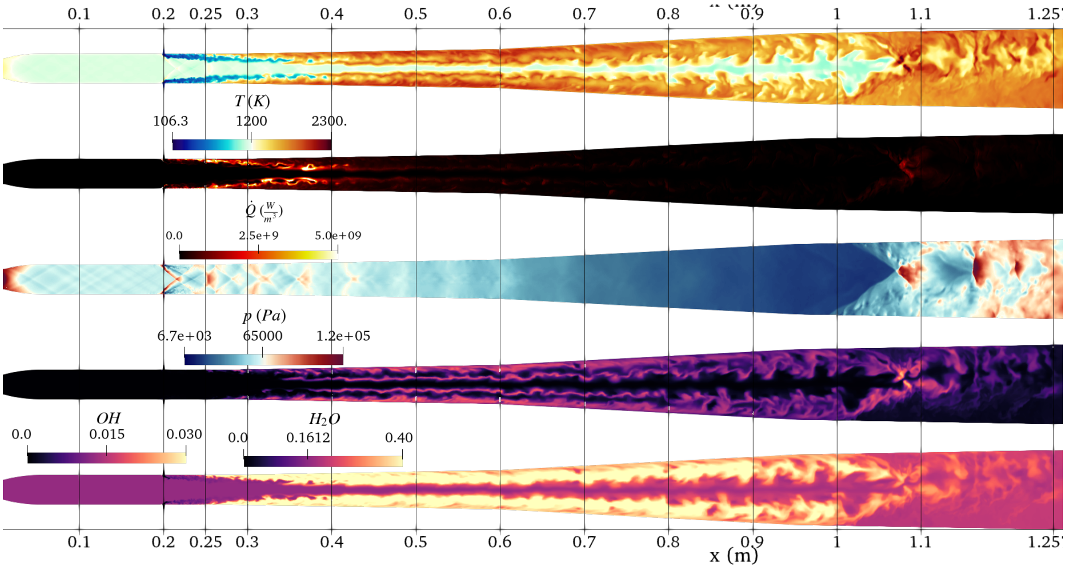

Figure D.11: 3D, combustion mode transition, t'=0.00703 [s]

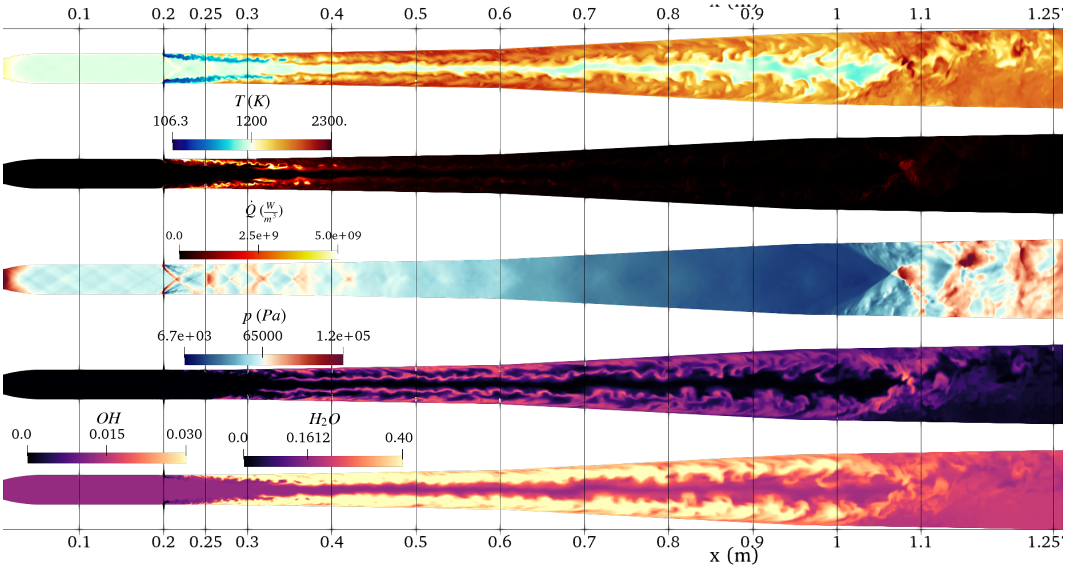

Figure D.12: 3D, combustion mode transition, t'=0.01018 [s]

The mode transition from the subsonic reacting case, is triggered by inlet temperature and pressure values. The disturbance changes the thermodynamic flow properties while being convected downstream, and ignition occurs at ∼0.3 [m] at the bottom and top walls. After that, the flame propagates until all the supersonic plume is burning, before the separation zone. After some time, the anchoring region of the flame display a tendency of crawling towards the injectors, while the new heat-release induced temperature rise causes distortion to the shock-train in the isolator and in the separation zone, now more downstream compared to the subsonic case. The goal was to reach case 4 (described in Tab. 4.1), representing a shock-induced combustion after injection. Unluckily, this configuration was not reached in the simulated time window, however, as also reported [21], a similar configuration needed 2 seconds to develop the desired configuration. Since the total simulationtime was in the order of cents of seconds, probably more time is needed to cause the desired shockwaves and separations variations. A factor that could be revised is also related to the boundary layer prediction near the inlet, where the flow develops from laminar, probably under-estimating the turbulence deriving from upstream parts of the experimental rig, as showed in Fig. 3.3. Temperature and water vapor mass fraction, show a more violent combustion occurring compared to the concentration observed in the subsonic mode, in Fig. 5.67.

Another set, highlights ignition and the slow counter-flow crawling of the flame towards the injectors by representing rescaled values for H_2O_2 and HO_2 mass fraction, heat-release and temperature.

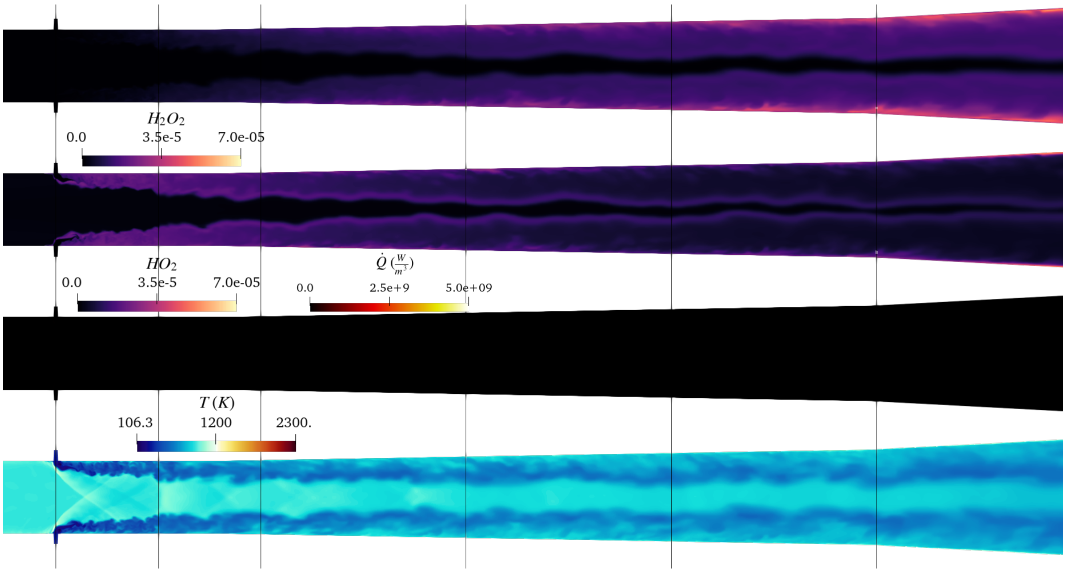

Figure D.13: 3D, supersonic combustion ignition, t_0=0 [s]

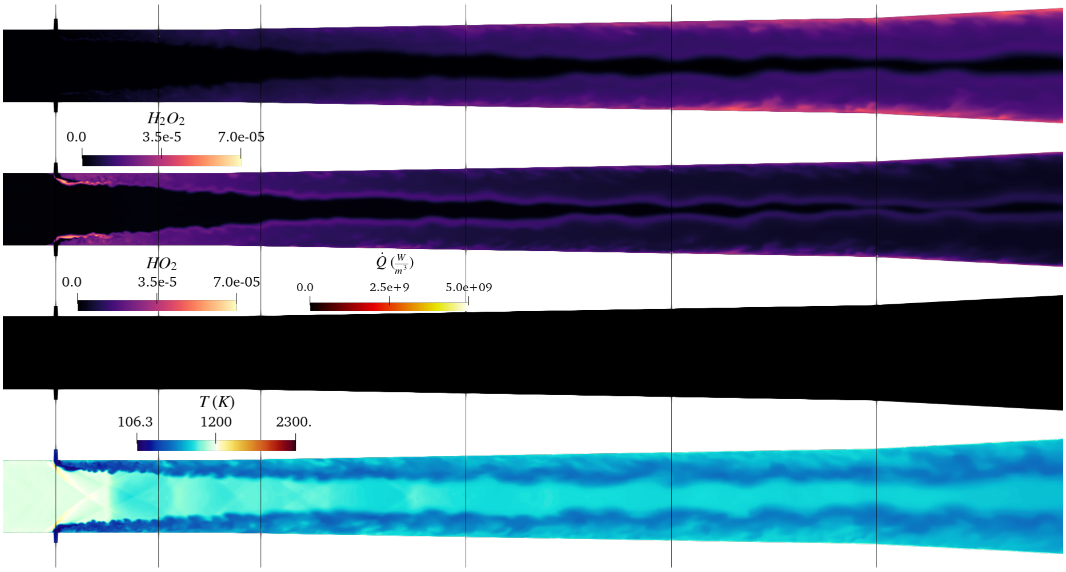

Figure D.14: 3D, supersonic combustion ignition, t'=0.00018 [s]

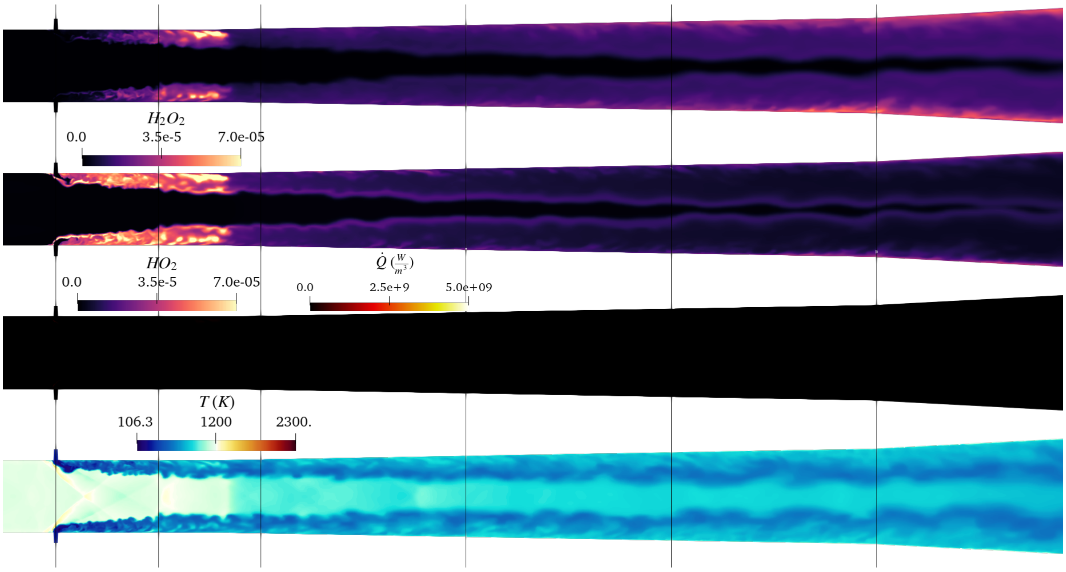

Figure D.15: 3D, supersonic combustion ignition, t'=0.00023 [s]

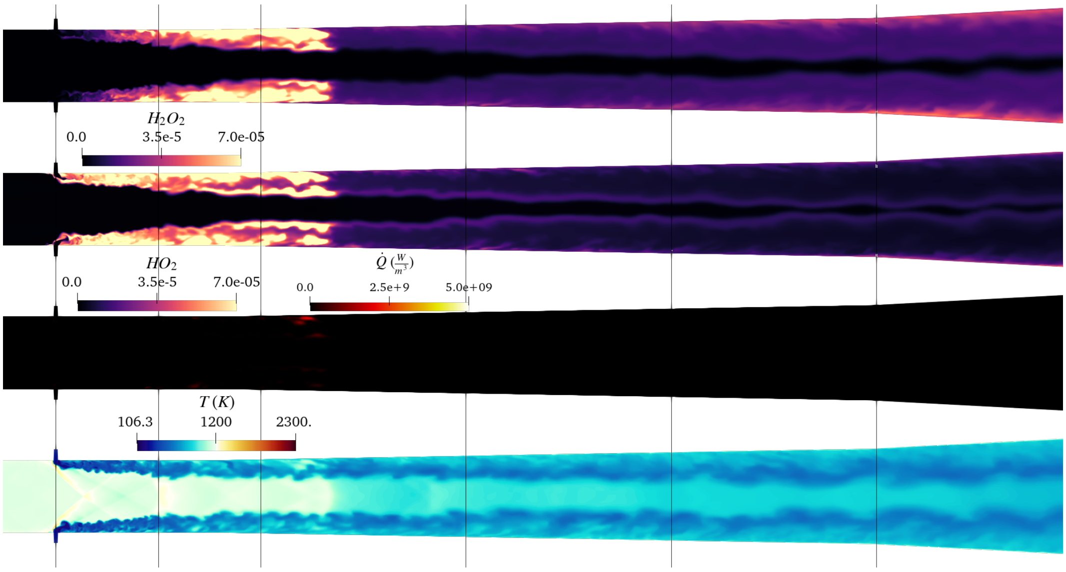

Figure D.16: 3D, supersonic combustion ignition, t'=0.00027 [s]

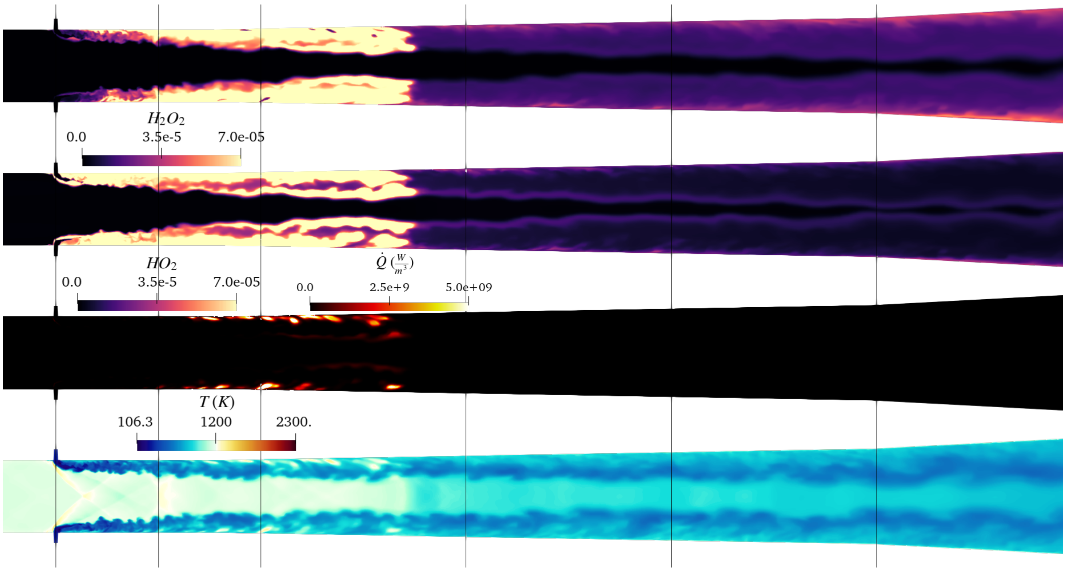

Figure D.17: 3D, supersonic combustion ignition, t'=0.0003 [s]

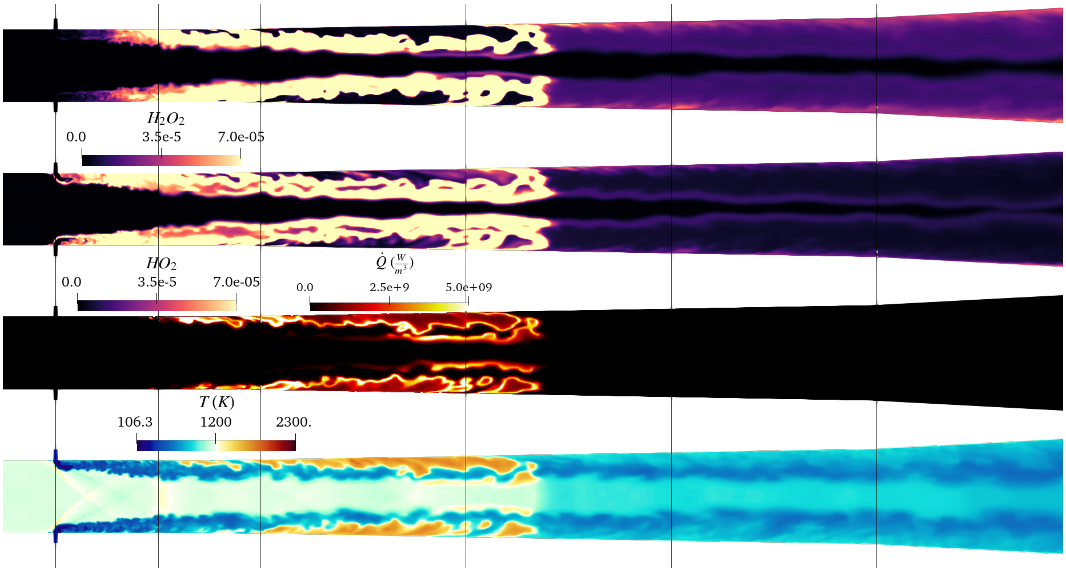

Figure D.18: 3D, supersonic combustion ignition, t'=0.00035 [s]

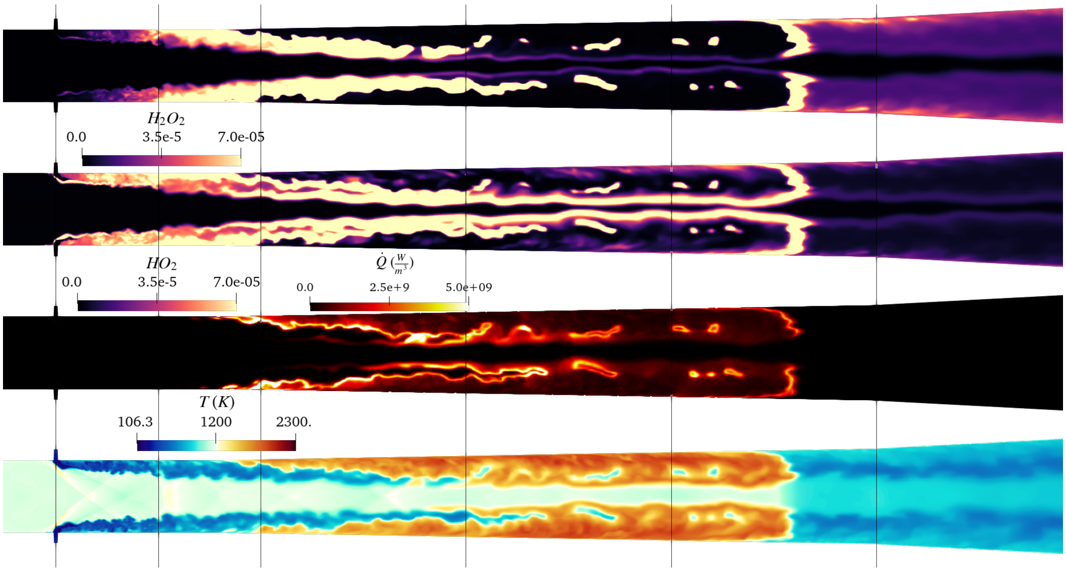

Figure D.19: 3D, supersonic combustion ignition, t'=0.00044 [s]

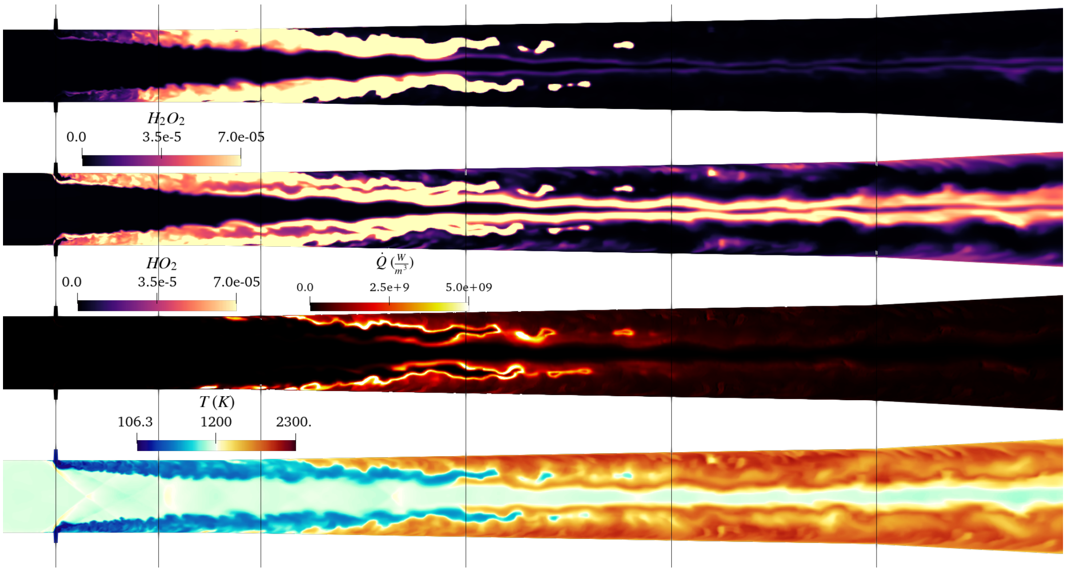

Figure D.20: 3D, supersonic combustion ignition, t'=0.00058 [s]

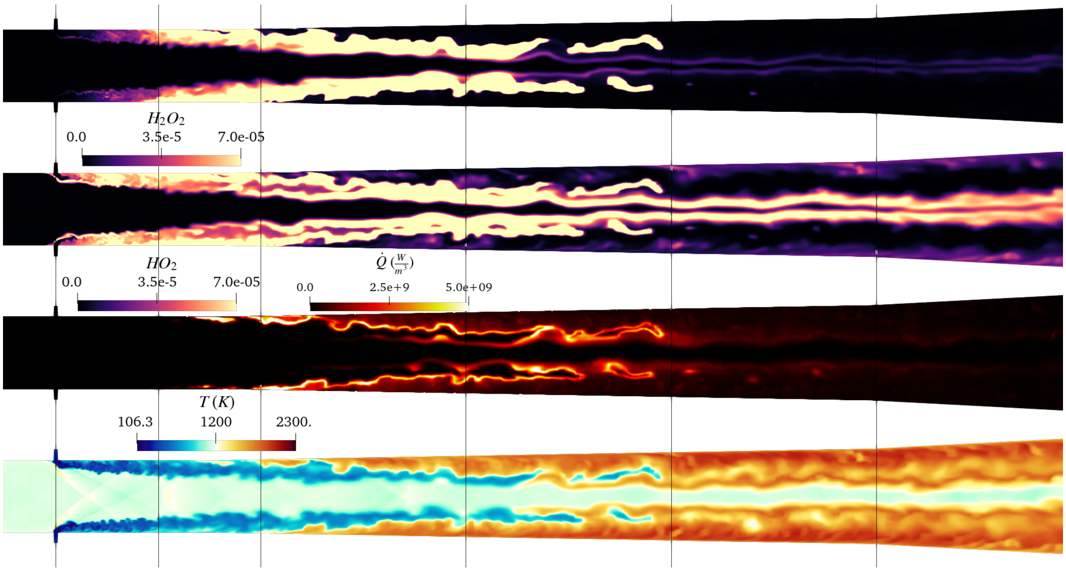

Figure D.21: 3D, supersonic combustion ignition, t'=0.00259 [s]

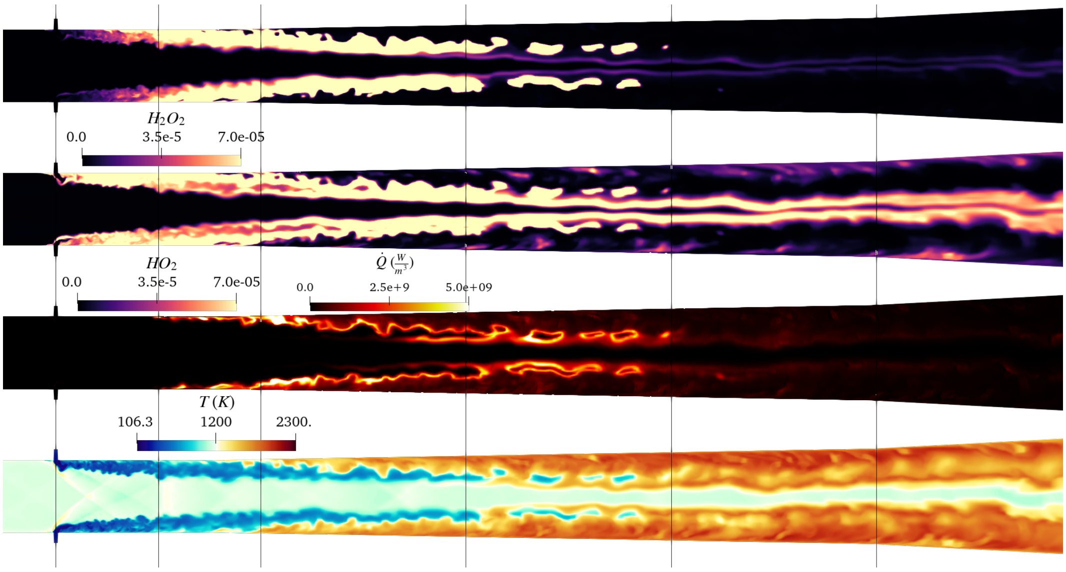

Figure D.22: 3D, supersonic combustion ignition, t'=0.00474 [s]

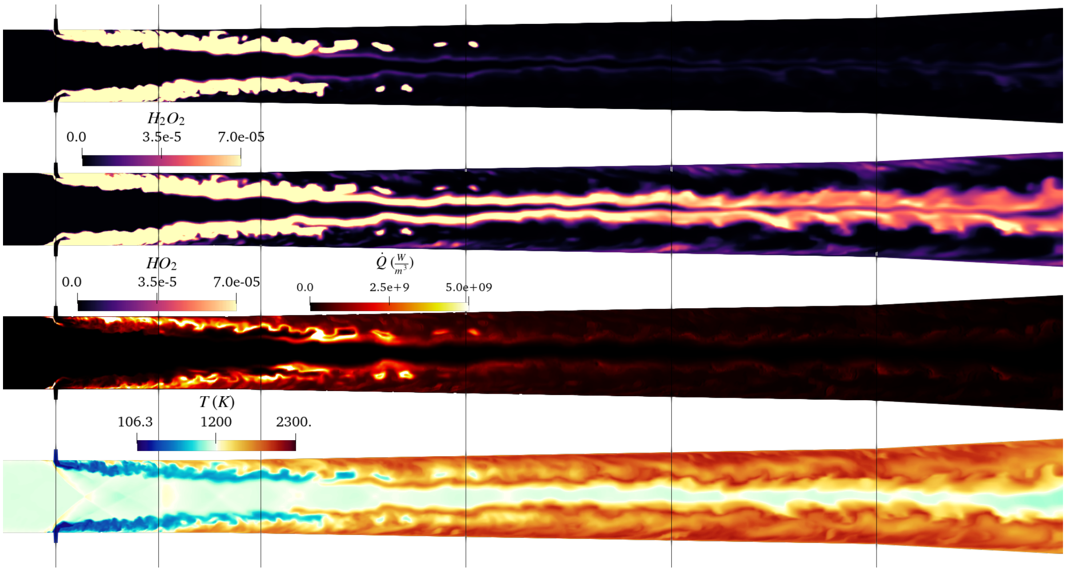

Figure D.23: 3D, supersonic combustion ignition, t'=0.01018 [s]

The ignition-radicals are generated after the propagation of inlet conditions, the generation of the species is violent, almost saturating the defined scale. The first notable heat release is at $t' = 0.00027[s]$, and the counter-flow flame propagation is justified by looking at high H_2O_2 and HO_2 mass fraction values. The first abrupt rise in temperature starts from the walls and then propagates both upstream and downstream, with the downstream propagation favored also by other hot spots along the flame while being convected. After having covered completely the supersonic jets, the slower counter-flow crawling is reported. As the latest snapshot shows, the ignition-related species display high mass fractions values, that favor stronger and upstream heat release, which in turn increases the temperature. The latter change, after some time, causes boundary layer, shockwaves and bulk flow distortions, that triggers more chemical activities upstream generating a feedback loop, until a limit condition will be meet, where the heat-release will not be powerful enough to trigger upstream changes. Unfortunately, this condition is not reached in the simulated window.

Bibliography

[1] Johan Steelant. “Sustained Hypersonic Flight in Europe: Technology Drivers for LAPCAT II”. In: *16th AIAA/DLR/DGLR International Space Planes and Hypersonic Systems and Technologies Conference*. Bremen, Germany: American Institute of Aeronautics and Astronautics (AIAA), Oct. 2009 (cit. on pp. 1, 10).

[2] Jean-Paul Rodrigue. *The Geography of Transport Systems*. 6th. New York: Routledge, 2024 (cit. on pp. 1, 3).

[3] A. Vincent-Randonnier, A. Ristori, V. Sabelnikov, N. Zettervall, and C. Fureby. “A Combined Experimental and Computational Study of the LAPCAT II Supersonic Combustor”. In: *22nd AIAA International Space Planes and Hypersonics Systems and Technologies Conference*. Orlando, United States, Sept. 2018 (cit. on pp. 1, 12, 14, 18–20, 22, 23, 31, 33, 37, 38, 42, 43, 52, 56, 63, 65, 67, 70, 71, 82, 83, 85, 96–98, 119).

[4] S. Balland and A. Vincent-Randonnier. “Numerical Study of the Hydrogen/Air Combustion with CEDRE on LAERTE Dual Mode Ramjet Combustion Experiment”. In: *20th AIAA International Space Planes and Hypersonics Systems and Technologies Conference*. Glasgow, Scotland, 2015 (cit. on pp. 1, 32, 92).

[5] Guillaume Pelletier, Marc Ferrier, Axel Vincent-Randonnier, and Arnaud Mura. “Wall Roughness Effects on Combustion Development in Confined Supersonic Flow”. In: *Journal of Propulsion and Power* 37.5 (Oct. 2020) (cit. on pp. 1, 96).

[6] William H. Heiser and David T. Pratt. *Hypersonic Airbreathing Propulsion*. AIAA Education Series. American Institute of Aeronautics and Astronautics, 1994 (cit. on pp. 3, 5, 6, 8).

[7] Dora Musielak. *Scramjet Propulsion: A Practical Introduction*. 1st. Aerospace Series. Hoboken, NJ: John Wiley & Sons, 2022 (cit. on pp. 3, 5).

[8] Corin Segal. *The Scramjet Engine: Processes and Characteristics*. Cambridge Aerospace Series. Cambridge: Cambridge University Press, 2009 (cit. on pp. 3, 4).

[9] Kenneth K. Kuo. *Principles of combustion*. John Wiley & Sons, 2005 (cit. on pp. 4, 40, 69).

[10] Barry Edney. *Anomalous Heat Transfer and Pressure Distributions on Blunt Bodies at Hypersonic Speeds in the Presence of an Impinging Shock.* Tech. rep. FFA Report 115. Stockholm, Sweden: Aeronautical Research Institute of Sweden (FFA), 1967 (cit. on p. 5).

[11] Javier Urzay. “Supersonic Combustion in Air-Breathing Propulsion Systems for Hypersonic Flight”. In: *Annual Review of Fluid Mechanics* 50.1 (2018), pp. 593–627 (cit. on pp. 5, 6, 43).

[12] John D. Anderson Jr. *Modern Compressible Flow: With Historical Perspective.* 4th. New York, NY: McGraw-Hill Education, 2020 (cit. on p. 5).

[13] Nicole Viola et al. “Main Challenges and Goals of the H2020 STRATOFLY Project”. In: *Aerotecnica Missili & Spazio* 100 (2021), pp. 95–110 (cit. on p. 7).

[14] STRATOFLY Consortium. *STRATOFLY: Stratospheric Flying Opportunities for High-Speed Propulsion Concepts.* Grant Agreement No. 769246. European Commission, Horizon 2020. 2021. URL: `https://www.h2020-stratofly.eu/` (cit. on p. 7).

[15] ILA-boy. *File:* $ILA_{2}008_{P}D_{4}46$*.jpg.* Wikimedia Commons. Public Domain. Available at: `https://commons.wikimedia.org/w/index.php?curid=4212871`. 2006. (Visited on 05/20/2024) (cit. on p. 8).

[16] MBDA Systems. *Meteor: Beyond Visual Range Air-to-Air Missile (BVRAAM).* Official Product Specification. 2023. URL: `https://www.mbda-systems.com/product/meteor/` (cit. on p. 8).

[17] MBDA Missile Systems. *MBDA: A World Leader in Complex Weapon Systems.* Official Corporate Website. 2024. URL: `https://www.mbda-systems.com/` (cit. on p. 8).

[18] James Schultz. *Rockwell X-30 NASP 3 concept.* Public Domain. Document ID: EL-2001-00432. Available at: `https://commons.wikimedia.org/w/index.php?curid=915543`. 2011 (cit. on p. 9).

[19] Dietrich E. Koelle. “SÄNGER II: A Hypersonic Flight and Space Transportation System”. In: *Proceedings of the 16th Congress of the International Council of the Aeronautical Sciences (ICAS).* ICAS-88-1.5.1. Presented by Messerschmitt-Bölkow-Blohm (MBB) Space Communications and Propulsion Systems Division. Jerusalem, Israel: ICAS/AIAA, 1988, pp. 687–693 (cit. on p. 8).

[20] François Falempin. “French Hypersonic Program PREPHA – System studies synthesis”. In: *Proceedings of the XIII International Symposium on Air Breathing Engines (ISABE).* Chattanooga, TN, Sept. 1997 (cit. on p. 10).

[21] A. Vincent-Randonnier, Y. Moule, and M. Ferrier. “Combustion of hydrogen in hot air flows within LAPCAT-II Dual Mode Ramjet combustor at Onera-LAERTE facility – Experimental and Numerical Investigation”. In: *19th AIAA International Space Planes and Hypersonics Systems and Technologies Confer-*

ence. Atlanta, GA, United States, 2014 (cit. on pp. 10–13, 21, 33, 35, 37, 49, 60, 92, 98, 131).

[22] Dominique Scherrer, Olivier Dessornes, Marc Ferrier, Axel Vincent-Randonnier, Yann Moule, and Vladimir Sabelnikov. "Research on Supersonic Combustion and Scramjet Combustors at ONERA". In: *AerospaceLab* 11 (May 2016) (cit. on p. 13).

[23] Joel Guerrero. *Introduction to OpenFOAM 8: Detailed Training Material.* Tech. rep. Wolf Dynamics, 2020. URL: `https://www.wolfdynamics.com/training/introOF8/all.pdf` (cit. on pp. 14, 20).

[24] OpenFOAM Foundation. *OpenFOAM version 7.* 2019. URL: `https://openfoam.org/version/7/` (cit. on p. 14).

[25] Henry G. Weller, G. Tabor, Hrvoje Jasak, and C. Fureby. "A Tensorial Approach to CFD using Object Oriented Techniques". In: *Computers in Physics* 12.6 (1997), pp. 620–631 (cit. on p. 14).

[26] Alexander Kurganov and Eitan Tadmor. "New High-Resolution Central Schemes for Nonlinear Conservation Laws and Convection-Diffusion Equations". In: *Journal of Computational Physics* 160.1 (2000), pp. 241–282. ISSN: 0021-9991 (cit. on p. 14).

[27] OpenFOAM Foundation. *rhoCentralFoam Source Code.* OpenFOAM Foundation. 2019. URL: `https://github.com/OpenFOAM/OpenFOAM-7/tree/master/applications/solvers/compressible/rhoCentralFoam` (cit. on p. 14).

[28] OpenFOAM Foundation. *reactingFoam Source Code.* OpenFOAM Foundation. 2019. URL: `https://github.com/OpenFOAM/OpenFOAM-7/tree/master/applications/solvers/combustion/reactingFoam` (cit. on p. 14).

[29] A. Vincent-Randonnier, V. Sabelnikov, A. Ristori, N. Zettervall, and C. Fureby. "An experimental and computational study of hydrogen–air combustion in the LAPCAT II supersonic combustor". In: *Proceedings of the Combustion Institute* 37.3 (2019), pp. 3703–3711 (cit. on pp. 14, 37, 42, 52).

[30] Suresh Menon and Christer Fureby. "Computational Combustion". In: *Encyclopedia of Aerospace Engineering.* Ed. by Richard Blockley and Wei Shyy. John Wiley & Sons, 2010. Chap. Aerothermodynamics and Combustion (cit. on pp. 14, 16).

[31] Dimitris Drikakis, Christer Fureby, Fernando F. Grinstein, and Mattias Liefendahl. "ILES with Limiting Algorithms". In: *Implicit Large Eddy Simulation: Computing Turbulent Fluid Dynamics.* Ed. by Fernando F. Grinstein, Len Margolin, and Bill Rider. Cambridge University Press, 2007. Chap. 4, pp. 94–124 (cit. on p. 15).

[32] Eugenio Giacomazzi, F. R. Picchia, and N. Arcidiacono. "On the Distribution of Lewis and Schmidt Numbers in Turbulent Flames". In: *Proceedings of the 30th Italian Meeting on Combustion.* Ischia, Italy, June 2007 (cit. on p. 15).

[33] Ernst Hairer and Gerhard Wanner. *Solving Ordinary Differential Equations II: Stiff and Differential-Algebraic Problems.* 2nd. Berlin, Heidelberg: Springer-Verlag, 1996 (cit. on p. 15).

[34] Christer Fureby and Tommie Nilsson. "Coarse-Graining Supersonic Combustion". In: *Coarse Graining Turbulence: Modeling and Data-Driven Approaches and their Applications.* Ed. by Fernando F. Grinstein, Filipe S. Pereira, and Massimo Germano. Cambridge University Press, 2025. Chap. 15 (cit. on pp. 15–18, 33).

[35] Alessandro Ercole, Daniel Lörstad, and Christer Fureby. "Large Eddy Simulations of a Turbulent Premixed Swirling Flame with Finite-Rate Chemistry and Flame-Wrinkling Turbulent Combustion Models". In: *Flow, Turbulence and Combustion* 114 (2025), pp. 1377–1404 (cit. on pp. 15, 17–19).

[36] OpenStack Foundation. *centralCourantNo.H Source File API Guide.* 2022 (cit. on p. 15).

[37] Alessandro Ercole. "Numerical Investigation of the HIFiRE 2 Combustion Chamber". MA thesis. Turin, Italy: Politecnico di Torino, 2022 (cit. on p. 15).

[38] Stephen B. Pope. *Turbulent Flows.* Cambridge: Cambridge University Press, 2000 (cit. on pp. 16, 17).

[39] David C. Wilcox. *Turbulence Modeling for CFD.* 3rd. La Canada, California: DCW Industries, 2006 (cit. on p. 16).

[40] Florian R. Menter. "Two-equation eddy-viscosity turbulence models for engineering applications". In: *AIAA Journal* 32.8 (1994), pp. 1598–1605 (cit. on p. 16).

[41] Pierre Sagaut. *Large Eddy Simulation for Incompressible Flows: An Introduction.* Berlin: Springer Science & Business Media, 2006 (cit. on p. 16).

[42] R. Byron Bird, Warren E. Stewart, and Edwin N. Lightfoot. *Transport Phenomena.* 2nd. New York: John Wiley & Sons, 2002 (cit. on p. 17).

[43] Vladimir Anatolievich Sabelnikov and Christer Fureby. "Extended LES-PaSR Model for Simulation of Turbulent Combustion". In: *Progress in Propulsion Physics.* Vol. 4. EUCASS Advances in Aerospace Sciences. EDP Sciences, 2013, pp. 539–568 (cit. on p. 18).

[44] Niklas Zettervall. *Reaction mechanisms for use in Computational Fluid Dynamics.* `https://mechanismsforcfd.com/` (cit. on p. 18).

[45] Sergei S. Sazhin, E. M. Sazhina, O. Faltsi-Saravelou, and P. Wild. "The P-1 model for thermal radiation transfer: Advantages and limitations". In: *Fuel* 75.3 (1996), pp. 289–294 (cit. on p. 19).

[46] Nitin P. Padture, Maurice Gell, and Eric H. Jordan. "Thermal Barrier Coatings for Gas-Turbine Engine Applications". In: *Science* 296.5566 (2002), pp. 280–284 (cit. on pp. 22, 63).

[47] Kunal Mondal, Luis Nuñez, Calvin M. Downey, and Isabella J. Van Rooyen. "Recent advances in the thermal barrier coatings for extreme environments". In: *Materials Science for Energy Technologies* 4 (2021), pp. 255–271 (cit. on pp. 22, 63).

[48] Guido Boffetta and Robert E Ecke. "Two-dimensional turbulence". In: *Annual Review of Fluid Mechanics* 44.1 (2012), pp. 427–451 (cit. on p. 34).

[49] Mehdi Jangi and Xue-Song Bai. "Multidimensional chemistry coordinate mapping approach for combustion modelling with finite-rate chemistry". In: *Combustion Theory and Modelling* 16.6 (2012), pp. 1109–1132 (cit. on p. 48).

[50] Theodore L. Bergman and Adrienne S. Lavine. *Fundamentals of Heat and Mass Transfer*. 8th. John Wiley & Sons, 2017 (cit. on p. 63).

[51] R. E. Taylor, X. Wang, and X. Xu. "Thermophysical properties of thermal barrier coatings". In: *Surface and Coatings Technology* 120–121 (1999), pp. 89–95 (cit. on p. 63).

[52] David L. Ellis. *Cu-Cr-Nb-Zr Alloy for Rocket Engines and Other High-Heat-Flux Applications*. Tech. rep. NASA/TM-2005-213566. Cleveland, Ohio: NASA Glenn Research Center, 2005 (cit. on p. 63).

[53] OpenFOAM Foundation. *Bug report #3473: wallHeatFlux does not account for radiation in all solvers*. OpenFOAM Issue Tracker. Available at: `https://bugs.openfoam.org/view.php?id=3473`. 2020 (cit. on pp. 64, 66, 79, 100, 104, 122).